

Optical Properties and Radiative Forcing of Southern African Biomass Burning  
Aerosol

Brian Indrek Magi

A dissertation  
submitted in partial fulfillment of the  
requirements for the degree of

Doctor of Philosophy

University of Washington

2006

Program Authorized to Offer Degree:  
Department of Atmospheric Sciences

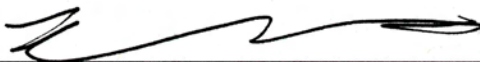
University of Washington  
Graduate School

This is to certify that I have examined this copy of a doctoral dissertation by

Brian Indrek Magi

and have found it is complete and satisfactory in all respects,  
and that any and all revisions required by the final  
examining committee have been made.

Chair of the Supervisory Committee:

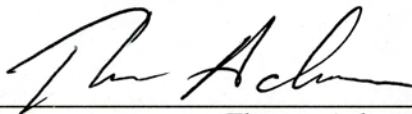


Qiang Fu

Reading Committee:



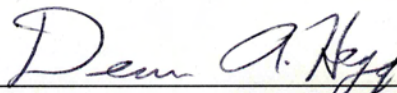
Qiang Fu



Thomas Ackerman



Theodore Anderson



Dean Hegg

Date: 26 July 2006

In presenting this dissertation in partial fulfillment of the requirements for the doctoral degree at the University of Washington, I agree that the Library shall make its copies freely available for inspection. I further agree that extensive copying of the dissertation is allowable only for scholarly purposes, consistent with "fair use" as prescribed in the U.S. Copyright Law. Requests for copying or reproduction of this dissertation may be referred to ProQuest Information and Learning, 300 North Zeeb Road, Ann Arbor, MI 48106-1346, 1-800-521-0600, or to the author.

Signature \_\_\_\_\_

Date \_\_\_\_\_

University of Washington

**Abstract**

Optical Properties and Radiative Forcing of Southern African Biomass Burning  
Aerosol

Brian Indrek Magi

Chair of the Supervisory Committee:  
Professor Qiang Fu  
Department of Atmospheric Sciences

Particles injected into the atmosphere by biomass burning, or the combustion of vegetation, attenuate incoming sunlight and change the radiative balance of the Earth. African biomass burning alone accounts for ~40% of all global biomass burning emissions. In this dissertation, we analyze data collected during the Southern African Research Initiative (SAFARI) field campaign in August and September 2000. We find that when the meteorology was controlled by large-scale subsidence, aerosol single scattering albedos at 550 nm ( $\omega_{o,550}$ ) averaged  $0.89 \pm 0.03$  with extinction coefficients at 550 nm ( $\sigma_{ext,550}$ ) ranging from ~50-100  $Mm^{-1}$  throughout lowest 4-5 km of the atmosphere. Tropical smoke transported to the south during a frontal passage that changed the airflow patterns revealed an aerosol with different physical, chemical, and optical properties. Average values of  $\omega_{o,550}$  decreased to  $0.83 \pm 0.03$  and  $\sigma_{ext,550}$  increased by a factor of two or more to ~100-200  $Mm^{-1}$ .

To incorporate the measurements into an atmospheric radiative transfer model, we design and describe an original retrieval algorithm which uses the measurements as constraints and finds an optically-equivalent size distribution and refractive index that produce a self-consistent set of aerosol optical properties for wavelengths spanning the solar spectrum. Using the retrieved aerosol optical properties as input to the radiative transfer model, we estimate the radiative forcing of southern African biomass burning aerosol. The diurnally-averaged shortwave aerosol direct radiative forcing ranges from  $-7.1 \pm 2.7 \text{ W m}^{-2}$  to  $-8.9 \pm 5.2 \text{ W m}^{-2}$  at the top of the atmosphere and  $-22.9 \pm 3.0 \text{ W m}^{-2}$  to  $-73.0 \pm 7.1 \text{ W m}^{-2}$  at the surface. The larger magnitudes of surface radiative forcing are a result of increased concentrations of absorbing particles in the lowest  $\sim 5 \text{ km}$  of the atmosphere which act to both increase  $\sigma_{\text{ext}}$  and decrease  $\omega_0$ . The increase in  $\sigma_{\text{ext}}$  and decrease in  $\omega_0$  reduces the range of radiative forcing at the top of the atmosphere, which has important implications for interpreting satellite data.

## TABLE OF CONTENTS

List of Figures .....	iii
List of Tables .....	iv
Chapter 1. Introduction .....	1
1.1. Climate Change and Biomass Burning .....	1
1.2. Aerosol Physical and Chemical Properties .....	3
1.3. Aerosol Optical Properties .....	10
1.4. Southern African Biomass Burning and SAFARI-2000 .....	17
1.5. Objectives and Organization of Dissertation .....	23
Chapter 2. Data .....	25
2.1. Airborne Instrumentation .....	25
2.2. Aerosol Robotic Network (AERONET) .....	35
Chapter 3. Data Analysis .....	38
3.1. SAFARI-2000 and the River of Smoke .....	38
3.2. The Effects of Relative Humidity on Biomass Burning Aerosol .....	41
3.3. Aerosol Optical Depth Comparison .....	58
3.4. Aerosol Vertical Profiles .....	71
3.5. SAFARI-2000 Data Analysis Summary .....	86
Chapter 4. Look-Up Table Methodology .....	89
4.1. Motivation .....	91
4.2. Description .....	92
4.3. Methodology .....	97
4.4. Application .....	113
4.5. Analysis .....	118
4.6. Summary of Look-Up Table Methodology .....	123
Chapter 5. Biomass Burning Aerosol Radiative Forcing .....	126
5.1. Fu-Liou Radiative Transfer Model Overview .....	126
5.2. Model Input .....	128
5.3. Vertical Profiles of Aerosol Radiative Effects .....	136
5.4. Uncertainty Analysis .....	139
5.5. Biomass Burning Aerosol Radiative Forcing .....	151
Chapter 6. Summary .....	157
6.1. Southern African Aerosol Characteristics .....	157
6.2. Southern African Radiative Forcing .....	158

6.3. Implications for Modeling Southern African Aerosol .....	159
6.4. Recommendation for Future Work .....	159
References .....	161

## LIST OF FIGURES

Figure Number	Page
1.1. Radiative Forcing .....	4
1.2. Aerosol Spatial Distribution.....	6
1.3. Global Carbon Emissions .....	18
1.4. Map of Africa .....	19
2.1. University of Washington Research Aircraft .....	26
3.1. Satellite View of The River of Smoke .....	40
3.2. Locations of Humidographs .....	46
3.3. Sample Humidograph from Regional Haze .....	52
3.4. Sample Humidograph from Smoke Plume .....	55
3.5. Locations of Vertical Profiles .....	60
3.6. Comparison of Aerosol Optical Depth Measurements .....	67
3.7. Absorption Angstrom Exponent Assumption .....	69
3.8. Vertical Profiles from 22 August 2000 .....	79
3.9. Vertical Profiles from 24 August 2000 .....	80
3.10. Vertical Profiles from 31 August 2000 .....	82
3.11. Vertical Profiles from 3 September 2000 .....	83
3.12. Vertical Profiles from 6 September 2000 .....	84
3.13. Vertical Profiles from 6 September 2000 .....	85
4.1. Look-up Table Optical Properties .....	98
4.2. Single Scattering Albedo Choices .....	107
4.3. Single Scattering Albedo Constraint .....	109
5.1. Vertical Profiles of Radiative Effects .....	137
5.2. Sensitivity of Top of the Atmosphere Radiative Forcing .....	142
5.3. Sensitivity of Surface Radiative Forcing .....	143



## LIST OF TABLES

Table Number	Page
3.1. Description of Humidographs .....	47
3.2a. Empirical Fit Coefficients for Humidographs ( $\lambda = 450$ nm) .....	48
3.2b. Empirical Fit Coefficients for Humidographs ( $\lambda = 550$ nm) .....	49
3.2c. Empirical Fit Coefficients for Humidographs ( $\lambda = 700$ nm) .....	50
3.3. Mean Humidographs .....	54
3.4. Description of Vertical Profiles .....	59
3.5. Comparison of Aerosol Optical Depth Measurements .....	64
3.6. Summary of the Comparison of Aerosol Optical Depth Measurements .....	66
3.7. Aerosol Mean Physical Properties .....	75
3.8. Aerosol Mean Optical Properties .....	77
4.1. Input to the Look-up Table .....	94
4.2. Retrieved Optically-Equivalent Size Distributions .....	119
4.3. Retrieved Optical Properties .....	121
5.1. Band- and Column- Averaged Optical Properties .....	133
5.2. Regression Statistics of Radiative Forcing Sensitivity .....	145
5.3. Sensitivity of Radiative Forcing to Optical Properties .....	148
5.4. Measurement-Based Estimate of Radiative Forcing .....	152

## ACKNOWLEDGEMENTS

I thank the late Peter V. Hobbs, first and foremost, for his dedication to science and for helping me develop the confidence necessary to critically analyze my own science as well as the work of other scientists. Peter pushed me when I needed it most and never let me forget how special the opportunity to study science could be.

I thank Qiang Fu for assuming the role of my Ph. D advisor after Peter passed away in July 2005. He has been a very positive influence for my research project and he is a great example of a successful and inspirational part of a university community. The rest of my Ph. D. committee, comprised of Tom Ackerman, Tad Anderson, and Dean Hegg, provided excellent advice and guidance, willingly participated in a number of informal meetings over the last year, and inspired me to really think about the Ph. D. process. I only wish I had talked to my committee members more.

My mom and dad, Mai and Mart Magi, have helped in ways they may never know and I do not know how to say what their support means to me in a few words. My favorite part of graduate school has been marrying the lovely Heidi Taylor in July 2003. Heidi has inspired me to think deeply about the privilege of being a part of a university. Her vision for a community of knowledge and learning is one I am proud to be able to know.

Finally, I want to acknowledge the members of the Cloud and Aerosol Research Group: Art Rangno, Tom Wilson, Debbie Wolf, Judy Opacki, John Locatelli, Mark Stoelinga, Ricky Sinha, Stan Rose, and Joerg Trentmann. This very social and entertaining group provided a great place for work. I have also been surrounded by diligent officemates and fellow graduate students, who included Tim Garrett, Chris Woods, Dave Reidmiller, and is currently Louise Leahy.

## **DEDICATION**

To my grandparents, who were willing to change their lives to make mine better.

## Chapter 1. Introduction

### 1.1. Climate Change and Biomass Burning

Climate change is a field of multi-disciplined scientific research that has tumbled into the public policy arena because of the real impacts the scientific evidence suggests. Major news sources and magazines regularly publish articles describing the policies and people affected by events such as heat waves, droughts, pollution [Appenzeller, 2006; Becker, 2004; Parfit, 2005], glacial retreat [Glick, 2004], rising sea levels, threatened ecosystems [Eliot, 2004; Montaigne, 2004; Eliot, 2005; Ehrlick, 2006], and even how we as a global community must begin to adapt to the forecasted changes in the next century [e.g. Appenzeller, 2004; Appenzeller and Dimick, 2004; Morell, 2004; Carroll, 2005; Kluger, 2005; Kolbert, 2005a-c; Mitchell, 2006]. The consensus of climate change scientists and the current research is summarized in the United Nations Intergovernmental Panel on Climate Change (IPCC) third assessment report (AR3) and is publicly available online [IPCC, 2001]. A fourth assessment report with significant updates is scheduled to be published by the IPCC in 2007 [e.g. Wild *et al.*, 2005; [www.climate-science.gov/Library/ipcc/wg14ar-review.htm](http://www.climate-science.gov/Library/ipcc/wg14ar-review.htm)].

Although climate change research is a global-scale, multivariate problem, research is often focused on smaller scales to understand the physical processes and the regional implications. Anthropogenic pollution is one example of a problem that is well-suited to a smaller scale examination. The disparate sources

of pollution in turn offer other specialized areas of study. The smoke from biomass burning is an example of a specialized branch of the general study of atmospheric pollution.

Biomass burning, or the combustion of vegetation, has affected the terrestrial ecosystem for thousands of years. Using a dynamic vegetation model of the Earth, *Bond et al.* [2005] showed that ~40% of the vegetation distribution on Earth appears to be controlled by fires rather than climatological parameters such as temperature and precipitation. *Miller et al.* [2005] suggested that the mechanism of a human-caused mass extinction of Australia's largest mammals that occurred ~50000 years ago was likely due to the introduction of anthropogenic biomass burning when the drought-adapted mosaic of trees shifted to fire-adapted grasslands and favored the survival of certain animals over others. This shifting from a tree-dominated landscape to one dominated by fire-adapted grasslands is similar to the modeling results of *Bond et al.* [2005] and, in the end, the evidence suggests that an Earth without human-induced fires would be a very different place.

Biomass burning originates from both natural and anthropogenic sources. Natural biomass burning is mainly the result of lightning igniting dry vegetation. Anthropogenic biomass burning is an ancient practice [*Delmas et al.*, 1999; *Sinha et al.*, 2003; *Miller et al.*, 2005] that is used to clear dead vegetation for new plant growth, hunting, signal generation, and domestic cooking and heating [*Bertschi et*

*al.*, 2003; *Roden et al.*, 2005]. Most biomass burning is anthropogenic in origin [*Bond et al.*, 2004].

In Fig. 1.1, we reproduce a figure from *Ramaswamy et al.* [2001] which concisely summarizes how different constituents of the Earth's atmosphere affect the radiative balance of the Earth-Sun system. According to Fig. 1.1, biomass burning is still in the process of being understood [*Penner et al.*, 1992; *Hobbs et al.*, 1997]. The emissions from biomass burning together with other sources of atmospheric pollution, contribute significantly to the uncertainty associated with effects of climate change [e.g. *Anderson et al.*, 2003a; *Schwartz*, 2004; *Andreae et al.*, 2005; *Delworth et al.*, 2005; *Palle et al.*, 2005]. By analyzing in situ aircraft observation, this dissertation examines the microphysical and optical characteristics of southern African biomass burning emissions and estimates the effects of the biomass burning aerosol on solar radiation.

## **1.2. Aerosol Physical and Chemical Properties**

An aerosol is a distribution of solid or liquid particles of varying physical size and chemical composition that are suspended in air. Particles in the smoke from biomass burning, pollution from power plants, and dust that is lifted into the atmosphere, are all examples of atmospheric aerosols. Most particles are in the lowest 5 km of the troposphere which extends from the surface to ~20 km. Good examples of observations of different aerosol vertical profiles from around the world can be found in *Magi et al.* [2003], *Redemann et al.* [2003], *Magi et al.*

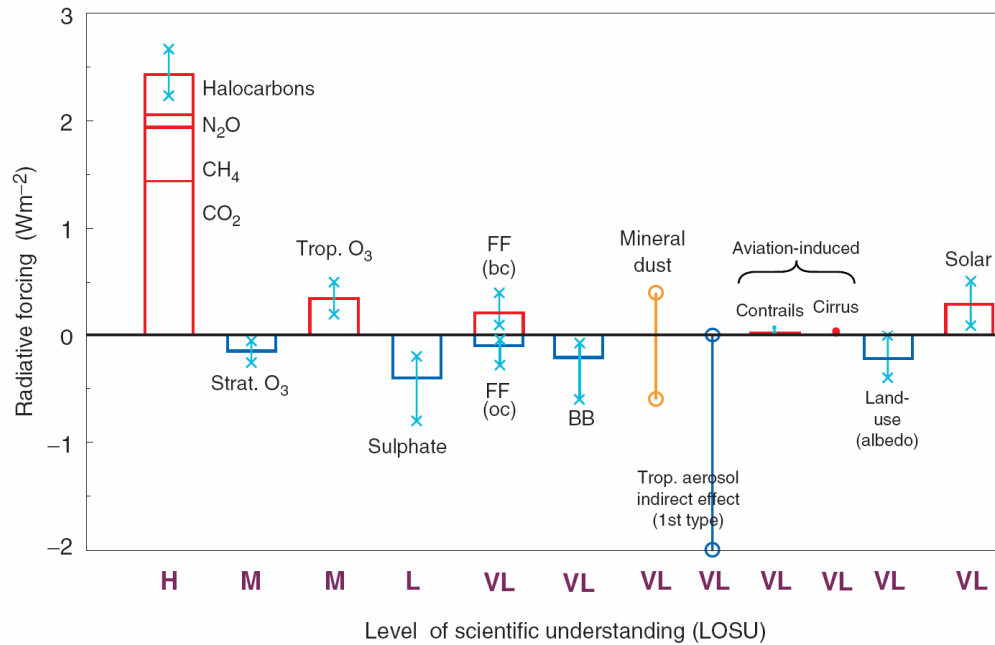


Fig. 1.1. Globally and annually averaged radiative forcing ( $\text{W m}^{-2}$ ) for a period from about 1750-2000 due to different atmospheric constituents. Positive (negative) radiative forcing implies a warming (cooling) effect. The height of the rectangles indicate the central or best estimate. The error bars with an 'x' are based on published literature while the error bars with an 'o' are uncertain due to a paucity of published values. The level of scientific understanding (LOSU) represents a qualitative summary of the understanding of the particular atmospheric constituent where H, M, L, VL, mean High, Medium, Low, and Very Low, respectively. Fossil fuel (FF) burning is separated into black carbon (BC) and organic carbon (OC) components, while the carbonaceous components of biomass burning (BB) are not. The figure and a full description can be found in *Ramaswamy et al.* [2001].

[2005], and *Schmid et al.* [2006]. The lifetime of particles in the troposphere ranges from a few days to weeks (compared to decades for greenhouse gases like carbon dioxide) and the sources are widely varying [*Ramaswamy et al.*, 2001]. This results in a globally heterogeneous spatial and temporal distribution as suggested by the global model input in *Reddy et al.* [2005a] and reproduced in Fig. 1.2, or similarly in the modeling studies of *Chung et al.* [2005] and *Takemura et al.* [2005]. One important note is that the aerosol source strengths and distributions in models are not necessarily the same.

Aerosols range in size from  $\sim 1$  nm ( $0.001 \mu\text{m}$ ) to as large as 1 mm ( $1000 \mu\text{m}$ ) diameter, but there is a tendency of aerosols to be grouped together in different size modes that are dependent on the age and the source. Particle diameter,  $D_p$ , is often used to differentiate between these modes of an aerosol size distribution [*Seinfeld and Pandis*, 1998]. For the purposes of terminology, we define the nucleation mode of an aerosol size distribution as  $D_p$  between  $0.003 - 0.1 \mu\text{m}$ , the accumulation mode as  $D_p$  between  $0.1 - 1 \mu\text{m}$ , and the coarse mode as  $D_p$  between  $1 - 10 \mu\text{m}$ . Nucleation mode particles are generally produced by direct injection of particles into the atmosphere or by processes like gas-to-particle conversion, and these very small particles rapidly change both in size and chemical composition through processes like coagulation [*Reist*, 1993; *Seinfeld and Pandis*, 1998; *van Poppel et al.*, 2005]. Accumulation mode particle concentrations are generally less than that of the nucleation mode, but these larger particles have a much greater impact on visible radiation [*Reist*, 1993; *Hegg et al.*,



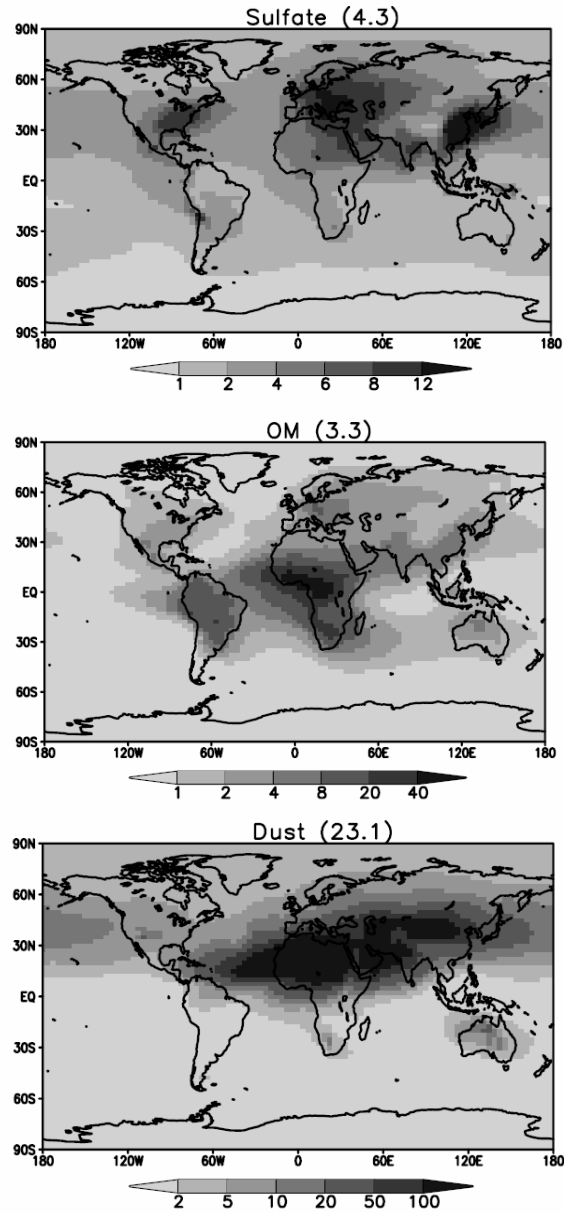


Fig 1.2. The heterogeneous spatial distribution of annually averaged aerosol mass burden (units are  $\text{mg m}^{-2}$ ) of sulfate, organic matter (OM), and dust aerosols (see Section 1.2) used in a general circulation model. The values in parentheses are the total mass burden. The overall larger mass burden of dust aerosols is mainly due to the larger average diameter of these particles. The actual spatial distributions of different types of aerosols vary from model to model [e.g. *Kinne et al.*, 2003, 2005] and are not always based on direct measurements. This figure was published in *Reddy et al.* [2005a].

1993]. Coarse mode particles (such as dust shown in Fig. 1.2) are globally significant as well, but we concentrate in this study on particles in the nucleation and accumulation modes with  $D_p < 1 \mu\text{m}$ , or submicron particles.

An aerosol size distribution is often described using a lognormal distribution that is defined as

$$N_a = n(D_p)dD_p = \frac{N_a}{\sqrt{2\pi} D_p \ln(\sigma_g)} \exp\left[-\frac{(\ln D_p - \ln D_g)^2}{2 \ln^2 \sigma_g}\right] dD_p \quad (1.1)$$

where  $n(D_p) dD_p$  is the particle number concentration (particles/cm<sup>3</sup>) in the diameter range of  $D_p$  to  $D_p+dD_p$ ,  $N_a$  is the total aerosol number concentration in units of particles/cm<sup>3</sup>,  $D_g$  is the geometric mean diameter in units of  $\mu\text{m}$ , and  $\sigma_g$  is the unitless geometric standard deviation. The value of  $D_g$  is defined as

$$\log D_g = \frac{\int_0^\infty n(D_p) \log D_p dD_p}{\int_0^\infty n(D_p) dD_p} \quad (1.2)$$

and  $\sigma_g$  is calculated using

$$\log \sigma_g = \sqrt{\frac{\int_0^\infty (\log D_g - \log D_p)^2 dD_p}{\int_0^\infty n(D_p) dD_p - 1}} \quad (1.3)$$

The sum of two or more lognormal distributions can be used to fully describe the various features of a submicron aerosol size distribution [Haywood *et al.*, 2003a] or the entire aerosol size distribution [Seinfeld and Pandis, 1998; Stier *et al.*, 2005], but often a single lognormal distribution (or unimodal distribution) suffices.

The chemical composition of aerosols is dependent on the source region and this affects the complex refractive index ( $m$ ) which is given by

$$m_{\lambda} = m_{r,\lambda} + im_{i,\lambda} \quad (1.4)$$

where  $m_{r,\lambda}$  is the real part of  $m_{\lambda}$ ,  $m_{i,\lambda}$  is the imaginary part, and  $\lambda$  implies the dependence of the values on the wavelength of radiation.

Common chemical components of aerosols are ionic species like sulfate ( $\text{SO}_4^{2-}$ ) [Charlson, 1999] and various carbonaceous mixtures that are often broadly classified as organic carbon (OC) or black carbon (BC) [d'Almeida *et al.*, 1991; Bond *et al.*, 2004; Reid *et al.* 2004a-b]. Distinguishing between OC and BC is based on the temperature of chemical evolution from particulate matter to a gas when an aerosol sample is heated [e.g. Kirchstetter *et al.*, 2003], but this temperature of particle evolution is not an exact value, resulting in potential overlaps between the OC and BC classifications. Organic aerosol chemistry research has been summarized in extensive reviews by Saxena and Hildemann [1996] and more recently in Kanakidou *et al.* [2005].

In terms of mass, the chemical composition of biomass burning aerosol is dominated by a vast suite of carbonaceous (both OC and BC) particles [Ruellan *et al.*, 1999; Eatough *et al.*, 2003; Kirchstetter *et al.*, 2003; Bond *et al.*, 2004; van Poppel *et al.*, 2005] with smaller contributions from inorganic particles like sulfate [Gao *et al.*, 2003; Li *et al.*, 2003; Ruellan *et al.*, 1999]. Biomass burning particles are mainly a secondary product of the combustion process [Reid *et al.*, 2004a] and form from gas-to-particle conversions [Sinha *et al.*, 2003a; Korontzi *et*

*al.*, 2003]. The vast majority of trace gas emissions from biomass burning are in the form of carbon dioxide (CO<sub>2</sub>) and carbon monoxide (CO) [Hobbs *et al.*, 2003; Reid *et al.*, 2004a] and CO is often used as a tracer for biomass burning emissions [Sinha *et al.*, 2003a].

Aerosol chemical composition also changes over time as aerosols originating from various sources interact. Evidence suggests that biomass burning aerosols age quickly [Hobbs *et al.*, 2003; Li *et al.*, 2003; Magi and Hobbs, 2003; Posfai *et al.*, 2003; Reid *et al.*, 2004a] and therefore measurements made away from the fires are considered to be a fully processed aerosol that is relatively stable until dry or wet deposition processes remove the particles from the atmosphere or until the aerosol interacts with a new airmass and is diluted in concentration.

The chemical properties of aerosols are also dependent on their mixing state [Chylek *et al.*, 1988; Fuller *et al.*, 1999]. Externally mixed aerosols mean that every unique chemical species exists independently of the other [Seinfeld and Pandis, 1998; Ming *et al.*, 2005]. Although this mixing rule is an ideal way of representing chemically varying aerosols, there are times when a real aerosol population is externally mixed [Posfai *et al.*, 2003]. Many studies assume an internally mixed aerosol or have shown that aerosols often exist in this state [Li *et al.*, 2003; Posfai *et al.*, 2004], but there are questions of whether the aerosols are homogeneously mixed together [Haywood *et al.*, 2003a] or whether the aerosols exist as a sort of core with a shell [Ackerman and Toon, 1981; Ross *et al.*, 1998].

The mixing state used to represent aerosols in models [*Jacobson, 2001; Chung and Seinfeld, 2005; Stier et al., 2005*] affects the way solar radiation interacts with the aerosols [*Chylek et al., 1995; Fuller et al., 1999; Ming et al., 2005*], but the treatment of aerosol mixing and aerosol chemistry varies depending on the study [*Textor et al., 2005*].

Aerosol optical properties are dependent on the chemical composition and the chemical mixing state as well as the physical size distribution. These fundamental properties are, however, difficult to fully characterize since aerosol lifetimes are short and the sources are heterogeneous. We discuss the interaction of an aerosol with radiation in the next section.

### 1.3. Aerosol Optical Properties

Radiative transfer theory quantifies the interaction of atmospheric aerosols with radiation using the physical and chemical properties of aerosols discussed in Section 1.2 [*Twomey, 1977; van de Hulst, 1981; Bohren and Huffman, 1983*]. We begin by describing the interaction of radiation with a single particle and then describe the interaction of radiation with a distribution of particles, or an aerosol.

Radiative flux in units of  $\text{W m}^{-2}$  incident on a single particle will be partly scattered or absorbed. The total energy removed from the beam of radiation incident on the particle is proportional to the extinction cross section,  $C_{\text{ext}}$ , which is the sum of the scattering and absorption cross sections

$$C_{\text{ext},\lambda} = C_{\text{sca},\lambda} + C_{\text{abs},\lambda} \quad (1.5)$$

where the “ $\lambda$ ” subscript implies a dependence on the wavelength ( $\lambda$ ) of the incident radiation. For a spherical particle with diameter,  $D_p$ , the unitless extinction efficiency ( $Q_{ext,\lambda}$ ) is then  $C_{ext,\lambda}$  divided by the geometric cross sectional area of the particle

$$Q_{ext,\lambda} = \frac{C_{ext,\lambda}}{\frac{1}{4}\pi D_p^2} \quad (1.6)$$

and can also be expressed as the sum of scattering efficiency ( $Q_{sca,\lambda}$ ) and absorption efficiency ( $Q_{abs,\lambda}$ ), analogous to Eq. 1.5. The values of  $Q_{sca,\lambda}$  and  $Q_{ext,\lambda}$  can be determined accurately using Mie theory [*van de Hulst*, 1981; *Bohren and Huffman*, 1983] given  $\lambda$ ,  $D_p$ , and  $m_\lambda$  [e.g. *Wiscombe*, 1987]. The accuracy of Mie theory is only limited by the knowledge of the physical and chemical properties of the particle and also only applies to spherical particles. There are many discussions of the implications and reality of a spherical aerosol assumption applied to real atmospheric aerosols [*Ruellan et al.*, 1999; *Fuller et al.*, 1999; *Mishchenko et al.*, 2000; *van Poppel et al.*, 2005], but evidence suggests that aerosols tend to become more spherical the longer they reside in the atmosphere [*Posfai et al.*, 2004; *Reid et al.*, 2004a].

The wavelength dependent single scattering albedo,  $\omega_{o,\lambda}$ , describes the probability that radiation incident on a particle will be scattered rather than absorbed and is defined as

$$\omega_{o,\lambda} = \frac{Q_{sca,\lambda}}{Q_{ext,\lambda}} \quad (1.7)$$

with values ranging theoretically between 0 and 1 (1 indicating a non-absorbing, or purely scattering, aerosol). Generally, values of  $\omega_o$  are  $\sim 0.8-0.95$  for mid-visible wavelengths [e.g. *Hess et al.*, 1998], but even over this small range,  $\omega_o$  can have a dramatically different impacts on the radiative balance of the atmosphere [*Russell et al.*, 2002].

If the incident radiation is scattered by a spherical particle, the probability of scattering within a certain differential angle ( $d\theta$ ) with respect to the direction of the incident radiation is given by the scattering phase function,  $P_\lambda(\theta)$ , which is a probability distribution function [e.g. *Twomey*, 1977] that is defined as

$$1 = \frac{1}{2} \int_0^\pi P_\lambda(\theta) \sin(\theta) d\theta \quad (1.8)$$

where the probability distribution function assumes no azimuth angle dependence (i.e. a spherical particle). The asymmetry parameter,  $g_\lambda$ , is defined as the flux-weighted average of the cosine of the scattering angle ( $\theta$ ) or

$$g_\lambda = \frac{1}{2} \int_0^\pi \cos(\theta) P_\lambda(\theta) \sin(\theta) d\theta \quad (1.9)$$

and varies between -1 and +1;  $g_\lambda = -1$  refers to complete back scattering of the incident radiation,  $g_\lambda = +1$  means that incident radiation is completely scattered in the forward direction, and  $g_\lambda = 0$  is isotropic scattering. Usually values of  $g_\lambda$  for aerosols are between 0 and +1, indicating the tendency of radiation to be scattered in the forward hemisphere rather than the backward hemisphere.

The Henyey-Greenstein phase function ( $P_{HG}$ ) is a common approximation to the complete scattering phase function [Wiscombe and Grams, 1976] and is dependent only on  $\theta$  and  $g_\lambda$

$$P_{HG}(\theta, g_\lambda) = \frac{1 - g_\lambda^2}{[1 + g_\lambda^2 - 2g_\lambda \cos(\theta)]^{3/2}} \quad (1.10)$$

The approximation, however, introduces errors into radiative transfer calculations. As shown in Boucher [1998], these errors are significant at small and large values of  $\theta$  and for accumulation mode size distributions.

When examining the effects of incident radiation on an entire population of particles, or an aerosol, the different sizes of the particles in the aerosol size distribution implies that the values of  $Q_{ext,\lambda}$  will also change. The total attenuating effects of an aerosol on incident radiation with wavelength  $\lambda$  can be described by extinction coefficient,  $\sigma_{ext,\lambda}$ , or

$$\sigma_{ext,\lambda} = \int_0^\infty \frac{\pi D_p^2}{4} Q_{ext,\lambda}(D_p) n(D_p) dD_p \quad (1.11)$$

where  $n(D_p)$  can be defined using a lognormal size distribution (Eq. 1.1) and the scattering coefficient ( $\sigma_{sca,\lambda}$ ) and absorption coefficient ( $\sigma_{abs,\lambda}$ ) are defined analogously using the respective efficiencies ( $Q_{sca,\lambda}$  or  $Q_{abs,\lambda}$ ). The units of  $\sigma_{ext,\lambda}$ ,  $\sigma_{sca,\lambda}$ , and  $\sigma_{abs,\lambda}$  are inverse length and stated in this study as  $Mm^{-1}$  (or  $10^{-6} m^{-1}$ ) The radiation scattered by an aerosol in the backwards direction ( $90^\circ$  to  $180^\circ$ ) with respect to the direction of the incident radiation is the backscattering coefficient ( $\sigma_{sca,back,\lambda}$ ). The unitless hemispheric backscatter ratio,  $\beta_\lambda$ , is defined as



$$\beta_{\lambda} = \frac{\sigma_{sca,back,\lambda}}{\sigma_{sca,\lambda}} \quad (1.12)$$

and gives the fraction of incident radiation that is scattered in the backwards direction relative to radiation scattered into all directions. The total amount of radiation attenuated from an incident beam for a vertical column of aerosols with an extinction coefficient  $\sigma_{ext,\lambda}$  is the vertical aerosol optical depth ( $\tau_{\lambda}$ ) and is defined as

$$\tau_{\lambda} = \int_0^{\infty} \sigma_{ext,\lambda}(z) dz \quad (1.13)$$

where  $z$  is the altitude in units of length such that  $\tau_{\lambda}$  is a unitless parameter and  $\sigma_{ext,\lambda}$  is a function of  $z$ .

The aerosol extinction coefficient (Eq. 1.11) and aerosol optical depth (Eq. 1.13) are dependent on the aerosol number concentration ( $N_a$ , see Eq. 1.1) and are called an *extensive* properties. Aerosol optical properties such as  $\omega_{o,\lambda}$  (Eq. 1.7) and  $g_{\lambda}$  (Eq. 1.9) are not dependent on  $N_a$  and are called *intensive* properties.

The wavelength dependence of  $\sigma_{ext,\lambda}$  can be described by the Angstrom exponent,  $\alpha_{ext}$ , which is defined as

$$\alpha_{ext,\lambda_1-\lambda_2} = - \frac{\log(\sigma_{ext,\lambda_1}) - \log(\sigma_{ext,\lambda_2})}{\log(\lambda_1) - \log(\lambda_2)} \quad (1.14)$$

where  $\lambda_1$  and  $\lambda_2$  describe the range of  $\lambda$  over which  $\alpha_{ext}$  is calculated and

$\sigma_{ext,\lambda_1}$  and  $\sigma_{ext,\lambda_2}$  are the  $\sigma_{ext}$  values at  $\lambda_1$  and  $\lambda_2$ . Values of  $\alpha_{ext,450-700}$  were  $\sim 1.7 - 2.0$  during SAFARI-2000 in the regional haze indicating an aerosol population

dominated by submicron particles rather than coarse mode particles (when values of  $\alpha_{\text{ext},450-700}$  are generally smaller), and this agrees with general biomass burning aerosol physical properties [e.g. *Reid et al.*, 2004a]. Analogous definitions can be stated for  $\alpha_{\text{sca}}$ ,  $\alpha_{\text{abs}}$ , and  $\alpha_{\tau}$ .

Radiative transfer theory requires quantification of  $\sigma_{\text{ext},\lambda}$ ,  $\omega_{o,\lambda}$ , and  $g_{\lambda}$ . For a particular time and location, each of these aerosol optical properties depends on  $\lambda$ ,  $z$ , and relative humidity (RH). The dependencies are themselves dependent on the chemical and physical aerosol properties described in Section 1.2. As we will discuss later in this study, biomass burning aerosol exhibits a strong dependence of  $\sigma_{\text{ext},\lambda}$  on  $\lambda$ ,  $z$ , and RH. Similarly,  $\omega_{o,\lambda}$  for a biomass burning aerosol is dependent on  $z$ , but the dependence of  $\omega_{o,\lambda}$  on  $\lambda$  and RH has not been measured directly. All aerosol optical properties are dependent on the time and space, but *Anderson et al.* [2003a] showed that homogenous aerosol number concentrations in the lower troposphere rarely exist for time scales longer than  $\sim 10$  hours and spatial scales larger than  $\sim 100$  km.

In this study, we examine aerosol optical properties in the solar (or shortwave) spectrum defined as  $\lambda = 200 - 4000$  nm and the effects of aerosols on the radiative balance of the Earth. Aerosol radiative effects are generally confined to the shortwave but modeling research indicates that aerosol longwave effects (primarily due to dust and sea salt aerosols) could also be globally significant [*Jacobson*, 2001; *Reddy et al.*, 2005a; *Reddy et al.*, 2005b].

The downward and upward fluxes ( $F_{\text{down}}$  and  $F_{\text{up}}$ , respectively) in units of  $\text{W m}^{-2}$  are calculated using radiative transfer theory. The net flux,  $F_{\text{net}}$ , at any level in the atmosphere is

$$F_{\text{net}} = F_{\text{down}} - F_{\text{up}} \quad (1.15)$$

and can be calculated for any range of  $\lambda$  (shortwave net flux at the surface, for example). The radiative effects of aerosols can be quantified by defining the aerosol radiative forcing (RF) in units of  $\text{W m}^{-2}$  on the atmosphere as

$$\text{RF} = F_{\text{net,a}} - F_{\text{net,n}} \quad (1.16)$$

where  $F_{\text{net,a}}$  is the net flux at some level in an atmosphere with aerosols and  $F_{\text{net,n}}$  is the net flux at the same level in an atmosphere with no aerosols. Thus, RF isolates the overall radiative effects of aerosols for a particular profile at some level in the atmosphere. Conventionally, RF is specified at the top of the atmosphere ( $\text{RF}_{\text{toa}}$ ) and at the bottom of the atmosphere ( $\text{RF}_{\text{boa}}$ ), or surface [Ramaswamy *et al.*, 2001], but radiation absorbed by the atmosphere can have important effects on the stability of the atmosphere and cloud formation [Ackerman *et al.*, 2000; Jiang and Feingold, 2006]. RF, or more specifically,  $F_{\text{up}}$ , is dependent on the surface albedo ( $F_{\text{up}}/F_{\text{down}}$ ) as well. Surface albedo over land exhibits varying degrees of seasonal and diurnal variability [Moody *et al.*, 2005], while ocean surfaces are not as variable.

#### 1.4. Southern African Biomass Burning and SAFARI-2000

The southern hemisphere is dramatically affected by fire ecology [*Bond et al.*, 2005]. As shown in Fig. 1.3, carbon emissions from biomass burning in Africa and South America alone account for nearly 50% of the global carbon emissions from prolific fossil fuel sources like those in the United States, Europe, and China as well as biomass burning in other parts of the world [*Bond et al.*, 2004].

Every year from about April to October, southern Africa (Fig 1.4) experiences a period of intense biomass burning during the southern hemisphere winter months [e.g. *Annegarn et al.*, 2002; *Swap et al.*, 2002a]. The aerosol and trace gas emissions from southern Africa interact with a persistent high pressure (anticyclonic circulation) system that remains in place ~80% of the time during the winter months over the sub-continent [*Garstang et al.*, 1996]. The large-scale subsidence resulting from the presence of the continental high pressure in turn creates multiple persistent layers of stability that occur throughout the atmosphere at nearly the same pressure levels (~850, 700, 500, and 300 hPa) and with a high degree of frequency throughout the year [*Cosijn and Tyson*, 1996; *Tyson et al.*, 1996]. The frequency of occurrence of these stable layers increases during the winter months since the continental high pressure is more persistent during that time [*Cosijn and Tyson*, 1996]. Westerly waves from the southern mid-latitudes and easterly tropical disturbances occasionally perturb the otherwise nearly permanent continental high pressure system [*Garstang et al.*, 1996].

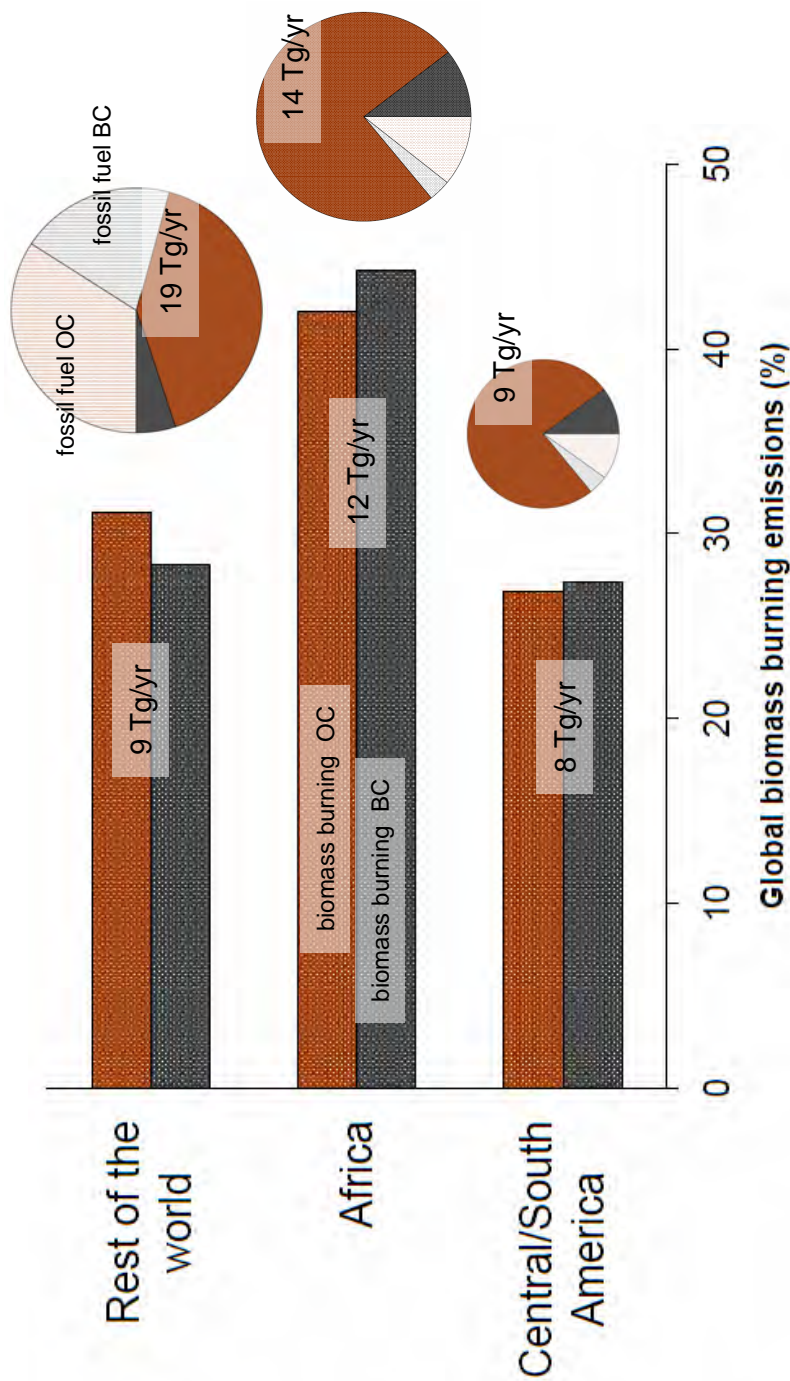


Fig. 1.3. Carbon emissions from combustion sources in Africa, Central and South America, and the rest of the world. Biomass burning organic carbon (OC) and black carbon (BC) are shown as solid brown and solid gray, respectively. Fossil fuel emissions of OC and BC are shown as translucent brown and translucent gray, respectively. The total annual biomass burning emissions for each source are shown as bars with the numerical value embedded in the bar. The total annual carbon emissions for each source are shown as pie graphs to the right of the bars. The values of total annual carbon emissions (from biomass burning and fossil fuel) are embedded in the pie graphs. Data source: *Bond et al. [2004]*.

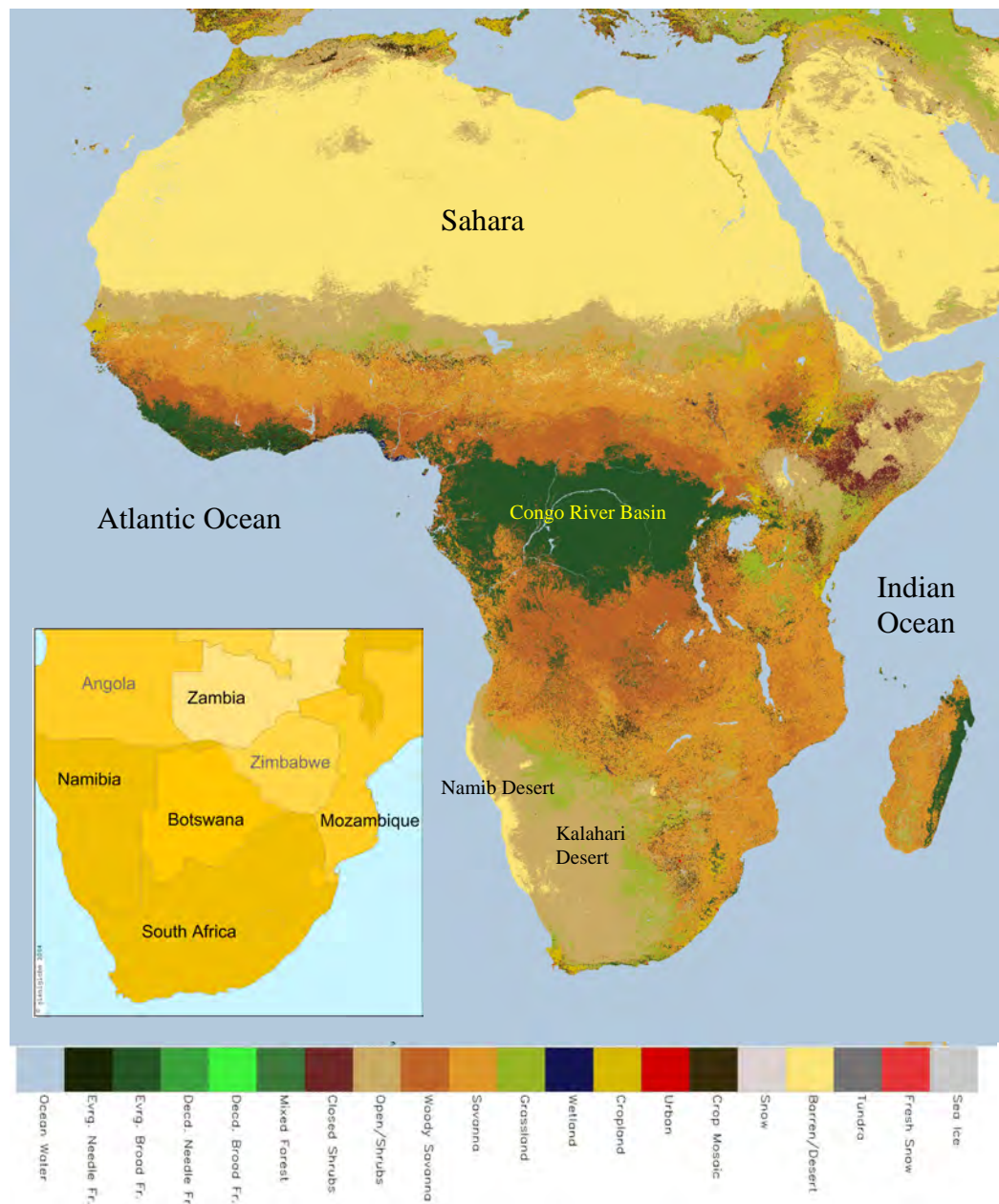


Fig. 1.4. The vegetation types on the continent of Africa in August, during the climatological dry season. Most of the biomass burning occurs in equatorial southern Africa in the tropical forests, the woody savannas of Zambia, Angola and northern Botswana, and in the grassland savannas of southern Botswana, Zimbabwe, eastern South Africa, and Mozambique. See the inset for political boundaries. The vegetation map is available at <http://modis-atmos.gsfc.nasa.gov/ECOSYSTEM/index.html> and the political map was created using [http://www.planiglobe.com/omc\\_set.html](http://www.planiglobe.com/omc_set.html).

The aerosol and trace gas concentrations from the biomass burning emissions depend on both the type of vegetation (Fig. 1.4) and the amount of vegetation available. The vegetation type and density varies strongly from equatorial southern Africa to the southern tip of the continent. The tropical forests of the Congo River basin [Delmas *et al.*, 1999] transition to woody savanna which changes to a grassland savanna [Sinha *et al.*, 2003] marked by a lower density of trees [also see photographs of surface types in Gatebe *et al.*, 2003]. The fire ecology of southern Africa has certainly had an effect on the development of the southern African ecosystem [Bond *et al.*, 2005].

The vegetation availability depends on the amount of precipitation during the wet summer months from the previous year and, in contrast to the nearly predictable behavior of the wintertime meteorology in southern Africa, the interannual precipitation variations are much larger [Anyamba *et al.*, 2003]. The amount of precipitation in southern Africa is partly linked to the Pacific Ocean El Nino Southern Oscillation (ENSO), where the warm phase ENSO results in below normal precipitation in southern Africa and the cold phase ENSO results in above normal precipitation [Anyamba *et al.*, 2002]. So although fires occur every year in southern Africa, evidence suggests that interannual variability is the most important consideration when accounting for African biomass burning emissions [Duncan *et al.*, 2003].

The persistent continental high pressure system enhances concentrations of aerosols and trace gases during the winter months of southern Africa by

inhibiting vertical mixing [Tyson *et al.*, 1996; Swap and Tyson, 1999]. The overall effect is that aerosols tend to accumulate below the stable layers in dense hazes, although often the haze layers are separated by thin clean slots with low aerosol number concentrations [Hobbs, 2003]. The vertical mixing increases somewhat during the day as solar insolation destabilizes the atmosphere, but the aerosol concentrations in the atmosphere are then simply uniformly high rather than vertically structured. The haze layers extend from the surface to ~500 hPa [Swap and Tyson, 1999; Magi *et al.*, 2003] and, after noting the marked decrease in visibility, one can hypothesize that the haze has a strong effect on sunlight.

The regional haze in southern Africa is dominated by biomass burning emissions. Bond *et al.* [2004] suggest that ~86% of the carbon from African combustion emissions are from biomass burning sources (compared to, for example, ~54% for North America and Europe). The anticyclonic circulation serves to transport aerosols and trace gases in a weak counterclockwise gyre with easterly transport in the northern part of the subcontinent and westerly transport in the southern part [Tyson *et al.*, 1996; Freiman and Piketh, 2003; Sinha *et al.*, 2004]. Most of the biomass burning occurs in the tropical latitudes of southern Africa. Significant burning also occurs in the woody and grassland savannas south of the tropical latitudes but changes from more variable precipitation patterns [Anyamba *et al.*, 2003]. Eck *et al.* [2003] show that aerosol optical depths (Eq. 1.13) in the woody and grassland savanna regions of southern Africa (Fig. 1.4) are determined by biomass burning emissions and field data presented



in *Ruellan et al.* [1999], *Gao et al.* [2003], and *Kirchstetter et al.* [2003] shows that aerosol mass concentrations are much higher than in western South Africa, which is mostly shrub and barren desert and is only indirectly affected by biomass burning emissions [*Piketh et al.*, 1999].

Several field campaigns have been organized to better understand the impacts of southern African biomass burning emissions [*Swap et al.*, 2002a, and references therein]. The largest field campaign was the Southern African Research Initiative (SAFARI) that took place in August and September 2000 during the dry wintertime months of southern Africa [*Annegarn et al.*, 2002; *Swap et al.*, 2002b; *Swap et al.* 2003]. One of the main objectives of SAFARI-2000 was to characterize the emissions of southern African biomass burning [*Swap et al.*, 2002b]. The University of Washington (UW) research aircraft, together with a number of other research groups listed in *Swap et al.* [2003], collected measurements of the physical, chemical, and optical properties of southern African biomass burning as a part of the SAFARI-2000 field campaign. Over 100 hours of flight time were logged by the UW research aircraft during the campaign. Many of the preliminary analyses of the data collected during SAFARI-2000 by the UW and other groups were published in a Special Issue of the *Journal of Geophysical Research* (vol. 108, no. D13, 2003). Many more detailed studies from SAFARI-2000 have been published since the Special Issue [*Haywood et al.*, 2004; *Osborne et al.*, 2004; *Sinha et al.*, 2004; *Abel et al.*, 2005]. Much of the

SAFARI-2000 data is available online as well at

<http://daac.ornl.gov/S2K/safari.html>.

## **Section 1.5. Objectives and Organization of Dissertation**

This study will focus on evaluating the magnitude and the uncertainties of clear-sky biomass burning aerosol direct radiative forcing in southern Africa [e.g. *Ramaswamy et al.*, 2001]. Since SAFARI-2000, the understanding of southern African biomass burning aerosols has improved dramatically [*Haywood et al.*, 2003a; *Myhre et al.*, 2003; *Osborne et al.*, 2004; *Abel et al.*, 2005], but there continue to be problems integrating the data into the models to evaluate the global impact of biomass burning aerosol radiative forcing [*Ackerman et al.*, 2004; *Kahn et al.*, 2004; *Kinne et al.*, 2005].

The analysis presented in this dissertation is based on aircraft data collected during vertical profiles and offers a supplementary and complementary analysis to the previous body of work [e.g. *Swap et al.*, 2003; *Abel et al.*, 2005]. We discuss a new aerosol optical property retrieval algorithm designed around the type of data collected during SAFARI-2000 and use the retrieval output to estimate the measurement-based direct radiative forcing [*Penner et al.*, 1992; *Hobbs et al.*, 1997; *Ramaswamy et al.*, 2001] due to southern African biomass burning aerosols. These values are compared with published work from southern African regional modeling studies [*Myhre et al.*, 2003; *Abel et al.*, 2005]. The uncertainty in the radiative forcing is assessed by performing sensitivity studies,

which is realistically the only method capable of evaluating uncertainties in radiative forcing estimates [*Redemann et al.*, 2000b].

In Chapter 2, the instruments used to collect the measurements are described and the analysis of the data collected from the aircraft is described in Chapter 3. In Chapter 4, we present and evaluate an original custom-designed aerosol optical property look-up table retrieval algorithm that uses the analyzed data in Chapter 3 as input. The output of the retrieval provides a table of the wavelength and altitude dependent aerosol optical properties needed as input to a column radiative transfer model. In Chapter 5, we describe the model, discuss the radiative forcing calculations, and evaluate the uncertainties in the estimates of radiative forcing due to southern African biomass burning aerosol. Finally, we summarize the findings and discuss the implications in Chapter 6.

## Chapter 2. Data

### 2.1. Airborne Instrumentation

The University of Washington (UW) Cloud and Aerosol Research Group has a long history of aircraft research [Hobbs, 1991]. A complete listing of the UW research aircraft flights in SAFARI 2000, the sampling strategies, and all of the instruments aboard the aircraft is summarized in the appendix of *Sinha et al.* [2003a] and is also publicly available at <http://cargsun2.atmos.washington.edu/sys/research/safari/>. The measurements obtained from the UW research aircraft (Fig. 2.1) during SAFARI 2000 and used in this study are described in this chapter. Many other details about specific instruments on the UW research aircraft can be found in *Reid et al.* [1998], *Ross et al.* [1998], *Hartley* [2000], and *Garrett* [2000].

Aircraft altitude and location were determined from an onboard global positioning system (GPS). The altitude was accurate to within ~5 m. During brief periods when the GPS did not record data, GPS altitude is replaced by the hypsometric altitude [e.g. *Wallace and Hobbs*, 2006]. The two methods agree to within ~1% at 700 hPa.

Meteorological data were collected continuously by a suite of standard instrumentation [*Sinha et al.*, 2003a]. This included temperature (T), pressure (p), and dew point temperature ( $T_d$ ). Relative humidity (RH) is derived from measurements of T and  $T_d$  using the empirical equation for saturation vapor



Fig. 2.1. The University of Washington research aircraft (Convair-580) used during SAFARI-2000 (Photograph available at <http://cargsun2.atmos.washington.edu/>).

pressure on pp. 350 in the 6<sup>th</sup> edition of the *Smithsonian Meteorological Tables* and equations found in *Wallace and Hobbs* [2006].

As a final note, all data collected from the UW research aircraft during SAFARI-2000 are archived and available by request using contact information found at <http://cargsun2.atmos.washington.edu/>.

### 2.1.1. Nephelometers

A nephelometer measures  $\sigma_{\text{sca}}$  (Eq 1.11 using  $Q_{\text{sca}}$ ) and  $\sigma_{\text{sca,back}}$  (Eq 1.12). The instrument design was first described by *Buettel and Brewer* [1949] and the first measurements were described by *Charlson et al.* [1967] and *Ahlquist and Charlson* [1968]. Now nephelometers are deployed in most aerosol measurement campaigns [*Hegg et al.*, 1997; *Reid et al.*, 1998; *Clarke et al.*, 2002; *Anderson et al.*, 2003c; *Magi et al.*, 2003; *Magi et al.*, 2005; *Schmid et al.*, 2006]. Evaluations of the nephelometer performance and a published calibration procedure [*Anderson et al.*, 1996; *Anderson and Ogren*, 1998] helped improve the usefulness of the measurements. The UW research aircraft used two independent nephelometers located inside the aircraft and the instruments used an inlet that sampled particles with diameters less than  $\sim 3 \mu\text{m}$  and has been described previously [e.g. *Hartley*, 2000; *Magi and Hobbs*, 2003].

One nephelometer, custom-built for the UW by the same person that designed the commercially-available TSI nephelometer [*Anderson and Ogren*, 1998], provided simultaneous measurements of  $\sigma_{\text{sca}}$  and  $\sigma_{\text{sca,back}}$  at three visible

wavelengths ( $\lambda = 450, 550, \text{ and } 700 \text{ nm}$ ) and will be referred to as the  $3\lambda$ -nephelometer. When necessary, we will refer to  $\sigma_{\text{sca}}$  measured at a wavelength  $\lambda$  as  $\sigma_{\text{sca},\lambda}$  (for example,  $\sigma_{\text{sca}}$  at  $\lambda = 550 \text{ nm}$  would be  $\sigma_{\text{sca},550}$ ). We will use similar notation for  $\sigma_{\text{sca,back}}$ . The  $3\lambda$ -nephelometer integrated over scattering angles from  $\sim 7^\circ$  to  $170^\circ$  for  $\sigma_{\text{sca}}$  and from  $\sim 90^\circ$  to  $170^\circ$  for  $\sigma_{\text{sca,back}}$ . The methods used to correct the measurements for forward ( $0^\circ$  to  $7^\circ$ ) and backward ( $170^\circ$  to  $180^\circ$ ) angular truncation and non-Lambertian light source illumination within the nephelometer sample chamber are described in *Hartley* [2000] and are similar to the correction methodology for the TSI nephelometer [*Anderson and Ogren*, 1998].

The  $3\lambda$ -nephelometer measurements were all made at ambient pressure but the airstream was heated to dry the aerosol to an RH of  $\sim 30\%$  to minimize the effects of ambient RH on  $\sigma_{\text{sca}}$  and  $\sigma_{\text{sca,back}}$  (Section 3.2). The measurements were made with  $\sim 10\%$  precision and, with the sample time set at 1 second, the lower detection limit was  $\sim 1 \text{ Mm}^{-1}$ . As will be shown in Section 3.4, measurements of  $\sigma_{\text{sca}}$  during SAFARI-2000 rarely reached the lower detection limit.

The other nephelometer on the UW research aircraft will be referred to as the  $1\lambda$ -nephelometer and measured  $\sigma_{\text{sca},537}$ . The airstream to the  $1\lambda$ -nephelometer was not deliberately heated. However, since ambient RH during SAFARI-2000 was generally low (e.g. Section 3.3) and the aircraft cabin was warmer than the ambient air temperature, the aerosol measured by the nephelometer was most

likely at  $RH < 40\%$ . Measurements from the  $1\lambda$ -nephelometer are only used in the analysis as a proxy substitute for brief instances when the  $3\lambda$ -nephelometer measurements were not available (Section 3.2).

Both nephelometers were calibrated before and during SAFARI-2000 by standard procedures described in *Anderson and Ogren* [1998]. Natural variability and instrument noise are averaged out to some degree by techniques described in Section 3.4, but *Anderson et al.* [1996, 2000] show that nephelometer measurements have a  $\sim 7\%$  systematic uncertainty that cannot be averaged out. Aside from the systematic uncertainty, all other forms of uncertainty are propagated using a standard quadratures method [*Bevington and Robinson*, 1992].

### 2.1.2. Particle and Soot Absorption Photometer

Measurements of  $\sigma_{\text{abs}}$  (Eq. 1.11 using  $Q_{\text{abs}}$ ) for  $D_a < \sim 3 \mu\text{m}$  were made at  $\lambda = 567 \text{ nm}$  using a Particle and Soot Absorption Photometer (PSAP) located inside the aircraft and sampling from the same inlet as the nephelometers (Section 2.1.1). The precision of the PSAP measurements is  $\sim 25\%$  and the lower detection limit is  $\sim 2 \text{ Mm}^{-1}$  using a 30 s running mean values of  $\sigma_{\text{abs}}$  with outputs every second. An internal flow meter in the PSAP monitored the flow rate at standard temperature and pressure ( $T = 273.15\text{K}$ ,  $p = 1013.25 \text{ hPa}$ ), but PSAP measurements were adjusted to ambient temperature and pressure in all analysis so that they could be compared to the  $3\lambda$ -nephelometer measurements. The airstream to the PSAP was also partly heated to  $RH < 40\%$ .



The PSAP measurements were corrected for typical errors in instrument-to-instrument variability, instrument noise, PSAP response to scattering, and PSAP response to absorption, following the procedures described by *Bond et al.* [1999], which implicitly account for a wavelength adjustment from 567 nm to 550 nm. The PSAP sample spot size diameter for the UW PSAP was measured at 4.7 mm (compared to the manufacturer stated 5.1 mm) and this correction was included as well [*Bond et al.*, 1999]. Potential corrections to the flow rate of the PSAP [*Bond et al.*, 1999] were not possible since the instrument was no longer available for verification, but personal communications with the SAFARI-2000 PSAP operator suggested that the flow rate for the UW PSAP was ~2 Lpm, which is the same as the flow rate stated by the manufacturer. Regardless of the correction procedures, *Bond et al.* [1999] show that there is a basic ~20% systematic uncertainty associated with the PSAP. Since we have no quantitative evidence of the potential difference in flow rate, we a slightly larger 25% systematic uncertainty in the values of  $\sigma_{\text{abs}}$  reported by the UW PSAP. All uncertainties, aside from the 25% systematic uncertainty, are propagated using the quadratures method [*Bevington and Robinson*, 1992].

The PSAP is a well-documented, but sometimes problematic instrument, and has been discussed in detail in many studies [*Bond et al.*, 1999; *Anderson et al.*, 2003c; *Sheridan et al.*, 2005; *Doherty et al.*, 2005]. This study presents data from the PSAP using methods that are completely traceable back the raw measurements should any further corrections be needed in the future. We will

refer to  $\sigma_{\text{abs}}$  measured at  $\lambda = 550$  nm as  $\sigma_{\text{abs},550}$ , similar to the notation for  $\sigma_{\text{sca}}$ .

Extrapolation of  $\sigma_{\text{abs},550}$  to other wavelengths is possible using  $\alpha_{\text{abs}}$  (Eq. 1.14).

We discuss this in Section 3.3.1.

### 2.1.3. Aerosol Number Concentration and Size

Measurements of aerosol number concentrations ( $N_a$  in Eq. 1.1) were made by two condensation nuclei counters (CNCs) manufactured by TSI. The CNCs were located inside the aircraft and sampled from the same inlet as the nephelometers (Section 2.1.2). TSI CNC models 3022 and 3025 counted aerosol particles (in units of particle number per unit volume, or simply  $\text{cm}^{-3}$ ) with diameters ranging from about  $0.007 - 1.0 \mu\text{m}$  and  $0.003 - 1.0 \mu\text{m}$ , respectively. The CNC 3022 measures  $N_a < 10^7 \text{ cm}^{-3}$  and the CNC 3025 measures  $N_a < 10^5 \text{ cm}^{-3}$ . *Kesten et al.* [1991] discuss the TSI model 3025 CNC, but aside from the general deployment in multiple ground and aircraft based field campaigns [*Heintzenberg and Ogren*, 1985; *Clarke et al.*, 2002], there is not very much published about any potential problems with the counters. There is also no calibration associated with the instruments but the coincident measurements obtained by the UW CNC 3022 and 3025 were intended to provide a level of validation. In theory, CNC 3025 should measure slightly more particles because of the larger range. The measurements by the CNC 3025 were on average  $\sim 15\%$  higher than those by the CNC 3022 during SAFARI-2000. The errors in  $N_a$  from the CNC ( $\delta N_a$ ) are calculated as counting errors ( $N_a^{-1/2}$ ) per the discussion in *Bevington and Robinson* [1992].

The Passive Cavity Aerosol Spectrometer Probe (PCASP) is commercially-built by Particle Measuring System, Inc. and the UW used a PCASP model 100x mounted on the wing of the aircraft. The PCASP measures  $N_a$  for fifteen size bins at a low RH to arrive at a size distribution for a dried aerosol [Strapp *et al.*, 1992]. The calibration procedure for the PCASP is based on using non-absorbing latex spheres with a known refractive index ( $m$ ) at the operating wavelength of the PCASP ( $\lambda = 632.8$  nm),  $m_{\text{latex},632.8} = 1.592 + 0i$ . For field use,  $m$  of the sampled aerosol,  $m_{a,632.8}$ , must be known and also must be nearly constant across the entire size range of the PCASP, which is  $D_p = 0.1 - 3.0$   $\mu\text{m}$  at  $m_{\text{latex},632.8}$ . The size bins, particularly with  $D_p > 1$   $\mu\text{m}$ , are quite sensitive to  $m_{a,632.8}$  [Liu and Daum, 2000; Hartley, 2000; Haywood *et al.*, 2003a], but without direct measurements, past studies have only been able to estimate  $m_{a,632.8}$  based on chemical mixing rules (Section 1.2) or by matching measurements to Mie theory calculations [Hartley *et al.*, 2001; Haywood *et al.*, 2003a].

Sampling efficiencies of the PCASP are also called into question by Liu *et al.* [1992]. The UW PCASP was located on the wing of the aircraft and may have experienced some issues with sampling efficiencies since the aircraft pitching may have compromised the isokineticity of the PCASP design. Haywood *et al.* [2003] and Osborne *et al.* [2004] discuss the difficulties of using the PCASP on an aircraft. Guyon *et al.* [2003], Osborne *et al.* [2004], and the data in this study suggest that  $\sigma_{\text{sca}}$  derived from PCASP measurements is systematically (and often substantially) less than  $\sigma_{\text{sca}}$  independently measured by nephelometry (Section

2.1.1). *Ross et al.* [1998] found better agreement, but also used multiple sizing probes to more completely characterize the size distribution.

We refer to the detailed size distributions reported by the UW PCASP during SAFARI-2000 only to emphasize the prominence of submicron aerosols during SAFARI-2000. Specifically, we combine the PCASP particle concentrations in the first ten sizing bins ( $0.1 < D_p < 1.0 \mu\text{m}$ ) to estimate the submicron ( $\sim$ fine mode) particle concentration and compare this to the particle concentrations in the last five sizing bins ( $1.0 < D_p < 3.0 \mu\text{m}$ ), which we use to estimate the supermicron ( $\sim$ coarse mode) particle concentration. This basic size distinction removes much of the uncertainty in the PCASP binning of particles discussed above, but still provides some insight into the general particle size.

#### 2.1.4. NASA Ames Airborne Tracking Sunphotometer

The NASA Ames Airborne Tracking Sunphotometer, which we simply call the Sunphotometer, was mounted on top of the UW research aircraft exterior (barely visible in Fig. 2.1). Under cloudless conditions, the Sunphotometer measures the aerosol optical depth of the column of air above the altitude of the aircraft at fourteen wavelengths. The column aerosol optical depth, or  $\tau_{\text{column},\lambda}$ , is defined as

$$\tau_{\text{column},\lambda} = \int_{z_{\min}}^{\infty} \sigma_{\text{ext},\lambda}(z) dz \quad (2.1)$$

and is similar to Eq. 1.13, only with a lower limit of integration,  $z_{\min}$ , that corresponds to the altitude of the aircraft. The method of determining  $\tau_{\text{column},\lambda}$  from the Sunphotometer measurements is described most recently in *Schmid et al.* [2006], but the instrument has been deployed in aircraft campaigns since the mid-1990s [e.g. *Redemann et al.*, 2000b, 2003, 2005a-b; *Schmid et al.*, 2000, 2003].

During SAFARI-2000, the Sunphotometer only reported  $\tau_{\text{column},\lambda}$  at twelve wavelengths ( $\lambda = 354, 380, 449, 499, 525, 606, 675, 778, 864, 1019, 1241$ , and  $1557$  nm) because one wavelength filter degraded during SAFARI-2000 and the data was unusable and measurements at  $\lambda = 940$  nm are used for column water vapor calculations [*Redemann et al.*, 2003; *Schmid et al.*, 2003]. Uncertainty in  $\tau_{\text{column},\lambda}$  are generally less than  $\sim 10\%$  depending on the wavelength and the magnitude of  $\tau_{\text{column}}$ . Horizontal variability can also contribute to uncertainty [*Redemann et al.*, 2005a].

Using measurements of  $\tau_{\text{column},\lambda}$ , values of  $\sigma_{\text{ext},\lambda}$  can be derived by differentiating  $\tau_{\text{column},\lambda}$  at two vertically separated points. This is not a direct measurement, however, and the uncertainty in  $\sigma_{\text{ext},\lambda}$  is  $\sim 10\text{-}30\%$ , with larger uncertainty for smaller values of  $\tau_{\text{column},\lambda}$  [*Schmid et al.*, 2003, 2006].

The Sunphotometer was calibrated prior to and after SAFARI-2000 [*Schmid et al.*, 2003] and data from the Sunphotometer is available for all field campaigns at <http://geo.arc.nasa.gov/sgg/AATS-website/>.

## 2.2. Aerosol Robotic Network (AERONET)

The worldwide Aerosol Robotic Network (AERONET) provided important ground-based radiometric measurements [Holben *et al.*, 1998; Holben *et al.*, 2001; Dubovik *et al.*, 2000] during SAFARI-2000 [Eck *et al.*, 2003].

AERONET measures the aerosol optical depth ( $\tau_\lambda$  in Eq. 1.13) at seven wavelengths ( $\lambda = 340, 380, 440, 500, 670, 870$ , and  $1020$  nm), but also retrieves a lognormal size distribution and  $\omega_o$ ,  $g$ ,  $m_r$  and  $m_i$  at four wavelengths ( $\lambda = 441, 673, 873, 1022$  nm) using information from sky-radiance scans [Dubovik and King, 2000; Dubovik *et al.*, 2000]. The retrieved aerosol properties are reported less frequently since the entire sky must be nearly clear of clouds and  $\tau_{440}$  must be greater than 0.3 [Dubovik *et al.*, 2000]. The retrieved measurements are also a “column-averaged” value in the sense that the ground-based measurements represent the aerosol properties of the entire column of aerosol above the AERONET site. AERONET data is available at <http://aeronet.gsfc.nasa.gov/>.

Comparisons between AERONET measured and retrieved data and other independent measurements are not common, but have been increasing in recent years as the satellite and modeling communities have started to rely on AERONET climatologies for validation [e.g. Chin *et al.*, 2002; Ichoku *et al.*, 2003; Chung *et al.*, 2005; Zhou *et al.*, 2005]. Haywood *et al.* [2003a] and Schmid *et al.* [2003] showed that comparisons between AERONET derived measurements and aircraft-based measurements were good. Measurements of  $\tau_{\text{column}}$  from the Sunphotometer and from AERONET stations also agree to within about 10-15%

[Schmid *et al.*, 2006]. However, in a global circulation model (GCM) intercomparison study, Kinne *et al.* [2003] showed that the GCM derived aerosol optical depths were generally smaller than those measured by AERONET, especially in regions affected by biomass burning. More recently, Kinne *et al.* [2005] showed that southern Africa in particular is not well represented in GCMs.

The retrieved AERONET aerosol properties are more difficult to validate since spatial and temporal differences can dramatically affect aerosol properties [Anderson *et al.*, 2003b; Redemann *et al.*, 2005a] and usually the best basis for comparison is between infrequent aircraft based measurements and the column-averaged AERONET data products. The problem of comparing AERONET data to in situ data is compounded with potentially undiagnosed aerosol sampling issues [Magi *et al.*, 2005; Schmid *et al.*, 2006]. The need for direct, careful, and dedicated validation of AERONET retrievals remains an issue [Ackerman *et al.*, 2004; Kahn *et al.*, 2004; Zhou *et al.*, 2005; Yu *et al.*, 2006] but is slowly being addressed by field studies.

SAFARI-2000 provided several unique opportunities for comparisons of aircraft in situ measurements and AERONET retrieved products. Haywood *et al.* [2003b] showed that the retrieved AERONET products generally agreed with aircraft-based in situ measurements for transported biomass burning aerosols in Namibia. Magi and Hobbs [2004] compared two cases of aircraft in situ data with AERONET data in South Africa and in Botswana and showed that there were discrepancies in the measured and retrieved values of  $\omega_0$ . Leahy [2006]

examined cases from South Africa, Botswana, Zambia, and Namibia and showed that carefully chosen comparisons between UW research aircraft derived properties and those reported by AERONET were generally in agreement (within instrumental errors). However, on a more global scale, *Reddy et al.* [2005a] found that even with careful comparisons, modeled absorption was biased low by about 24% with respect to AERONET absorption.



### **Chapter 3. Data Analysis**

Over 100 hours of research time was logged on the UW research aircraft during the 12 Aug to 16 Sep 2000 sample period of SAFARI-2000 [*Sinha et al.*, 2003]. The flights ranged from northeastern South Africa, southern Mozambique, eastern Botswana, southern Zambia, to Namibia on the west coast sampling a wide range of vegetation types (Fig. 1.4) and subsequently, a wide range of biomass being burned (Section 1.4).

#### **3.1. SAFARI-2000 and the River of Smoke**

The general climate of southern African, especially during the southern hemisphere winter months, is dominated by a continental high pressure system that remains in place ~80% of the time [*Garstang et al.*, 1996]. SAFARI-2000 took place during a cold phase El Nino Southern Oscillation (ENSO) and this resulted in a weakening and a reduction in the frequency of the high pressure system [*Stein et al.*, 2003]. Prior to SAFARI-2000, the cold phase ENSO, or La Nina, contributed to above average rainfall and vegetation growth [*Anyamba et al.*, 2003]. During the burning season of SAFARI-2000, this resulted in above average biomass burning emissions [*Eck et al.*, 2003], a weaker easterly transport of the emissions, and the more frequent passage of westerly disturbances [*Stein et al.*, 2003], especially compared to the climate of southern Africa during a warm phase ENSO [*Garstang et al.*, 1996]. However, even under weakened conditions,

the subsidence from the presence of the continental high pressure still dominated the structuring of the southern African atmosphere.

One westerly disturbance dramatically affected eastern southern Africa for about a week during the SAFARI-2000 sample period. Fig. 3.1 shows a satellite image of southern Africa captured on 4 Sep 2000, during the passage of the westerly disturbance that affected the region from about 2-10 Sep 2000. The red arrow on the figure emphasizes the transport of gray-colored smoke in a broad northwest-southeast channel from Zambia through southern Mozambique, passing over the main part of the SAFARI-2000 sample area. The low pressure system associated with the westerly disturbance is located southwest of the tongue of smoke shown in Fig. 3.1 [Stein *et al.*, 2003]. This fascinating event was qualitatively described as the “River of Smoke” by Annegarn *et al.* [2002] and Swap *et al.* [2003].

A back trajectory analysis of SAFARI-2000 meteorology presented in Magi and Hobbs [2003] and in Stein *et al.* [2003] confirmed that air parcels generally originated from the south or the east during anticyclonic circulation, but changed to a northerly or northwesterly direction during the westerly disturbance that created the River of Smoke. The smoke visible in Fig. 3.1 was transported over the period of a few days from regions of heavy biomass burning in the woody savannas of Angola and Zambia and the tropical forests in the southern Congo River Basin (Fig. 1.4), southeast over eastern Botswana, Zimbabwe, southern Mozambique, and northeastern South Africa before exiting to the

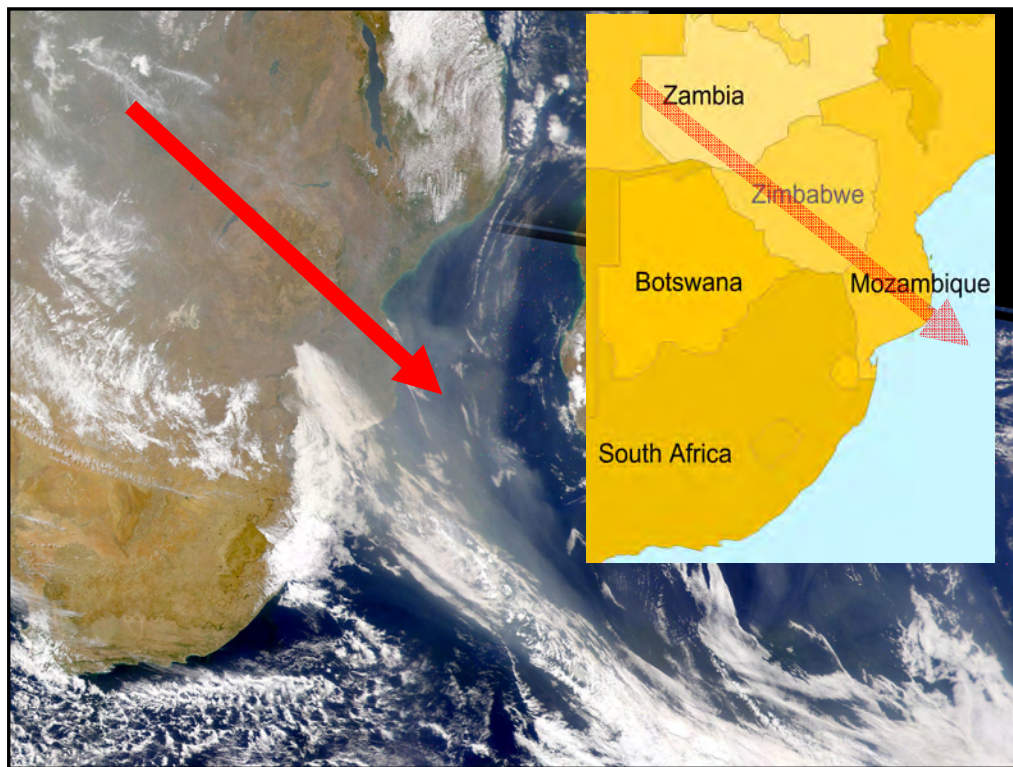


Fig. 3.1. Satellite image of the River of Smoke event during SAFARI-2000 [Annegarn *et al.*, 2002]. The red arrow indicates the direction of the northwesterly flow of gray-colored smoke aerosols from the heavy burning region, over the SAFARI-2000 study area in northeast South Africa, eastern Botswana, and southern Zambia, and finally out to the Indian Ocean. This flow pattern persisted from 2-7 Sep 2000. This image was captured from the SeaWiFs satellite on 4 September 2000 and can be found at [http://visibleearth.nasa.gov/view\\_rec.php?vev1id=3346](http://visibleearth.nasa.gov/view_rec.php?vev1id=3346). The political map was created at [http://www.planiglobe.com/omc\\_set.html](http://www.planiglobe.com/omc_set.html)

southern Indian Ocean. There was also a marked difference in measured aerosol optical properties between the anticyclonic circulation and the River of Smoke.

### 3.2. The Effects of Relative Humidity on Biomass Burning Aerosol

The dependence of aerosol optical properties on relative humidity, RH, is crucial to understanding the effects of aerosols on climate [Haywood *et al.*, 1997; Charlson, 1999]. As an aerosol is exposed to increasing RH, the water vapor pressure around the individual particles increases and condenses onto the particles causing the particles to increase in size [Hanel, 1976]. The particles can act as a solid substrate for the condensed water vapor, but if the water vapor pressure increases enough, the solid particle will dissolve into the condensed water. This phase transformation from solid to liquid is known as *deliquescence*, while the transformation from liquid to solid (which generally occurs at a different RH) is known as *efflorescence* [Tang and Munkelwitz, 1994]. As discussed in Hegg *et al.* [1993] and Reist [1993], an increase in submicron particle size (i.e.  $D_g$  in Eq. 1.1) corresponds to an increase in  $\sigma_{sca}$  at midvisible wavelengths.

The degree and rate of the increase in  $\sigma_{sca}$  are dependent on the chemical properties of the aerosol [Tang and Munkelwitz, 1994; Carrico *et al.*, 2003; Topping *et al.*, 2005a-b]. In that regard, the effects of humidity on an aerosol (or the “hygroscopicity”) can give some indication of the overall chemical composition [Saxena *et al.*, 1995; Quinn *et al.*, 2005] since some aerosols grow more readily under increasing RH than others [Tang, 1997]. Marine aerosol

[*Tang et al.*, 1997; *Hegg et al.*, 2002], for example, is more hygroscopic than biomass burning aerosol [*Kotchenruther and Hobbs.*, 1998]. In SAFARI-2000, the aerosol exhibited varying degrees hygroscopic growth with no apparent discontinuity due to deliquescence [e.g. *Kotchenruther et al.*, 1999; *Carrico et al.*, 2003].

### 3.2.1. Methods

A plot showing the change in  $\sigma_{\text{sca}}$  or  $\beta$  (at a specified wavelength) with increasing RH is called a humidograph. To obtain a humidograph for a particular aerosol, the  $3\lambda$ -nephelometer (Section 2.1.1) was used. A preheater dried the incoming particles to ~30% RH for measurements by the  $3\lambda$ -nephelometer, but during a humidograph, the RH in the sample chamber was steadily increased from ~30% to ~85% over a period of about five minutes. During the period of increasing RH,  $\sigma_{\text{sca}}$  and  $\sigma_{\text{sca,back}}$  were measured continuously.

Practically, humidographs are needed to adjust  $\sigma_{\text{sca}}$  and  $\sigma_{\text{sca,back}}$  measured by the  $3\lambda$ -nephelometer at ~30% RH to ambient RH. This low RH measurement protocol with nephelometers is common, although not universal. Without humidification measurements, closure between in situ and remote sensing measurements can be poor, especially in regions of the world with high aerosol concentrations and high ambient RH [e.g. *Kotchenruther et al.*, 1999; *Magi et al.*, 2005; *Schmid et al.*, 2006].

Various empirical relationships have been used to describe the nonlinear dependence of  $\sigma_{\text{sca}}$  on RH [e.g., *Kasten, 1969; Grant et al., 1999*]. *Kotchenruther and Hobbs [1998]* showed that the RH dependence of  $\sigma_{\text{sca}}$  for South American biomass burning aerosol could be described by an empirical function of the form

$$\sigma_{\text{sca},\lambda}(\text{RH}) = \sigma_{\text{sca},d,\lambda} \left[ 1 - a_{1,\lambda} \left( \frac{\text{RH}}{100} \right)^{a_{2,\lambda}} \right] \quad (3.1)$$

where  $\sigma_{\text{sca},d,\lambda}$  is the scattering coefficient for the dried aerosol (at RH  $\sim$  30%),  $a_{1,\lambda}$  and  $a_{2,\lambda}$  are empirical fitting parameters (the  $\lambda$  subscript indicates a wavelength dependence), and RH is in units of percent. Although simpler functions to describe the hygroscopic growth have been used [*Hegg et al., 1996*] and fits that are based on theory are also possible [*Kasten, 1969; Quinn et al., 2005; Topping et al., 2005a-b*], we adopt the empirical function in Eq. 3.1 to describe the hygroscopic growth of southern African biomass burning aerosols. The weakness in Eq. 3.1 is the lack of physical basis, but the strength is in the accuracy of the fit for RH  $<$  80%, which was always the case during SAFARI-2000.

The best fit to the data in the humidograph was determined using a standard nonlinear least squares optimization routine for each of the three wavelengths of the 3 $\lambda$ -nephelometer ( $\lambda = 450, 550, \text{ and } 700 \text{ nm}$ ). A measure of the accuracy of the fit to each humidograph was determined by the reduced chi-squared ( $\chi^2$ ) parameter [*Bevington and Robinson, 1992*].

Values of  $\beta$  (Eq. 1.12), also at  $\lambda = 450, 550, \text{ and } 700 \text{ nm}$ , decreased approximately linearly with increasing RH, so we used a linear regression of the form

$$\beta_{\lambda}(RH) = b_{1,\lambda} \left( \frac{RH}{100} \right) + b_{2,\lambda} \quad (3.2)$$

where RH is in units of percent,  $b_{1,\lambda}$  and  $b_{2,\lambda}$  are fitting parameters (the slope and intercept, respectively), and the  $\lambda$  subscript indicates a wavelength dependence. The linear correlation coefficient,  $r^2$ , is used to assess the accuracy of the linear regression [Bevington and Robinson, 1992].

We define the humidification factor for  $\sigma_{\text{sca}}$  at a wavelength  $\lambda$ ,  $f_{\text{sca},\lambda}$ , as the ratio of  $\sigma_{\text{sca}}$  at a particular RH to  $\sigma_{\text{sca},d}$  (at RH = 30%). Hence, the humidification factor at 80% RH,  $f_{\text{sca},\lambda}(80)$ , is

$$f_{\text{sca},\lambda}(80) = \frac{\sigma_{\text{sca},\lambda}(80)}{\sigma_{\text{sca},d,\lambda}} \quad (3.3)$$

where  $\sigma_{\text{sca},\lambda}(80)$  is determined from Eq. 3.1 and  $\sigma_{\text{sca},d,\lambda}$  divides out. The definition of the corresponding humidification factor  $\beta$  at a wavelength  $\lambda$  is analogous.

Thus,  $f_{\beta,\lambda}(80)$  is

$$f_{\beta,\lambda}(80) = \frac{\beta_{\lambda}(80)}{\beta_{d,\lambda}} \quad (3.4)$$

where  $\beta_{\lambda}(80)$  is determined from Eq. 3.2 and  $\beta_{d,\lambda}$  divides out.

### 3.2.2. Analysis

A total of fifty-four humidographs were obtained by the UW research aircraft during SAFARI-2000 from aerosols sampled near the fires and aerosols sampled in the regional haze (Figure 3.2). The general information about each of the humidographs is listed in Table 3.1, where we have categorized the samples as regional haze in South Africa, Botswana, Mozambique, and Zambia (Table 3.1i), samples collected directly from smoke plumes (Table 3.1ii) and samples collected near Namibia (Table 3.1iii), where there are few local sources of biomass burning (due to low vegetation density) and the atmosphere is generally affected by transported biomass burning smoke from the east [Haywood *et al.*, 2003a-b; Keil and Haywood, 2003]. The humidographs were collected from the continuous airflow passing through the  $3\lambda$ -nephelometer for the regional haze samples, but smoke sampled directly from biomass burning was collected in a sample chamber and passed through the  $3\lambda$ -nephelometer separately. The smoke sampling procedure is discussed in detail in Magi and Hobbs [2003].

The curve fitting parameters for Eqs. 3.1 and 3.2, and the derived values of  $f_{\text{sca},\lambda}(80)$  and  $f_{\beta,\lambda}(80)$  based on the humidographs obtained during SAFARI-2000 are listed in Table 3.2. We use the same categories as Table 3.1 to differentiate between the geographical location of the regional haze humidographs and humidographs from smoke plumes. To show the magnitude of the change in  $\sigma_{\text{sca},\lambda}$  or  $\beta_{\lambda}$  with RH for a particular sample, we present the calculations of  $f_{\text{sca},\lambda}(80)$  and  $f_{\beta,\lambda}(80)$  in Table 3.2, but it should be made clear that  $f_{\text{sca},\lambda}$  and  $f_{\beta,\lambda}$



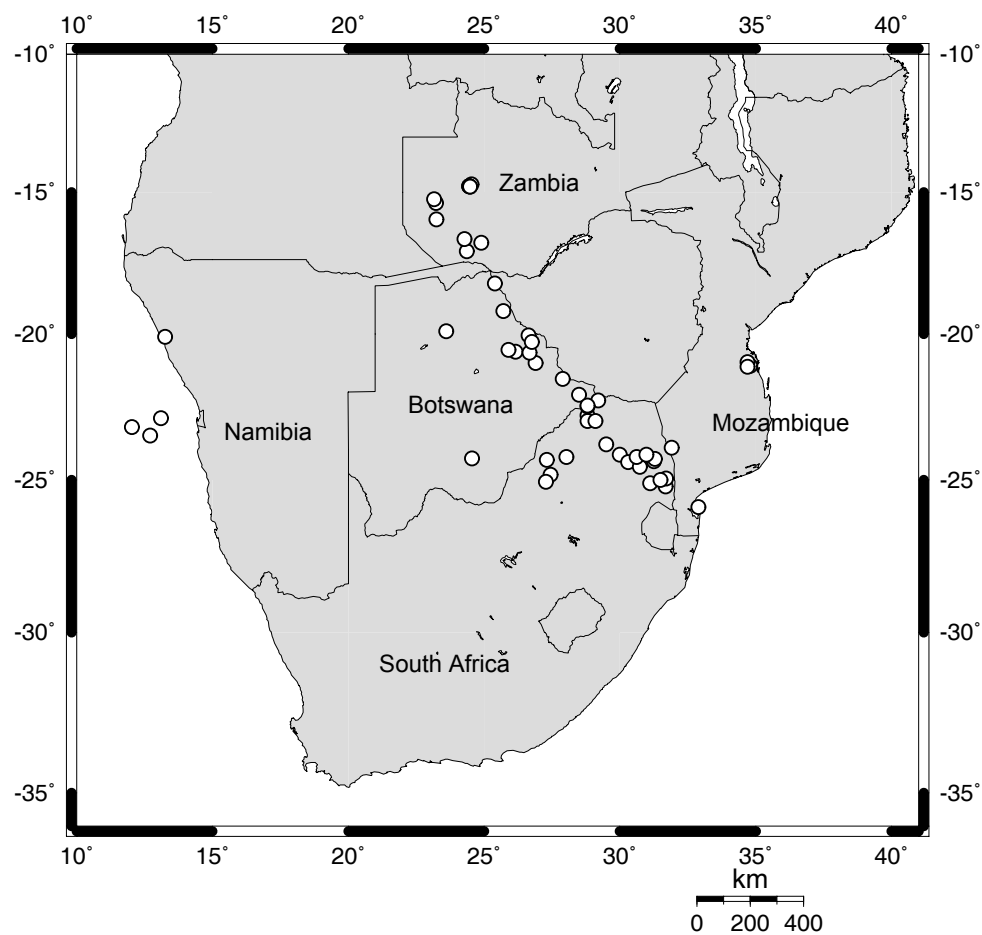


Fig. 3.2. Locations of the fifty-four humidographs collected during SAFARI-2000 by the UW research aircraft (denoted with open circles). Further details are listed in Table 3.1. The map was produced using <http://www.aquarius.geomar.de/omc/>.

Table 3.1. Description date, time, and location of the humidographs collected during SAFARI-2000. The sample conditions are summarized by the back trajectory descriptions. The numerical identifications (ID) in the first column are a cross-referencing tool for information in Tables 3.2 and 3.3.

ID	Date (2000)	Flight Number	UTC Time (hhmm)	Latitude (°S)	Longitude (°E)	Parcel back trajectory <sup>a</sup>		Altitude <sup>c</sup> (m)	Pressure (hPa)
i. Samples from regional haze (South Africa, Mozambique, Botswana, Zambia)									
1	14-Aug	1812	1312	24.82	27.44	S/SE	C	2327 ± 12	781 ± 0.7
2	14-Aug	1812	1337	25.06	27.28	S/SE	C	2330 ± 10	782 ± 0.8
3	15-Aug	1814	912	25.11	31.11	S	M/C	972 ± 200	919 ± 1.8
4	17-Aug	1815	826	25.22	31.71	SE/N	M/C	1266 ± 4	883 ± 0.4
5	20-Aug	1819	1151	24.22	28.06	W	C	3362 ± 4	685 ± 0.4
6	22-Aug	1820	721	24.15	29.99	W	C	3057 ± 5	710 ± 0.4
7	22-Aug	1820	951	24.95	31.70	E/NE	M/C	883 ± 273	918 ± 1.9
8	23-Aug	1821	1227	23.80	29.50	S	C	2944 ± 6	724 ± 0.5
9	24-Aug	1822	709	24.40	30.30	W/SW	C	3551 ± 17	670 ± 1.6
10	24-Aug	1822	945	25.90	32.88	W/S	M/C	2066 ± 0.4	763 ± 0.3
11	29-Aug	1823	858	22.80	28.80	S	C	2896 ± 5	726 ± 0.4
12	29-Aug	1823	928	22.30	29.20	S	C	2876 ± 4	727 ± 0.3
13	29-Aug	1823	1005	23.00	28.80	E	C	1603 ± 5	847 ± 0.5
14	29-Aug	1824	1317	24.55	30.73	SW	C	3510 ± 5	672 ± 0.5
15	29-Aug	1824	1337	25.00	31.50	E	C	963 ± 23	909 ± 2.1
16	31-Aug	1825	932	23.90	31.90	SW	C	2953 ± 4	717 ± 0.3
17	31-Aug	1825	1108	21.10	34.80	S	M/C	1125 ± 5	889 ± 0.4
18	1-Sep	1826	612	22.10	28.50	SE	C	3830 ± 4	645 ± 0.5
19	1-Sep	1826	718	19.20	25.70	E/N	C	3237 ± 4	696 ± 0.3
20	1-Sep	1826	802	16.80	24.90	NE	C	1896 ± 12	816 ± 1.2
21	2-Sep	1829	852	21.00	26.90	W/NE	C	3169 ± 4	701 ± 0.4
22	2-Sep	1829	1019	19.90	23.60	NE	C	1581 ± 15	843 ± 1.5
23	3-Sep	1830	733	22.50	28.80	N/NW	C	3150 ± 3	700 ± 0.4
24	3-Sep	1830	843	20.60	26.16	NE/N	C	963 ± 26	904 ± 2.6
25	3-Sep	1830	1021	20.55	25.90	NE/N	C	2523 ± 5	754 ± 0.5
26	3-Sep	1830	1058	20.65	26.67	N	C	2389 ± 8	766 ± 0.8
27	3-Sep	1830	1124	21.57	27.89	N	C	2362 ± 14	769 ± 0.9
28	5-Sep	1831	910	22.48	28.81	N	C	3181 ± 5	700 ± 0.4
29	5-Sep	1831	1005	20.05	26.63	NW/N	C	3584 ± 4	668 ± 0.4
30	5-Sep	1831	1040	18.23	25.39	N	C	4226 ± 2	617 ± 0.4
31	5-Sep	1831	1245	14.71	24.53	N	C	1637 ± 10	836 ± 0.9
32	6-Sep	1832	728	17.10	24.36	NE	C	3865 ± 3	645 ± 0.4
33	6-Sep	1832	755	15.92	23.25	NE	C	1162 ± 25	885 ± 1.6
34	6-Sep	1832	911	15.38	23.22	NE	C	1240 ± 22	878 ± 1.4
35	6-Sep	1832	951	15.25	23.16	NE/E	C	1678 ± 172	835 ± 15.6
36	6-Sep	1832	1030	16.67	24.28	NE	C	4277 ± 2	612 ± 0.4
37	6-Sep	1833	1234	20.28	26.75	NE	C	3813 ± 3	649 ± 0.4
38	6-Sep	1833	1332	23.00	29.10	N	C	2372 ± 18	770 ± 1.7
39	7-Sep	1834	826	24.22	30.61	SW	M/C	3496 ± 5	672 ± 0.4
40	10-Sep	1835	644	24.31	27.30	NW	C	3807 ± 4	648 ± 0.4
41	10-Sep	1835	733	24.27	24.55	NW	C	3792 ± 3	650 ± 0.3
ii. Samples obtained from smoke plumes									
42	31-Aug	1825	1136	20.97	34.69	-	P	222 ± 12	987 ± 1.2
43	31-Aug	1825	1222	21.14	34.69	-	P	355 ± 35	971 ± 3.6
44	1-Sep	1826	920	14.78	24.45	-	P	1653 ± 154	837 ± 14.7
45	1-Sep	1826	1004	14.78	24.45	-	P	1993 ± 34	807 ± 3.2
46	5-Sep	1831	1212	14.8	24.49	-	P	1834 ± 182	818 ± 17.9
47	5-Sep	1831	1224	14.79	24.48	-	P	1307 ± 26	868 ± 2.4
48	7-Sep	1834	859	24.36	31.25	-	P	653 ± 27	938 ± 2.9
49	7-Sep	1834	947	24.29	31.29	-	P	653 ± 25	940 ± 2.6
50	7-Sep	1834	1037	24.15	30.97	-	P	540 ± 123	950 ± 1.7
iii. Samples from regional haze (Namibia)									
51	11-Sep	1836	910	22.9	13.1	NW	M	3870 ± 4	645 ± 0.3
52	11-Sep	1836	1041	23.2	12.03	NW	M	169 ± 64	996 ± 7.3
53	11-Sep	1836	1059	23.5	12.7	NW	M	3732 ± 4	655 ± 0.5
54	13-Sep	1837	1140	20.1	13.25	E	C	3908 ± 3	640 ± 0.4

<sup>a</sup> Describes the 72 hour parcel back trajectory. For example, 'NW' means the parcel originated from the NW, and passed over the continent (C), maritime (M), a combination (M/C), or was sampled directly from a plume (P). Back trajectories are archived at <http://www.arl.noaa.gov/ready/hysplit4.html>.

<sup>b</sup> Altitudes are listed as above mean sea level (MSL); the standard deviation is the variation during the five minute period required for a humidograph

Table 3.2a. The values of  $f_{\text{sca}}(80)$  and  $f_{\beta}(80)$  and the empirical fit coefficients for Eqs. 3.1 and 3.2 at  $\lambda = 450$  nm. The numerical identification (ID) can be cross-referenced with information in Table 3.1.

ID	$f_{\text{sca}}$ - fit coefficients				$f_{\beta}$ - fit coefficients			
	$f_{\text{sca}}(80)$	$a_1$	$a_2$	$\chi^2$	$f_{\beta}(80)$	slope ( $b_1$ )	intercept ( $b_2$ )	$r^2$
i. Samples from regional haze (South Africa, Mozambique, Botswana, Zambia)								
1	1.93	$3.63 \pm 0.97$	$6.05 \pm 1.15$	36	0.78	$-0.04 \pm 0.01$	$0.11 \pm 0.01$	0.72
2	1.90	$2.55 \pm 0.67$	$1.31 \pm 0.36$	31	0.71	$-0.05 \pm 0.01$	$0.11 \pm 0.01$	0.93
3	1.93	$4.84 \pm 0.23$	$7.38 \pm 0.19$	8	0.92	$-0.01 \pm 0.02$	$0.09 \pm 0.01$	0.11
4	1.58	$2.19 \pm 0.28$	$5.95 \pm 0.47$	28	0.75	$-0.06 \pm 0.02$	$0.14 \pm 0.01$	0.63
5	1.95	$3.68 \pm 1.29$	$1.08 \pm 0.25$	10	0.68	$-0.05 \pm 0.01$	$0.10 \pm 0.01$	0.93
6	2.06	$2.42 \pm 0.32$	$1.85 \pm 0.41$	14	0.71	$-0.04 \pm 0.01$	$0.09 \pm 0.01$	0.91
7	1.88	$1.99 \pm 0.08$	$3.36 \pm 0.19$	6	0.72	$-0.06 \pm 0.01$	$0.12 \pm 0.01$	0.78
8	1.80	$1.64 \pm 0.10$	$2.21 \pm 0.29$	7	0.74	$-0.04 \pm 0.01$	$0.10 \pm 0.01$	0.92
9	1.71	$1.46 \pm 0.02$	$2.67 \pm 0.06$	3	0.71	$-0.05 \pm 0.01$	$0.11 \pm 0.01$	0.88
10	1.99	$2.09 \pm 0.02$	$2.28 \pm 0.03$	3	0.75	$-0.04 \pm 0.01$	$0.10 \pm 0.01$	0.71
11	2.01	$2.59 \pm 0.39$	$4.07 \pm 1.20$	25	0.66	$-0.07 \pm 0.02$	$0.13 \pm 0.02$	0.77
12	2.05	$2.52 \pm 0.20$	$3.67 \pm 0.47$	13	0.58	$-0.09 \pm 0.02$	$0.14 \pm 0.01$	0.80
13	1.85	$2.32 \pm 0.19$	$4.41 \pm 0.42$	15	0.70	$-0.06 \pm 0.01$	$0.12 \pm 0.01$	0.75
14	1.61	$1.27 \pm 0.22$	$2.85 \pm 0.72$	27	0.74	$-0.05 \pm 0.01$	$0.11 \pm 0.01$	0.70
15	1.91	$2.02 \pm 0.09$	$3.20 \pm 0.19$	14	0.74	$-0.05 \pm 0.01$	$0.11 \pm 0.01$	0.66
16	2.36	$3.73 \pm 0.14$	$4.40 \pm 0.19$	12	0.66	$-0.07 \pm 0.02$	$0.13 \pm 0.02$	0.85
17	1.48	$1.42 \pm 0.32$	$4.76 \pm 0.97$	6	0.75	$-0.05 \pm 0.02$	$0.13 \pm 0.02$	0.87
18	2.05	$2.57 \pm 0.02$	$3.79 \pm 0.05$	3	0.68	$-0.06 \pm 0.02$	$0.12 \pm 0.01$	0.74
19	1.77	$1.96 \pm 0.03$	$4.00 \pm 0.10$	4	0.69	$-0.07 \pm 0.02$	$0.13 \pm 0.02$	0.91
20	1.43	$1.44 \pm 0.02$	$5.43 \pm 0.08$	1	0.74	$-0.06 \pm 0.02$	$0.14 \pm 0.02$	0.90
21	1.81	$3.16 \pm 0.19$	$6.07 \pm 0.29$	5	0.68	$-0.07 \pm 0.02$	$0.13 \pm 0.02$	0.91
22	1.40	$1.25 \pm 0.23$	$5.02 \pm 0.86$	7	0.80	$-0.04 \pm 0.02$	$0.12 \pm 0.02$	0.69
23	1.51	$1.23 \pm 0.02$	$3.74 \pm 0.12$	1	0.73	$-0.05 \pm 0.02$	$0.12 \pm 0.01$	0.82
24	1.37	$0.95 \pm 0.12$	$4.13 \pm 0.58$	2	0.80	$-0.04 \pm 0.02$	$0.11 \pm 0.02$	0.92
25	1.40	$1.80 \pm 0.17$	$6.71 \pm 0.34$	1	0.76	$-0.05 \pm 0.02$	$0.11 \pm 0.02$	0.74
26	1.58	$1.23 \pm 0.50$	$2.94 \pm 2.57$	17	0.76	$-0.05 \pm 0.02$	$0.11 \pm 0.02$	0.82
27	1.27	$0.58 \pm 0.16$	$3.19 \pm 1.32$	6	0.73	$-0.05 \pm 0.02$	$0.11 \pm 0.02$	0.84
28	1.46	$1.75 \pm 0.09$	$5.99 \pm 0.30$	2	0.76	$-0.05 \pm 0.02$	$0.11 \pm 0.01$	0.81
29	1.45	$1.01 \pm 0.06$	$3.40 \pm 0.39$	2	0.77	$-0.04 \pm 0.02$	$0.10 \pm 0.01$	0.82
30	1.51	$1.08 \pm 0.10$	$3.06 \pm 0.61$	4	0.76	$-0.04 \pm 0.02$	$0.10 \pm 0.01$	0.89
31	1.39	$1.20 \pm 0.48$	$4.99 \pm 1.41$	4	0.89	$-0.02 \pm 0.02$	$0.10 \pm 0.02$	0.37
32	1.31	$1.83 \pm 0.54$	$7.92 \pm 1.69$	4	0.78	$-0.04 \pm 0.02$	$0.10 \pm 0.02$	0.87
33	1.18	$0.96 \pm 0.21$	$7.49 \pm 1.16$	2	0.82	$-0.04 \pm 0.02$	$0.11 \pm 0.02$	0.82
34	1.35	$0.87 \pm 0.11$	$4.01 \pm 0.55$	2	0.84	$-0.03 \pm 0.02$	$0.10 \pm 0.02$	0.74
35	1.38	$1.17 \pm 0.92$	$5.03 \pm 2.85$	21	0.85	$-0.03 \pm 0.01$	$0.10 \pm 0.01$	0.75
36	1.43	$1.15 \pm 0.42$	$4.25 \pm 1.61$	3	0.79	$-0.03 \pm 0.02$	$0.09 \pm 0.02$	0.57
37	1.67	$1.52 \pm 0.60$	$3.36 \pm 1.77$	18	0.76	$-0.04 \pm 0.02$	$0.10 \pm 0.02$	0.80
38	1.56	$1.13 \pm 0.33$	$2.43 \pm 1.71$	19	0.76	$-0.04 \pm 0.02$	$0.10 \pm 0.02$	0.77
39	1.81	$2.90 \pm 0.03$	$5.69 \pm 0.05$	7	0.71	$-0.05 \pm 0.02$	$0.10 \pm 0.01$	0.25
40	1.47	$1.44 \pm 0.05$	$4.98 \pm 0.16$	3	0.75	$-0.04 \pm 0.01$	$0.10 \pm 0.01$	0.89
41	1.48	$1.35 \pm 0.02$	$4.57 \pm 0.07$	1	0.77	$-0.04 \pm 0.02$	$0.10 \pm 0.01$	0.89
ii. Samples obtained from smoke plumes								
42	1.66	$1.70 \pm 0.42$	$4.12 \pm 1.30$	3	0.77	$-0.07 \pm 0.02$	$0.18 \pm 0.02$	0.89
43	1.39	$1.04 \pm 0.29$	$4.24 \pm 1.10$	4	1.00	$0.00 \pm 0.02$	$0.15 \pm 0.01$	0.00
44	1.42	$1.03 \pm 0.15$	$3.87 \pm 0.64$	2	0.89	$-0.03 \pm 0.02$	$0.14 \pm 0.02$	0.51
45	1.51	$1.31 \pm 0.17$	$4.09 \pm 0.45$	2	1.09	$0.02 \pm 0.02$	$0.11 \pm 0.02$	0.15
46	1.46	$1.81 \pm 0.33$	$6.11 \pm 0.69$	1	0.98	$-0.01 \pm 0.02$	$0.12 \pm 0.02$	0.04
47	1.24	$0.59 \pm 0.11$	$4.05 \pm 0.88$	2	0.96	$-0.01 \pm 0.02$	$0.12 \pm 0.02$	0.16
48	1.70	$2.20 \pm 2.13$	$5.05 \pm 4.47$	4	0.75	$-0.07 \pm 0.02$	$0.16 \pm 0.01$	0.88
49	1.75	$1.94 \pm 0.20$	$4.12 \pm 0.51$	3	0.82	$-0.05 \pm 0.02$	$0.16 \pm 0.02$	0.72
50	1.38	$1.17 \pm 0.17$	$5.04 \pm 0.56$	1	0.77	$-0.06 \pm 0.02$	$0.15 \pm 0.02$	0.78
iii. Samples from regional haze (Namibia)								
51	1.74	$2.49 \pm 0.05$	$5.38 \pm 0.10$	4	0.76	$-0.039 \pm 0.02$	$0.09 \pm 0.01$	0.81
52	2.82	$4.49 \pm 0.11$	$3.68 \pm 0.14$	27	0.75	$-0.054 \pm 0.01$	$0.13 \pm 0.01$	0.82
53	1.30	$1.32 \pm 0.08$	$6.59 \pm 0.22$	3	0.70	$-0.052 \pm 0.02$	$0.10 \pm 0.02$	0.72
54	1.56	$1.67 \pm 0.02$	$4.81 \pm 0.05$	1	0.73	$-0.054 \pm 0.02$	$0.12 \pm 0.02$	0.90

Table 3.2b. As per Table 3.2a, but at  $\lambda = 550$  nm

ID	$f_{\text{sca}}$ - fit coefficients				$f_{\text{b}}$ - fit coefficients			
	$f_{\text{sca}}(80)$	$a_1$	$a_2$	$\chi^2$	$f_{\text{b}}(80)$	slope ( $b_1$ )	intercept ( $b_2$ )	$r^2$
i. Samples from regional haze (South Africa, Mozambique, Botswana, Zambia)								
1	1.97	$3.82 \pm 0.69$	$6.10 \pm 0.78$	39	0.75	$-0.06 \pm 0.01$	$0.14 \pm 0.01$	0.78
2	1.96	$2.63 \pm 0.41$	$1.39 \pm 0.24$	34	0.68	$-0.07 \pm 0.02$	$0.14 \pm 0.01$	0.97
3	1.93	$5.26 \pm 0.17$	$7.76 \pm 0.13$	10	0.97	$-0.01 \pm 0.02$	$0.12 \pm 0.02$	0.02
4	1.57	$1.95 \pm 0.14$	$5.47 \pm 0.26$	25	0.84	$-0.05 \pm 0.02$	$0.17 \pm 0.02$	0.45
5	2.00	$3.69 \pm 0.82$	$1.14 \pm 0.18$	11	0.66	$-0.07 \pm 0.02$	$0.13 \pm 0.01$	0.92
6	2.19	$2.69 \pm 0.25$	$1.99 \pm 0.29$	16	0.66	$-0.06 \pm 0.01$	$0.11 \pm 0.01$	0.94
7	1.93	$2.17 \pm 0.05$	$3.50 \pm 0.10$	5	0.69	$-0.08 \pm 0.01$	$0.15 \pm 0.01$	0.82
8	1.86	$1.79 \pm 0.07$	$2.21 \pm 0.17$	6	0.68	$-0.07 \pm 0.01$	$0.13 \pm 0.01$	0.95
9	1.75	$1.56 \pm 0.02$	$2.74 \pm 0.05$	4	0.71	$-0.07 \pm 0.01$	$0.14 \pm 0.01$	0.95
10	2.05	$2.23 \pm 0.01$	$2.41 \pm 0.02$	2	0.67	$-0.07 \pm 0.01$	$0.13 \pm 0.01$	0.89
11	2.02	$2.76 \pm 0.24$	$4.33 \pm 0.72$	23	0.61	$-0.11 \pm 0.02$	$0.17 \pm 0.02$	0.89
12	2.10	$2.70 \pm 0.15$	$3.79 \pm 0.32$	14	0.62	$-0.10 \pm 0.02$	$0.16 \pm 0.02$	0.85
13	1.90	$2.38 \pm 0.11$	$4.21 \pm 0.23$	12	0.66	$-0.09 \pm 0.02$	$0.16 \pm 0.01$	0.81
14	1.66	$1.42 \pm 0.15$	$3.09 \pm 0.43$	24	0.69	$-0.07 \pm 0.02$	$0.14 \pm 0.01$	0.78
15	1.95	$2.14 \pm 0.09$	$3.29 \pm 0.18$	20	0.67	$-0.08 \pm 0.01$	$0.14 \pm 0.01$	0.80
16	2.39	$3.89 \pm 0.09$	$4.46 \pm 0.12$	14	0.64	$-0.10 \pm 0.02$	$0.17 \pm 0.02$	0.86
17	1.51	$1.54 \pm 0.27$	$4.85 \pm 0.75$	8	0.73	$-0.08 \pm 0.02$	$0.17 \pm 0.02$	0.85
18	2.09	$2.73 \pm 0.01$	$3.90 \pm 0.02$	2	0.65	$-0.09 \pm 0.02$	$0.15 \pm 0.02$	0.82
19	1.83	$2.05 \pm 0.03$	$3.85 \pm 0.09$	7	0.65	$-0.10 \pm 0.02$	$0.18 \pm 0.02$	0.92
20	1.46	$1.39 \pm 0.02$	$4.93 \pm 0.07$	1	0.75	$-0.07 \pm 0.02$	$0.17 \pm 0.02$	0.84
21	1.86	$3.50 \pm 0.17$	$6.27 \pm 0.23$	6	0.66	$-0.09 \pm 0.02$	$0.17 \pm 0.02$	0.93
22	1.42	$1.29 \pm 0.19$	$4.96 \pm 0.67$	9	0.76	$-0.07 \pm 0.02$	$0.16 \pm 0.02$	0.86
23	1.53	$1.29 \pm 0.02$	$3.79 \pm 0.09$	2	0.74	$-0.07 \pm 0.02$	$0.14 \pm 0.02$	0.90
24	1.40	$1.06 \pm 0.08$	$4.23 \pm 0.33$	2	0.77	$-0.06 \pm 0.02$	$0.14 \pm 0.02$	0.96
25	1.41	$1.82 \pm 0.13$	$6.63 \pm 0.25$	2	0.76	$-0.06 \pm 0.02$	$0.15 \pm 0.02$	0.75
26	1.62	$1.33 \pm 0.31$	$3.00 \pm 1.46$	16	0.75	$-0.06 \pm 0.02$	$0.13 \pm 0.02$	0.84
27	1.29	$0.63 \pm 0.10$	$3.20 \pm 0.78$	5	0.73	$-0.06 \pm 0.02$	$0.14 \pm 0.02$	0.77
28	1.46	$1.96 \pm 0.08$	$6.45 \pm 0.24$	3	0.74	$-0.06 \pm 0.02$	$0.13 \pm 0.02$	0.88
29	1.48	$1.10 \pm 0.05$	$3.52 \pm 0.27$	3	0.73	$-0.06 \pm 0.02$	$0.13 \pm 0.02$	0.88
30	1.54	$1.15 \pm 0.07$	$3.06 \pm 0.40$	4	0.73	$-0.06 \pm 0.02$	$0.12 \pm 0.02$	0.94
31	1.40	$1.17 \pm 0.33$	$4.77 \pm 1.02$	5	0.85	$-0.04 \pm 0.03$	$0.13 \pm 0.02$	0.62
32	1.33	$1.91 \pm 0.36$	$7.86 \pm 1.09$	3	0.78	$-0.05 \pm 0.02$	$0.11 \pm 0.02$	0.82
33	1.20	$0.86 \pm 0.10$	$6.53 \pm 0.62$	2	0.79	$-0.05 \pm 0.02$	$0.14 \pm 0.02$	0.88
34	1.36	$0.88 \pm 0.08$	$3.89 \pm 0.40$	2	0.79	$-0.05 \pm 0.02$	$0.14 \pm 0.02$	0.90
35	1.40	$1.19 \pm 0.62$	$4.90 \pm 1.87$	23	0.84	$-0.04 \pm 0.01$	$0.13 \pm 0.01$	0.85
36	1.46	$1.15 \pm 0.23$	$3.97 \pm 0.93$	3	0.69	$-0.06 \pm 0.02$	$0.12 \pm 0.02$	0.83
37	1.70	$1.59 \pm 0.44$	$3.36 \pm 1.25$	21	0.73	$-0.06 \pm 0.02$	$0.12 \pm 0.02$	0.78
38	1.61	$1.23 \pm 0.21$	$2.47 \pm 1.03$	17	0.73	$-0.06 \pm 0.02$	$0.13 \pm 0.02$	0.92
39	1.86	$2.62 \pm 0.02$	$4.91 \pm 0.05$	15	0.66	$-0.09 \pm 0.02$	$0.15 \pm 0.02$	0.53
40	1.52	$1.59 \pm 0.05$	$4.98 \pm 0.14$	4	0.73	$-0.06 \pm 0.01$	$0.12 \pm 0.01$	0.90
41	1.51	$1.47 \pm 0.02$	$4.69 \pm 0.06$	1	0.76	$-0.05 \pm 0.02$	$0.12 \pm 0.02$	0.87
ii. Samples obtained from smoke plumes								
42	1.68	$1.78 \pm 0.28$	$4.16 \pm 0.84$	3	0.83	$-0.07 \pm 0.02$	$0.22 \pm 0.02$	0.82
43	1.43	$1.07 \pm 0.18$	$3.93 \pm 0.71$	5	1.01	$0.00 \pm 0.02$	$0.19 \pm 0.02$	0.01
44	1.45	$1.08 \pm 0.12$	$3.73 \pm 0.54$	3	0.93	$-0.02 \pm 0.02$	$0.18 \pm 0.02$	0.40
45	1.58	$1.42 \pm 0.13$	$3.82 \pm 0.34$	3	1.14	$0.04 \pm 0.02$	$0.14 \pm 0.02$	0.40
46	1.49	$1.88 \pm 0.30$	$5.96 \pm 0.61$	2	1.02	$0.01 \pm 0.02$	$0.15 \pm 0.02$	0.05
47	1.26	$0.66 \pm 0.07$	$4.06 \pm 0.50$	1	1.01	$0.003 \pm 0.02$	$0.15 \pm 0.02$	0.01
48	1.70	$2.18 \pm 1.31$	$5.04 \pm 2.78$	4	0.82	$-0.06 \pm 0.02$	$0.19 \pm 0.02$	0.81
49	1.79	$2.05 \pm 0.12$	$4.15 \pm 0.30$	3	0.90	$-0.04 \pm 0.02$	$0.19 \pm 0.02$	0.53
50	1.41	$1.24 \pm 0.11$	$4.97 \pm 0.34$	1	0.78	$-0.07 \pm 0.02$	$0.19 \pm 0.02$	0.80
iii. Samples from regional haze (Namibia)								
51	1.80	$2.75 \pm 0.03$	$5.51 \pm 0.06$	4	0.74	$-0.05 \pm 0.02$	$0.11 \pm 0.02$	0.88
52	2.89	$4.68 \pm 0.12$	$3.69 \pm 0.15$	32	0.83	$-0.03 \pm 0.01$	$0.11 \pm 0.01$	0.71
53	1.33	$1.54 \pm 0.06$	$6.84 \pm 0.14$	3	0.79	$-0.04 \pm 0.02$	$0.10 \pm 0.02$	0.53
54	1.61	$1.83 \pm 0.02$	$4.85 \pm 0.05$	1	0.73	$-0.06 \pm 0.02$	$0.14 \pm 0.02$	0.86

Table 3.2c. As per Table 3.2a, but at  $\lambda = 700$  nm

ID	$f_{sca}$ - fit coefficients				$\chi^2$	$f_0$ - fit coefficients			
	$f_{sca}(80)$	$a_1$	$a_2$	$f_0(80)$		slope ( $b_1$ )	intercept ( $b_2$ )	$r^2$	
i. Samples from regional haze (South Africa, Mozambique, Botswana, Zambia)									
1	2.05	$4.12 \pm 0.45$	$6.10 \pm 0.47$	43	0.74	$-0.08 \pm 0.02$	$0.18 \pm 0.01$	0.80	
2	2.08	$2.79 \pm 0.22$	$1.56 \pm 0.15$	33	0.68	$-0.09 \pm 0.02$	$0.17 \pm 0.02$	0.98	
3	1.99	$5.41 \pm 0.12$	$7.62 \pm 0.09$	13	0.92	$-0.02 \pm 0.02$	$0.14 \pm 0.02$	0.16	
4	1.59	$2.10 \pm 0.07$	$5.69 \pm 0.12$	18	0.86	$-0.05 \pm 0.02$	$0.19 \pm 0.02$	0.68	
5	2.10	$3.68 \pm 0.44$	$1.27 \pm 0.12$	14	0.65	$-0.10 \pm 0.02$	$0.17 \pm 0.02$	0.96	
6	2.33	$3.01 \pm 0.18$	$2.13 \pm 0.20$	20	0.62	$-0.09 \pm 0.01$	$0.15 \pm 0.01$	0.97	
7	2.03	$2.35 \pm 0.03$	$3.34 \pm 0.06$	6	0.69	$-0.10 \pm 0.02$	$0.19 \pm 0.01$	0.82	
8	1.97	$2.05 \pm 0.05$	$2.26 \pm 0.11$	7	0.64	$-0.10 \pm 0.02$	$0.17 \pm 0.01$	0.98	
9	1.84	$1.79 \pm 0.01$	$2.88 \pm 0.02$	4	0.70	$-0.09 \pm 0.02$	$0.17 \pm 0.01$	0.98	
10	2.14	$2.46 \pm 0.01$	$2.33 \pm 0.01$	3	0.65	$-0.10 \pm 0.02$	$0.18 \pm 0.01$	0.95	
11	2.14	$3.10 \pm 0.13$	$4.37 \pm 0.32$	19	0.58	$-0.15 \pm 0.03$	$0.23 \pm 0.02$	0.92	
12	2.19	$3.06 \pm 0.10$	$4.06 \pm 0.19$	15	0.60	$-0.13 \pm 0.02$	$0.20 \pm 0.02$	0.94	
13	1.97	$2.61 \pm 0.07$	$4.33 \pm 0.14$	13	0.65	$-0.11 \pm 0.02$	$0.19 \pm 0.02$	0.91	
14	1.72	$1.58 \pm 0.13$	$3.13 \pm 0.33$	33	0.70	$-0.08 \pm 0.02$	$0.16 \pm 0.02$	0.87	
15	2.01	$2.31 \pm 0.08$	$3.34 \pm 0.15$	27	0.71	$-0.08 \pm 0.02$	$0.16 \pm 0.01$	0.75	
16	2.49	$4.18 \pm 0.05$	$4.48 \pm 0.07$	12	0.65	$-0.12 \pm 0.02$	$0.20 \pm 0.02$	0.90	
17	1.60	$1.88 \pm 0.18$	$5.07 \pm 0.42$	9	0.75	$-0.09 \pm 0.02$	$0.21 \pm 0.02$	0.82	
18	2.09	$2.90 \pm 0.01$	$4.22 \pm 0.02$	3	0.65	$-0.11 \pm 0.02$	$0.20 \pm 0.02$	0.90	
19	1.90	$2.34 \pm 0.02$	$4.11 \pm 0.05$	6	0.69	$-0.11 \pm 0.02$	$0.21 \pm 0.02$	0.91	
20	1.52	$1.60 \pm 0.01$	$4.96 \pm 0.04$	1	0.76	$-0.09 \pm 0.02$	$0.22 \pm 0.02$	0.88	
21	1.98	$3.43 \pm 0.08$	$5.59 \pm 0.11$	7	0.67	$-0.12 \pm 0.02$	$0.22 \pm 0.02$	0.93	
22	1.49	$1.57 \pm 0.12$	$5.19 \pm 0.36$	10	0.77	$-0.08 \pm 0.02$	$0.20 \pm 0.02$	0.80	
23	1.59	$1.43 \pm 0.01$	$3.83 \pm 0.06$	2	0.73	$-0.09 \pm 0.02$	$0.19 \pm 0.02$	0.91	
24	1.47	$1.21 \pm 0.05$	$4.06 \pm 0.20$	2	0.76	$-0.08 \pm 0.02$	$0.18 \pm 0.02$	0.94	
25	1.50	$1.91 \pm 0.06$	$5.99 \pm 0.12$	2	0.75	$-0.09 \pm 0.02$	$0.20 \pm 0.02$	0.89	
26	1.71	$1.52 \pm 0.24$	$3.02 \pm 1.00$	21	0.73	$-0.09 \pm 0.03$	$0.19 \pm 0.02$	0.88	
27	1.37	$0.80 \pm 0.07$	$3.22 \pm 0.42$	6	0.71	$-0.09 \pm 0.02$	$0.19 \pm 0.02$	0.90	
28	1.55	$2.29 \pm 0.05$	$6.40 \pm 0.13$	3	0.72	$-0.09 \pm 0.02$	$0.18 \pm 0.02$	0.89	
29	1.53	$1.25 \pm 0.03$	$3.63 \pm 0.16$	3	0.73	$-0.08 \pm 0.02$	$0.16 \pm 0.02$	0.91	
30	1.60	$1.36 \pm 0.07$	$3.41 \pm 0.33$	6	0.71	$-0.08 \pm 0.02$	$0.16 \pm 0.02$	0.95	
31	1.48	$1.41 \pm 0.17$	$4.76 \pm 0.45$	5	0.82	$-0.06 \pm 0.03$	$0.17 \pm 0.03$	0.70	
32	1.36	$2.35 \pm 0.39$	$8.42 \pm 0.97$	5	0.76	$-0.06 \pm 0.02$	$0.15 \pm 0.02$	0.80	
33	1.23	$1.10 \pm 0.10$	$7.07 \pm 0.47$	2	0.82	$-0.06 \pm 0.02$	$0.18 \pm 0.02$	0.82	
34	1.43	$1.05 \pm 0.05$	$3.84 \pm 0.22$	2	0.79	$-0.07 \pm 0.02$	$0.18 \pm 0.02$	0.90	
35	1.44	$1.31 \pm 0.26$	$4.78 \pm 0.71$	17	0.84	$-0.05 \pm 0.01$	$0.17 \pm 0.01$	0.88	
36	1.52	$1.32 \pm 0.19$	$4.01 \pm 0.67$	4	0.69	$-0.08 \pm 0.03$	$0.15 \pm 0.02$	0.93	
37	1.81	$1.87 \pm 0.28$	$3.43 \pm 0.66$	19	-	-	-	-	
38	1.72	$1.50 \pm 0.16$	$2.63 \pm 0.61$	17	-	-	-	-	
39	1.81	$3.30 \pm 0.03$	$6.29 \pm 0.05$	14	-	-	-	-	
40	1.60	$1.81 \pm 0.06$	$4.90 \pm 0.15$	6	0.71	$-0.08 \pm 0.01$	$0.16 \pm 0.01$	0.92	
41	1.60	$1.79 \pm 0.01$	$4.86 \pm 0.03$	1	0.69	$-0.09 \pm 0.02$	$0.17 \pm 0.02$	0.94	
ii. Samples obtained from smoke plumes									
42	1.75	$1.98 \pm 0.23$	$4.19 \pm 0.63$	5	0.92	$-0.04 \pm 0.02$	$0.25 \pm 0.02$	0.51	
43	1.54	$1.32 \pm 0.19$	$3.88 \pm 0.61$	8	1.07	$0.04 \pm 0.02$	$0.24 \pm 0.02$	0.40	
44	1.53	$1.32 \pm 0.10$	$3.89 \pm 0.37$	4	1.04	$0.01 \pm 0.03$	$0.20 \pm 0.02$	0.16	
45	1.72	$1.75 \pm 0.11$	$3.77 \pm 0.22$	5	1.28	$0.10 \pm 0.03$	$0.16 \pm 0.02$	0.83	
46	1.59	$2.07 \pm 0.14$	$5.56 \pm 0.27$	2	1.06	$0.02 \pm 0.03$	$0.18 \pm 0.02$	0.47	
47	1.34	$0.89 \pm 0.06$	$4.23 \pm 0.30$	2	1.05	$0.02 \pm 0.02$	$0.18 \pm 0.02$	0.46	
48	1.71	$2.25 \pm 0.76$	$5.12 \pm 1.57$	4	1.52	$0.01 \pm 0.01$	$0.01 \pm 0.00$	0.76	
49	1.88	$2.31 \pm 0.09$	$4.21 \pm 0.18$	3	2.44	$0.08 \pm 0.01$	$0.004 \pm 0.01$	0.96	
50	1.47	$1.47 \pm 0.09$	$5.01 \pm 0.23$	2	0.69	$-0.01 \pm 0.01$	$0.03 \pm 0.01$	0.94	
iii. Samples from regional haze (Namibia)									
51	1.83	$2.95 \pm 0.03$	$5.64 \pm 0.05$	4	0.71	$-0.07 \pm 0.02$	$0.14 \pm 0.02$	0.88	
52	3.11	$5.23 \pm 0.14$	$3.66 \pm 0.15$	35	0.78	$-0.04 \pm 0.01$	$0.11 \pm 0.01$	0.89	
53	1.36	$1.29 \pm 0.01$	$5.77 \pm 0.03$	1	0.71	$-0.07 \pm 0.02$	$0.14 \pm 0.02$	0.90	
54	1.67	$1.89 \pm 0.02$	$4.60 \pm 0.04$	1	0.73	$-0.08 \pm 0.02$	$0.17 \pm 0.02$	0.93	

can be calculated for any RH between 30-80%. When the ambient RH is less than 30%, we assume that  $f_{\text{sca},\lambda}$  and  $f_{\beta,\lambda}$  are 1.

We separately analyzed the humidographs collected in South Africa, Botswana, Mozambique, and Zambia when the anticyclonic circulation was in place and during the River of Smoke (Section 3.1). In general, the dates of the humidographs listed in Table 3.1 were used to segregate the humidographs, but the exceptions to this general categorization are as follows. Humidographs obtained at 11:08 UTC on August 31, 8:02 UTC on September 1 and 10:19 UTC on September 2 were considered with of River of Smoke samples since the most recent airflow was from the north (Table 3.1) or the humidographs were obtained in tropical Zambia (where most of the River of Smoke aerosol originated). The humidograph on September 7 was considered with samples collected during the anticyclonic circulation since the airflow was from the southwest (Table 3.1).

Humidographs for a typical sample collected during the anticyclonic circulation and during the River of Smoke, together with the corresponding best fit curves to Eq. 3.1, are shown in Figure 3.3. These two humidographs are quite different, although they were obtained at nearly identical locations in northeastern South Africa and just two days apart. As listed in Table 3.1, the sample on September 1 shown in Figure 3.3 was in southeasterly airflow, and the sample on September 3 shown in Figure 3.3 was in airflow from the north-northwest, which transported heavy smoke from tropical Africa. Values of  $\sigma_{\text{sca}}$  for the sample of regional haze on September 1 increase much more quickly with increasing RH

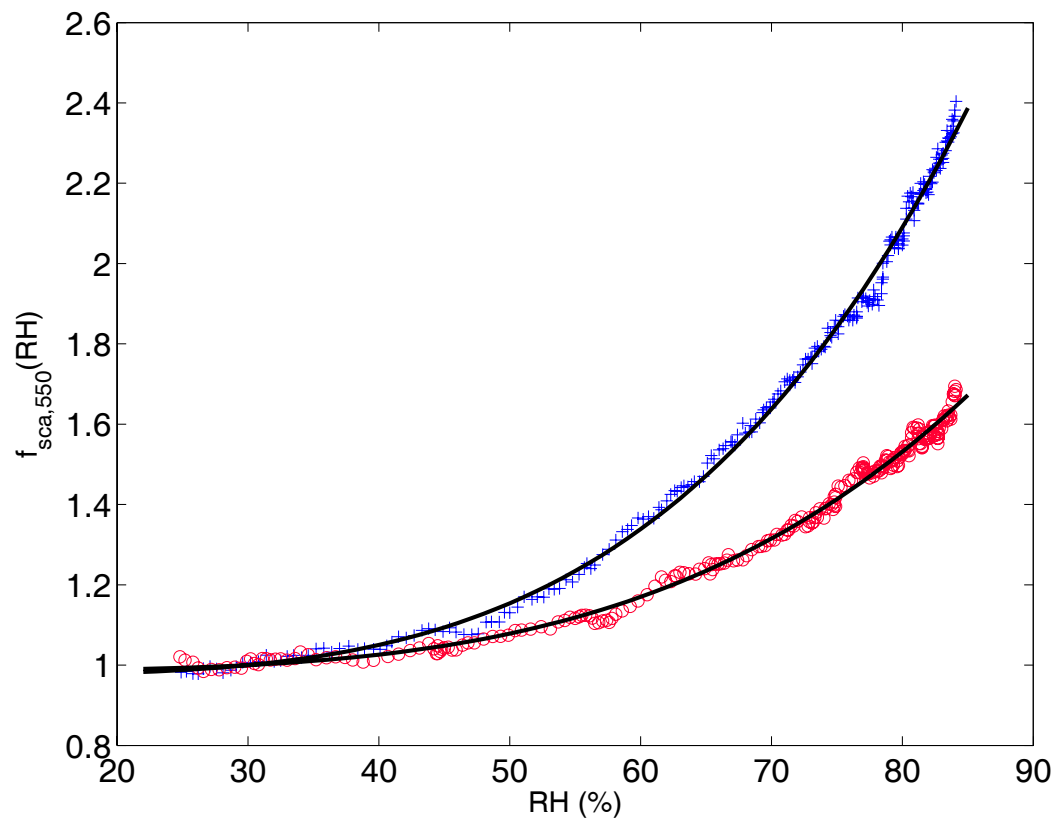


Fig. 3.3. Humidographs (at  $\lambda = 550$  nm) of regional haze collected in northern South Africa at 6:12 UTC on 1 September 2000 (blue crosses), and regional haze with heavy smoke collected at 7:33 UTC on 3 September 2000 (red circles). The humidograph for 1 September 2000 is characteristic of those obtained prior to the River of Smoke, and the humidograph for 3 September 2000 is characteristic of those obtained during the River of Smoke. The crosses and circles indicate actual data collected by the  $3\lambda$ -nephelometer during the humidograph. The solid curves are the non-linear fits to the data based on Eq. 3.1 and the coefficients in Table 3.2.

than  $\sigma_{\text{sca}}$  for the sample of regional haze on September 3 during the River of Smoke.

We also categorize the smoke sampled directly from the fire emissions based on the estimated time since emission from the fire. We estimate the “age” of the smoke by the average windspeed measured from the aircraft and categorize the smoke as either having aged less than 10 minutes or somewhere between 10-50 minutes, keeping in mind that the sample size is small for direct smoke samples (Table 3.1).

In Figure 3.4, we show two characteristic humidographs of smoke collected downwind of a large biomass fire on 7 Sep 2000 in the Timbavati game park [Hobbs *et al.*, 2003; Trentmann *et al.*, 2005]. The age of the smoke is estimated from average wind speed measurements obtained from the UW research aircraft. The comparison suggests that the hygroscopicity decreases as the smoke ages.

Listed in Table 3.3 are the mean values for the fit coefficients and the mean values of  $f_{\text{sca},\lambda}(80)$  and  $f_{\beta,\lambda}(80)$  for the different sampling conditions discussed above, where we have also separately listed the samples collected in Namibia. The specific samples that comprise each category in Table 3.3 are listed below the Table and can be cross-referenced with information in Tables 3.1-3.2.

The most noticeable result in Table 3.3 is the ~24% and ~9% respective differences between the mean values of  $f_{\text{sca},\lambda}(80)$  and  $f_{\beta,\lambda}(80)$  for the regional haze with during the River of Smoke and the mean values of  $f_{\text{sca},\lambda}(80)$  and  $f_{\beta,\lambda}(80)$



Table 3.3. Mean values ( $\pm 1$  standard deviation) of  $f_{\text{sca}}(80)$ ,  $f_{\text{p}}(80)$ , and the empirical fit coefficients for Eqs. 3.1 and 3.2, for the different aerosol types encountered during SAFARI-2000.

Aerosol type	Number of samples	$\lambda$ (nm)	$f_{\text{sca}}(80)$	$a_1$	$a_2$	$f_{\text{p}}(80)$	slope ( $b_1$ )	intercept ( $b_2$ )
Regional haze <sup>a</sup>	20	450	1.90 $\pm$ 0.18	2.56 $\pm$ 0.90	3.71 $\pm$ 1.72	0.72 $\pm$ 0.07	-0.06 $\pm$ 0.02	0.11 $\pm$ 0.02
		550	1.95 $\pm$ 0.19	2.70 $\pm$ 0.96	3.79 $\pm$ 1.72	0.69 $\pm$ 0.08	-0.08 $\pm$ 0.02	0.15 $\pm$ 0.02
		700	2.03 $\pm$ 0.20	2.91 $\pm$ 0.94	3.83 $\pm$ 1.64	0.69 $\pm$ 0.08	-0.10 $\pm$ 0.03	0.18 $\pm$ 0.02
Regional haze with heavy smoke <sup>b</sup>	21	450	1.45 $\pm$ 0.13	1.33 $\pm$ 0.47	4.69 $\pm$ 1.45	0.78 $\pm$ 0.04	-0.04 $\pm$ 0.01	0.11 $\pm$ 0.01
		550	1.48 $\pm$ 0.14	1.37 $\pm$ 0.43	4.59 $\pm$ 1.35	0.75 $\pm$ 0.04	-0.06 $\pm$ 0.01	0.14 $\pm$ 0.02
		700	1.54 $\pm$ 0.14	1.62 $\pm$ 0.54	4.72 $\pm$ 1.43	0.75 $\pm$ 0.04	-0.08 $\pm$ 0.01	0.18 $\pm$ 0.02
Smoke collected within 10 minutes of emission <sup>c</sup>	4	450	1.63 $\pm$ 0.15	1.72 $\pm$ 0.50	4.29 $\pm$ 0.52	0.81 $\pm$ 0.06	-0.06 $\pm$ 0.020	0.16 $\pm$ 0.02
		550	1.66 $\pm$ 0.14	1.77 $\pm$ 0.49	4.27 $\pm$ 0.55	0.87 $\pm$ 0.05	-0.05 $\pm$ 0.021	0.19 $\pm$ 0.02
		700	1.72 $\pm$ 0.14	1.96 $\pm$ 0.45	4.35 $\pm$ 0.53	1.48 $\pm$ 0.69	0.02 $\pm$ 0.046	0.11 $\pm$ 0.13
Smoke collected within 10-50 minutes of emission <sup>d</sup>	5	450	1.40 $\pm$ 0.10	1.18 $\pm$ 0.44	4.71 $\pm$ 0.88	0.96 $\pm$ 0.12	-0.01 $\pm$ 0.030	0.13 $\pm$ 0.02
		550	1.44 $\pm$ 0.12	1.26 $\pm$ 0.45	4.55 $\pm$ 0.91	0.99 $\pm$ 0.13	-0.004 $\pm$ 0.042	0.16 $\pm$ 0.03
		700	1.53 $\pm$ 0.14	1.50 $\pm$ 0.45	4.49 $\pm$ 0.77	1.03 $\pm$ 0.21	0.03 $\pm$ 0.044	0.16 $\pm$ 0.08
Regional haze in Namibia <sup>e</sup>	4	450	1.86 $\pm$ 0.67	2.49 $\pm$ 1.42	5.11 $\pm$ 1.21	0.73 $\pm$ 0.03	-0.05 $\pm$ 0.007	0.11 $\pm$ 0.01
		550	1.91 $\pm$ 0.68	2.70 $\pm$ 1.42	5.22 $\pm$ 1.31	0.77 $\pm$ 0.05	-0.05 $\pm$ 0.014	0.11 $\pm$ 0.02
		700	1.99 $\pm$ 0.77	2.84 $\pm$ 1.73	4.92 $\pm$ 0.99	0.73 $\pm$ 0.03	-0.07 $\pm$ 0.016	0.14 $\pm$ 0.02

<sup>a</sup> Samples with ID = 1-16, 18, 19, 21 or from about 14 Aug-2 Sep, per Tables 3.1 and 3.2.

<sup>b</sup> Samples with ID = 17, 22-41 or from about 2 Sep-7 Sep, per Tables 3.1 and 3.2.

<sup>c</sup> Samples with ID = 42, 44, 48, 49, per Tables 3.1 and 3.2.

<sup>d</sup> Samples with ID = 43, 45-47, 50, per Tables 3.1 and 3.2.

<sup>e</sup> Samples with ID = 51-54, per Tables 3.1 and 3.2.

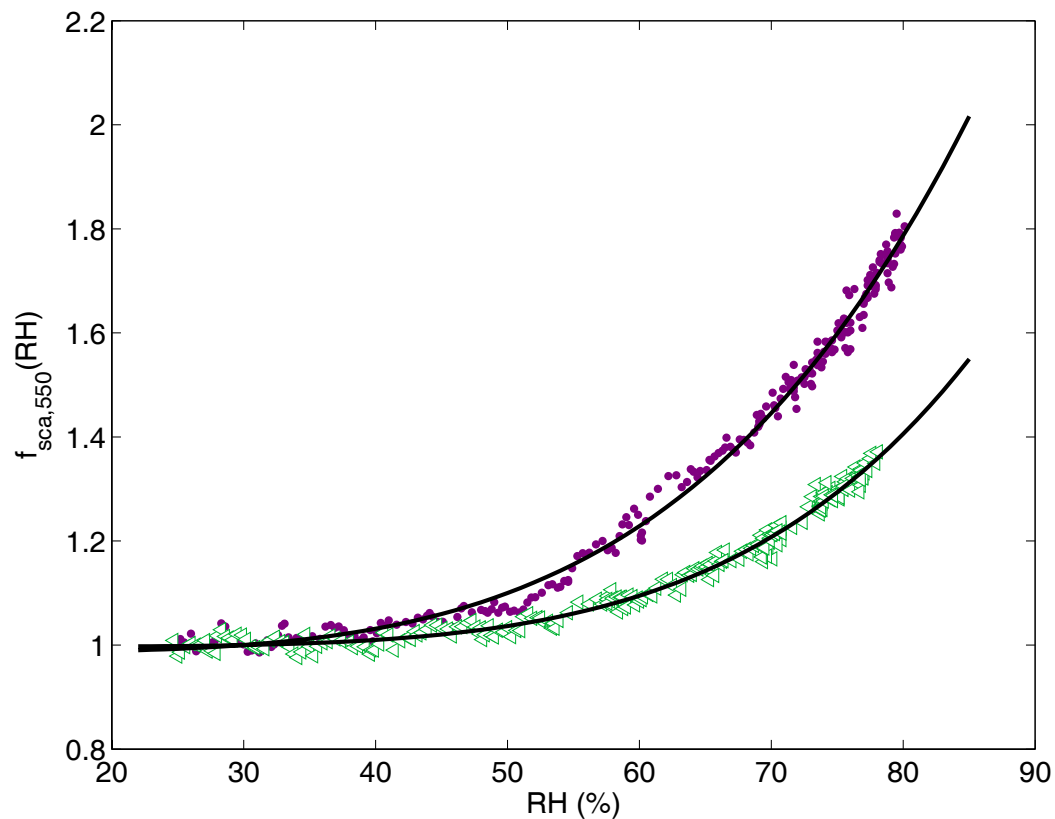


Fig. 3.4. Humidographs (at  $\lambda = 550$  nm) of smoke collected within  $\sim 10$  minutes of emission from a biomass fire at 8:59 UTC on 7 September 2000 (purple dots) and within  $\sim 50$  minutes of emission from the same fire at 10:37 UTC (green triangles). The y-axis shows the ratio increase in scattering as a function of relative humidity (RH) and the points are actual data collected by the  $3\lambda$ -nephelometer during the humidograph. The solid curves are the non-linear fits to the data based on Eq. 3.1 and the coefficients in Table 3.2.

when the anticyclonic circulation was in place. Based on back-trajectories (Table 3.1), the transported smoke during the River of Smoke had, on average, aged ~2-3 days in the atmosphere while traveling from tropical Africa. Besides biomass burning, however, there are a very limited number of aerosol sources from this region [Eck *et al.*, 2003], implying that the smoke chemical composition changed very little during transport. During the anticyclonic circulation, however, smoke back-trajectories frequently passed over urban development near Johannesburg in northeastern South Africa (Fig. 1.4). The mixing of the smoke aerosols with ambient aerosols from industrial sources [Piketh *et al.*, 1999] was limited during the River of Smoke.

Further evidence of this lack of mixing is from the data collected directly from the fires. Figure 3.4 and the data in Table 3.3 implies a rapid aging of the smoke once it is emitted. The mean values for samples collected within ~10 minutes of emission from the fire indicate a more hygroscopic aerosol than smoke samples collected within ~10-50 minutes of emission, noting the sample size is small in both cases. This is contrary to the findings of Kotchenruther and Hobbs [1998] for Brazilian biomass burning and what is generally assumed about fresh smoke emissions [Reid *et al.*, 2004a-b], but there are very few measurements available, so knowledge of the phenomenon is limited.

There is an indication that the aging of smoke away from the plume does result in higher concentrations of less hygroscopic materials [Posfai *et al.*, 2003; Li *et al.*, 2003], and Chan *et al.* [2005] showed that southern African biomass

burning aerosol chemical composition discussed in *Gao et al.* [2003] is consistent with the measurements discussed here and in *Magi and Hobbs* [2003].

Vegetation differences may have also contributed to a different chemical composition for smoke in Brazil versus smoke in southern Africa. However, as pointed out by *Reid et al.* [2004a], there are simply not enough measurements of the effects of RH on biomass burning aerosols to draw any further conclusions regarding the differences.

The analysis of the effects of RH on southern African aerosol shows that smoke ages rapidly (within hours) after emission from the fire. The results also show that smoke transported from tropical Africa over the period of days has remarkably similar mean characteristics (Table 3.3) as smoke sampled within 10-50 minutes of emission from the fire. We suggest that this indicates the chemical stability of smoke aerosol in the dry, vertically-stratified wintertime atmosphere of southern African. During periods dominated by anticyclonic circulation, the smoke aerosol was more hygroscopic, possibly due to enhanced mixing with low level background sources of industrial and dust aerosols [*Piketh et al.*, 1999]. The differences in the hygroscopic growth of southern African biomass burning aerosols will be a factor when considering both the radiative effects [*Charlson*, 1999] and the efficiency of biomass burning aerosols to act as cloud condensation nuclei [*Ross et al.*, 2003; *Reid et al.*, 2004a; *Jiang and Feingold*, 2006].

### 3.3. Aerosol Optical Depth Comparison

The UW research aircraft flew twenty vertical profiles during SAFARI-2000 to characterize the aerosol optical properties. The profiles were flown from near the surface to ~4-5 km altitude (above mean sea level) or ~500 hPa. In order to minimize the spatial and temporal variability common to aerosols [Anderson *et al.*, 2003b], most of the profiles were confined to small spatial areas and took ~15 minutes to complete. Details about the vertical profiles are listed in Table 3.4 and the locations are shown in Figure 3.5.

#### 3.3.1. Methods

We compare the aerosol optical depth ( $\tau$ ) derived by two independent aircraft-based methods. The value of  $\tau$  for a finite layer ( $\tau_{\text{layer}}$ ) defined by the minimum altitude ( $z_{\text{min}}$ ) and maximum altitude ( $z_{\text{max}}$ ) of the aircraft vertical profile (Table 3.4) can be calculated as

$$\tau_{\text{layer},\lambda} = \int_{z_{\text{min}}}^{z_{\text{max}}} \sigma_{\text{ext},\lambda}(z) dz \quad (3.5)$$

where  $\sigma_{\text{ext}}(z)$  is the extinction coefficient (Eq. 1.11) at the ambient RH and pressure as a function of altitude,  $z$ . Eq. 3.5 is similar to Eqs. 1.13 and 2.1, only with more tightly bounded limits of integration.

By combining the corrected measurements of  $\sigma_{\text{sca}}(z)$  and  $\sigma_{\text{abs}}(z)$  obtained from the  $3\lambda$ -nephelometer (Section 2.1.1) and PSAP (Section 2.1.2) during a vertical profile,  $\tau_{\text{layer}}$  for in situ data ( $\tau_{\text{is,layer}}$ ) can be calculated as

Table 3.4. The date, time, and location of the vertical profiles collected by the UW research aircraft during SAFARI-2000. The UW research aircraft flight numbers are also listed for additional cross-referencing. The numbers in the first column are used for numerical identification (ID) in Tables 3.5-3.8 as well as in Fig. 3.5.

ID	Date (2000)	Flight Number	Latitude <sup>a</sup> (°S)	Longitude <sup>a</sup> (°E)	UTC Time (hhmm)	Altitude <sup>b</sup> (km)
1	14-Aug	1811	25.90 ± 0.09	27.89 ± 0.04	1114 - 1126	1.44 - 3.56
2	14-Aug	1812	25.48 ± 0.30	27.68 ± 0.19	1228 - 1247	1.45 - 3.71
3	17-Aug	1815	24.06 ± 0.16	29.75 ± 0.21	0708 - 0725	1.28 - 3.21
4	20-Aug	1819	23.95 ± 0.08	29.01 ± 0.27	1132 - 1146	1.59 - 3.72
5	22-Aug	1820	24.98 ± 0.04	31.61 ± 0.06	0816 - 1006	0.37 - 3.82
6	24-Aug	1822	25.98 ± 0.03	32.91 ± 0.02	0810 - 0824	0.21 - 4.12
7	29-Aug	1823	23.10 ± 0.15	28.82 ± 0.08	1030 - 1047	1.65 - 3.77
8	31-Aug	1825	21.62 ± 0.17	34.27 ± 0.13	1229 - 1244	0.64 - 3.89
9	1-Sep	1826	17.48 ± 0.13	25.09 ± 0.02	1051 - 1059	2.15 - 3.77
10	2-Sep	1829	19.89 ± 0.02	23.55 ± 0.02	0952 - 1009	1.12 - 4.42
11	3-Sep	1830	20.59 ± 0.03	26.17 ± 0.02	0831 - 0850	1.08 - 4.58
12	3-Sep	1830	20.56 ± 0.07	25.90 ± 0.02	1012 - 1035	0.99 - 4.57
13	6-Sep	1832	16.24 ± 0.11	23.42 ± 0.12	0746 - 0755	1.23 - 3.79
14	6-Sep	1832	15.19 ± 0.05	23.16 ± 0.03	0917 - 0929	1.37 - 4.77
15	6-Sep	1832	15.31 ± 0.08	23.11 ± 0.05	0934 - 0950	1.65 - 4.77
16	6-Sep	1832	15.47 ± 0.22	23.46 ± 0.16	0957 - 1014	1.64 - 5.27
17	7-Sep	1834	23.61 ± 0.03	31.12 ± 0.19	1135 - 1147	1.25 - 4.10
18	11-Sep	1836	21.99 ± 0.11	12.39 ± 0.07	0925 - 0933	0.75 - 3.76
19	13-Sep	1837	20.24 ± 0.05	13.22 ± 0.02	1116 - 1135	1.02 - 5.10
20	16-Sep	1839	19.19 ± 0.04	15.84 ± 0.04	1052 - 1107	1.35 - 4.76

<sup>a</sup> These are the mean ± standard deviation of the latitude and longitude during the period of the vertical profile.

<sup>b</sup> Altitude is above mean sea level; the surface elevation in southern Africa varies.

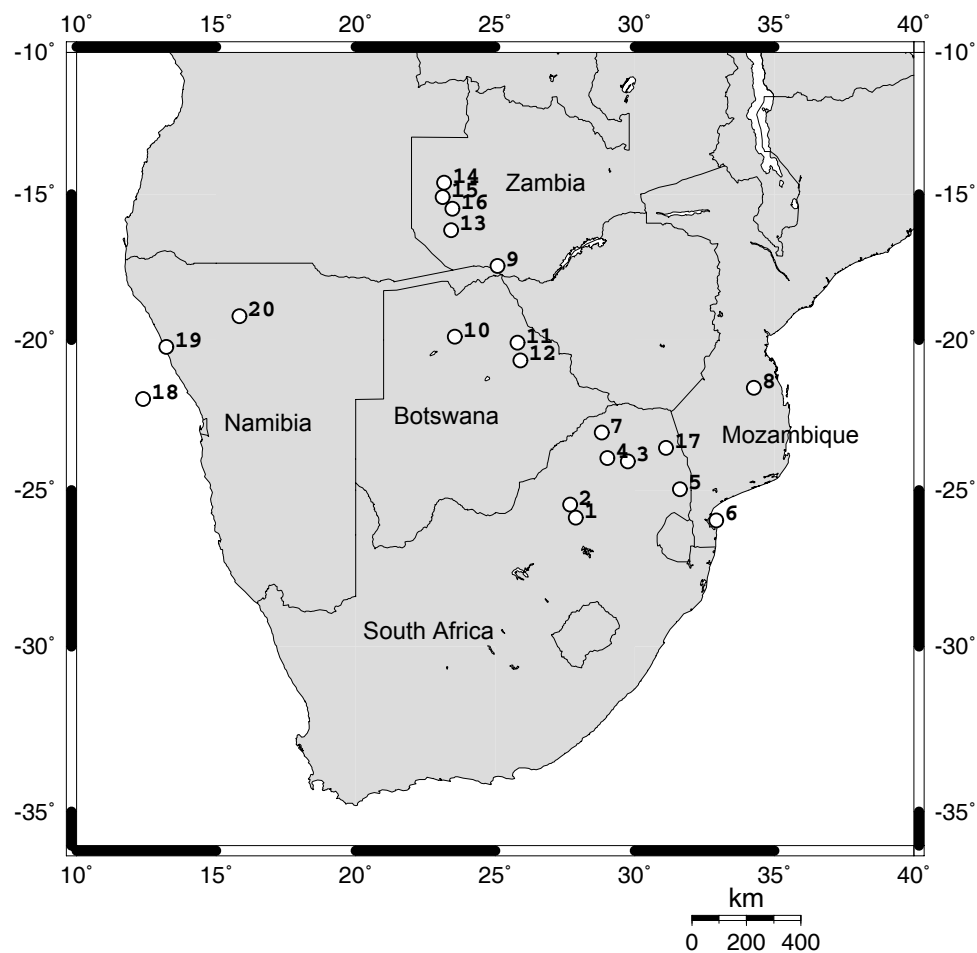


Fig. 3.5. Locations of the twenty vertical profiles collected during SAFARI-2000 by the UW research aircraft (denoted with open circles). The numbers correspond to the IDs listed in Tables 3.4-3.8 and more specific information about each profile can also be found in the same tables. The map was produced using <http://www.aquarius.geomar.de/omc/>.

$$\tau_{is,layer,\lambda} = \int_{z_{min}}^{z_{max}} [f_{sca,\lambda}(RH)\sigma_{sca,d,\lambda}(z) + f_{abs,\lambda}(RH)\sigma_{abs,d,\lambda}(z)]dz \quad (3.6)$$

where,  $\sigma_{sca,d}(z)$  is the dry (low RH) aerosol scattering coefficient,  $\sigma_{abs,d}(z)$  the dry aerosol absorption coefficient, and  $f_{sca}(RH)$  and  $f_{abs}(RH)$  are the empirical hygroscopic growth factors by which  $\sigma_{sca,d}(z)$  and  $\sigma_{abs,d}(z)$ , respectively, must be multiplied to adjust their values to the ambient RH. As described in Sections 3.2 and in *Magi and Hobbs* [2003],  $f_{sca}(RH)$  was determined from humidographs (Eq. 3.3, Table 3.2). The value of  $f_{abs}(RH)$ , however, was not measured. *Hegg et al.* [1997] and *Redemann et al.* [2001] suggest that  $f_{abs}(RH)$  should lie between 1 and  $f_{sca}(RH)$ , but since the ambient RH in this study was generally <50%, and  $\sigma_{abs,d} \ll \sigma_{sca,d}$ , we assume that  $f_{abs}(RH) = 1$ .

As mentioned in Section 2.1.2, extrapolation of  $\sigma_{abs,550}$  measured by the PSAP to other wavelengths is possible by assuming a value for  $\alpha_{abs}$  (Eq. 1.14). Often, for extrapolation to other wavelengths in the visible (in the PSAP correction from 567 nm to 550 nm described in *Bond et al.* [1999], for example),  $\alpha_{abs}$  is assumed to be 1. The value of  $\alpha_{abs}$ , however, varies from ~1-4 depending on the source of the aerosols [*Bond*, 2001; *Kirchstetter et al.*, 2004; *Ganguly et al.*, 2005; *Roden et al.*, 2005]. *Bergstrom et al.* [2003] showed that in SAFARI-2000,  $\alpha_{abs,450-700} \sim 1$  for the period when the anticyclonic circulation dominated the meteorology and  $\alpha_{abs,450-700} \sim 2$  during the River of Smoke (Section 3.1). Based on this, we extrapolate  $\sigma_{abs,550}$  to  $\sigma_{abs,450}$  and  $\sigma_{abs,700}$  using  $\alpha_{abs,450-700} = 2$  for measurements made between 1-6 Sep (during the River of Smoke) and using



$\alpha_{\text{abs},450-700} = 1$  for other vertical profiles. The vertical profile on 7 Sep (Table 3.4) was obtained in a location not affected by the River of Smoke (see the back-trajectories listed in Table 3.1). Using this extrapolation, we derive  $\omega_o$  at  $\lambda = 450$ , 550, and 700 nm (Eq. 1.7) by combining measurements from the  $3\lambda$ -nephelometer and the PSAP. The values of  $\alpha_{\text{abs},450-700}$  are listed in Table 3.7 and we discuss the uncertainty associated with the extrapolation in Section 3.4.1.

Occasionally, the continuous data from the  $3\lambda$ -nephelometer was interrupted during the collection of a humidograph (Section 3.2) during a vertical profile. During these times, we estimate the missing  $3\lambda$ -nephelometer measurements by calculating the average difference between  $\sigma_{\text{sca},d,537}$  measured by the  $1\lambda$ -nephelometer (Section 2.1.1) and  $\sigma_{\text{sca},d}$  measured by the  $3\lambda$ -nephelometer during periods when both instruments were operating normally and use this average difference to fill in the missing  $3\lambda$ -nephelometer data. For brief periods ( $\sim 30$  s) when the filter was being changed in the PSAP [Bond *et al.*, 1999], we interpolate to fill in the missing  $\sigma_{\text{abs},d}$  data.

As described in Section 2.1.4, the Sunphotometer measured  $\tau_{\text{column},\lambda}$  at twelve wavelengths [Schmid *et al.*, 2003]. No adjustment to ambient RH is necessary since the Sunphotometer does not directly sample or dry the aerosol. Values of the layer aerosol optical depth from the Sunphotometer,  $\tau_{\text{sp},\text{layer}}$ , can be calculated by subtracting  $\tau_{\text{sp},\text{column},\lambda}$  at the top of the aircraft profile from the entire  $\tau_{\text{sp},\text{column}}$  profile. To directly compare  $\tau_{\text{is},\text{layer}}$  and  $\tau_{\text{sp},\text{layer}}$ , we interpolate  $\tau_{\text{sp},\text{layer}}$

from the measured wavelengths (Section 2.1.4) to the three wavelengths of the 3 $\lambda$ -nephelometer ( $\lambda = 450, 550, 700$  nm) using a quadratic function of  $\ln(\lambda)$  versus  $\ln(\tau_{\text{sp,column}})$  suggested in *Schmid et al.* [2003]. The coefficients of the quadratic polynomial are determined by a standard polynomial fit to the Sunphotometer data and are not listed here.

The most straightforward comparison of  $\tau_{\text{is,layer}}$  and  $\tau_{\text{sp,layer}}$  is at  $\lambda = 550$  nm since this involves the fewest adjustments or assumptions (Section 2.1.1, 2.1.2, 2.1.4). This comparison of  $\tau_{\text{is,layer}}$  and  $\tau_{\text{sp,layer}}$  at  $\lambda = 550$  nm for fifteen vertical profiles has been described in *Magi et al.* [2003], but we describe five more vertical profiles in this analysis to bring the total to twenty. We also compare  $\tau_{\text{is,layer}}$  and  $\tau_{\text{sp,layer}}$  at  $\lambda = 450$  and 700 nm using the assumed value for  $\alpha_{\text{abs}}$  discussed above and listed in Table 3.7. The values of  $\tau_{\text{is,layer}}$  and  $\tau_{\text{sp,layer}}$  for  $\lambda = 450, 550$ , and 700 nm are listed in Table 3.5.

To compare the two methods, we use several different calculations based on protocol suggested in *Schmid et al.* [2006]. The root mean squared difference ( $\delta_{\text{rms}}$ ) between  $\tau_{\text{is,layer}}$  and  $\tau_{\text{sp,layer}}$  is calculated as

$$\delta_{\text{rms}} = \sqrt{\sum_{j=1}^{N_{\text{vp}}} (\tau_{\text{is,layer}}^j - \tau_{\text{sp,layer}}^j)^2} \quad (3.8)$$

where the superscript  $j$  indicates one of the  $N_{\text{vp}} = 20$  vertical profiles analyzed here. Values of  $\delta_{\text{rms}}$  indicates the magnitude of the random errors between  $\tau_{\text{is,layer}}$  and  $\tau_{\text{sp,layer}}$ . The root mean squared percentage,  $\rho_{\text{rms}}$ , is

Table 3.5. Comparison of layer aerosol optical depth ( $\tau_{\text{layer}}$ ) measured by the Sunphotometer ( $\tau_{\text{sp,layer}}$ ) and by in situ instruments ( $\tau_{\text{is,layer}}$ ) at three visible wavelengths ( $\lambda$ ) during aircraft vertical profiles. Also listed is  $\tau_{\text{sp,above}}$  which is  $\tau$  measured by the Sunphotometer at the maximum altitude of the vertical profile listed in Table 3.4.

ID	Date (2000)	$\lambda = 450 \text{ nm}$			$\lambda = 550 \text{ nm}$			$\lambda = 700 \text{ nm}$		
		$\tau_{\text{sp,layer}}$	$\tau_{\text{is,layer}}$	$\tau_{\text{sp,above}}$	$\tau_{\text{sp,layer}}$	$\tau_{\text{is,layer}}$	$\tau_{\text{sp,above}}$	$\tau_{\text{sp,layer}}$	$\tau_{\text{is,layer}}$	$\tau_{\text{sp,above}}$
1	14-Aug	0.21 $\pm$ 0.03	0.14 $\pm$ 0.02	0.01	0.15 $\pm$ 0.03	0.11 $\pm$ 0.02	0.01	0.10 $\pm$ 0.010	0.07 $\pm$ 0.01	0.01
2	14-Aug	0.23 $\pm$ 0.04	0.15 $\pm$ 0.02	0.01	0.17 $\pm$ 0.03	0.10 $\pm$ 0.01	0.01	0.12 $\pm$ 0.013	0.07 $\pm$ 0.01	0.004
3	17-Aug	0.14 $\pm$ 0.01	0.11 $\pm$ 0.02	0.01	0.09 $\pm$ 0.01	0.08 $\pm$ 0.01	0.01	0.06 $\pm$ 0.003	0.05 $\pm$ 0.01	0.005
4	20-Aug	0.13 $\pm$ 0.01	0.12 $\pm$ 0.02	0.04	0.09 $\pm$ 0.02	0.08 $\pm$ 0.01	0.03	0.06 $\pm$ 0.003	0.05 $\pm$ 0.01	0.02
5	22-Aug	0.43 $\pm$ 0.02	0.38 $\pm$ 0.03	0.04	0.30 $\pm$ 0.04	0.25 $\pm$ 0.02	0.03	0.19 $\pm$ 0.005	0.14 $\pm$ 0.01	0.02
6	24-Aug	0.31 $\pm$ 0.01	0.22 $\pm$ 0.03	0.06	0.23 $\pm$ 0.02	0.20 $\pm$ 0.02	0.04	0.17 $\pm$ 0.003	0.11 $\pm$ 0.01	0.03
7	29-Aug	0.14 $\pm$ 0.01	0.14 $\pm$ 0.02	0.06	0.10 $\pm$ 0.02	0.10 $\pm$ 0.01	0.05	0.07 $\pm$ 0.003	0.06 $\pm$ 0.01	0.03
8	31-Aug	0.33 $\pm$ 0.01	0.36 $\pm$ 0.03	0.04	0.23 $\pm$ 0.02	0.24 $\pm$ 0.03	0.03	0.15 $\pm$ 0.003	0.14 $\pm$ 0.02	0.02
9	1-Sep	0.13 $\pm$ 0.01	0.21 $\pm$ 0.03	0.11	0.09 $\pm$ 0.02	0.14 $\pm$ 0.02	0.08	0.06 $\pm$ 0.004	0.08 $\pm$ 0.01	0.06
10	2-Sep	0.41 $\pm$ 0.02	0.39 $\pm$ 0.05	0.02	0.27 $\pm$ 0.03	0.25 $\pm$ 0.04	0.01	0.17 $\pm$ 0.006	0.14 $\pm$ 0.02	0.01
11	3-Sep	0.91 $\pm$ 0.02	0.90 $\pm$ 0.09	0.11	0.63 $\pm$ 0.02	0.59 $\pm$ 0.06	0.08	0.40 $\pm$ 0.007	0.34 $\pm$ 0.04	0.06
12	3-Sep	0.76 $\pm$ 0.02	0.79 $\pm$ 0.07	0.05	0.52 $\pm$ 0.03	0.52 $\pm$ 0.05	0.03	0.33 $\pm$ 0.005	0.29 $\pm$ 0.03	0.02
13	6-Sep	0.77 $\pm$ 0.02	0.96 $\pm$ 0.11	0.68	0.54 $\pm$ 0.02	0.64 $\pm$ 0.07	0.50	0.34 $\pm$ 0.006	0.37 $\pm$ 0.05	0.33
14	6-Sep	1.09 $\pm$ 0.02	1.18 $\pm$ 0.10	0.24	0.78 $\pm$ 0.03	0.78 $\pm$ 0.08	0.18	0.50 $\pm$ 0.008	0.46 $\pm$ 0.05	0.13
15	6-Sep	0.95 $\pm$ 0.02	1.10 $\pm$ 0.10	0.25	0.68 $\pm$ 0.03	0.73 $\pm$ 0.07	0.19	0.44 $\pm$ 0.007	0.43 $\pm$ 0.05	0.13
16	6-Sep	1.03 $\pm$ 0.02	1.18 $\pm$ 0.11	0.16	0.73 $\pm$ 0.03	0.79 $\pm$ 0.08	0.13	0.47 $\pm$ 0.009	0.47 $\pm$ 0.05	0.09
17	7-Sep	0.13 $\pm$ 0.01	0.11 $\pm$ 0.02	0.04	0.10 $\pm$ 0.03	0.08 $\pm$ 0.01	0.03	0.07 $\pm$ 0.005	0.05 $\pm$ 0.01	0.03
18	11-Sep	0.23 $\pm$ 0.02	0.22 $\pm$ 0.02	0.28	0.18 $\pm$ 0.04	0.16 $\pm$ 0.02	0.21	0.12 $\pm$ 0.004	0.10 $\pm$ 0.01	0.15
19	13-Sep	0.52 $\pm$ 0.02	0.46 $\pm$ 0.04	0.12	0.39 $\pm$ 0.03	0.32 $\pm$ 0.03	0.09	0.26 $\pm$ 0.005	0.20 $\pm$ 0.02	0.06
20	16-Sep	0.26 $\pm$ 0.02	0.29 $\pm$ 0.03	0.11	0.20 $\pm$ 0.04	0.20 $\pm$ 0.02	0.09	0.13 $\pm$ 0.004	0.13 $\pm$ 0.01	0.07

$$\rho_{rms} = 100 \frac{\overline{\delta_{rms}}}{0.5\overline{\tau_{is,layer}} + 0.5\overline{\tau_{sp,layer}}} \quad (3.9)$$

where  $\overline{\tau_{is,layer}}$  and  $\overline{\tau_{sp,layer}}$  are the mean values of  $\tau_{is,layer}$  and  $\tau_{sp,layer}$ , respectively (and are listed in Table 3.6). We also calculate the bias of  $\tau_{is,layer}$  with respect to  $\tau_{sp,layer}$  as

$$\delta_{bias} = \tau_{is,layer} - \tau_{sp,layer} \quad (3.10)$$

where the  $\delta_{bias}$  is an indicator of systematic difference between  $\tau_{is,layer}$  and  $\tau_{sp,layer}$ .

The bias percentage,  $\rho_{bias}$ , is

$$\rho_{bias} = 100 \frac{\overline{\delta_{bias}}}{\overline{\tau_{sp,layer}}} \quad (3.11)$$

and  $\overline{\tau_{sp,layer}}$  is the mean value of  $\tau_{sp,layer}$ .

Since we expect  $\tau_{is,layer}$  and  $\tau_{sp,layer}$  to be linearly related, a least squares bisector linear regression is used. The slope of the best fit line in the least squares bisector method is the slope of the line that bisects the minor angle between the regression of  $\tau_{is,layer}$  on  $\tau_{sp,layer}$  and the regression of  $\tau_{sp,layer}$  on  $\tau_{is,layer}$  [Schmid *et al.*, 2006].

### 3.3.2. Analysis

Figure 3.6 shows the comparison of  $\tau_{is,layer}$  and  $\tau_{sp,layer}$  for  $\lambda = 450, 550$ , and 700 nm and includes the corresponding statistics for each of the three wavelengths individually as well as all wavelengths considered together (“all  $\lambda$ ”

Table 3.6. Statistics from the comparison of the layer aerosol optical depth ( $\tau_{\text{layer}}$ ) measured by the Sunphotometer ( $\tau_{\text{sp,layer}}$ ) and derived from the in situ measurements ( $\tau_{\text{is,layer}}$ ). The statistics of the twenty vertical profiles in Table 3.4 are given for each wavelength ( $\lambda$ ), but also considered together under the category "all".

$\lambda$ (nm)	number of cases	SAFARI-2000 mean values <sup>a</sup>					rms <sup>b</sup>		bias <sup>c</sup>		linear regression <sup>d</sup>	
		$\tau_{\text{sp,layer}}$	$\tau_{\text{is,layer}}$	$\tau_{\text{sp,above}}$ <sup>e</sup>	$\delta_{\text{rms}}$	$\rho_{\text{rms}}$	$\delta_{\text{bias}}$	$\rho_{\text{bias}}$	slope	intercept	$r^2$	
450	20	0.46 ± 0.34	0.47 ± 0.39	0.12 ± 0.16	0.08	17	0.015	3	1.16 ± 0.04	-0.06 ± 0.03	0.97	
550	20	0.32 ± 0.24	0.32 ± 0.26	0.09 ± 0.12	0.04	13	-0.006	-2	1.08 ± 0.04	-0.03 ± 0.02	0.98	
700	20	0.21 ± 0.15	0.19 ± 0.15	0.06 ± 0.08	0.03	17	-0.023	-12	0.99 ± 0.04	-0.02 ± 0.01	0.97	
all	60	0.33 ± 0.27	0.32 ± 0.30	0.09 ± 0.12	0.06	17	-0.005	-1	1.13 ± 0.02	-0.05 ± 0.01	0.98	

<sup>a</sup> The mean is stated as mean  $\pm$  standard deviation; large standard deviations indicate the variability of  $\tau$  during SAFARI-2000

<sup>b</sup> Root mean squared (rms) calculations are described in Equations 3.8 and 3.9

<sup>c</sup> Bias calculations are described in Equations 3.10 and 3.11; negative bias indicates that  $\tau_{\text{is,layer}} < \tau_{\text{sp,layer}}$

<sup>d</sup> The linear regression is done using a least squares bisector method [e.g. Schmid *et al.*, 2006]

<sup>e</sup> This is the mean value of  $\tau$  above the maximum altitude of the aircraft (Table 3.4)

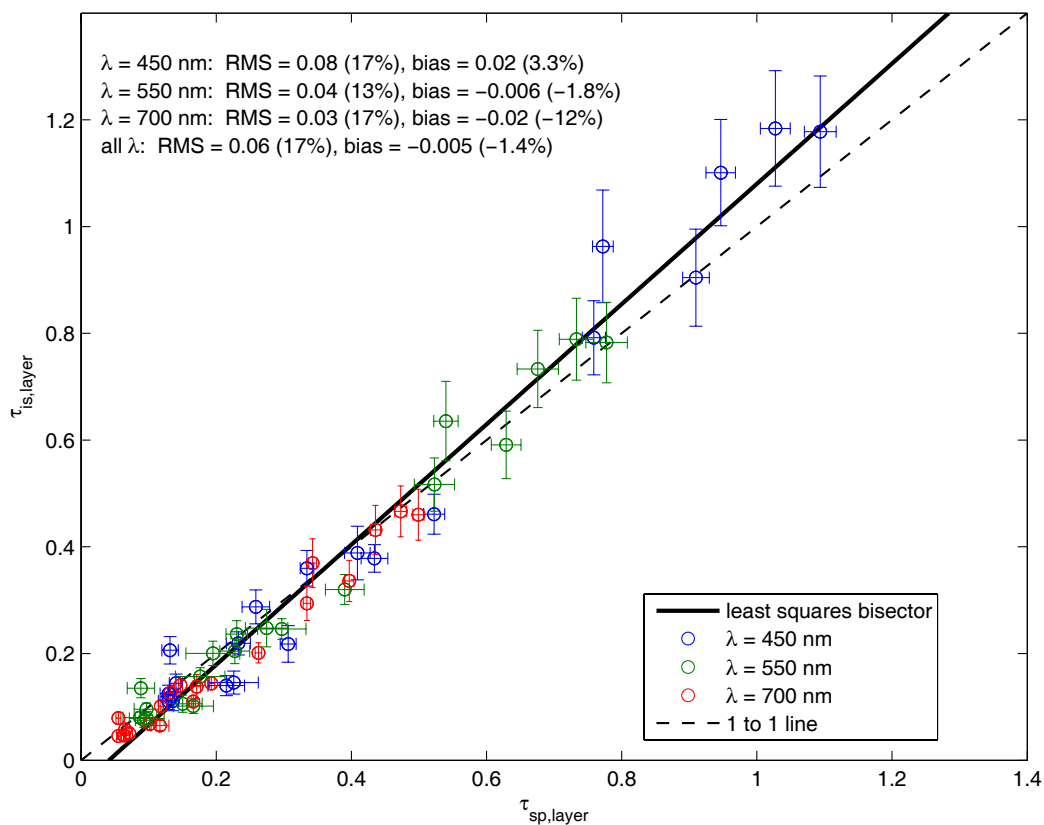


Fig. 3.6. Comparison of layer aerosol optical depth ( $\tau_{layer}$ ) measured by the Sunphotometer ( $\tau_{sp,layer}$ ) and derived from in situ measurements ( $\tau_{is,layer}$ ) using an absorption angstrom exponent of 1 and 2 depending on the particular flight (Table 3.7) to extrapolate the in situ absorption coefficient from a wavelength,  $\lambda$ , of 550 nm to 450 and 700 nm. The statistics on the top left are described in Table 3.6.

in Fig. 3.6). Table 3.5 lists the statistics and values used to calculate them. The errors listed in Table 3.5 are determined by propagating the errors associated with the instrumentation, the corrections, and vertical variability by the standard quadratures method [Bevington and Robinson, 1992]. We discuss the error propagation for all aerosol properties in more detail in Section 3.4.1.

The values of  $\delta_{\text{bias}}$  are very low, but show an increasingly negative trend with increasing  $\lambda$ . Schmid *et al.* [2006] found the same increasingly negative  $\delta_{\text{bias}}$  with increasing  $\lambda$  in the central USA. Previous studies have found  $\delta_{\text{bias}}$  is typically negative, by as much as 20-30% in some cases [Hegg *et al.*, 1997; Hartley *et al.*, 2000; Schmid *et al.*, 2000; Magi *et al.*, 2005], but the inverse relationship of  $\delta_{\text{bias}}$  with  $\lambda$  is a relatively new observation. As discussed in Section 3.3.1, we have assumed a value of  $\alpha_{\text{abs}}$  (listed in Table 3.7). Changing the assumed  $\alpha_{\text{abs}}$  such that every vertical profile uses  $\alpha_{\text{abs}} = 1$  or  $\alpha_{\text{abs}} = 2$  changes the values of  $\delta_{\text{rms}}$  and  $\delta_{\text{bias}}$  (listed in Fig. 3.7), and the best overall fit is produced if we simply use  $\alpha_{\text{abs}} = 1$  for every vertical profile (Fig. 3.7a). However, the statistical significance of the difference in using one value of  $\alpha_{\text{abs}}$  or some combination is questionable.

Regardless of the assumed value of  $\alpha_{\text{abs}}$ , the inverse relationship of  $\delta_{\text{bias}}$  with  $\lambda$  still remains a feature of the three wavelength analysis and warrants further investigation. The simplest explanation for the discrepancy between  $\tau_{\text{is,layer}}$  and  $\tau_{\text{sp,layer}}$  is that there is an undiagnosed sampling problem with the nephelometer

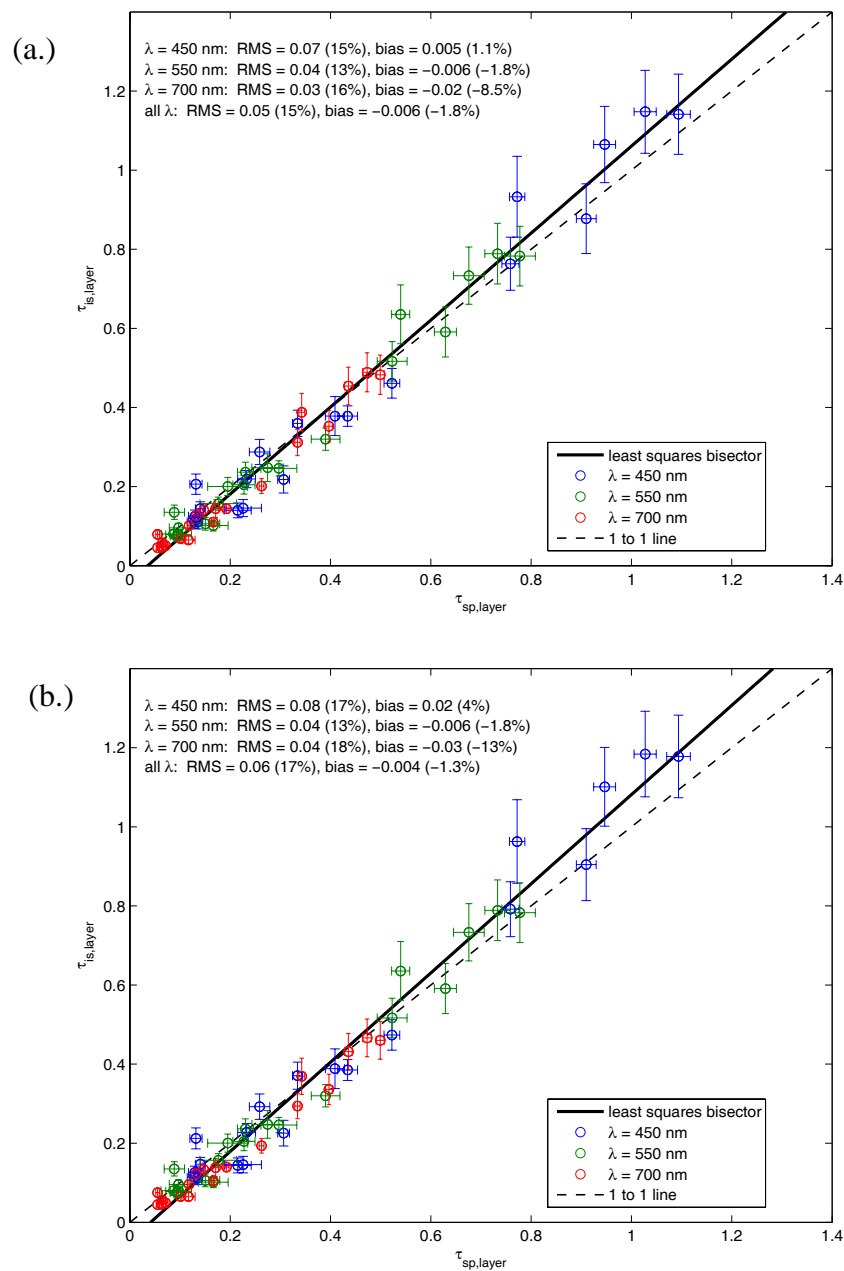


Fig. 3.7. Comparison of layer aerosol optical depth ( $\tau_{\text{layer}}$ ) measured by the Sunphotometer ( $\tau_{\text{sp,layer}}$ ) and derived from in situ measurements ( $\tau_{\text{is,layer}}$ ) using (a) an absorption angstrom exponent of 1 or (b) and absorption angstrom exponent of 2 to extrapolate the in situ absorption coefficient from a wavelength,  $\lambda$ , of 550 nm to 450 and 700 nm. The statistics on the top left are described in Table 3.6.



and PSAP. Results in *Schmid et al.* [2006] suggest that this discrepancy is certainly not unique to SAFARI-2000, but applies to a wide range of aerosol types. In a study off of the United States east coast, *Hartley et al.* [2000] suggested that the discrepancy is primarily due to the loss of volatile or semi-volatile organic compounds (SVOCs) to the instrument plumbing. Organic particles were a dominant part of the mass fraction of regional haze aerosols in SAFARI-2000 [*Kirchstetter et al.*, 2003; *Gao et al.*, 2003], and direct measurements of SVOCs by *Eatough et al.* [2003] suggest that, on average, nearly 40% of the particulate mass was composed of SVOCs, which are inherently difficult to sample with in situ methods. If there is a sampling problem, then the data presented in Table 3.6 and Figs. 3.6-3.7 suggests that larger particles (those that would affect the values of  $\tau_{700}$  more significantly) are systematically under-sampled. Quantifying the potential effect of volatile particle loss is beyond the scope of this study, so we simply point out the possibility.

Regardless of the discrepancy, values of  $\delta_{\text{rms}}$  are 13% and  $\delta_{\text{bias}}$  are -2% at  $\lambda = 550$  nm, while  $\delta_{\text{rms}} = 17\%$  and  $\delta_{\text{bias}} = -1\%$  when the three visible wavelengths are considered together. These values are similar to or better than values summarized in the multiple-campaign analysis of *Schmid et al.* [2006]. The agreement between the two methods of measuring aerosol optical depth serves as a basis for instrument validation and we proceed in the next section to analyze the detailed information offered by the in situ instruments.

### 3.4. Aerosol Vertical Profiles

In this section, we present the vertical profiles of aerosol optical properties measured by instruments described in Chapter 2. The details of the twenty vertical profiles are listed in Table 3.4. The goal of the profiles was to collect in situ measurements of the majority of the polluted boundary layers, which typically were confined to the lowest 5 km of the atmosphere by a persistent stable layer that inhibited vertical mixing at ~500 hPa [*Cosijn and Tyson, 1996; Swap and Tyson, 1999*]. The aircraft often climbed through the polluted layers into a region that was nearly free of aerosol. This transition was accompanied by, among other things, a sudden decrease in aerosol number concentrations and relative humidity. Most of the profiles successfully characterized the part of the atmosphere most affected by biomass burning aerosol.

#### 3.4.1. Methods

The aerosol properties are averaged into evenly spaced 0.15 km bins. The bin width is limited to 0.15 km by the 30 second sampling time of the PSAP and the research aircraft ascent or descent speed ~50 m/s. The bin width reduces the ability of the measurements to resolve features in the vertical profiles such as narrow clean slots [*Hobbs, 2003*]. However, the averaging also significantly reduces the random errors in the measurements by

$$\delta \bar{X} = \frac{1}{M} \sqrt{\sum_{j=1}^M \delta X_j^2} \quad (3.14)$$

where  $\overline{X}$  is the vertically averaged aerosol optical property ( $\sigma_{\text{abs}}$ , for example),  $\delta\overline{X}$  is the error in the vertically averaged aerosol optical property ( $\delta\sigma_{\text{abs}}$ , for example),  $M$  is the number of measurements made within a vertical bin, and  $\delta X_j$  is the error associated with each of the values in the vertical bin. This is important for values of  $\sigma_{\text{abs}}$  and subsequent estimates of  $\omega_o$ , although systematic errors are unaffected by the averaging.

We present the vertical profiles such that the data are plotted at the center of the bin. For example, if  $\omega_{o,550} = 0.85$  at  $z = 1.5$  km, this means that the average value from 1.35 – 1.65 km is  $\omega_{o,550} = 0.85$ . We also show the surface height (dark horizontal black line) in the figures to provide a sense for the aircraft altitude with respect to the ground level (as opposed to above mean sea level, as we report in the tables).

After applying correction procedures discussed in Chapter 2, the values of  $\sigma_{\text{sca},\lambda}$ ,  $\sigma_{\text{abs},\lambda}$ ,  $\omega_{o,\lambda}$ , and  $\beta_\lambda$  are determined by adjusting the values from low RH of the measurement to the ambient RH using Eq. 3.3-3.4. We use the empirical fit coefficients in Table 3.2 from a specific flight when available, and the mean value of the empirical fit coefficients specific to the time period in Table 3.3 when humidographs for a specific flight are not available. Thus the corrected values of  $\sigma_{\text{sca},\lambda,d}$  measured by the 3 $\lambda$ -nephelometer at 30% RH are adjusted to ambient RH by

$$\sigma_{\text{sca},\lambda} = \sigma_{\text{sca},\lambda,d} * f_{\text{sca},\lambda}(\text{RH}) \quad (3.12)$$

where we propagate the errors associated with  $\sigma_{\text{sca},\lambda,\text{d}}$  and  $f_{\text{sca},\lambda}(\text{RH})$  using the standard quadratures method [e.g. *Bevington and Robinson, 1992*] to calculate the uncertainty in  $\sigma_{\text{sca},\lambda}$  ( $\delta\sigma_{\text{sca},\lambda}$ ). We use an analogous method to calculate  $\beta_\lambda$  and  $\delta\beta_\lambda$  at ambient RH. All measurements by the  $3\lambda$ -nephelometer are systematically uncertain by 7% [*Anderson et al., 1996; Anderson et al., 2000*].

As discussed in Section 3.3, there are no measurements of  $f_{\text{abs},\lambda}(\text{RH})$ , so we assume that  $f_{\text{abs},\lambda}(\text{RH}) = 1$  for all cases. Considering the very low ambient RH throughout the vertical profiles listed in Table 3.7, the uncertainty associated with the assumption that  $\sigma_{\text{abs},\lambda} \approx \sigma_{\text{abs},\lambda,\text{d}}$  is minimal. We propagate all errors discussed in *Bond et al. [1999]* to the (effectively) ambient RH values of  $\sigma_{\text{abs},\lambda}$ , as discussed in Section 2.1.2. Uncertainty in the PSAP measurements is systematically uncertain by  $\sim 20\%$ , but since we were not able to correct the PSAP for potential flow rate differences, the systematic uncertainty associated with the instrument is set at 25%. This systematic uncertainty applies strictly to  $\sigma_{\text{abs},550}$ . We propagate an additional 10% and 12% uncertainty for measurements of  $\sigma_{\text{abs},450}$  and  $\sigma_{\text{abs},700}$  due to the uncertainty associated with the assumption of a value of  $\alpha_{\text{abs}}$  from *Bergstrom et al. [2003]*. The values of 10% and 12% arise by assuming that half of the full range of the difference between extrapolating  $\sigma_{\text{abs},550}$  to  $\sigma_{\text{abs},450}$  and  $\sigma_{\text{abs},700}$  using  $\alpha_{\text{abs}} = 1$  and  $\alpha_{\text{abs}} = 2$  is the uncertainty.

The values of  $\omega_{o,\lambda}$  reported at ambient RH use values of  $\sigma_{sca,\lambda}$  and  $\sigma_{abs,\lambda}$ , and therefore uncertainty in  $\omega_{o,\lambda}$ , or  $\delta\omega_{o,\lambda}$ , is calculated by propagating  $\delta\sigma_{sca,\lambda}$  and  $\delta\sigma_{abs,\lambda}$  as

$$\delta\omega_{o,\lambda}^2 = \frac{\delta\sigma_{abs,\lambda}^2}{\left[\sigma_{sca,\lambda} \left(1 + \sigma_{abs,\lambda} / \sigma_{sca,\lambda}\right)^2\right]^2} + \frac{\sigma_{abs,\lambda}^2 \delta\sigma_{sca,\lambda}^2}{\left[\sigma_{sca,\lambda}^2 \left(1 + \sigma_{abs,\lambda} / \sigma_{sca,\lambda}\right)^2\right]^2} \quad (3.13)$$

Hence,  $\delta\omega_{o,\lambda}$  is strongly weighted by  $\sigma_{sca,\lambda}$ , which even for biomass burning particles, accounts for over 80% of  $\omega_{o,\lambda}$ .

### 3.4.2. Analysis

The column-averaged, extinction-weighted mean aerosol properties from the twenty vertical profiles are summarized in Table 3.7. The mean values of  $N_a$  measured by the CNCs and PCASP (Section 2.1.3) in Table 3.7 show that although  $N_a$  measured by the PCASP increased by a factor of  $\sim 2$  from the anticyclonic circulation period to the River of Smoke period, the particles with  $D_p < 0.1 \mu\text{m}$  exhibited no clear trend. The coarse mode to fine mode volume ratio in Table 3.7 is calculated from the PCASP measurements and described in Section 2.1.3. Roughly, this ratio is calculated for fine mode particles with  $D_p = 0.1\text{-}1 \mu\text{m}$  and for coarse mode particles with  $D_p = 1\text{-}3 \mu\text{m}$ . The slight decrease in the coarse to fine mode volume ratio suggests that changes in the aerosol size distribution from the anticyclonic circulation period to the River of Smoke are primarily influenced by an enhancement in the number concentration of particles with  $D_p \sim$

Table 3.7. A summary of the properties of the particles measured in the twenty vertical profiles collected during SAFARI-2000. The extinction weighted mean values of the relative humidity (RH), aerosol number concentration ( $N_a$ ), and extinction Angstrom exponent derived from in situ measurements ( $\alpha_{\text{ext},450-700,\text{is}}$ ) and Sunphotometer measurements ( $\alpha_{\text{ext},450-700,\text{sp}}$ ). Also listed are the assumed absorption Angstrom exponents ( $\alpha_{\text{abs}}$ ). The different  $N_a$  values are from the CNCs and from the PCASP (Section 2.1.3). The coarse/fine mode particle volume ratio is also determined from the PCASP data.

ID	Date (2000)	RH (%)	$N_a$ (cm <sup>-3</sup> ) 0.007 < $D_p$ < 1 $\mu$ m	$N_a$ (cm <sup>-3</sup> ) 0.003 < $D_p$ < 1 $\mu$ m	$N_a$ (cm <sup>-3</sup> ) 0.1 < $D_p$ < 3 $\mu$ m	Coarse/Fine (%)	$\alpha_{\text{ext},450-700,\text{is}}$	$\alpha_{\text{ext},450-700,\text{sp}}$	$\alpha_{\text{abs}}$
1	14-Aug	31 $\pm$ 3	-	-	817 $\pm$ 520	2.7 $\pm$ 1.2	1.83 $\pm$ 0.06	1.73 $\pm$ 0.10	1
2	14-Aug	28 $\pm$ 4	-	-	323 $\pm$ 185	4.9 $\pm$ 1.9	1.83 $\pm$ 0.08	1.63 $\pm$ 0.10	1
3	17-Aug	31 $\pm$ 7	-	698 $\pm$ 160	752 $\pm$ 242	3.0 $\pm$ 0.2	1.96 $\pm$ 0.12	1.68 $\pm$ 0.10	1
4	20-Aug	33 $\pm$ 11	-	1255 $\pm$ 629	438 $\pm$ 232	1.9 $\pm$ 0.3	2.28 $\pm$ 0.08	1.93 $\pm$ 0.07	1
5	22-Aug	29 $\pm$ 5	-	2904 $\pm$ 415	614 $\pm$ 183	2.6 $\pm$ 1.9	2.19 $\pm$ 0.04	1.85 $\pm$ 0.05	1
6	24-Aug	37 $\pm$ 8	-	1759 $\pm$ 254	-	-	1.95 $\pm$ 0.12	1.44 $\pm$ 0.20	1
7	29-Aug	32 $\pm$ 4	5153 $\pm$ 1884	6175 $\pm$ 2334	443 $\pm$ 54	2.9 $\pm$ 0.8	2.08 $\pm$ 0.03	1.76 $\pm$ 0.07	1
8	31-Aug	31 $\pm$ 8	5805 $\pm$ 808	7170 $\pm$ 1015	649 $\pm$ 343	1.4 $\pm$ 0.9	2.13 $\pm$ 0.03	1.87 $\pm$ 0.02	1
9	1-Sep	21 $\pm$ 4	3886 $\pm$ 54	4708 $\pm$ 72	1147 $\pm$ 296	1.6 $\pm$ 0.5	2.17 $\pm$ 0.01	2.01 $\pm$ 0.03	1
10	2-Sep	13 $\pm$ 1	3485 $\pm$ 284	4149 $\pm$ 349	906 $\pm$ 738	1.5 $\pm$ 0.7	2.34 $\pm$ 0.02	1.95 $\pm$ 0.05	2
11	3-Sep	17 $\pm$ 2	4099 $\pm$ 562	4969 $\pm$ 736	1586 $\pm$ 221	0.9 $\pm$ 0.1	2.24 $\pm$ 0.01	1.85 $\pm$ 0.08	2
12	3-Sep	13 $\pm$ 1	3834 $\pm$ 480	4337 $\pm$ 564	1043 $\pm$ 534	1.7 $\pm$ 1.3	2.24 $\pm$ 0.01	1.90 $\pm$ 0.11	2
13	6-Sep	25 $\pm$ 2	4959 $\pm$ 559	5688 $\pm$ 658	1610 $\pm$ 486	1.4 $\pm$ 0.5	2.17 $\pm$ 0.02	1.85 $\pm$ 0.03	2
14	6-Sep	27 $\pm$ 2	4420 $\pm$ 688	4930 $\pm$ 819	1337 $\pm$ 643	1.3 $\pm$ 0.4	2.13 $\pm$ 0.02	1.77 $\pm$ 0.03	2
15	6-Sep	28 $\pm$ 2	4359 $\pm$ 643	5181 $\pm$ 817	929 $\pm$ 719	1.9 $\pm$ 1.6	2.12 $\pm$ 0.03	1.76 $\pm$ 0.03	2
16	6-Sep	28 $\pm$ 3	4271 $\pm$ 791	4716 $\pm$ 916	1326 $\pm$ 399	1.4 $\pm$ 0.2	2.11 $\pm$ 0.03	1.76 $\pm$ 0.04	2
17	7-Sep	29 $\pm$ 11	10297 $\pm$ 4115	11344 $\pm$ 4455	336 $\pm$ 199	5.1 $\pm$ 1.5	1.78 $\pm$ 0.07	1.37 $\pm$ 0.07	1
18	11-Sep	4 $\pm$ 1	701 $\pm$ 49	694 $\pm$ 62	169 $\pm$ 70	3.7 $\pm$ 2.0	1.75 $\pm$ 0.04	1.53 $\pm$ 0.02	1
19	13-Sep	9 $\pm$ 2	1656 $\pm$ 102	2211 $\pm$ 196	474 $\pm$ 172	2.5 $\pm$ 0.5	1.88 $\pm$ 0.05	1.56 $\pm$ 0.04	1
20	16-Sep	65 $\pm$ 8	1017 $\pm$ 79	1108 $\pm$ 101	224 $\pm$ 121	8.2 $\pm$ 9.4	1.86 $\pm$ 0.10	1.54 $\pm$ 0.09	1
<hr/>									
Mean values from 12-Aug to 1-Sep		30 $\pm$ 4	4948 $\pm$ 976	3524 $\pm$ 2528.2	648 $\pm$ 262.001	2.6 $\pm$ 1.1	2.05 $\pm$ 0.16	1.77 $\pm$ 0.17	
Mean values from 2-Sep to 6-Sep		22 $\pm$ 7	4204 $\pm$ 467	4853 $\pm$ 517	1248 $\pm$ 294	1.4 $\pm$ 0.3	2.19 $\pm$ 0.09	1.83 $\pm$ 0.07	
Mean values from 12-Aug to 16-Sep		27 $\pm$ 3	4139 $\pm$ 1067	4111 $\pm$ 1054	796 $\pm$ 214	2.7 $\pm$ 2.1	2.05 $\pm$ 0.04	1.74 $\pm$ 0.04	

0.1-1  $\mu\text{m}$ . The lack of significant change in the extinction Angstrom exponent is also evidence that the mean size of the particles did not change as dramatically as the number concentration.

The column-averaged and extinction-weighted mean values of the optical properties for the vertical profiles are listed in Table 3.8 and offer further evidence of the influx of particles discussed above. Similar to  $\tau_{\text{layer},\lambda}$  listed in Table 3.5, the mean values of  $\sigma_{\text{ext},\lambda}$  from both the Sunphotometer and in situ instruments increased by a factor of  $\sim 2$  during the River of Smoke, while the values of  $\omega_{o,\lambda}$  decreased by  $\sim 6$ -10%. An increase in  $\sigma_{\text{ext},\lambda}$  could be caused by an increase in the size of small particles or simply an increase in  $N_a$ . Again, since the evidence presented in Table 3.7 showed that the mean size of the particles did not change dramatically, we suggest that the primary cause of the increase in  $\sigma_{\text{ext},\lambda}$  was due to an increase in  $N_a$ , specifically for particles with  $D_p \sim 0.1$ -1  $\mu\text{m}$ . The change in  $\omega_{o,\lambda}$  was primarily due to the enhanced presence of absorbing aerosol species, as discussed in *Kirchstetter et al.* [2003] and *Magi et al.* [2003].

At this point, we focus the discussion on six vertical profiles chosen as the basis for a more detailed analysis in Chapters 4 and 5. Some vertical profiles not explicitly discussed in this study have been presented in detail in *Magi et al.* [2003] and in *Leahy* [2006]. Data from the six vertical profiles are shown in Figs. 3.8-3.13 and these correspond to information in Table 3.4 for ID numbers of 5, 6, 8, 11, 14, and 16. The three profiles in August were selected because they

Table 3.8. A summary of the extinction-weighted mean values of the wavelength ( $\lambda$ ) dependent extinction coefficient derived from in situ measurements ( $\sigma_{\text{ext, is}}$ ) and the Sunphotometer ( $\sigma_{\text{ext, sp}}$ ) as well as the single scattering albedo derived from in situ measurements ( $\omega_{\text{0, is}}$ ). The mean value and the standard deviation of the optical properties for different time intervals are listed in the last rows for comparison.

ID	Date (2000)	$\lambda = 450 \text{ nm}$			$\lambda = 550 \text{ nm}$			$\lambda = 700 \text{ nm}$		
		$\sigma_{\text{ext, is}}$	$\sigma_{\text{ext, sp}}$	$\omega_{\text{0, is}}$	$\sigma_{\text{ext, is}}$	$\sigma_{\text{ext, sp}}$	$\omega_{\text{0, is}}$	$\sigma_{\text{ext, is}}$	$\sigma_{\text{ext, sp}}$	$\omega_{\text{0, is}}$
1	14-Aug	79.6 $\pm$ 11.8	140.8 $\pm$ 39.9	0.869 $\pm$ 0.052	57.5 $\pm$ 7.5	106.0 $\pm$ 28.1	0.859 $\pm$ 0.026	37.0 $\pm$ 4.8	70.9 $\pm$ 17.4	0.827 $\pm$ 0.026
2	14-Aug	87.6 $\pm$ 19.7	271.6 $\pm$ 117.1	0.989 $\pm$ 0.024	60.2 $\pm$ 13.2	191.2 $\pm$ 80.4	0.987 $\pm$ 0.023	38.3 $\pm$ 8.0	128.1 $\pm$ 51.9	0.985 $\pm$ 0.028
3	17-Aug	78.2 $\pm$ 18.5	99.1 $\pm$ 16.9	0.917 $\pm$ 0.036	51.9 $\pm$ 11.9	68.7 $\pm$ 11.9	0.900 $\pm$ 0.042	31.2 $\pm$ 6.8	46.3 $\pm$ 8.2	0.874 $\pm$ 0.048
4	20-Aug	64.8 $\pm$ 10.8	76.7 $\pm$ 17.4	0.957 $\pm$ 0.023	41.0 $\pm$ 6.5	51.1 $\pm$ 11.1	0.945 $\pm$ 0.029	23.3 $\pm$ 3.5	31.9 $\pm$ 6.6	0.924 $\pm$ 0.038
5	22-Aug	115.0 $\pm$ 12.3	132.4 $\pm$ 12.0	0.919 $\pm$ 0.012	74.0 $\pm$ 7.6	90.1 $\pm$ 8.1	0.898 $\pm$ 0.014	43.0 $\pm$ 4.3	57.8 $\pm$ 5.0	0.863 $\pm$ 0.017
6	24-Aug	99.0 $\pm$ 16.1	127.9 $\pm$ 19.5	0.848 $\pm$ 0.059	65.8 $\pm$ 9.1	79.8 $\pm$ 17.1	0.865 $\pm$ 0.029	38.7 $\pm$ 6.5	63.4 $\pm$ 13.0	0.805 $\pm$ 0.032
7	29-Aug	64.9 $\pm$ 3.8	70.5 $\pm$ 6.4	0.918 $\pm$ 0.005	43.0 $\pm$ 2.4	48.4 $\pm$ 4.4	0.899 $\pm$ 0.006	25.9 $\pm$ 1.4	32.4 $\pm$ 2.9	0.868 $\pm$ 0.007
8	31-Aug	126.5 $\pm$ 18.6	118.7 $\pm$ 13.1	0.864 $\pm$ 0.015	83.3 $\pm$ 12.3	82.0 $\pm$ 9.0	0.830 $\pm$ 0.018	49.4 $\pm$ 7.3	51.9 $\pm$ 5.6	0.776 $\pm$ 0.022
9	1-Sep	114.7 $\pm$ 2.6	88.6 $\pm$ 10.2	0.868 $\pm$ 0.003	75.2 $\pm$ 1.8	58.8 $\pm$ 7.1	0.835 $\pm$ 0.003	43.9 $\pm$ 1.0	36.4 $\pm$ 4.5	0.778 $\pm$ 0.005
10	2-Sep	137.6 $\pm$ 14.6	149.0 $\pm$ 20.0	0.856 $\pm$ 0.016	87.8 $\pm$ 9.4	101.6 $\pm$ 15.0	0.849 $\pm$ 0.016	49.1 $\pm$ 5.3	63.3 $\pm$ 9.4	0.832 $\pm$ 0.017
11	3-Sep	284.9 $\pm$ 42.0	247.1 $\pm$ 71.3	0.835 $\pm$ 0.009	186.8 $\pm$ 27.9	172.5 $\pm$ 49.5	0.831 $\pm$ 0.010	106.1 $\pm$ 15.8	108.4 $\pm$ 31.0	0.817 $\pm$ 0.010
12	3-Sep	270.5 $\pm$ 44.2	286.5 $\pm$ 38.7	0.804 $\pm$ 0.006	177.5 $\pm$ 29.3	199.8 $\pm$ 27.0	0.799 $\pm$ 0.006	101.2 $\pm$ 16.7	122.0 $\pm$ 16.5	0.782 $\pm$ 0.007
13	6-Sep	361.0 $\pm$ 20.1	312.3 $\pm$ 20.6	0.828 $\pm$ 0.008	238.2 $\pm$ 13.0	217.6 $\pm$ 16.2	0.826 $\pm$ 0.008	138.2 $\pm$ 7.1	138.0 $\pm$ 10.6	0.815 $\pm$ 0.009
14	6-Sep	333.4 $\pm$ 19.5	337.5 $\pm$ 26.6	0.830 $\pm$ 0.007	221.3 $\pm$ 12.4	240.1 $\pm$ 19.0	0.829 $\pm$ 0.007	130.0 $\pm$ 7.1	153.9 $\pm$ 12.3	0.820 $\pm$ 0.008
15	6-Sep	338.3 $\pm$ 13.7	340.8 $\pm$ 19.3	0.820 $\pm$ 0.007	225.3 $\pm$ 8.9	243.6 $\pm$ 14.3	0.819 $\pm$ 0.007	132.7 $\pm$ 5.1	156.7 $\pm$ 9.3	0.810 $\pm$ 0.008
16	6-Sep	324.4 $\pm$ 21.5	315.0 $\pm$ 18.4	0.831 $\pm$ 0.008	215.7 $\pm$ 13.7	224.5 $\pm$ 14.0	0.831 $\pm$ 0.009	127.2 $\pm$ 7.7	144.5 $\pm$ 9.5	0.823 $\pm$ 0.010
17	7-Sep	83.6 $\pm$ 26.1	99.4 $\pm$ 26.1	0.906 $\pm$ 0.038	58.8 $\pm$ 18.4	75.8 $\pm$ 20.8	0.890 $\pm$ 0.045	38.4 $\pm$ 12.3	55.8 $\pm$ 15.6	0.867 $\pm$ 0.050
18	11-Sep	77.3 $\pm$ 8.0	90.8 $\pm$ 13.7	0.826 $\pm$ 0.041	55.1 $\pm$ 5.7	68.8 $\pm$ 10.5	0.802 $\pm$ 0.045	35.2 $\pm$ 3.5	45.5 $\pm$ 7.1	0.759 $\pm$ 0.049
19	13-Sep	125.8 $\pm$ 9.7	147.0 $\pm$ 8.4	0.879 $\pm$ 0.016	86.6 $\pm$ 6.7	109.5 $\pm$ 6.4	0.858 $\pm$ 0.018	53.9 $\pm$ 4.2	72.6 $\pm$ 4.3	0.822 $\pm$ 0.021
20	16-Sep	113.9 $\pm$ 21.8	95.8 $\pm$ 13.0	0.923 $\pm$ 0.023	77.1 $\pm$ 14.5	70.7 $\pm$ 9.6	0.909 $\pm$ 0.025	46.8 $\pm$ 8.6	46.1 $\pm$ 6.0	0.887 $\pm$ 0.028
Mean values										
from 12-Aug to 1-Sep		92.3 $\pm$ 22.7	125.2 $\pm$ 60.4	0.906 $\pm$ 0.047	61.3 $\pm$ 14.6	86.2 $\pm$ 43.6	0.891 $\pm$ 0.051	36.7 $\pm$ 8.6	57.7 $\pm$ 29.8	0.856 $\pm$ 0.069
Mean values										
from 2-Sep to 6-Sep		292.9 $\pm$ 75.3	284.0 $\pm$ 67.6	0.829 $\pm$ 0.016	193.2 $\pm$ 51.2	200.0 $\pm$ 49.7	0.826 $\pm$ 0.015	112.1 $\pm$ 31.1	126.7 $\pm$ 32.8	0.814 $\pm$ 0.016
Mean values										
from 12-Aug to 16-Sep		164.1 $\pm$ 10.6	177.4 $\pm$ 25.8	0.874 $\pm$ 0.017	109.1 $\pm$ 7.1	125.0 $\pm$ 17.7	0.863 $\pm$ 0.013	64.5 $\pm$ 4.1	81.3 $\pm$ 11.3	0.837 $\pm$ 0.015



characterized the atmosphere of southern Africa during the anticyclonic circulation, while the three profiles in September were selected since they were obtained during the River of Smoke.

In Figs. 3.8-3.13 are vertical profiles of  $\sigma_{\text{sca},\lambda}$ ,  $\sigma_{\text{abs},\lambda}$ ,  $\omega_{0,\lambda}$ ,  $\beta_{\lambda}$ , and  $N_{\text{a}}$ , (Sections 1.2 – 1.3) as well as temperature (T) and RH. The wavelength dependent properties are shown in the figures at  $\lambda = 450, 550$ , and  $700$  nm with the line and bar colors approximately matching the wavelength ( $\lambda = 450$  nm is blue,  $\lambda = 550$  nm is green, and  $\lambda = 700$  nm is red). The width of the horizontal bars corresponds to the  $0.15$  km vertical resolution discussed previously and the data is presented such that each value represents the average value for the region  $75$  m above and below the particular value. The surface elevation is drawn as a solid black line near the bottom of the individual figures.

The vertical profiles shown in Figure 3.8 were obtained on 22 August 2000. Values of  $\sigma_{\text{sca},\lambda}$  are fairly uniform until  $\sim 3.5$  km, when  $N_{\text{a}}$  drops to nearly aerosol-free conditions. This upper boundary to the polluted layer is common in southern Africa and often the transition is very sharp. Other studies have discussed how the large-scale continental subsidence over southern Africa creates this layering effect [*Cosijn and Tyson, 1996; Swap and Tyson, 1999*].

The vertical profile in Figure 3.9 (24 August 2000) shows a polluted layer that is more vertically structured. Seemingly separated layers exist between the surface and  $\sim 1.5$  km,  $1.6$ - $3$  km, and  $3.5$ - $4$  km, with the possibility of high elevation aerosol layer about  $4$  km. The haze layers are separated by clean slots

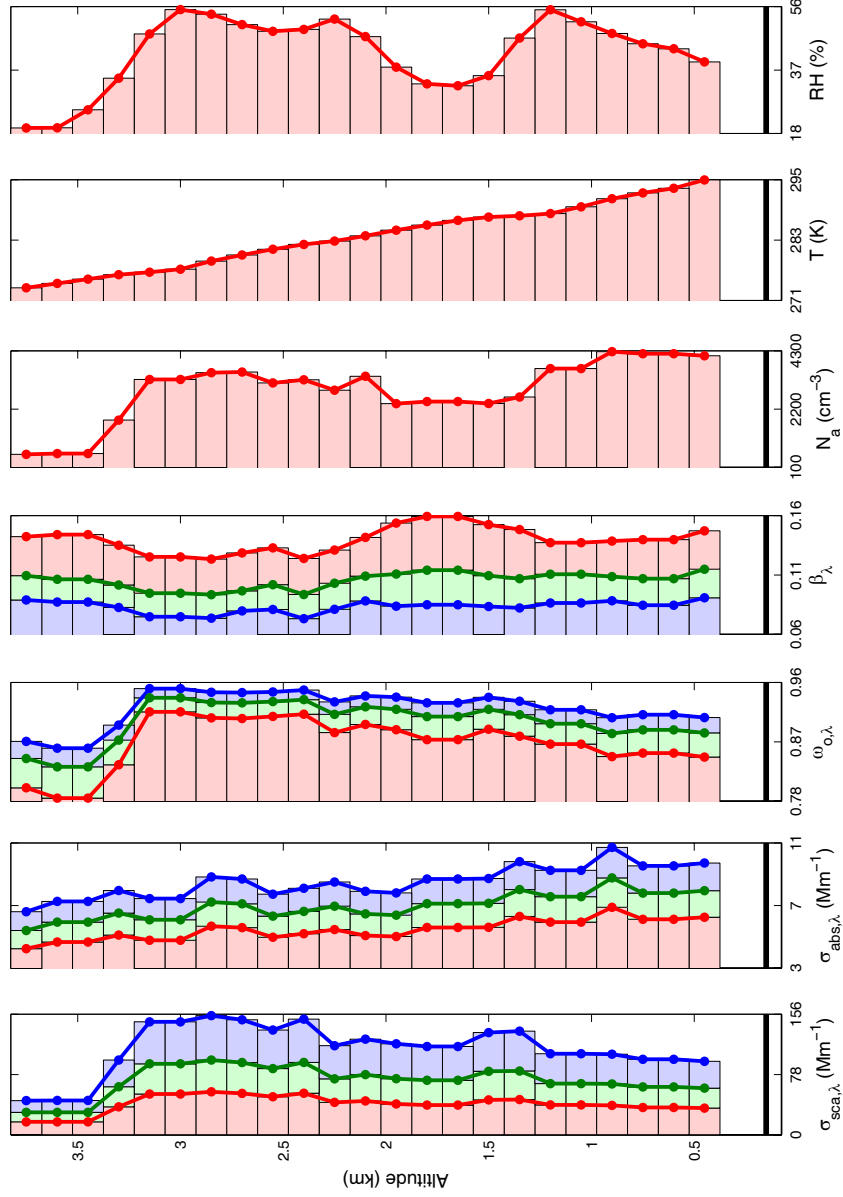


Fig. 3.8. Vertical profiles of the scattering ( $\sigma_{\text{sca},\lambda}$ ) and absorption coefficients ( $\sigma_{\text{abs},\lambda}$ ), single scattering albedo ( $\omega_{\text{a},\lambda}$ ), backscatter ratio ( $\beta_{\lambda}$ ), aerosol number concentration ( $N_{\text{a}}$ ), temperature ( $T$ ), and relative humidity (RH). The 150 m width of the horizontal bars denotes the vertical resolution of the measurements, while blue, green, and red bars and lines correspond to wavelengths,  $\lambda$ , of 450, 550 and 700 nm, respectively (where applicable). The solid black line is the surface and the altitudes are above mean sea level. These vertical profiles were obtained on 22 August 2000 at 8:16 UTC.

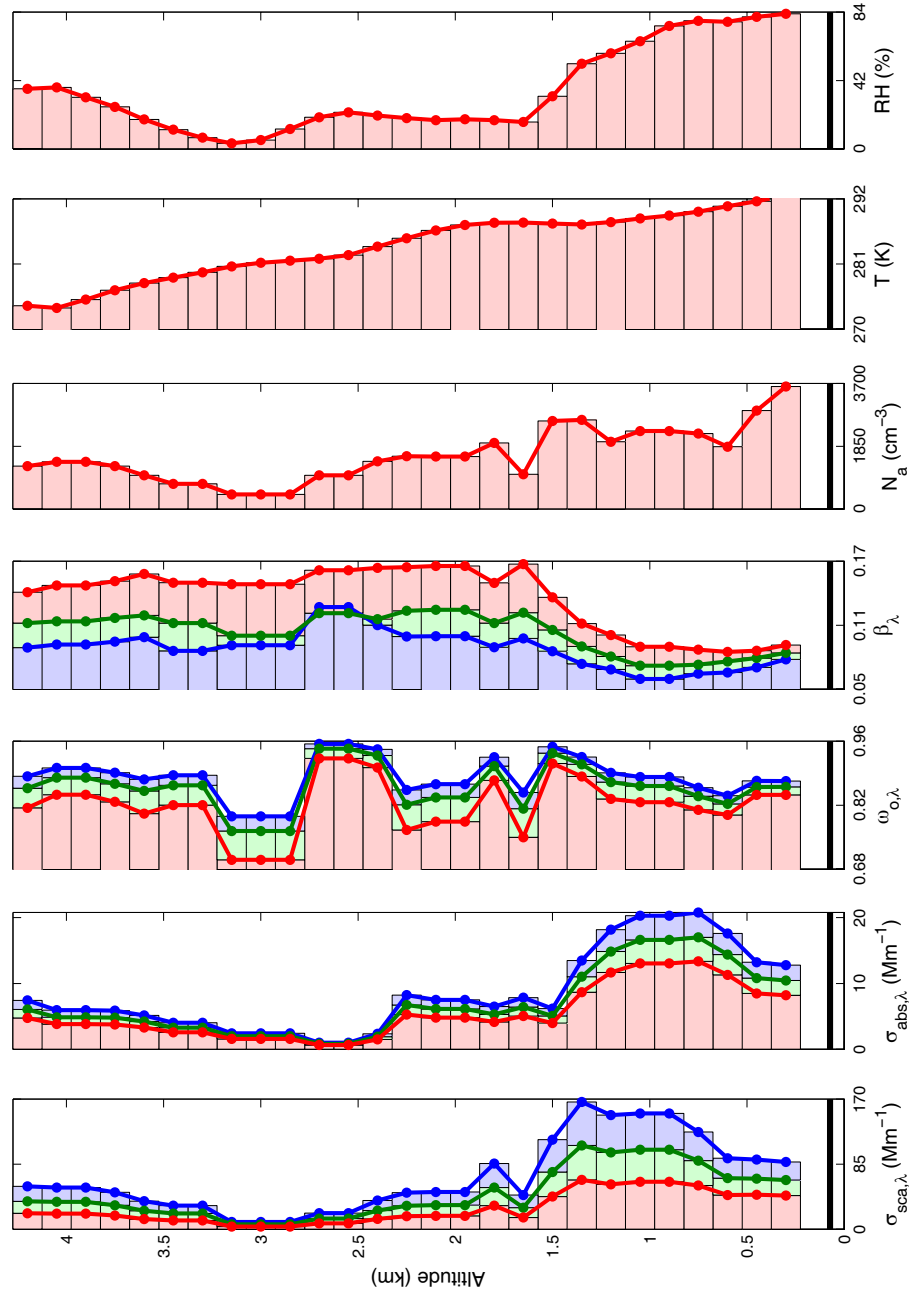


Fig. 3.9. As per Fig. 3.8, but for the vertical profiles obtained on 24 August 2000 at 8:10 UTC.

discussed in *Hobbs* [2003], evident in low values of  $\sigma_{\text{sca},\lambda}$ . Values of  $\sigma_{\text{sca},\lambda}$  are highest near the surface indicating the influence of local biomass burning on the lower part of the atmosphere, with a high level layer probably resulting from transported smoke aerosol. Values of  $\omega_{\text{o},\lambda}$  are noisy due to the low signal and rapid fluctuations in the aerosol vertical profile.

The profiles shown in Fig. 3.10 were obtained on 31 August 2000, on the coast of Mozambique, where the lower boundary layer (from ~0.6-1.25 km) was dominated by smoke from extensive localized biomass burning. We started the vertical profile above this lower layer to better characterize the haze (as opposed to the fresh smoke emissions). Even then, the atmosphere above the lowest surface layer has high  $\sigma_{\text{sca},\lambda}$  and  $N_{\text{a}}$  values, but they are similar in magnitude to the haze layers in Fig. 3.8-3.9. The averaged values in Table 3.8 also show this similarity. The sharp fall off in  $\sigma_{\text{sca},\lambda}$ ,  $N_{\text{a}}$ , and RH above ~3.6 km marks the top of the polluted layer.

The vertical profiles in Figs. 3.11-3.13 were obtained during the River of Smoke and, comparing these vertical profiles with those shown in Figs. 3.8-3.10, there is a strong indication that the aerosol was markedly different than during the anticyclonic circulation. We discussed some of the differences above and suggested that an increase in  $N_{\text{a}}$  and a stronger influence of absorbing particles were the primary reason for the differences. Other differences are evident by the more detailed presentation of the data in Figs. 3.11-3.13.

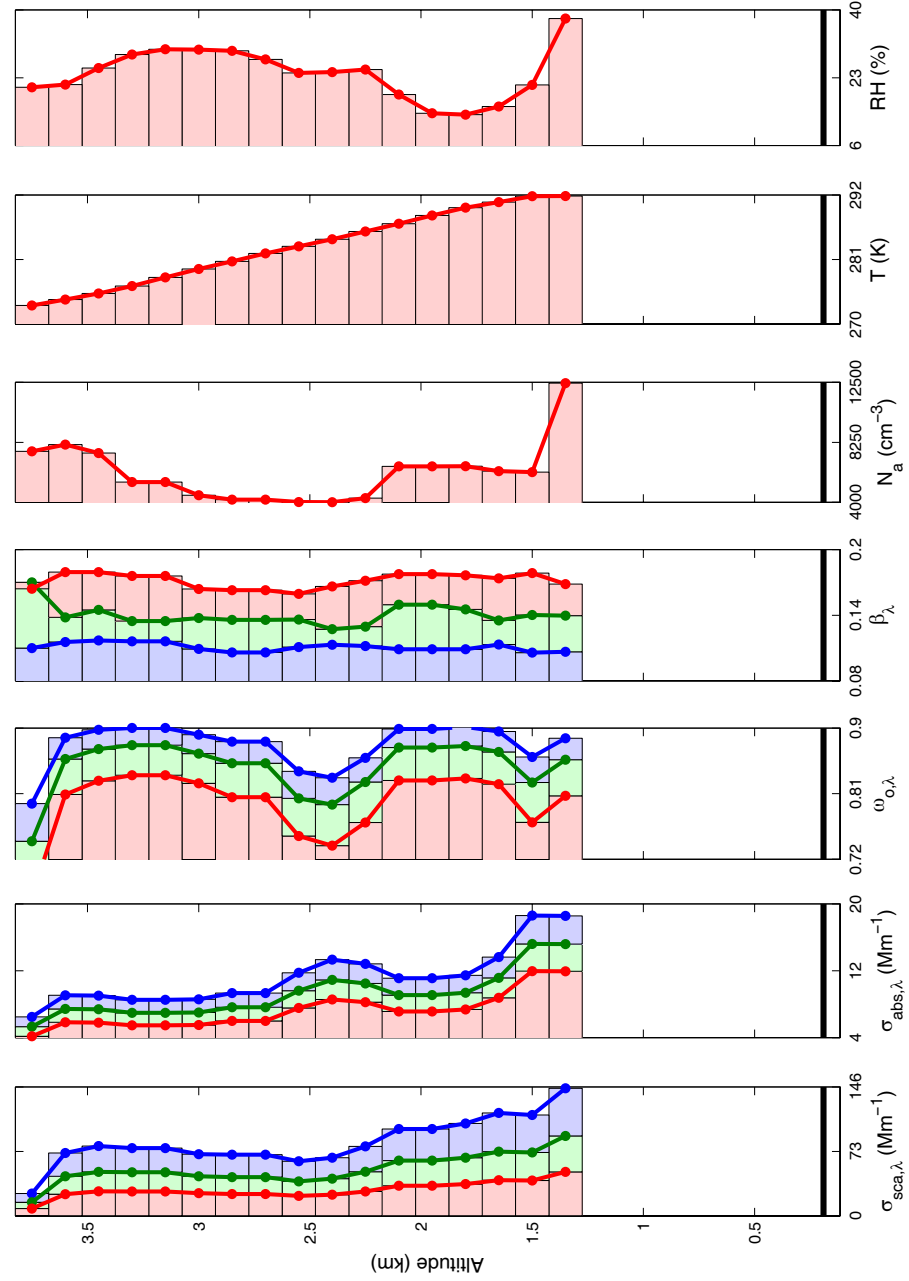


Fig. 3.10. As per Fig. 3.8, but for the vertical profiles obtained on 31 August 2000 at 12:29 UTC.

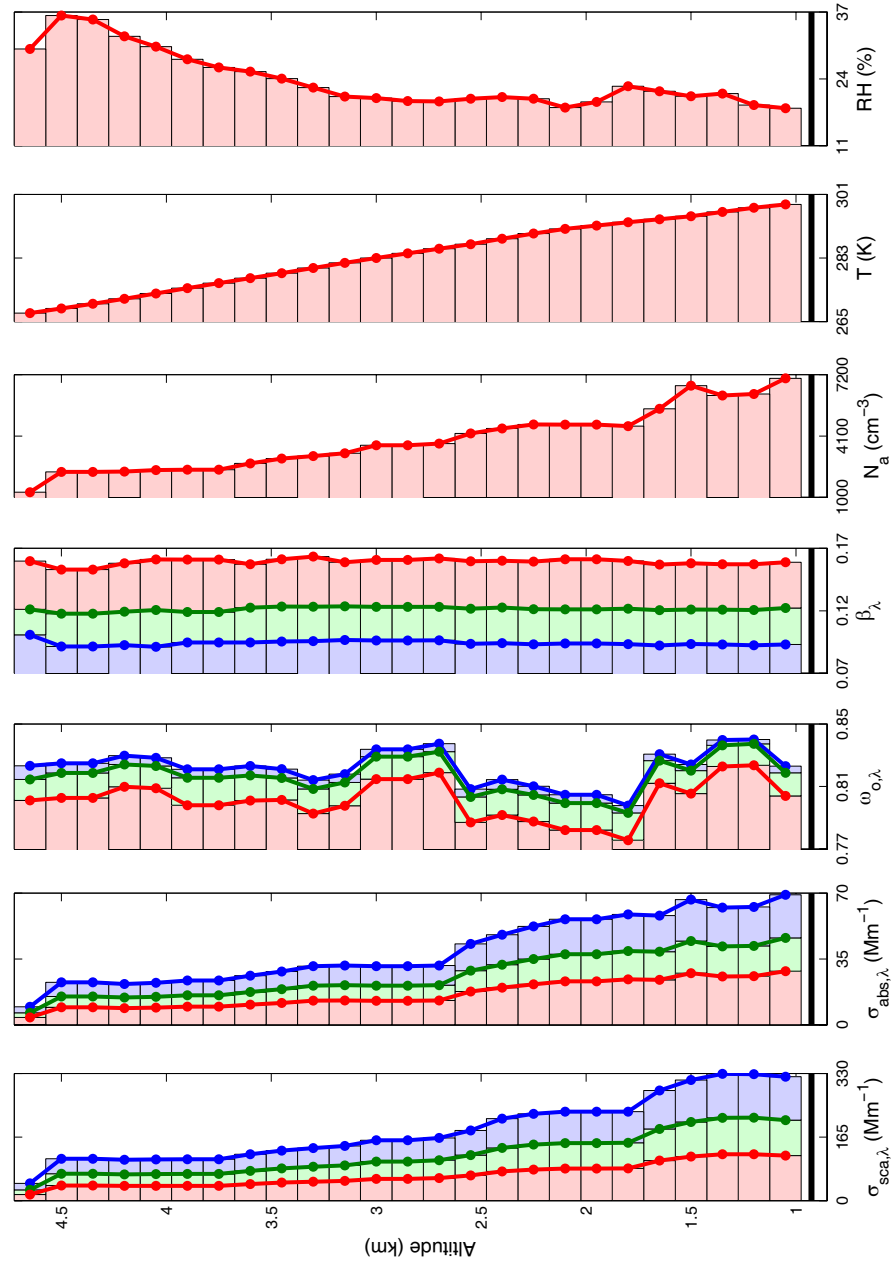


Fig. 3.11. As per Fig. 3.8, but for the vertical profiles obtained on 3 September 2000 at 8:31 UTC.

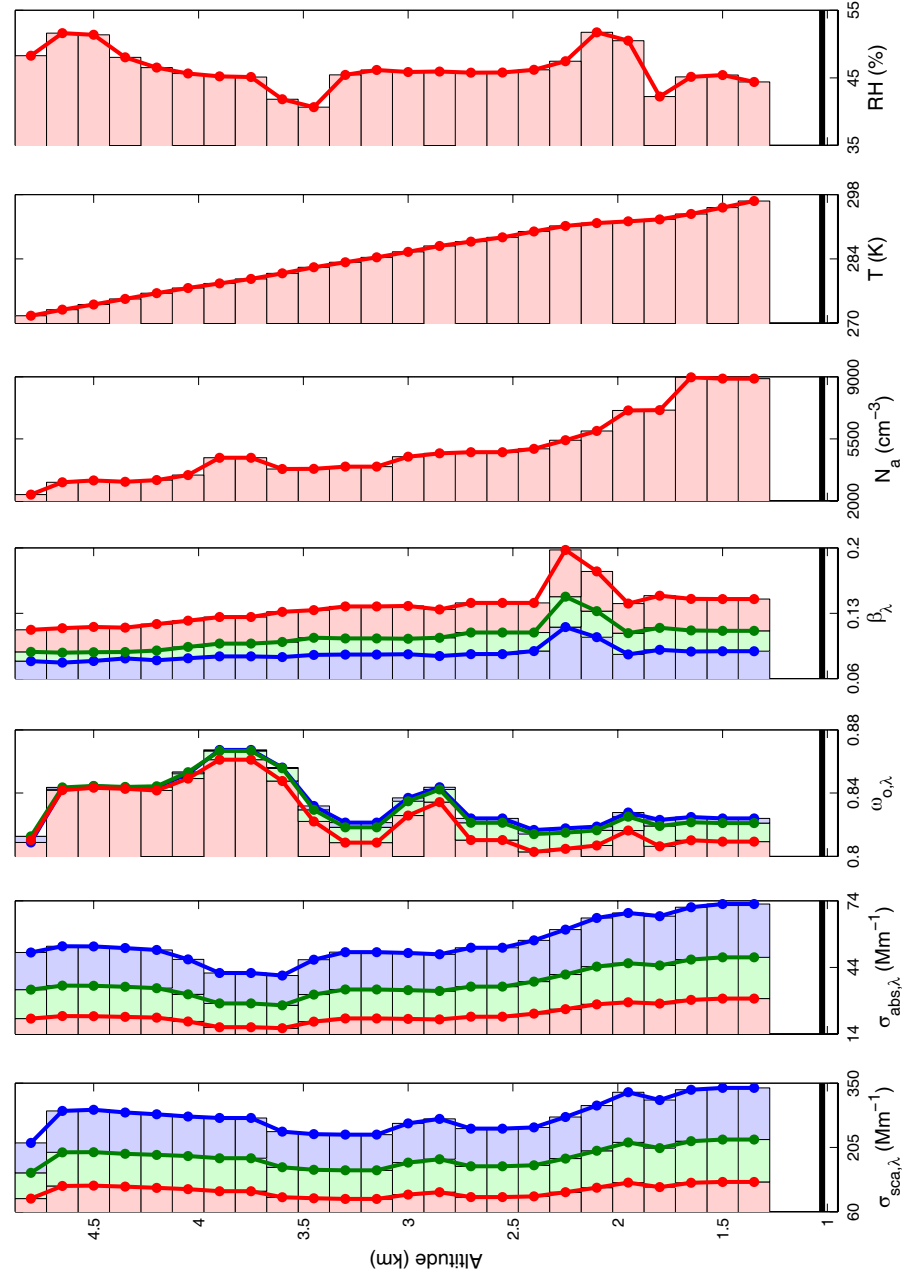


Fig. 3.12. As per Fig. 3.8, but for the vertical profiles obtained on 6 September 2000 at 9:17 UTC.

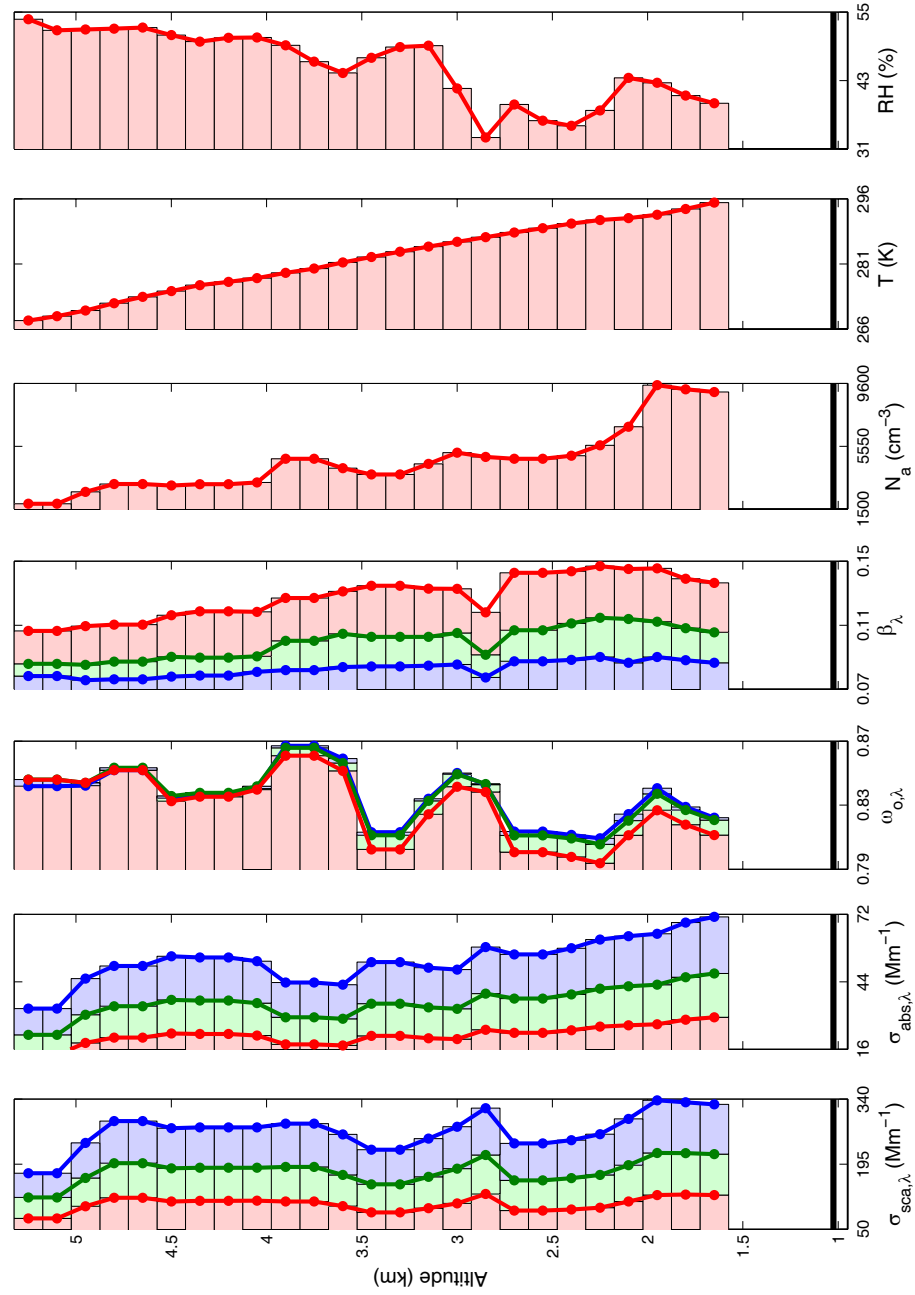


Fig. 3.13. As per Fig. 3.8, but for the vertical profiles obtained on 6 September 2000 at 9:57 UTC.



In Fig. 3.11, the values of  $\sigma_{\text{sca},\lambda}$ ,  $\sigma_{\text{abs},\lambda}$ , and  $N_a$  decrease slowly to well above 4.5 km. The polluted layer is much deeper than those shown in Figs. 3.8-3.10. This is true for the vertical profiles shown in Figs. 3.12-3.13 as well. There is some evidence of structuring, but the aerosol appears to be more uniformly distributed throughout the lowest 5 km of the atmosphere. In fact, values of  $\sigma_{\text{sca},\lambda}$  and  $\sigma_{\text{abs},\lambda}$  even at ~4-5 km in the atmosphere of the vertical profiles in Figs. 3.11-3.13 are greater than any of the values of  $\sigma_{\text{sca},\lambda}$  and  $\sigma_{\text{abs},\lambda}$  at any point in the profiles shown in Figs. 3.8-3.10. The vertical mixing was probably enhanced by the increase in absorption of solar radiation. This may have served to destabilize the atmosphere to some degree and break through the typical stable layers [Cosijn and Tyson, 1996].

The vertical profiles during the River of Smoke may be an indication of biomass burning aerosol properties for regions of tropical Africa. Very few measurements from this region even exist [Delmas *et al.*, 1999; Ruellan *et al.*, 1999]. The rapid transport of the tropical smoke over regions with very few other sources of particles [Piketh *et al.*, 1999; Li *et al.*, 2003] implies that the River of Smoke provided a glimpse of the potential impact of tropical southern African biomass burning.

### 3.5. SAFARI-2000 Data Analysis Summary

In a comprehensive analysis of the aerosol optical properties measured from the UW research aircraft, we showed in Section 3.2 that smoke from

biomass burning ages rapidly in the atmosphere and remains in a relatively stable chemical state provided the interaction with other aerosol sources are limited. The River of Smoke provided an opportunity to study an aerosol that primarily originated from a single source. The more prevalent anticyclonic circulation in southern African wintertime meteorology [Swap and Tyson, 1999; Stein *et al.*, 2003] resulted in a biomass burning aerosol that is more hygroscopic, possibly due to the regional low level industrial sources [Piketh *et al.*, 1999; Li *et al.*, 2003].

Airborne measurements of  $\tau$  by two independent methods agreed to within ~13-17%, but the analysis revealed that the in situ instruments were biased low (-1 to -12%, depending on  $\lambda$ ) compared to the remote sensing measurements by the Sunphotometer. The bias was inversely related to  $\lambda$ , suggesting that in situ instruments did not efficiently sample larger particles. The statistics from the comparison of the two methods was as good as or better than similar comparisons described in Schmid *et al.* [2006] for other parts of the world.

We described the general column characteristics of the twenty vertical profiles in Tables 3.5, 3.7 and 3.8. Based on the trajectory analysis in Section 3.2 and the aerosol analysis in Sections 3.3-3.4, we suggest that the River of Smoke aerosol is distinctly different than the aerosol more typical of the SAFARI-2000 study region and measured when the anticyclonic circulation dominated the meteorology. We also suggest that the River of Smoke aerosol may in fact be

more representative of tropical biomass burning aerosol that has not been as rigorously characterized as the aerosol in southern Africa.

In Chapter 4, we use the data presented in Figs. 3.8-3.13 to determine other aerosol properties using a Mie scattering look-up table methodology. In Chapter 5, we use the results of Chapters 3 and 4 to explore the radiative impact of southern African aerosol from the six vertical profiles and also explore the sensitivity of the radiative calculations to uncertainty in the measurements.

## Chapter 4. Look-Up Table Methodology

This chapter describes a new methodology to retrieve aerosol optical properties from large, multi-dimensional look-up tables of pre-calculated aerosol optical properties constructed using Mie theory. Mie theory is described in textbooks such as *Van de Hulst* [1981], *Bohren and Huffman* [1983], and *Seinfeld and Pandis* [1998], and in the literature by *Dave* [1970], *Ackerman and Toon* [1981], and *Wiscombe* [1980]. The basic input and output of Mie theory calculations is also discussed in Section 1.3.

We apply this methodology to six vertical profiles from the twenty vertical profiles described in Chapter 3. Referring to Table 3.4, we examine the vertical profiles collected on 22 August from 8:16-10:06 UTC, 24 August from 8:10-8:24 UTC, 31 August from 12:29-12:44, 3 September from 8:31-8:50, 6 September from 9:17-9:29, and 6 September from 9:57-10:14. The vertical profiles of the aerosol properties are in Figure 3.8-3.13 and also summarized in and Tables 3.5, 3.7, and 3.8.

Of these six vertical profiles, the first three from 22, 24, and 31 August were obtained during the period when the region was dominated by the anticyclonic circulation common during the winter months [*Garstang et al.*, 1996]. The last three vertical profiles from 3 and 6 September were collected during the River of Smoke [*Annegarn et al.*, 2002]. The general synoptic meteorological conditions during SAFARI-2000 were described in Section 3.1.

We also limit the data used in this study to these six cases to prove that the methodology presented in this chapter is sound and that the sensitivity studies in the next chapter can be better understood. There are basic computational logistics involved as well. Other vertical profiles are the subject of future work.

In Chapter 3, we characterized the aerosol optical properties measured during SAFARI-2000. These measurements as well as similar in situ measurements from other groups [*Haywood et al.*, 2003a; *Haywood et al.*, 2003b] provide important information about the optical properties of southern African biomass burning aerosol, but the properties are limited to a small wavelength range. Since direct measurements are the most rigorous method of characterizing aerosol optical properties, the interaction of models and measurements is an important issue [*Ackerman et al.*, 2004; *Kahn et al.*, 2004]. To some degree, this interaction is being addressed [e.g. *Reddy et al.*, 2005a; *Chung et al.*, 2005], but discrepancies between models and measurements on a regional level, particularly in southern Africa, continue to be a problem [*Kinne et al.*, 2003; *Kinne et al.*, 2005].

Most of the measurements made from the UW research aircraft during SAFARI-2000 and described in Chapter 3 have not been incorporated into any model. We hope to organize and generalize the information collected by the UW during SAFARI-2000 into a database that is both available for general use within larger scale models and traceable back to in situ measurements. This chapter describes a new look-up table retrieval methodology that uses SAFARI-2000

measurements to derive a complete, self-consistent characterization of southern African biomass burning aerosol shortwave optical properties.

#### 4.1. Motivation

A Mie look-up table can be used to quickly determine both extensive ( $\sigma_{\text{ext},\lambda}$ , Eq. 1.11) and intensive ( $\omega_{o,\lambda}$ ,  $\beta_\lambda$ , and  $g_\lambda$ , described by Eqs. 1.7, 1.12, and 1.9, respectively) aerosol optical properties given an aerosol size distribution (such as the lognormal size distribution in Eq. 1.1) and  $m_\lambda$  (Eq. 1.4). This is a “forward” calculation in the sense that the dependent variables, or the aerosol optical properties, are determined from the physical and chemical properties (or the independent variables) of an aerosol. Alternatively, as shown in *Hartley* [2000], a Mie look-up table can also be used to find a size distribution and values of  $m_\lambda$  using measurements of  $\sigma_{\text{ext},\lambda}$ ,  $\omega_{o,\lambda}$ , and  $\beta_\lambda$ . This is the “inverse” problem, where we find the independent variables using the dependent variables. Usually the solution to the inverse problem is not unique.

In this analysis, similar to *Hartley et al.* [2001] and in *Redemann et al.* [2000a], we present a method to solve the inverse problem. In contrast to those studies, however, we solve the inverse problem at multiple wavelengths. The methodology is designed to search for a set of so-called *optically-equivalent* aerosol physical and chemical properties that together reproduce the available optical measurements (the dependent variables). Although this method does not require any assumption about the mixing state of the aerosol [*Ackerman and*

*Toon*, 1981; *Chylek et al.*, 1988], it should be emphasized that an optically-equivalent refractive index may correspond to no known material. This is different than studies that assume an aerosol chemical composition, usually based on limited measurements, to derive the optical properties [*Ross et al.*, 1998; *Jacobson*, 2000; *Jacobson*, 2001; *Chung and Seinfeld*, 2005].

#### 4.2. Description

To construct the look-up table, we define a six dimensional matrix that will be used as input to a well-documented, publicly-available Mie scattering code [*Dave*, 1970; *Wiscombe*, 1980; <ftp://climate1.gsfc.nasa.gov/wiscombe/>]. The input matrix ( $\mathbf{M}_{\text{input}}$ ) is defined as

$$\mathbf{M}_{\text{input}} = [\lambda, m_{r,\lambda}, m_{i,\lambda}, D_g, \sigma_g, N_a] \quad (4.1)$$

where  $\lambda$  is the wavelength of incident radiation,  $m_{r,\lambda}$  and  $m_{i,\lambda}$  are the wavelength dependent real and imaginary parts, respectively, of the complex refractive index,  $m_\lambda$  (Eq. 1.4),  $D_g$  is the geometric mean diameter (Eq. 1.2),  $\sigma_g$  is the geometric standard deviation (Eq. 1.3), and  $N_a$  is the total combined nucleation and accumulation mode aerosol number concentration (Section 1.2).

The Mie scattering code then calculates  $Q_{\text{ext},\lambda}$  and  $Q_{\text{sca},\lambda}$  for a single particle of diameter  $D_p$  and with  $m_\lambda$  [*Bohren and Huffman*, 1983]. Using Eq. 1.11, we integrate  $Q_{\text{ext},\lambda}$  and  $Q_{\text{sca},\lambda}$  over the range of  $D_p$  in a size distribution given

by  $D_g$ ,  $\sigma_g$ , and  $N_a$  in  $\mathbf{M}_{\text{input}}$  to produce a four dimensional output matrix ( $\mathbf{M}_{\text{output}}$ ) defined as

$$\mathbf{M}_{\text{output}} = [\sigma_{\text{ext},\lambda}, \omega_{o,\lambda}, \beta_\lambda, g_\lambda] \quad (4.2)$$

where  $\sigma_{\text{ext},\lambda}$ ,  $\omega_{o,\lambda}$ ,  $\beta_\lambda$ , and  $g_\lambda$  are described in Eq. 1.11, 1.7, 1.12, and 1.9. Thus, a Mie calculation describes the interaction of radiation with wavelength  $\lambda$  with the input described by  $\mathbf{M}_{\text{input}}$ .

The range of the elements of  $\mathbf{M}_{\text{input}}$  is limited and discrete to reduce both the potentially infinite size of the look-up table and the subsequent computation time associated with the retrieval, which will be described in Section 4.3. A detailed listing of the dimensions of  $\mathbf{M}_{\text{input}}$  is provided in Table 4.1. Although  $N_a$  for real aerosols varies tremendously (e.g. Figs. 3.8-3.13), we calculate values for  $\mathbf{M}_{\text{output}}$  at  $N_a = 1000 \text{ cm}^{-3}$ . The value of  $N_a$  only affects calculations of  $\sigma_{\text{ext},\lambda}$  in  $\mathbf{M}_{\text{output}}$  since this is the only extensive parameter ( $\omega_{o,\lambda}$ ,  $\beta_\lambda$ , and  $g_\lambda$  are intensive parameters). Assuming the aerosol can be represented by a unimodal lognormal size distribution, we can combine Equations 1.1 and 1.11 to calculate  $\sigma_{\text{ext},\lambda}$  from Mie theory as

$$\sigma_{\text{ext},\lambda} = N_a \int_0^\infty \frac{\pi D_p Q_{\text{ext},\lambda}(D_p)}{4\sqrt{2\pi} \ln(\sigma_g)} \exp\left[-\frac{(\ln D_p - \ln D_g)^2}{2 \ln^2 \sigma_g}\right] dD_p \quad (4.3)$$

where  $N_a$  is not dependent on  $D_p$  and can be taken outside the integrand. In effect,  $N_a$  becomes a scaling parameter for  $\sigma_{\text{ext},\lambda}$ . In other words, if for a real



Table 4.1. The dimensions of the input ( $\mathbf{M}_{\text{input}}$  in Eq. 4.1) used to build the aerosol optical properties look-up table. This includes the individual wavelengths ( $\lambda$ ), the real and imaginary parts of the refractive index ( $m_r$  and  $m_i$ , respectively), the geometric mean diameter ( $D_g$ ), geometric standard deviation ( $\sigma_g$ ), and the aerosol number concentration ( $N_a$ ), with units (if applicable) listed in the table. Bold values of  $\lambda$  indicate in situ measurement wavelengths, while the remaining values of  $\lambda$  correspond to the Sunphotometer.

Parameter	Range	Step size	Number of values
$\lambda$ (nm)	354, 380, 449, <b>450</b> , 499, 525, <b>550</b> , 606, 675, <b>700</b> , 778, 865, 1019, 1241, 1557	variable	15
$m_r$	1.4 - 1.95	0.05	12
$m_i$	0 - 0.1	0.005	26
	0.1 - 0.6	0.1	
$D_g$ ( $\mu\text{m}$ )	0.06 - 0.985	0.025	38
$\sigma_g$	1.1 - 3.1	0.05	41
$N_a$ ( $\text{cm}^{-3}$ )	1000	N/A	1

aerosol,  $N_{a,example} = 1500 \text{ cm}^{-3}$ , then we re-scale our calculation of  $\sigma_{ext,\lambda}$  at  $N_a = 1000 \text{ cm}^{-3}$  by

$$\sigma_{ext,\lambda}(N_{a,example}) = \sigma_{ext,\lambda}(N_a) \frac{N_{a,example}}{N_a} \quad (4.4)$$

This assumption implies that the entire aerosol size distribution increases or decreases uniformly, provided  $D_g$  and  $\sigma_g$  do not change. Variations in  $N_a$  can be accounted for with no loss in accuracy after we have compiled  $\mathbf{M}_{output}$ . This saves computation time and significantly reduces the size of  $\mathbf{M}_{output}$ .

The ranges of the five remaining dimensions of  $\mathbf{M}_{input}$  are larger. The wavelength dimension is set to fifteen wavelengths between  $\lambda = 354 - 1557 \text{ nm}$  that correspond to the twelve wavelengths of the Sunphotometer (Section 2.1.4) and the three wavelengths ( $\lambda = 450, 550, \text{ and } 700 \text{ nm}$ ) of the  $3\lambda$ -nephelometer (Section 2.1.1). Each wavelength dimension is treated as a separate look-up table in the sense that we specifically calculate optical properties at each of the fifteen wavelengths for the same range of sizes.

There are 12 values of  $m_r$  between 1.4-1.95, and 26 values of  $m_i$  between 0-0.6 in  $\mathbf{M}_{input}$ . The range is based on information published in *d'Almeida et al. [1991]* and covers values of  $m$  ranging from water with inclusions to a pure soot aerosol. The lower limit of  $m_r$  is set at 1.4 because the low ambient RH during SAFARI-2000 (Section 3.2) suggests that  $m$  should be greater than that of pure water ( $m_{r,water} = 1.33$ ). The upper limits of  $m_r$  and  $m_i$  are the values listed in *d'Almeida et al. [1991]* for a pure soot particle, but except in areas close to

combustion sources (urban highway, near a cookstove), an aerosol is unlikely to be composed of pure soot [Kirchstetter *et al.*, 2004; Roden *et al.*, 2005].

We use 38 evenly spaced values of  $D_g$  from 0.06 – 0.985  $\mu\text{m}$  and 41 evenly spaced values of  $\sigma_g$  from 1.1 – 3.1 in  $\mathbf{M}_{\text{input}}$ . Limiting  $D_g$  to values less than 1  $\mu\text{m}$  implies that we are assuming the aerosol optical properties can be represented by primarily submicron particles. Since  $\sigma_g$  determines the width of the size distribution, the range of  $\sigma_g$  in  $\mathbf{M}_{\text{input}}$  allows for size distributions that extend beyond 1  $\mu\text{m}$  diameter (for example, if  $D_g = 0.985 \mu\text{m}$  and  $\sigma_g = 3.1$ ). As pointed in Reid *et al.* [2004a-b], however, we expect that the (lognormal) size distributions of biomass burning particles generally have  $D_g < 0.3 \mu\text{m}$ . This is consistent with the very small average aerosol submicron volume fraction of  $(3 \pm 2)\%$  listed in Table 3.7 for the vertical profiles collected during SAFARI-2000.

Constructing the look-up table is a forward calculation since at this point we are developing the search space to solve the inverse problem. Each set of independent variables corresponds to a position in the look-up table space and this position defines the corresponding values of the dependent variables. Computationally, we reduce the access time of the look-up table by separating the  $\lambda$  dimension into fifteen  $\lambda$ -dependent look-up tables according to the values listed in Table 4.1.

The range of the dimensions of  $\mathbf{M}_{\text{output}}$  for five of the fifteen wavelengths are shown in Fig. 4.1 and these are completely determined by the range of each of the dimensions of  $\mathbf{M}_{\text{input}}$  listed in Table 4.1. For the dimensions of  $\mathbf{M}_{\text{input}}$  described in Table 4.1, each element of  $\mathbf{M}_{\text{output}}$  will have  $12*26*38*41 = 486096$  possible values for each of the fifteen wavelengths. The distribution of  $\omega_{o,\lambda}$  shown in Fig. 4.1 has a noticeable dip between about 0.45 and 0.6 that arises from the discontinuity in the resolution of the  $m_i$  dimension of  $\mathbf{M}_{\text{input}}$ . For  $m_i > 0.1$ , we change the step size from 0.005 to 0.1 to limit the size of the look-up tables.

We can also examine the distance between adjacent values, or step size, or  $\mathbf{M}_{\text{output}}$ . The median step sizes of the dimensions of  $\mathbf{M}_{\text{output}}$  are  $\sim 10^{-3} \text{ Mm}^{-1}$  for  $\sigma_{\text{ext},\lambda}$  and  $\sim 10^{-7}$  for  $\omega_{o,\lambda}$ ,  $\beta_\lambda$ , and  $g_\lambda$ , and 99% of the step sizes are less than 0.23  $\text{Mm}^{-1}$  for  $\sigma_{\text{ext},\lambda}$  (for  $N_a = 1000 \text{ cm}^{-3}$ ) and  $\sim 10^{-5}$  for  $\omega_{o,\lambda}$ ,  $\beta_\lambda$ , and  $g_\lambda$  indicating a high sensitivity to aerosol optical parameters. We explicitly examine the resolution of the look-up table with respect to measurement uncertainty in Section 4.4.2.

### 4.3. Methodology

The goal of the retrieval is to search the space defined by  $\mathbf{M}_{\text{input}}$  for corresponding values of  $\mathbf{M}_{\text{output}}$  that most closely match measured aerosol optical properties. The final output is then a completely self-consistent set of physical, chemical, and optical aerosol properties, keeping in mind that the physical and chemical properties are *optically-equivalent* and not necessarily equal to the *real* physical and chemical properties. In this section, we describe the technique used

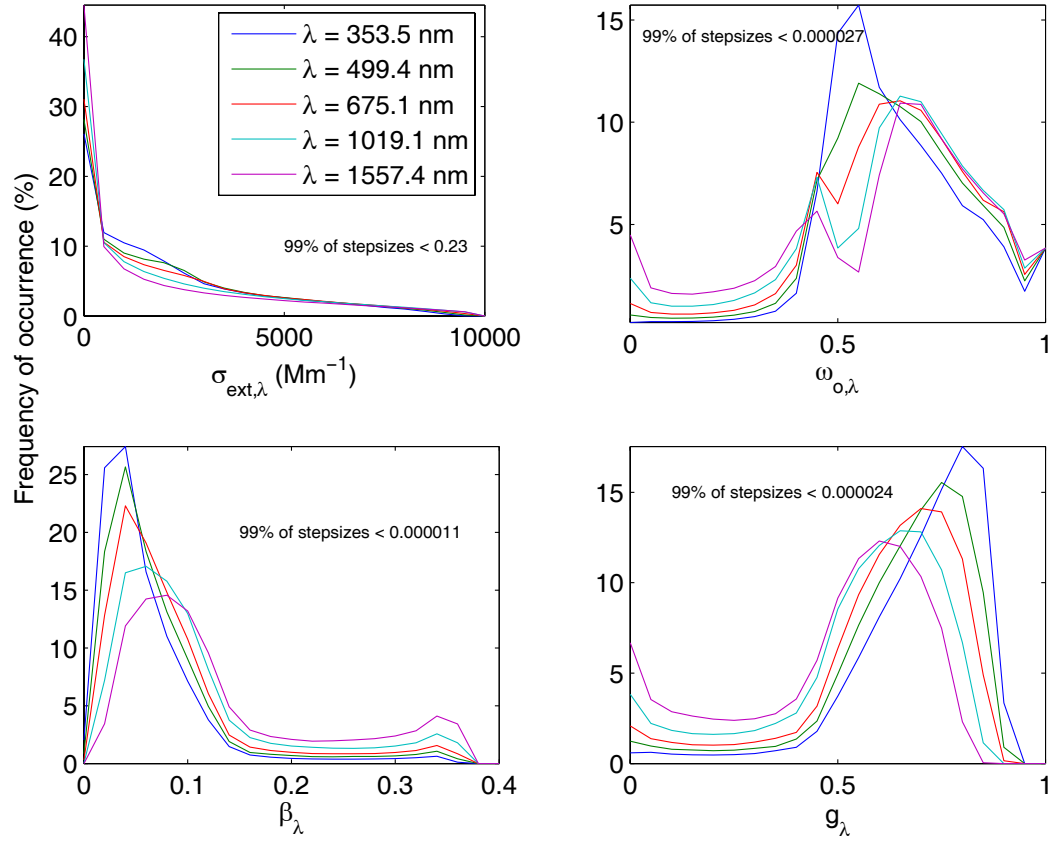


Fig. 4.1. The distribution of the wavelength-dependent extinction coefficient ( $\sigma_{\text{ext},\lambda}$ ) using  $N_a = 1000 \text{ cm}^{-3}$ , single scattering albedo ( $\omega_{o,\lambda}$ ), backscatter ratio ( $\beta_\lambda$ ), and asymmetry parameter ( $g_\lambda$ ) calculated from input listed in Table 4.1 and stored in the look-up tables, listed as a frequency of occurrence (%) in the look-up tables. Five of the fifteen wavelengths in the Mie look-up table are shown in each of the figures. The total number of possible values for each optical property at each wavelength ( $\lambda$ ) is 486096, which is determined by the dimensions in Table 4.1. The “stepsize” is the difference between adjacent values of the individual optical properties in the look-up table, suggesting a nearly continuous spectrum of possible values.

to find the best match between calculations of aerosol optical properties from Mie theory in the look-up table and measurements of aerosol optical properties described in Sections 3.3-3.4.

#### 4.3.1. Optically-Equivalent Size Distribution

The first part of the retrieval finds a unimodal lognormal submicron size distribution and values of  $m_\lambda$  that together most closely reproduce the measured values of  $\sigma_{\text{ext},\lambda}$ ,  $\omega_{o,\lambda}$ , and  $\beta_\lambda$  at  $\lambda = 450, 550$ , and  $700$  nm. We will refer to this size distribution and the values of  $m_\lambda$  as the optically-equivalent size distribution (described by  $D_{g,\text{oe}}$ ,  $\sigma_{g,\text{oe}}$ , and  $N_{a,\text{oe}}$ ) and optically-equivalent refractive index ( $m_{\text{oe},\lambda}$ ) since they are completely determined by solving the inverse problem rather than based on physical measurements.

The measurements are defined as a vector of values

$$\Psi_{\text{meas},\lambda} = [\sigma_{\text{ext,meas},\lambda}, \omega_{o,\text{meas},\lambda}, \beta_{\text{meas},\lambda}] \quad (4.5)$$

and, similarly, the uncertainty in the measurements are

$$\delta_{\text{meas},\lambda} = [\delta\sigma_{\text{ext,meas},\lambda}, \delta\omega_{o,\text{meas},\lambda}, \delta\beta_{\text{meas},\lambda}] \quad (4.6)$$

where each element of  $\delta_{\text{meas},\lambda}$  is a vector of the measurement uncertainties associated with the values in Eq. 4.5. The calculated values from the look-up table are defined as

$$\Psi_{\text{calc},\lambda} = [\sigma_{\text{ext,calc},\lambda}, \omega_{o,\text{calc},\lambda}, \beta_{\text{calc},\lambda}] \quad (4.7)$$

and are determined from the optically-equivalent physical and chemical properties, which are defined as a

$$\phi_{oe,\lambda} = [m_{r,oe,\lambda}, m_{i,oe,\lambda}, D_{g,oe}, \sigma_{g,oe}, N_{a,oe}] \quad (4.8)$$

To solve the inverse problem, or find  $\phi_{oe,\lambda}$ , we begin by search the look-up tables for values of  $\psi_{calc,\lambda}$  that meet the criterion

$$|\psi_{meas,\lambda} - \psi_{calc,\lambda}| < \delta_{meas,\lambda} \quad (4.9)$$

for each element of  $\psi_{meas,\lambda}$ , where the “|” indicates the absolute value of the difference. Since all values of  $\mathbf{M}_{output}$  are calculated at a single value of  $N_a$ , we actually re-scale  $\mathbf{M}_{output}$  to the mean value of  $N_a$  measured by the CNC (Section 2.1.3, Figs. 3.8-3.13, Table 3.7) and expand the search to include values of  $N_a \pm 5\delta N_a$ , where  $\delta N_a$  is the counting error of the CNC. Thus, we assume that  $N_{a,oe}$  lies somewhere in the range of  $N_a \pm 5\delta N_a$ .

If a look-up table location matches the criterion in Eq. 4.9, we calculate the sum of the  $\chi^2$  differences at each wavelength ( $\chi_\lambda^2$ ) and for each element of  $\psi_{meas,\lambda}$  such that

$$\chi_\lambda^2 = \sum_{j=1}^3 \frac{(\psi_{meas,\lambda,j} - \psi_{calc,\lambda,j})^2}{\delta_{meas,\lambda,j}^2} \quad (4.10)$$

where  $\psi_{meas,\lambda,1} = \sigma_{ext,meas,\lambda}$ ,  $\psi_{meas,\lambda,2} = \omega_{o,meas,\lambda}$ , and  $\psi_{meas,\lambda,3} = \beta_{meas,\lambda}$ , with analogous definitions for  $\psi_{calc,\lambda,j}$  and  $\delta_{meas,\lambda,j}$ . In this  $\chi_\lambda^2$  difference calculation, we use the uncertainties in the elements of  $\psi_{meas,\lambda}$  to both constrain the size of the

search space as well as weighting the search to measurements with smaller relative uncertainties.

The  $\chi_\lambda^2$  values are stored in wavelength dependent vectors as  $\chi_\lambda^2$ . We require the number of possible solutions for each wavelength (based on Eq. 4.9) to fall between 20-100. To implement these limits, we allow the constraints to be flexible. If  $[[\chi_\lambda^2]] > 100$  (where “[[ ]]” indicates the number of elements), the constraints ( $\delta_{\text{meas},\lambda}$ ) are reduced by 5% and we search the look-up table for solutions within these reduced constraints. If  $[[\chi_\lambda^2]] < 20$ , we increase  $\delta_{\text{meas},\lambda}$  by 10-50%. Additionally, we reduce or increase the range of possible values of  $N_a$  to decrease or increase the size of the search space, again emphasizing the point that we are looking for an *optically-equivalent* size distribution rather than one that is confined to a specific value (i.e. the exact value of  $N_a$  reported by CNC, which is inherently uncertain).

We iteratively search the look-up tables until  $20 < [[\chi_\lambda^2]] < 100$ , during which we may have to either reduce or increase the constraints multiple times. The goal in this is to build an adequate search space for a global minimum. We can define this reduced search space as a structure ( $\epsilon$ ) of  $\chi_\lambda^2$  vectors

$$\epsilon = \{\chi_{450}^2, \chi_{550}^2, \chi_{700}^2\} \quad (4.11)$$

where each element of  $\epsilon$  may be a different length such that  $20 < [[\chi_\lambda^2]] < 100$ .

Thus  $\epsilon$  is the final piece required to retrieve  $\phi_{\text{oe},\lambda}$ .



Each element of  $\chi_\lambda^2$  (i.e.  $\chi_\lambda^2$ ) qualifies as a possible solution to  $\phi_{oe,\lambda}$  by Eq. 4.9-4.10, so once we have  $\mathbf{\epsilon}$ , we search every combination of the three (wavelength-dependent) elements of the  $\mathbf{\epsilon}$ -space for the minimum difference in the size distribution parameters across the three elements (or wavelengths). This is the optically-equivalent size distribution that, together with  $m_{r,oe,\lambda}$  and  $m_{i,oe,\lambda}$ , best reproduces the available optical properties at  $\lambda = 450, 550$ , and  $700$  nm. In other words, we now have the best solution to  $\phi_{oe,\lambda}$ . Values of  $g_\lambda$  are determined from  $\phi_{oe,\lambda}$ .

The methodology follows a very basic search algorithm and can be readily visualized with a concrete example. At a specific level in a vertical profile, say we have

$$\psi_{\text{meas},550} = [100, 0.85, 0.10] \quad (4.12)$$

and

$$\delta_{\text{meas},550} = [10, 0.01, 0.02] \quad (4.13)$$

for  $N_a = 2500 \pm 50 \text{ cm}^{-3}$  measured by the CNC. The possible solutions for  $\phi_{oe,550}$  then emerge from a set of pre-calculated values in the look-up table that fall into the range

$$\psi_{\text{calc},550} = [90-110, 0.84-0.86, 0.08-0.12] \quad (4.14)$$

for  $N_a$  values ranging from  $2250-2750 \text{ cm}^{-3}$  ( $N_a \pm 5\delta N_a$ ) such that the criterion described by Eq. 4.9 is satisfied. Hence we can now calculate  $\chi_{550}^2$  per Eq. 4.10.

The same process is repeated for measurements at  $\lambda = 450$  and  $700$  nm, from which we derive  $\chi_{450}^2$  and  $\chi_{700}^2$ , and hence  $\epsilon$  (Eq. 4.11).

Suppose in this example that we now have 20, 50, and 100 matches in the look-up table for  $\chi_{450}^2$ ,  $\chi_{550}^2$ , and  $\chi_{700}^2$  (respectively) that satisfy the criterion in Eq 4.9. The final part of the search for  $\phi_{oe,\lambda}$  combines all variations of  $\epsilon$  into a search space of size  $20 \times 50 \times 100 = 100000$  possible solutions (which is why we limit the number of solutions to 20-100). Finally, we search this  $\epsilon$ -space to find the single optically-equivalent size distribution that best fits all three wavelengths. It is important to emphasize that this search does not necessarily find the minimum in  $\chi_\lambda^2$  at *each* wavelength, but instead finds the minimum across all three wavelengths simultaneously. With the location of single optically-equivalent size distribution that best fits all three wavelengths, we can look up the values of the corresponding *wavelength-dependent* optically-equivalent refractive indices (and now have  $\phi_{oe,\lambda}$ ) and the asymmetry parameter.

The degrees of freedom in this calculation warrant some discussion as well. To retrieve  $\phi_{oe,\lambda}$ , we constrain the search with the nine parameters described by  $\psi_{meas,\lambda}$  (and  $\delta_{meas,\lambda}$ ). The number of parameters being retrieved in  $\phi_{oe}$  is nine as well (accounting for the wavelength dependence of  $m_{oe,\lambda}$ ). However, as discussed in Section 3.4.1, determining  $\omega_{o,\lambda}$  involves an assumption of the wavelength dependence of  $\sigma_{abs}$  ( $\alpha_{abs}$ ) for extrapolation from  $\lambda = 550$  nm to  $\lambda = 450$  and  $700$  nm. The degrees of freedom are reduced to eight by this assumption. Then again,

$N_a$  is actually not purely a free parameter, as discussed above. It is based on measurements, but is simply allowed a wider range in the retrieval. In the retrieval then, we have eight independently determined parameters being used to retrieve eight more parameters. We examine the results of the retrieval of  $\phi_{oe,\lambda}$  for the six vertical profiles in Section 4.5.

#### 4.3.2. Retrieving the Single Scattering Albedo

The second part of the retrieval accesses the look-up tables differently because we have different inputs to use as constraints. The goal of the second part of the retrieval is to retrieve  $\omega_{o,\lambda}$  within constraints set by the  $\sigma_{sp,ext,\lambda}$  and using the information gained by the retrieval of  $\phi_{oe,\lambda}$ .

Values of  $\omega_{o,\lambda}$ , however, cannot be retrieved if there is no constraint on absorption. We approach this problem by defining boundary conditions on the search for  $\omega_{o,\lambda}$ . Fig. 4.1 showed that for the range of input values specified by  $\mathbf{M}_{input}$ ,  $\omega_{o,\lambda}$  is most likely 0.4-1.0, but limiting our search to this wide range still results in diverging solutions for the retrieval. We know from multiple SAFARI-2000 studies that the biomass burning aerosol is composed of a high percentage of carbonaceous particles [Eatough *et al.*, 2003; Formenti *et al.*, 2003; Gao *et al.*, 2003; Kirchstetter *et al.*, 2003] and that these carbonaceous particles absorb radiation [Eck *et al.*, 2003; Magi *et al.*, 2003; Kirchstetter *et al.*, 2004]. Thus we do not expect  $\omega_{o,\lambda}$  to ever approach a value of unity (purely scattering), especially

since scattering aerosols like sulfate become more absorbing with increasing wavelength [*d’Almeida et al.*, 1991]. Even if the boundary conditions of  $\omega_{o,\lambda}$  are confined to 0.4-0.9, however, we still are exploring a huge range of potential values.

To further reduce the range of possible  $\omega_{o,\lambda}$  values, we examine the literature. We emphasize initially that there are no *direct* (e.g. PSAP) measurements of  $\omega_{o,\lambda}$  beyond 550 nm from SAFARI-2000. The values of  $\omega_{o,450}$  and  $\omega_{o,700}$  are based on an assumed (and uncertain) value of  $\alpha_{\text{abs}}$  per the discussion in Section 3.4.1. There are, however, some studies that *derive*  $\omega_{o,\lambda}$  using remote sensing methods. *Bergstrom et al.* [2003] derived column-averaged  $\omega_{o,\lambda}$  values for  $\lambda = 350\text{-}1650$  nm from two SAFARI-2000 case studies using an indirect method, but interestingly found higher values of  $\omega_{o,\lambda}$  during the smoke-impacted River of Smoke than during the anticyclonic circulation period. This is contrary to other studies from SAFARI-2000 [*Eck et al.*, 2003; *Haywood et al.*, 2003b; *Magi et al.*, 2003] and to data presented in Section 3.4, Figs. 3.8-3.13, and Table 3.8. *Eck et al.* [2003] describe ground-based AERONET (Section 2.2) retrievals of column-averaged  $\omega_{o,\lambda}$  for  $\lambda = 440, 670, 870$ , and 1020 nm.

Generally, however,  $\omega_{o,\lambda}$  is derived by assuming a chemical composition and mixing state of the aerosol [*Kinne et al.*, 2005]. Using the optical properties of individual aerosol chemical components published in *d’Almeida et al.* [1991] or *Hess et al.* [1998], together with a core-shell or mixing rule assumption

[Ackerman and Toon, 1981; Chylek *et al.*, 1988], the aerosol in question can be easily modeled. For example, Ross *et al.* [1998] model submicron Brazilian biomass burning aerosols as a black carbon core surrounded by an organic liquid shell [Ackerman and Toon, 1981]. Haywood *et al.* [2003a] combine a volume-weighted mixing rule assumption [Chylek *et al.*, 1988] with published characteristics of biomass burning aerosol from Brazil [Ross *et al.*, 1998] to estimate properties of southern African biomass burning aerosols transported over Namibia.

The problems with this method are determining the aerosol chemical components, the relative fractions of the chemical components, and whether the information in *d'Almeida et al.* [1991] or *Hess et al.* [1998] should be applied. There is, for example, no generic “biomass burning” aerosol described in *d'Almeida et al.* [1991] or *Hess et al.* [1998]. To make the problem more complex, *Jacobson* [2001] and *Chung and Seinfeld* [2005] describe results of modeling studies that imply that even the mixing state assumption for an aerosol with absorbing particles (i.e. black carbon) affects the overall radiative effect on climate. The mixing state, however, usually changes with time as well [Posfai *et al.*, 2004; van Poppel *et al.*, 2005].

Fig. 4.2 summarizes the challenge in attempting to understand  $\omega_{o,\lambda}$ . The in situ values of  $\omega_{o,\lambda}$  in Fig. 4.2 are based on PSAP and nephelometer measurements at  $\lambda = 550$  nm and extrapolated to  $\lambda = 450$  and 700 nm using the suggested value of  $\alpha_{\text{abs}}$  by *Bergstrom et al.* [2003] and listed in Table 3.7. The

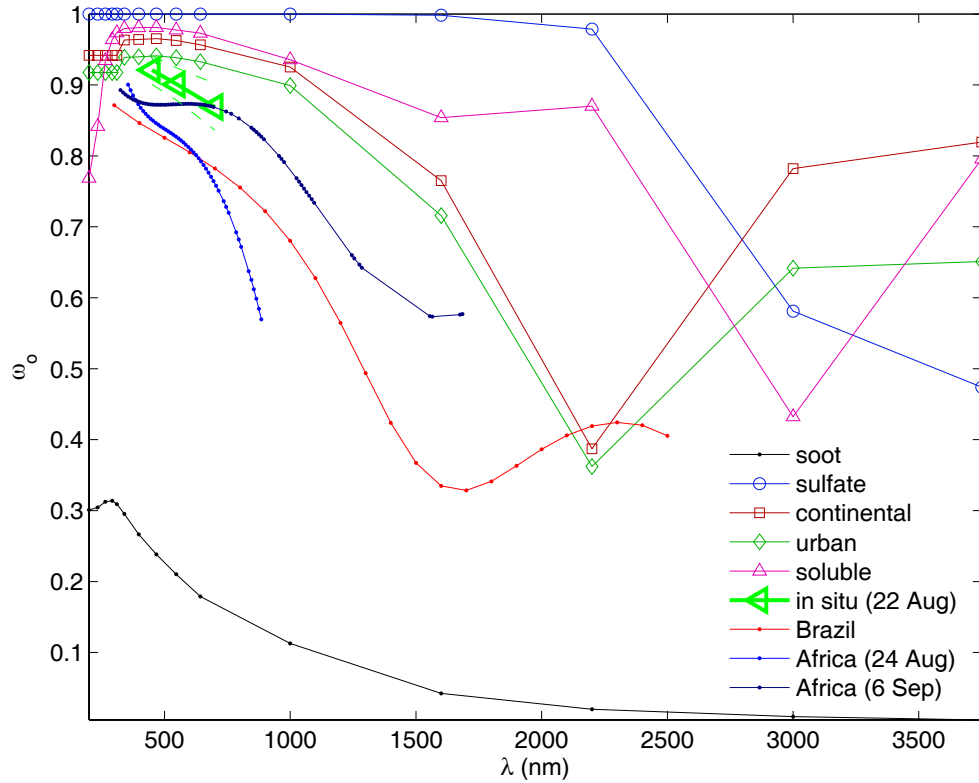


Fig. 4.2. Constraints on the wavelength ( $\lambda$ ) dependent single scattering albedo,  $\omega_{0,\lambda}$ . The values of  $\omega_{0,\lambda}$  for soot, sulfate, continental, urban, and soluble aerosols are from *d'Almeida et al.* [1991]. The values of  $\omega_{0,\lambda}$  labeled “Brazil” are from the empirical function for South American biomass burning in *Ross et al.* [1998]. The values of  $\omega_{0,\lambda}$  labeled “Africa” are derived from remote sensing measurements made from the UW research aircraft on 24 Aug and 6 Sep 2000 during SAFARI-2000 and published in *Bergstrom et al.* [2003]. The in situ values of  $\omega_{0,\lambda}$  are based on PSAP and nephelometer data at  $\lambda = 550$  nm and extrapolated to  $\lambda = 450$  and 700 nm using the the absorption angstrom exponent ( $\alpha_{\text{abs}}$ ) suggested by *Bergstrom et al.* [2003]. The in situ data is from the vertical profile on 22 Aug 2000. The absolute values of  $\omega_{0,\lambda}$  from the different data sources are shown in the main figure and the inset magnifies the region around the in situ measurements. The dashed green lines bracketing the in situ values of  $\omega_{0,\lambda}$  are the uncertainty propagated from measurements.

values of  $\omega_{o,\lambda}$  in Fig. 4.2 for soot, sulfate, continental, urban, and soluble aerosols are from the generic aerosol types in *d'Almeida et al.* [1991]. The values of  $\omega_{o,\lambda}$  labeled “Brazil” are from the empirical function for South American biomass burning in *Ross et al.* [1998]. The values of  $\omega_{o,\lambda}$  labeled “Africa” are derived from remote sensing measurements made from the UW research aircraft on 24 Aug and 6 Sep 2000 during SAFARI-2000 and published in *Bergstrom et al.* [2003].

In Fig. 4.2, we see that the range of  $\omega_{o,\lambda}$  encompasses nearly all possible values. Realistically, an atmospheric aerosol dominated by pure soot particles is rare, but even disregarding soot and limiting the examination to the derived values of  $\omega_{o,\lambda}$  from *Ross et al.* [1998] and *Bergstrom et al.* [2003], considerable discrepancy from the in situ values of  $\omega_{o,\lambda}$  (Fig. 4.2) remains and choosing a constraint is unclear.

In Fig. 4.3, the values of  $\omega_{o,\lambda}$  from Fig. 4.2 have been set to match the in situ values of  $\omega_{o,\lambda}$  at 450 and 700 nm by

$$\omega_{o,\lambda} = \kappa \omega_{o,\lambda,\text{soot}} + (1 - \kappa) \omega_{o,\lambda,x} \quad (4.15)$$

where  $\kappa$  and  $(1 - \kappa)$  are the percentages listed in the legend of Fig. 4.3 and  $\omega_{o,\lambda,x}$  is the value of  $\omega_{o,\lambda}$  for the *d'Almeida et al.* [1991] component that is linearly combined with soot. The percentages that we had to scale the Brazil [*Ross et al.*, 1998] and SAFARI-2000 data [*Bergstrom et al.*, 2003] to match the in situ values are also listed in the figure legend (109% means the curve was increased by 9%).

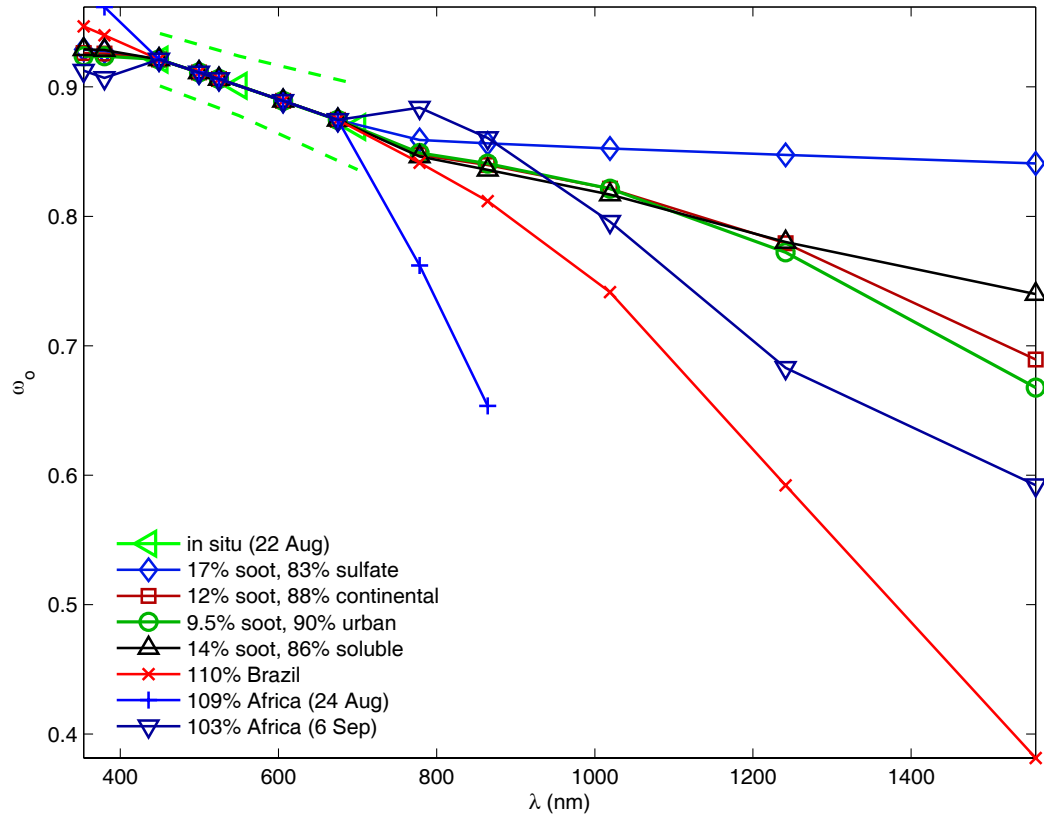


Fig. 4.3. As per Fig. 4.2, but now the values of  $\omega_{o,\lambda}$  have been adjusted to match the in situ values of  $\omega_{o,\lambda}$  at 450 and 700 nm by either linearly adding soot aerosol to the another aerosol type from *d'Almeida et al.* [1991] or by increasing or decreasing the curves in *Ross et al.* [1998] or *Bergstrom et al.* [2003]. The percentage of soot required to match the in situ values of  $\omega_{o,\lambda}$  for each aerosol type are listed in the legend, as are the values the Brazil and African data were adjusted (109% means the curve was increased by 9% to match in situ data). The dashed green lines bracketing the in situ values of  $\omega_{o,\lambda}$  are the uncertainty propagated from measurements.



The dashed green lines bracketing the in situ values of  $\omega_{o,\lambda}$  in the figure are the uncertainty determined from the measurements and the extrapolation (Section 3.4).

Returning to the main issue, we are searching for some level of constraint on absorption for the retrieval of a best fit value. Since the *d'Almeida et al.* [1991] climatology can be adjusted to match any available value of  $\omega_{o,\lambda}$  by plausibly adding more absorbing soot aerosol, we use a linear combination of soot and urban aerosol that matches the measurements of visible wavelength  $\omega_{o,\lambda}$  for each vertical profile obtained by the UW research aircraft. The soot and continental aerosol combination is an intuitive choice as well, but the values (after being scaled to in situ data) are negligibly different. The linear combination implies an externally mixed aerosol as opposed to an internally mixed aerosol [Ackerman and Toon, 1981; Chylek et al., 1988; Jacobson, 2001; Chung and Seinfeld, 2005], but the goal in this step is to find a relationship that provides a *constraint* rather than a specific value. In that light, we apply about  $\pm 10\%$  bounds to constrain the retrieval of  $\omega_{o,\lambda}$  for  $\lambda < 450$  nm and  $\lambda > 700$  nm. For comparison, the uncertainty in  $\omega_{o,\lambda}$  measured at visible wavelengths is generally less than  $\sim 3\%$ .

The soot and urban aerosol model also is qualitatively in the middle of the range of other combinations of *d'Almeida et al.* [1991] aerosol types and the relationships suggested by *Ross et al.* [1998] and *Bergstrom et al.* [2003]. It is interesting to note that no linear combination of aerosols from the *d'Almeida et al.*

[1991] climatology can reproduce the falloff in  $\omega_{o,\lambda}$  in the near infrared wavelengths suggested by *Ross et al.* [1998] and *Bergstrom et al.* [2003] for biomass burning aerosol. We explore the radiative implications of assuming a non-visible  $\omega_{o,\lambda}$  constraint in Section 5.4.2.

With a constraint on  $\omega_{o,\lambda}$ , we can now find the value of  $\omega_{o,\lambda}$  that is the best fit to the Sunphotometer measurements of  $\sigma_{\text{ext},\lambda}$  and  $\phi_{\text{oe},\lambda}$  (Eq. 4.8). In this case, the measurement vector is defined as

$$\Psi_{\text{meas},\lambda} = [\sigma_{\text{ext},\text{sp},\lambda}, \omega_{o,\lambda}, D_{\text{g,oe}}, \sigma_{\text{g,oe}}, N_{\text{a,oe}}] \quad (4.16)$$

where  $\sigma_{\text{ext},\text{sp},\lambda}$ ,  $\omega_{o,\lambda}$  are at the twelve wavelengths of the Sunphotometer (Section 2.1.4) and  $D_{\text{g,oe}}$ ,  $\sigma_{\text{g,oe}}$ ,  $N_{\text{a,oe}}$  are from Eq. 4.8. The uncertainties in the measurements determined from the analysis presented in Chapter 3 (or artificial constrained in the case of non-visible wavelength values of  $\omega_{o,\lambda}$ , as discussed above) are defined as

$$\Delta_{\text{meas},\lambda} = [\delta\sigma_{\text{ext},\text{sp},\lambda}, \delta\omega_{o,\lambda}, \delta D_{\text{g,oe}}, \delta\sigma_{\text{g,oe}}, \delta N_{\text{a,oe}}] \quad (4.17)$$

where each element of  $\Delta_{\text{meas},\lambda}$  is a vector of the measurement uncertainties associated with the values in Eq 4.16. The calculated values from the look-up table are defined as

$$\Psi_{\text{calc},\lambda} = [\sigma_{\text{ext,calc},\lambda}, \omega_{\text{o,calc},\lambda}, D_{\text{g,calc}}, \sigma_{\text{g,calc}}, N_{\text{a,calc}}] \quad (4.18)$$

We find the best fit values of  $m_{\text{oe},\lambda}$  or

$$\Phi_{\text{oe},\lambda} = [m_{\text{r,oe},\lambda}, m_{\text{i,oe},\lambda}] \quad (4.19)$$

by searching the look-up tables for all values that meet the criterion

$$|\Psi_{\text{meas},\lambda} - \Psi_{\text{calc},\lambda}| < \Delta_{\text{meas},\lambda} \quad (4.20)$$

where the “|” indicates the absolute value of the difference. We have to re-scale any parameter that is dependent on  $N_a$ , per Eq. 4.4, and we search for values using  $N_{a,\text{oe}} \pm \delta N_{a,\text{oe}}$  (rather than the less constrained range of  $N_a \pm 5\delta N_a$  from Section 4.3.1). If a look-up table location matches the criterion in Eq. 4.20, we calculate the  $X^2$  difference as

$$X_\lambda^2 = \sum_{j=1}^5 \frac{(\Psi_{\text{meas},\lambda,j} - \Psi_{\text{calc},\lambda,j})^2}{\Delta_{\text{meas},\lambda,j}^2} \quad (4.21)$$

where we sum the values of  $X_\lambda^2$  for all the elements of  $\Psi_{\text{meas},\lambda}$ ,  $\Psi_{\text{calc},\lambda}$ , and  $\Delta_{\text{meas},\lambda}$ . The possible solutions that meet the criterion described in Eq. 4.20 are compiled in a vector of  $X_\lambda^2$  values ( $\mathbf{X}_\lambda^2$ ). The best fit value for  $\Phi_{\text{oe},\lambda}$  is the minimum value of  $X_\lambda^2$ .

The second part of the retrieval is much more limited by the simple fact that we base the retrieval on measurements by the Sunphotometer and apply an artificial constraint on  $\omega_{\text{o},\lambda}$  for non-visible wavelengths. Strictly speaking, we have twelve independent measurements of  $\sigma_{\text{ext},\lambda}$ , one actual measurement of  $\omega_{\text{o},\lambda}$ , and two relationships describing the wavelength dependence (either the artificial constraint or the value of  $\alpha_{\text{abs}}$  from *Bergstrom et al.* [2003]). We also have the nine parameters retrieved in  $\phi_{\text{oe},\lambda}$  (Eq. 4.8).

The goal of the retrieval is to find the twenty-four elements of  $\Phi_{\text{oe},\lambda}$  such that we can use  $\Phi_{\text{oe},\lambda}$  together with  $\phi_{\text{oe},\lambda}$  to calculate any aerosol optical property

from Mie theory. The elements of  $\Phi_{oe,\lambda}$  at visible wavelengths are much better constrained since we have  $\phi_{oe,\lambda}$ , so we are actually finding about fourteen non-visible elements (five wavelengths of the Sunphotometer are in the visible, as shown in Table 4.1). In principle, we have twelve to twenty-four constraints on a problem with fourteen to twenty-four free parameters. Although the retrieval does indeed produce a self-consistent set of aerosol physical, chemical, and optical properties, measurements of  $\omega_{o,\lambda}$  beyond the visible wavelengths would provide a more solid physical basis for the retrieval.

## 4.4. Application

### 4.4.1. Retrieval of Aerosol Vertical Profiles

In this section, we describe the general method used to apply the retrieval to real aerosol vertical profiles. The altitude-dependent matrix of measurement vectors,  $\Psi_{meas,\lambda}$  (Eq. 4.5), is defined as

$$\Psi_{meas,\lambda,z} = [\sigma_{ext,meas,\lambda,z}, \omega_{o,meas,\lambda,z}, \beta_{meas,\lambda,z}] \quad (4.22)$$

where  $\sigma_{ext,\lambda}$ ,  $\omega_{o,\lambda}$ , and  $\beta_\lambda$  are from the measurements described in Section 3.4 and the “z” subscript indicates the altitude dependence. The discrepancy between  $\tau_{is,layer}$  and  $\tau_{sp,layer}$  (Section 3.3), which also results in a discrepancy of ~15-30% between  $\sigma_{ext,is}$  and  $\sigma_{ext,sp}$  [e.g. *Schmid et al.*, 2006], is resolved by adjusting all values of  $\sigma_{is,ext,\lambda}$  to equal  $\sigma_{sp,ext,\lambda}$ . This adjustment is not applied to  $\omega_{o,\lambda}$  and  $\beta_\lambda$  since these are intensive quantities. Therefore, we assume that the difference

between  $\sigma_{\text{sp,ext},\lambda}$  and  $\sigma_{\text{is,ext},\lambda}$  is due particles lost during sampling (Section 3.3.2) and that the particles lost do not significantly alter the intensive parameters. This assumption also implies that the particles lost have an approximately equal effect on the scattering and absorbing components of the optical properties.

Using uncertainty in the measurements determined in Section 3.4.1, we define an altitude-dependent matrix of uncertainties as

$$\delta_{\text{meas},\lambda,z} = [\delta\sigma_{\text{ext,meas},\lambda,z}, \delta\omega_{\text{o,meas},\lambda,z}, \delta\beta_{\text{meas},\lambda,z}] \quad (4.23)$$

and this combined with Eq. 4.22 is used retrieve the altitude-dependent optically-equivalent physical and chemical properties defined as

$$\phi_{\text{oe},\lambda,z} = [m_{\text{r,oe},\lambda,z}, m_{\text{i,oe},\lambda,z}, D_{\text{g,oe},z}, \sigma_{\text{g,oe},z}, N_{\text{a,oe},z}] \quad (4.24)$$

where again the “z” subscript indicates the altitude dependence.

Using  $\phi_{\text{oe},\lambda,z}$ , the data from the Sunphotometer, and the artificial urban and soot aerosol constraint on values of  $\omega_{\text{o},\lambda}$  beyond the visible wavelengths (Section 4.3.2), the measurement vector,  $\Psi_{\text{meas},\lambda}$  (Eq. 4.16), is defined at each altitude in the vertical profile as

$$\Psi_{\text{meas},\lambda,z} = [\sigma_{\text{ext,sp},\lambda,z}, \omega_{\text{o},\lambda,z}, D_{\text{g,oe},z}, \sigma_{\text{g,oe},z}, N_{\text{a,oe},z}] \quad (4.25)$$

analogous to measurement matrix in Eq. 4.22. Similarly, the altitude-dependent uncertainty matrix,  $\Delta_{\text{meas},\lambda}$  (Eq. 4.16), is

$$\Delta_{\text{meas},\lambda,z} = [\delta\sigma_{\text{ext,sp},\lambda,z}, \delta\omega_{\text{o},\lambda,z}, \delta D_{\text{g,oe},z}, \delta\sigma_{\text{g,oe},z}, \delta N_{\text{a,oe},z}] \quad (4.26)$$

Values of  $\delta\sigma_{\text{ext,sp},\lambda,z}$  are ~15-20% [Schmid *et al.* 2003; Schmid *et al.*, 2006], while  $\delta\omega_{\text{o},\lambda,z}$  are based on the measurement and extrapolation uncertainties for  $\lambda = 450$ -

700 nm and an ascribed uncertainty of  $\sim 10\%$  outside of this  $\lambda$  range (Section 4.3.2). The values of  $\delta D_{g,oe,z}$ ,  $\delta \sigma_{g,oe,z}$ , and  $\delta N_{a,oe,z}$  are based on variability that arises from the final determination of  $\phi_{oe,\lambda,z}$  (Eq. 4.22) and are generally less than 10%, but depend on the particular vertical profile.

#### 4.4.2. Resolution

To test the retrieval methodology, we use idealized test cases to confirm that the methodology works when we already know the solution. If we choose a random location in  $\mathbf{M}_{input}$  and use the corresponding values in  $\mathbf{M}_{output}$  as an artificial “measurement” vector,  $\psi_{meas,\lambda}$ , with  $\delta_{meas,\lambda} = 0.05 * \psi_{meas,\lambda}$  (referring to Eqs. 4.5-4.6), the retrieved values in  $\phi_{oe,\lambda}$  match  $\mathbf{M}_{input}$  100% of the time. This is true even as we increase  $\delta_{meas,\lambda}$  from  $0.05 * \psi_{meas,\lambda}$  to  $0.30 * \psi_{meas,\lambda}$  (i.e. 5% uncertainty to 30% uncertainty), suggesting that the retrieval successfully settles on the global minimum.

In Section 4.2, we showed that even the seemingly coarse resolution of  $\mathbf{M}_{input}$  listed in Table 4.1 produces values in  $\mathbf{M}_{output}$  that are separated by step sizes (the difference between adjacent values in  $\mathbf{M}_{output}$ ). Now we directly use the retrieval methodology presented in Sections 4.2-4.3 to assess the resolution of the look-up table with respect to typical uncertainties associated with  $\psi_{meas,\lambda}$ , or  $\delta_{meas,\lambda}$ . In other words, are the values in  $\delta_{meas,\lambda}$  greater than the step sizes in  $\mathbf{M}_{output}$ ?

To test the resolution, we use data from six vertical profiles, artificially adjust  $\psi_{\text{meas},\lambda}$  by a fraction of  $\delta_{\text{meas},\lambda}$  away from the original value, and use each  $\psi_{\text{meas},\lambda}$  as input to the retrieval. The resolution of the look-up table is adequate if  $\phi_{\text{oe},\lambda}$  retrieved for the original value of  $\psi_{\text{meas},\lambda}$  is different than  $\phi_{\text{oe},\lambda}$  retrieved for  $\psi_{\text{meas},\lambda}$  adjusted by  $1 * \delta_{\text{meas},\lambda}$ . We adjusted  $\psi_{\text{meas},\lambda}$  for fractional values of  $\delta_{\text{meas},\lambda}$  ranging from 0-1.5, where 0 implies no adjustment. Adjusting  $\psi_{\text{meas},\lambda}$  by  $1 * \delta_{\text{meas},\lambda}$  produced values in  $\phi_{\text{oe},\lambda}$  that were unique compared to the retrieved  $\psi_{\text{meas},\lambda}$  using the original  $\psi_{\text{meas},\lambda}$ . In fact, even adjusting  $\psi_{\text{meas},\lambda}$  by  $0.5 * \delta_{\text{meas},\lambda}$  nearly always produced unique values of  $\phi_{\text{oe},\lambda}$ . This implies that the pre-determined resolution specified by  $\mathbf{M}_{\text{input}}$  is more than adequate to resolve the values in  $\psi_{\text{meas},\lambda}$  within measurement uncertainties specified by  $\delta_{\text{meas},\lambda}$ .

#### 4.4.3. Structural Uncertainty

Having confirmed that the resolution of the look-up table is adequate to resolve typical measurement uncertainties, we now examine the uncertainty in the retrieved values of the aerosol optical properties that are calculated from the values in  $\phi_{\text{oe},\lambda}$ . This is an important step since uncertainty gained through the retrieval must be propagated together with any uncertainty associated with a particular optical property. We call the uncertainty that arises from the retrieval itself the *structural uncertainty*.

To calculate the structural uncertainty, we calculate a set of aerosol optical properties from a pre-determined size distribution and refractive index, but instead of using one of the discrete values specific to the look-up table used in the retrieval, we calculate the optical properties from a value *between* the discrete steps used to build the look-up table. For example, referring to Table 4.1, we could calculate the optical properties at  $\lambda = 550$  nm using  $D_g = 0.1475$   $\mu\text{m}$ ,  $\sigma_g = 1.7$ , and  $m_{550} = 1.60 - 0.02i$ , noting that the value of  $D_g$  falls *between* the values in Table 4.1 (i.e.  $D_g = 0.135$  and  $0.160$   $\mu\text{m}$ ) used to build the look-up table in this analysis. Thus, although we have an exact solution using Mie theory, this particular exact solution is *not* explicitly in the look-up table.

We retrieve  $\phi_{\text{oe},\lambda}$  and compare the calculated optical properties with the exact solution. The average percent difference between the exact solution and the calculated optical properties for each dimension of  $\mathbf{M}_{\text{input}}$  (i.e.  $D_g$ ,  $\sigma_g$ ,  $m_r$ , and  $m_i$ ) is the structural error.

The structural errors associated with each dimension of  $\mathbf{M}_{\text{input}}$  are propagated together by quadratures for each of the calculated aerosol optical properties. Using this method, we calculate  $\pm 4.1\%$  uncertainty in  $\sigma_{\text{ext},\lambda}$ ,  $\pm 1.2\%$  in  $\omega_{\text{o},\lambda}$ , and  $\pm 3.8\%$  in  $g_\lambda$ . Partitioning the structural uncertainty, we find that the smallest contribution to the structural uncertainty in all calculated optical properties arises from the values of  $D_g$  used to build the look-up table. The greatest contribution to the structural uncertainty arises from the values of  $m_r$  for



$\sigma_{\text{ext},\lambda}$  and  $g_\lambda$ , but from  $m_i$  for  $\omega_{o,\lambda}$ . This partitioning offers some insight into how to most efficiently reduce the structural uncertainty associated with the look-up table used in the retrieval. Specifically, increasing the resolution of the values of  $m_r$  and  $m_i$  used to build the look-up table will have the most immediate impact on the uncertainty associated with the retrieval.

#### 4.5. Analysis

Using the data in the vertical profiles shown Figs. 3.8-3.13 and described in Section 3.4.2, we retrieve  $\phi_{\text{oe},\lambda,z}$  per the discussion in Section 4.4.1. Using the values in  $\phi_{\text{oe},\lambda,z}$ , combined with  $\sigma_{\text{ext},\lambda,z}$  from the Sunphotometer, and the artificial urban and soot aerosol combination constraint on  $\omega_{o,\lambda,z}$ , we find a self-consistent set of aerosol physical, chemical, and optical properties for every point in the vertical profiles.

The column-averaged, extinction-weighted mean values for the optically-equivalent physical properties (i.e. the size distributions) are listed in Table 4.2. The lognormal distributions that best reproduce the measured optical properties range from  $D_g = 0.15 - 0.23 \mu\text{m}$ , with the width of the distribution,  $\sigma_g$ , ranging from 1.6 – 2.0. The values of submicron aerosol number concentration ( $N_a$ ) for the optically-equivalent size distributions range from  $1600 - 5200 \text{ cm}^{-3}$ . The optically-equivalent size distributions reported here are in general agreement with the measured distributions discussed for Brazilian biomass burning aerosol [Reid *et al.*, 1998; Ross *et al.*, 1998] and for transported smoke in southern Africa

Table 4.2. Information about the six vertical profiles used in the retrieval as well as the column-averaged, extinction-weighted mean values of the geometric mean diameter ( $D_g$ ), geometric standard deviation ( $\sigma_g$ ), and aerosol number concentration ( $N_a$ ) of the lognormal optically-equivalent size distribution. The vertical profiles can also be cross-referenced with information in Table 4.3 using the numerical identification (ID), but can also be cross-referenced with Table 3.4 using the date and time. Namely, the IDs here correspond to IDs 5, 6, 8, 11, 14, 16 in Table 3.4.

ID	Date (2000)	Flight Number	Latitude (°S)	Longitude (°E)	UTC Time (hhmm)	Altitude (km)	Surface elevation (km)	optically-equivalent size distribution parameters		
								$D_g$ ( $\mu\text{m}$ )	$\sigma_g$	$N_a$ ( $\text{cm}^{-3}$ )
1	22-Aug	1820	24.98 ± 0.04	31.61 ± 0.06	0816 - 1006	0.37 - 3.82	0.15	0.157 ± 0.015	2.009 ± 0.189	2379 ± 63
2	24-Aug	1822	25.98 ± 0.03	32.91 ± 0.02	0810 - 0824	0.21 - 4.12	0.07	0.183 ± 0.023	1.935 ± 0.191	1636 ± 213
3	31-Aug	1825	21.62 ± 0.17	34.27 ± 0.13	1229 - 1244	0.64 - 3.89	0.19	0.149 ± 0.020	1.748 ± 0.074	5164 ± 72
4	3-Sep	1830	20.59 ± 0.03	26.17 ± 0.02	0831 - 0850	1.08 - 4.58	0.93	0.232 ± 0.013	1.622 ± 0.053	3679 ± 118
5	6-Sep	1832	15.19 ± 0.05	23.16 ± 0.03	0917 - 0929	1.37 - 4.77	1.03	0.201 ± 0.007	1.793 ± 0.066	4423 ± 139
6	6-Sep	1832	15.47 ± 0.22	23.46 ± 0.16	0957 - 1014	1.64 - 5.27	1.03	0.191 ± 0.007	1.859 ± 0.059	4050 ± 99

[*Haywood et al.*, 2003a]. The submicron part of the AERONET retrieved size distributions from SAFARI-2000 are also similar to those retrieved using the methodology based on instrument measurements [*Eck et al.*, 2003]. *Magi and Hobbs* [2004] showed that the shape and peaks of measured size distributions matched AERONET retrieved size distributions reasonably well for SAFARI-2000. The values of  $N_a$  reported here are larger than those reported in *Haywood et al.*, [2003a], but we report  $N_a$  for a range of particle diameters that includes very small ( $D_p < 0.1 \mu\text{m}$ ) particles. As seen in Table 3.7, it is common that small particles typical of biomass burning [*Reid et al.*, 2004a-b] often comprise a large fraction of the total submicron aerosol number concentration.

The column-averaged, extinction-weighted mean values of the wavelength-dependent optically-equivalent refractive indices for each vertical profile are listed in Table 4.3. AERONET retrieves the complex refractive index for a limited wavelength range [*Dubovik et al.*, 2002] and *Haywood et al.* [2003a-b] find an optically-equivalent refractive index for  $\lambda = 550 \text{ nm}$  of  $1.54-0.18i$ . Examining AERONET data discussed in *Leahy* [2006], the real part of the refractive indices reported by AERONET during SAFARI-2000 are ~10-20% less than those shown in Table 4.3. The imaginary part of the refractive indices from AERONET are ~30-90% less than the optically-equivalent values that we suggest. The AERONET retrieval, however, is intended to characterize the full size distribution rather than the submicron part, whereas our retrieval is strictly for submicron size distributions (Table 4.2). Although some difference between

Table 4.3. The column-averaged and extinction-weighted mean values of the real ( $m_r$ ) and imaginary ( $m_i$ ) parts optically-equivalent refractive index ( $m_{oe}$ ) as a function of wavelength ( $\lambda$ ) for the six vertical profiles that can be cross-referenced using the numerical identification (ID) in Table 4.2. Also listed are the column-averaged and extinction-weighted extinction coefficient ( $\sigma_{ext}$ ), single scattering albedo ( $\omega_o$ ), asymmetry parameter ( $g$ ) and backscatter ratio ( $\beta$ ) calculated using  $m_{oe}$  and the optically-equivalent size distributions reported in Table 4.2.

ID	Date (2000)	$\lambda$ (nm)	$m_{oe}$		calculated optical properties			
			$m_r$	$m_i$	$\sigma_{ext} (Mm^{-1})$	$\omega_o$	$g$	$\beta$
1	22-Aug	354	$1.55 \pm 0.01$	$0.013 \pm 0.002$	$199.7 \pm 15.7$	$0.927 \pm 0.008$	$0.653 \pm 0.007$	$0.076 \pm 0.002$
		380	$1.54 \pm 0.01$	$0.013 \pm 0.002$	$182.4 \pm 14.4$	$0.926 \pm 0.008$	$0.653 \pm 0.006$	$0.076 \pm 0.001$
		449	$1.57 \pm 0.02$	$0.012 \pm 0.002$	$140.0 \pm 11.9$	$0.928 \pm 0.009$	$0.630 \pm 0.010$	$0.084 \pm 0.003$
		450	$1.54 \pm 0.02$	$0.012 \pm 0.003$	$133.5 \pm 11.3$	$0.930 \pm 0.009$	$0.632 \pm 0.008$	$0.082 \pm 0.002$
		499	$1.57 \pm 0.03$	$0.015 \pm 0.003$	$111.6 \pm 10.1$	$0.918 \pm 0.010$	$0.601 \pm 0.007$	$0.093 \pm 0.003$
		525	$1.62 \pm 0.03$	$0.017 \pm 0.003$	$104.4 \pm 8.6$	$0.912 \pm 0.010$	$0.579 \pm 0.009$	$0.102 \pm 0.003$
		550	$1.62 \pm 0.04$	$0.017 \pm 0.003$	$89.7 \pm 6.9$	$0.908 \pm 0.011$	$0.569 \pm 0.009$	$0.105 \pm 0.003$
		606	$1.69 \pm 0.04$	$0.021 \pm 0.004$	$83.9 \pm 8.5$	$0.897 \pm 0.012$	$0.543 \pm 0.011$	$0.116 \pm 0.004$
		675	$1.76 \pm 0.05$	$0.025 \pm 0.004$	$61.4 \pm 4.9$	$0.883 \pm 0.013$	$0.495 \pm 0.012$	$0.136 \pm 0.004$
		700	$1.77 \pm 0.06$	$0.026 \pm 0.005$	$59.4 \pm 5.3$	$0.878 \pm 0.014$	$0.487 \pm 0.012$	$0.139 \pm 0.004$
		778	$1.80 \pm 0.06$	$0.030 \pm 0.005$	$46.4 \pm 3.4$	$0.855 \pm 0.015$	$0.451 \pm 0.013$	$0.154 \pm 0.005$
		865	$1.80 \pm 0.07$	$0.031 \pm 0.005$	$38.8 \pm 3.2$	$0.848 \pm 0.014$	$0.443 \pm 0.014$	$0.158 \pm 0.005$
		1019	$1.79 \pm 0.07$	$0.031 \pm 0.005$	$28.8 \pm 2.3$	$0.830 \pm 0.017$	$0.424 \pm 0.017$	$0.166 \pm 0.007$
		1241	$1.82 \pm 0.06$	$0.038 \pm 0.005$	$23.0 \pm 1.7$	$0.786 \pm 0.015$	$0.401 \pm 0.018$	$0.177 \pm 0.008$
		1557	$1.84 \pm 0.06$	$0.059 \pm 0.009$	$17.2 \pm 1.8$	$0.673 \pm 0.017$	$0.366 \pm 0.018$	$0.193 \pm 0.008$
2	24-Aug	354	$1.54 \pm 0.02$	$0.020 \pm 0.003$	$165.5 \pm 27.6$	$0.896 \pm 0.012$	$0.655 \pm 0.017$	$0.074 \pm 0.005$
		380	$1.53 \pm 0.03$	$0.020 \pm 0.003$	$150.5 \pm 25.2$	$0.894 \pm 0.012$	$0.655 \pm 0.019$	$0.074 \pm 0.006$
		449	$1.53 \pm 0.03$	$0.021 \pm 0.003$	$126.3 \pm 22.4$	$0.888 \pm 0.013$	$0.635 \pm 0.023$	$0.081 \pm 0.007$
		450	$1.52 \pm 0.03$	$0.021 \pm 0.003$	$119.1 \pm 20.2$	$0.886 \pm 0.013$	$0.636 \pm 0.022$	$0.080 \pm 0.007$
		499	$1.55 \pm 0.03$	$0.024 \pm 0.003$	$108.6 \pm 19.0$	$0.876 \pm 0.014$	$0.616 \pm 0.022$	$0.088 \pm 0.007$
		525	$1.57 \pm 0.03$	$0.025 \pm 0.004$	$99.7 \pm 17.6$	$0.871 \pm 0.015$	$0.601 \pm 0.022$	$0.093 \pm 0.008$
		550	$1.56 \pm 0.03$	$0.025 \pm 0.004$	$91.2 \pm 16.0$	$0.868 \pm 0.015$	$0.597 \pm 0.024$	$0.095 \pm 0.008$
		606	$1.58 \pm 0.02$	$0.028 \pm 0.004$	$82.4 \pm 14.2$	$0.855 \pm 0.014$	$0.575 \pm 0.025$	$0.103 \pm 0.009$
		675	$1.60 \pm 0.04$	$0.032 \pm 0.004$	$70.4 \pm 12.4$	$0.835 \pm 0.016$	$0.551 \pm 0.032$	$0.113 \pm 0.012$
		700	$1.62 \pm 0.04$	$0.033 \pm 0.004$	$68.6 \pm 12.5$	$0.833 \pm 0.017$	$0.542 \pm 0.032$	$0.117 \pm 0.012$
		778	$1.66 \pm 0.05$	$0.038 \pm 0.005$	$60.7 \pm 11.0$	$0.809 \pm 0.017$	$0.518 \pm 0.037$	$0.127 \pm 0.015$
		865	$1.65 \pm 0.04$	$0.038 \pm 0.004$	$55.3 \pm 10.1$	$0.802 \pm 0.016$	$0.510 \pm 0.036$	$0.131 \pm 0.015$
		1019	$1.65 \pm 0.05$	$0.041 \pm 0.005$	$50.0 \pm 9.6$	$0.779 \pm 0.016$	$0.502 \pm 0.038$	$0.135 \pm 0.016$
		1241	$1.71 \pm 0.06$	$0.056 \pm 0.007$	$47.4 \pm 9.1$	$0.725 \pm 0.014$	$0.481 \pm 0.034$	$0.144 \pm 0.015$
		1557	$1.74 \pm 0.05$	$0.080 \pm 0.009$	$45.6 \pm 8.6$	$0.643 \pm 0.016$	$0.471 \pm 0.038$	$0.149 \pm 0.016$
3	31-Aug	354	$1.59 \pm 0.03$	$0.022 \pm 0.003$	$170.6 \pm 22.8$	$0.891 \pm 0.011$	$0.588 \pm 0.004$	$0.097 \pm 0.002$
		380	$1.59 \pm 0.03$	$0.022 \pm 0.002$	$153.4 \pm 21.0$	$0.888 \pm 0.011$	$0.583 \pm 0.005$	$0.099 \pm 0.003$
		449	$1.59 \pm 0.04$	$0.022 \pm 0.003$	$115.7 \pm 16.9$	$0.883 \pm 0.013$	$0.551 \pm 0.006$	$0.111 \pm 0.002$
		450	$1.59 \pm 0.04$	$0.021 \pm 0.003$	$112.2 \pm 15.6$	$0.886 \pm 0.011$	$0.553 \pm 0.004$	$0.110 \pm 0.002$
		499	$1.65 \pm 0.04$	$0.026 \pm 0.003$	$95.7 \pm 14.3$	$0.866 \pm 0.012$	$0.513 \pm 0.011$	$0.126 \pm 0.004$
		525	$1.66 \pm 0.04$	$0.027 \pm 0.004$	$86.3 \pm 11.7$	$0.858 \pm 0.013$	$0.498 \pm 0.010$	$0.133 \pm 0.004$
		550	$1.70 \pm 0.04$	$0.030 \pm 0.004$	$77.4 \pm 10.7$	$0.850 \pm 0.014$	$0.481 \pm 0.009$	$0.140 \pm 0.004$
		606	$1.72 \pm 0.05$	$0.032 \pm 0.005$	$66.5 \pm 9.7$	$0.835 \pm 0.018$	$0.457 \pm 0.010$	$0.150 \pm 0.004$
		675	$1.78 \pm 0.07$	$0.036 \pm 0.005$	$52.8 \pm 7.7$	$0.812 \pm 0.017$	$0.418 \pm 0.010$	$0.168 \pm 0.004$
		700	$1.84 \pm 0.05$	$0.039 \pm 0.005$	$49.2 \pm 6.9$	$0.811 \pm 0.018$	$0.409 \pm 0.009$	$0.172 \pm 0.004$
		778	$1.84 \pm 0.07$	$0.040 \pm 0.006$	$38.2 \pm 5.0$	$0.774 \pm 0.019$	$0.361 \pm 0.012$	$0.193 \pm 0.005$
		865	$1.85 \pm 0.06$	$0.039 \pm 0.005$	$31.8 \pm 4.2$	$0.770 \pm 0.018$	$0.354 \pm 0.012$	$0.197 \pm 0.006$
		1019	$1.87 \pm 0.06$	$0.039 \pm 0.006$	$24.1 \pm 3.2$	$0.751 \pm 0.016$	$0.330 \pm 0.015$	$0.208 \pm 0.007$
		1241	$1.85 \pm 0.05$	$0.040 \pm 0.005$	$19.1 \pm 2.7$	$0.693 \pm 0.018$	$0.298 \pm 0.010$	$0.224 \pm 0.005$
		1557	$1.87 \pm 0.05$	$0.048 \pm 0.007$	$15.7 \pm 2.3$	$0.595 \pm 0.018$	$0.262 \pm 0.011$	$0.241 \pm 0.005$

(cont.)

Table 4.3. (cont.)

ID	Date (2000)	$\lambda$ (nm)	$m_{oe}$		$\sigma_{ext}$ (Mm <sup>-1</sup> )	calculated optical properties		
			$m_r$	$m_i$		$\omega_o$	$g$	$\beta$
4	3-Sep	354	1.60 ± 0.01	0.040 ± 0.002	410.3 ± 56.6	0.837 ± 0.005	0.623 ± 0.003	0.083 ± 0.001
		380	1.59 ± 0.01	0.039 ± 0.002	378.4 ± 53.5	0.834 ± 0.005	0.616 ± 0.003	0.085 ± 0.001
		449	1.58 ± 0.02	0.039 ± 0.002	295.8 ± 41.5	0.824 ± 0.005	0.591 ± 0.004	0.094 ± 0.001
		450	1.58 ± 0.02	0.039 ± 0.002	291.7 ± 42.0	0.822 ± 0.007	0.591 ± 0.002	0.094 ± 0.001
		499	1.61 ± 0.02	0.040 ± 0.002	249.0 ± 34.4	0.819 ± 0.005	0.558 ± 0.004	0.106 ± 0.001
		525	1.64 ± 0.03	0.041 ± 0.002	222.9 ± 30.2	0.817 ± 0.006	0.537 ± 0.004	0.115 ± 0.002
		550	1.65 ± 0.03	0.040 ± 0.003	200.8 ± 27.3	0.820 ± 0.005	0.522 ± 0.002	0.121 ± 0.001
		606	1.67 ± 0.04	0.040 ± 0.003	169.9 ± 23.6	0.812 ± 0.005	0.491 ± 0.003	0.134 ± 0.001
		675	1.71 ± 0.04	0.040 ± 0.003	136.5 ± 19.0	0.804 ± 0.006	0.451 ± 0.006	0.152 ± 0.002
		700	1.81 ± 0.06	0.047 ± 0.004	123.8 ± 16.8	0.801 ± 0.008	0.436 ± 0.003	0.159 ± 0.001
		778	1.78 ± 0.05	0.046 ± 0.004	99.9 ± 14.3	0.775 ± 0.007	0.394 ± 0.003	0.177 ± 0.001
		865	1.78 ± 0.04	0.044 ± 0.004	82.0 ± 12.2	0.770 ± 0.006	0.376 ± 0.008	0.186 ± 0.004
		1019	1.74 ± 0.06	0.041 ± 0.006	59.3 ± 9.9	0.742 ± 0.009	0.354 ± 0.004	0.197 ± 0.002
		1241	1.72 ± 0.08	0.043 ± 0.008	45.4 ± 8.4	0.700 ± 0.009	0.337 ± 0.006	0.205 ± 0.003
		1557	1.80 ± 0.07	0.060 ± 0.009	38.1 ± 7.5	0.593 ± 0.012	0.289 ± 0.008	0.228 ± 0.004
5	6-Sep	354	1.58 ± 0.01	0.033 ± 0.002	479.7 ± 37.3	0.847 ± 0.007	0.643 ± 0.008	0.078 ± 0.002
		380	1.57 ± 0.02	0.033 ± 0.002	449.5 ± 35.7	0.845 ± 0.007	0.642 ± 0.008	0.079 ± 0.002
		449	1.58 ± 0.02	0.036 ± 0.002	358.3 ± 26.9	0.835 ± 0.007	0.619 ± 0.009	0.086 ± 0.003
		450	1.58 ± 0.02	0.036 ± 0.002	352.0 ± 27.8	0.833 ± 0.007	0.620 ± 0.009	0.086 ± 0.003
		499	1.60 ± 0.02	0.036 ± 0.002	313.6 ± 26.6	0.834 ± 0.006	0.595 ± 0.011	0.095 ± 0.004
		525	1.62 ± 0.03	0.036 ± 0.003	278.6 ± 20.7	0.833 ± 0.006	0.581 ± 0.013	0.100 ± 0.005
		550	1.60 ± 0.03	0.035 ± 0.003	247.7 ± 18.7	0.833 ± 0.006	0.572 ± 0.013	0.103 ± 0.005
		606	1.64 ± 0.03	0.036 ± 0.003	223.1 ± 18.6	0.831 ± 0.008	0.545 ± 0.015	0.114 ± 0.006
		675	1.69 ± 0.04	0.036 ± 0.004	174.8 ± 13.6	0.831 ± 0.008	0.507 ± 0.016	0.129 ± 0.007
		700	1.74 ± 0.05	0.040 ± 0.004	160.1 ± 12.5	0.826 ± 0.008	0.494 ± 0.016	0.135 ± 0.007
		778	1.77 ± 0.06	0.044 ± 0.005	127.5 ± 9.7	0.803 ± 0.010	0.457 ± 0.019	0.150 ± 0.008
		865	1.74 ± 0.05	0.041 ± 0.005	104.8 ± 8.9	0.797 ± 0.009	0.446 ± 0.018	0.155 ± 0.008
		1019	1.69 ± 0.06	0.037 ± 0.005	68.7 ± 4.9	0.777 ± 0.010	0.426 ± 0.022	0.165 ± 0.010
		1241	1.68 ± 0.08	0.039 ± 0.007	45.1 ± 3.0	0.729 ± 0.011	0.397 ± 0.023	0.178 ± 0.010
		1557	1.69 ± 0.08	0.050 ± 0.010	34.0 ± 4.6	0.633 ± 0.013	0.361 ± 0.018	0.195 ± 0.008
6	6-Sep	354	1.58 ± 0.01	0.031 ± 0.002	436.5 ± 24.5	0.849 ± 0.007	0.651 ± 0.006	0.077 ± 0.002
		380	1.57 ± 0.02	0.032 ± 0.002	406.9 ± 24.1	0.847 ± 0.007	0.649 ± 0.006	0.077 ± 0.002
		449	1.58 ± 0.02	0.034 ± 0.002	328.4 ± 19.7	0.836 ± 0.007	0.627 ± 0.007	0.084 ± 0.002
		450	1.57 ± 0.02	0.034 ± 0.002	315.3 ± 19.1	0.838 ± 0.007	0.629 ± 0.007	0.083 ± 0.002
		499	1.59 ± 0.03	0.034 ± 0.002	279.6 ± 17.7	0.836 ± 0.007	0.608 ± 0.010	0.091 ± 0.004
		525	1.60 ± 0.03	0.034 ± 0.003	253.0 ± 15.3	0.836 ± 0.007	0.594 ± 0.011	0.096 ± 0.004
		550	1.61 ± 0.03	0.034 ± 0.002	229.7 ± 15.2	0.838 ± 0.007	0.585 ± 0.011	0.099 ± 0.004
		606	1.63 ± 0.03	0.035 ± 0.003	198.9 ± 12.7	0.834 ± 0.008	0.562 ± 0.012	0.108 ± 0.005
		675	1.67 ± 0.04	0.036 ± 0.004	157.6 ± 10.9	0.832 ± 0.009	0.524 ± 0.013	0.123 ± 0.006
		700	1.71 ± 0.05	0.038 ± 0.004	146.7 ± 9.7	0.828 ± 0.010	0.515 ± 0.013	0.127 ± 0.005
		778	1.72 ± 0.06	0.041 ± 0.005	117.8 ± 8.1	0.810 ± 0.010	0.485 ± 0.017	0.139 ± 0.007
		865	1.69 ± 0.05	0.039 ± 0.005	93.7 ± 6.4	0.801 ± 0.009	0.472 ± 0.017	0.144 ± 0.007
		1019	1.63 ± 0.06	0.035 ± 0.005	63.7 ± 4.3	0.780 ± 0.008	0.460 ± 0.017	0.150 ± 0.007
		1241	1.61 ± 0.07	0.036 ± 0.007	41.4 ± 2.5	0.731 ± 0.011	0.430 ± 0.018	0.164 ± 0.008
		1557	1.60 ± 0.07	0.043 ± 0.008	27.6 ± 2.1	0.631 ± 0.010	0.385 ± 0.019	0.184 ± 0.008

the retrievals should be expected, *Haywood et al.* [2003a] showed that the submicron part of the size distribution played a very significant role and we corroborate this assertion with the coarse mode to fine mode ratio presented in Table 3.7. More evidence is required to further assess the reasons for the discrepancy.

The wavelength-dependent optical properties calculated from the optically-equivalent size distributions (Table 4.2) and refractive indices are also listed in Table 4.3. The *calculated* optical properties are determined from the *optically-equivalent* physical and chemical properties. We compare the calculated optical properties with the available *measured* optical properties and find that for the six vertical profiles examined, the calculated optical properties are on average within  $\sim 3\%$  of  $\sigma_{\text{ext, meas}, \lambda, z}$ ,  $\sim 1\%$  of  $\omega_{\text{o, meas}, \lambda, z}$ , and  $\sim 2\%$  of  $\beta_{\text{meas}, \lambda, z}$ . Values of  $g_{\lambda, z}$  are not measured and are strictly a product of the retrieval, but agree to within 5-10% with the values reported by AERONET.

#### 4.6. Summary of Look-Up Table Methodology

To summarize, we have designed an original and straight-forward retrieval algorithm that searches look-up tables constructed using Mie theory to find a size distribution and refractive index that most closely reproduce in situ and remote sensing measurements of aerosol optical properties. This *optically-equivalent* size distribution and refractive index are not physically based, but offer some insight into what size distribution is need to reproduce measurement. The resolution of

the look-up tables used in the retrieval is more than adequate to resolve the optical properties to within typical uncertainties. However, structural errors in calculated optical properties that arise from the discrete input used to build the look-up table are  $\pm 4.1\%$  in the extinction coefficient,  $\pm 1.2\%$  in the single scattering albedo, and  $\pm 3.8\%$  in the asymmetry parameter. These errors are propagated together with instrumental and measurement uncertainties. Otherwise, the accuracy of the retrieval is excellent, returning retrieved (or calculated) aerosol optical properties that are within  $\sim 3\%$  of the measured aerosol optical properties.

The most significant problem with the retrieval is the fact that there is very little information published about the wavelength dependence of the single scattering albedo. We explored the various options and chose a simple linear combination of the soot and urban aerosol models in *d'Almeida et al.* [1991] as a constraint on single scattering albedo. Using this assumption provides the necessary constraint on the retrieval to find aerosol physical, chemical, and optical properties that are self-consistent for  $\lambda = 354\text{-}1557$  nm.

Although the optically-equivalent size distribution and bulk refractive index from the retrieval are not grounded in a physically-based approach to diagnosing aerosol chemistry [*Jacobson*, 2000; ], the values still provide some guidelines for other studies. The most surprising result from the retrieval discussed here are the very high values of both the real and imaginary parts of the refractive index that are required to reproduce the available measurements (Table 4.3). Compared to AERONET data, there is a significant discrepancy. The

optically-equivalent size distributions listed in Table 4.2 are much closer to size distributions published in other biomass burning studies [*Reid et al.*, 1998; *Ross et al.*, 1998; *Eck et al.*, 2003; *Haywood et al.*, 2003a]. This important method of closure with very well-documented optical measurements might be a useful tool for other field studies with similar instrumentation [e.g. *Clarke et al.*, 2002; *Doherty et al.*, 2005; *Quinn et al.*, 2005; *Redemann et al.*, 2005b; *Schmid et al.*, 2006].

The retrieval presented here is particularly well-suited for SAFARI-2000 data since the aerosol was dominated by submicron particles. More information would be required to constrain a retrieval of a bi-modal (optically-equivalent) size distribution, but studies such as *Doherty et al.* [2005] show that coarse and submicron particles can be individually characterized. Closure between physical, chemical, and optical properties also provides insight into any potential problems with sampling [e.g. *Guyon et al.*, 2003; *Osborne et al.*, 2004; *Haywood et al.*, 2004]. In every way, however, aerosol measurements should be self-consistent. The retrieval we present provides a method of finding closure and highlighting potential discrepancies.



## Chapter 5. Biomass Burning Aerosol Radiative Forcing

We estimate the overall radiative effect of southern African biomass burning aerosol using a measurement-based approach that has become more common as data from polluted airsheds around the world continues to be analyzed [Yu *et al.*, 2006]. The calculation of radiative forcing was described in Section 1.3, but can also be found in numerous sources [e.g. Ramaswamy *et al.*, 2001; Anderson *et al.*, 2005]. Estimates of radiative forcing are, however, often accompanied by only a *qualitative* estimate of the uncertainty [Schwartz, 2004]. Some studies have attempted to address this issue [e.g. Redemann *et al.*, 2000b], while many others point out the dire need to both address and reduce the uncertainty in aerosol radiative forcing [Anderson *et al.*, 2003a; Ackerman *et al.*, 2004; Schwartz, 2004] since the overall climate sensitivity is directly affected by the lack of knowledge about aerosols [Andreae *et al.*, 2005; Delworth *et al.*, 2005], both past and present [Kinne *et al.*, 2005]. We offer a method to estimate the radiative forcing due to biomass burning aerosol, but also provide a quantitative assessment of the uncertainty in radiative forcing due to uncertainty in the input.

### 5.1. Fu-Liou Radiative Transfer Model Overview

The Fu-Liou radiative transfer model (RTM) has been extensively documented [Liou *et al.*, 1988; Fu and Liou, 1992] and also been applied in

aerosol studies [e.g. *Liao and Seinfeld*, 1998; *Christopher et al.*, 2000; *Redemann et al.*, 2000b; *Zhou et al.*, 2005], and cloud and radiative balance studies [e.g. *Fu et al.*, 1995; *Hartmann et al.*, 2001; *Gettelman et al.*, 2004]. The model uses a delta-four-stream approximation to calculate shortwave and longwave radiative fluxes in a vertically non-homogenous atmosphere. The shortwave spectrum is divided into ten discrete wavelength bands from 175-690 nm and five bands from 700-4000 nm. The longwave spectrum is divided into twelve discrete bands, but are not used in this study since biomass burning aerosols generally have a more significant effect on shortwave radiation [*Jacobson*, 2001; *Reddy et al.*, 2005b].

Uncertainties in the flux calculations associated with the approximations used in this computationally-efficient RTM were assessed in *Liou et al.* [1988] and are less than  $\pm 1 \text{ W m}^{-2}$  for the range of aerosol optical depths in Table 3.5 in atmospheres with some absorption (i.e.  $\omega_0 < 1.0$ ). The RTM, however, uses the simplified Henyey-Greenstein phase function approximation (Eq. 1.10) and *Boucher* [1998] showed that errors introduced into calculations of radiative forcing for a purely scattering aerosol can be significant at small and large values of solar zenith angles and for submicron particles. The effect of the approximation for a range of real and imaginary refractive indices has not been published, but we attempt to account for this potential error by doubling the uncertainty in the flux calculated by the RTM [*Liou et al.*, 1988] to  $\pm 2 \text{ W m}^{-2}$ .

## 5.2. Model Input

We use the Fu-Liou RTM to calculate fluxes at 100 levels from the surface to 500 hPa and 50 levels from 500 hPa to 25 hPa in vertically non-homogeneous atmospheres modeled using observations made during SAFARI-2000 (Chapter 3) and input based on the retrieval described in Chapter 4.

Vertical profiles of temperature (T) and water vapor mixing ratio (in units of kg/kg) are compiled using UW research aircraft measurements of T and relative humidity (RH) from the surface to ~500 hPa and archived model re-analysis data from the Fleet Naval Laboratory (FNL) global model from ~500 hPa to 25 hPa. FNL archived data is publicly available at <http://www.arl.noaa.gov/ready/amet.html> for locations around the world.

Carbon dioxide (CO<sub>2</sub>) and methane (CH<sub>4</sub>) concentrations are set at 377 ppmv and 1770 ppbv, respectively [Sinha *et al.*, 2003b]. Nitrous oxide (N<sub>2</sub>O) concentrations are based on Thompson *et al.* [2004] and set at 310 ppbv. Results presented in Sinha *et al.* [2003b] suggest that there are deviations from the globally-averaged concentrations of CO<sub>2</sub> and CH<sub>4</sub> in the lowest ~5 km of the atmosphere of southern Africa during SAFARI-2000 due to the prevalence of biomass burning, but we do not attempt to model the effects of the vertical structure of these gases.

Vertical profiles of ozone (O<sub>3</sub>) are constructed using UW research aircraft measurements of ozone [Sinha *et al.*, 2003b] and data from the Southern Hemisphere Additional Ozonesondes (SHADOZ) network that operated during

SAFARI-2000 [Thompson *et al.*, 2002]. The SHADOZ data is publicly available at [http://croc.gsfc.nasa.gov/shadoz/Shadoz\\_hmpg2.html](http://croc.gsfc.nasa.gov/shadoz/Shadoz_hmpg2.html) and the data processing is discussed in Thompson *et al.* [2003]. Generally, we use the UW research aircraft vertical profiles of O<sub>3</sub> from near the surface to ~500 hPa and use data from the SHADOZ network for the remainder of the profile from ~500 hPa to 25 hPa. Since SHADOZ data is not available every day and not necessarily spatially co-located with the aircraft vertical profile, we use data from the closest day and location for each individual vertical profile. The largest daily fluctuations in O<sub>3</sub> are generally between the surface and 500 hPa and are due to the daily variability in biomass burning [Sinha *et al.*, 2003b], but these fluctuations are captured by the aircraft vertical profiles.

Fluxes from the Fu-Liou RTM are averaged for the entire day using a range of latitude-dependent solar zenith angles ( $\theta_o$ ). The output is the *diurnally-averaged* flux. Values of  $\theta_o$  were calculated every 30 minutes using Equations 2.2.1, 2.2.10, and Table 2.2 in Liou [2002] and the latitude and day of the year of the vertical profiles listed in Table 4.2. We also use the empirical relation provided by Eq. 2.2.9 and Table 2.2 in Liou [2002] to calculate the Sun-Earth distance, or *eccentricity*, which is dependent on the day of the year.

### 5.2.1. Aerosol Optical Properties

The aircraft in situ profiles described in Chapters 3-4 showed that the majority of the aerosols in southern Africa are between the surface and ~500 hPa,

which agrees with past studies of southern African climatology [*Cosijn and Tyson, 1996; Swap and Tyson, 1999*]. We use the retrieval methodology described in Sections 4.3-4.4 to derive aerosol optical properties for  $\lambda = 354 - 1557$  nm. The required input to the Fu-Liou RTM, however, are the extinction coefficient ( $\sigma_{\text{ext}}$ ) and aerosol optical depth ( $\tau$ ), the single scattering albedo ( $\omega_o$ ), and the asymmetry parameter ( $g$ ) for wavelengths in the entire shortwave spectrum, or  $\lambda = 200 - 4000$  nm. We use the Angstrom exponent for extinction ( $\alpha_{\text{ext}}$ ), aerosol optical depth ( $\alpha_{\tau}$ ), and scattering ( $\alpha_{\text{sca}}$ ) described by Eq. 1.14 to extrapolate to wavelengths where we have no measurements. To extrapolate  $\sigma_{\text{ext}}$  to  $\lambda = 200 - 354$  nm, we use  $\alpha_{\text{ext},354-380}$ ; to extrapolate to  $\lambda = 1557 - 4000$  nm, we use  $\alpha_{\text{ext},1241-1557}$ . We use an analogous approach to extrapolate  $\sigma_{\text{sca}}$ . With these extrapolated values of  $\sigma_{\text{ext}}$  and  $\sigma_{\text{sca}}$ , we can calculate  $\omega_o$  ( $\sigma_{\text{sca}}/\sigma_{\text{ext}}$ ) for the shortwave spectrum as well. Extrapolation of  $g$  to  $\lambda < 354$  nm is done by using a linear regression to values of  $g$  at 354, 380, and 449 nm. Similarly, we extrapolate  $g$  to  $\lambda > 1557$  nm using a linear regression to values of  $g$  at 1019, 1241, and 1557 nm.

We also need to ascribe characteristics to the upper atmospheric aerosol optical properties. The upper atmosphere in this study refers to the part of the atmosphere from 25 hPa to ~500 hPa, which is approximately the maximum altitude of the UW research aircraft vertical profiles (see Table 3.4). We use recent satellite-derived upper atmospheric values of  $\sigma_{\text{ext},500}$  from a year 2003

climatology provided by *Vanhellemont et al.* [2005]; we do not expect any significant variations since there were no large volcanic eruptions between 2000 and 2003. Based on the *Vanhellemont et al.* [2005] study, we extrapolate  $\sigma_{\text{ext},500}$  across the shortwave spectrum using  $\alpha_{\text{ext}} = 1$ .

For upper atmospheric values of  $\omega_{o,\lambda}$  and  $g_\lambda$ , we use the climatology provided in *Fenn et al.* [1985], which are given for  $\lambda = 200\text{--}4000$  nm. We use an exponential function to smoothly transition from the measured lower atmospheric aerosol optical properties (from  $\sim 500$  hPa to the surface) to the upper atmospheric properties to prevent a discontinuity between the different data sets.

Finally, since the aerosol vertical profiles measured by the aircraft never quite reach the surface (See Figs. 3.8-3.13, for example), we fill the part of the profile from the minimum altitude of the aircraft vertical profile to the surface by simply assuming the aerosol optical properties continue from the bottom of the profile to the surface with no variability. There is the possibility of using coincident ground-based measurements from AERONET (Section 2.2) combined with Sunphotometer measurements to estimate the unmeasured aerosol optical depth, but this requires coordination both in time and space of the aircraft vertical profile and the AERONET retrieval [*Anderson et al.*, 2003b; *Reddy et al.*, 2005b; *Leahy*, 2006].

After we have the shortwave aerosol optical properties for the entire atmosphere from the surface to 25 hPa, we integrate the values at discrete wavelengths over the fifteen shortwave wavelength bands of the Fu-Liou RTM

(see Table 5.1 for a detailed listing of the Fu-Liou wavelength bands). This band-averaging is necessary to account for potential non-linear variations in the specific aerosol property for a specific wavelength band. For example, the band-averaged value of  $\omega_o$  for the  $\lambda = 700\text{-}1300$  nm wavelength band of the Fu-Liou radiative transfer ( $\omega_{o,700-1300}$ ) is calculated using

$$\omega_{o,700-1300} = \frac{\int_{700}^{1300} \omega_o d\lambda}{\int_{700}^{1300} d\lambda} \quad (5.1)$$

where we calculate the band-averaged values of  $\sigma_{\text{ext}}$  or  $g$  analogously. This calculation is done for every Fu-Liou RTM band.

The band- and column-averaged values of  $\sigma_{\text{ext},\lambda}$ ,  $\omega_{o,\lambda}$ , and  $g_\lambda$  are listed in Table 5.1 along with the corresponding wavelength bands used in the Fu-Liou RTM. The mean values are weighted by  $\sigma_{\text{ext},\lambda}$  to emphasize the properties of the atmosphere with the highest number concentrations (or the most significant effect on shortwave radiation) as opposed to the upper atmospheric aerosol optical properties. The 95%, or two standard deviation, confidence intervals in the weighted mean values are also listed in Table 5.1..

An important note about the input is that we do not include diurnal variations of the model input (except for  $\theta_o$ ). Biomass burning has a diurnal cycle that is stronger in countries more directly affected by heavy burning such as Zambia and weaker in the region around northern South Africa (see Fig. 1.4 for a map) and this results in variations in the extensive aerosol optical properties [Eck

Table 5.1. The surface albedo ( $A_s$ ), aerosol optical depth ( $\tau$ ), and the band- and column- averaged extinction coefficient ( $\sigma_{\text{ext}}$ ), single scattering albedo ( $\omega_o$ ), and asymmetry parameter ( $g$ ) used as input to the different wavelength ( $\lambda$ ) bands of the Fu-Liou radiative transfer model for each of the six vertical profiles examined. The actual input varies in the vertical with most of the aerosols residing between the surface and 5 km ( $\sim 500$  hPa). The average are weighted by extinction and are listed with the two standard deviation variability about the weighted average. The numerical identifications (IDs) can be cross-referenced with Table 4.2.

Date		band-averaged optical properties					
ID	(2000)	$\lambda$ (nm)	$A_s$	$\tau$	$\sigma_{\text{ext}}$ (Mm <sup>-1</sup> )	$\omega_o$	g
1	22-Aug	175 - 225	0.055	1.34	390.9 ± 34.2	0.932 ± 0.006	0.7107 ± 0.0054
		225 - 244	0.055	1.12	318.3 ± 27.9	0.930 ± 0.006	0.6990 ± 0.0052
		244 - 286	0.055	0.98	273.9 ± 24.0	0.929 ± 0.006	0.6886 ± 0.0052
		286 - 299	0.055	0.87	241.4 ± 21.2	0.928 ± 0.006	0.6791 ± 0.0053
		299 - 323	0.055	0.81	223.3 ± 19.6	0.928 ± 0.006	0.6725 ± 0.0054
		323 - 358	0.055	0.73	199.3 ± 17.5	0.927 ± 0.006	0.6612 ± 0.0056
		358 - 438	0.055	0.62	164.5 ± 14.6	0.926 ± 0.007	0.6451 ± 0.0063
		438 - 498	0.055	0.44	119.4 ± 10.9	0.923 ± 0.008	0.6180 ± 0.0074
		498 - 595	0.075	0.34	90.6 ± 8.0	0.906 ± 0.009	0.5721 ± 0.0086
		595 - 690	0.114	0.26	66.8 ± 6.6	0.887 ± 0.011	0.5206 ± 0.0113
		700 - 1300	0.302	0.12	31.7 ± 2.8	0.826 ± 0.013	0.4296 ± 0.0134
		1300 - 1900	0.351	0.06	15.5 ± 1.5	0.672 ± 0.017	0.3751 ± 0.0124
		1900 - 2500	0.351	0.04	9.6 ± 0.9	0.536 ± 0.015	0.3477 ± 0.0117
		2500 - 3500	0.351	0.02	6.1 ± 0.6	0.418 ± 0.015	0.3088 ± 0.0127
		3500 - 4000	0.351	0.02	4.3 ± 0.4	0.353 ± 0.017	0.2742 ± 0.0125
2	24-Aug	175 - 225	0.035	1.15	332.3 ± 50.9	0.915 ± 0.011	0.7064 ± 0.0107
		225 - 244	0.035	0.90	268.0 ± 41.1	0.911 ± 0.011	0.6973 ± 0.0112
		244 - 286	0.035	0.76	228.9 ± 35.1	0.908 ± 0.011	0.6891 ± 0.0118
		286 - 299	0.035	0.65	200.6 ± 30.8	0.905 ± 0.011	0.6816 ± 0.0125
		299 - 323	0.035	0.59	184.9 ± 28.4	0.904 ± 0.011	0.6763 ± 0.0130
		323 - 358	0.035	0.52	164.1 ± 25.2	0.902 ± 0.011	0.6674 ± 0.0136
		358 - 438	0.035	0.43	138.0 ± 21.5	0.896 ± 0.010	0.6546 ± 0.0158
		438 - 498	0.035	0.34	109.6 ± 17.3	0.887 ± 0.012	0.6348 ± 0.0170
		498 - 595	0.066	0.27	88.6 ± 14.0	0.872 ± 0.013	0.6034 ± 0.0186
		595 - 690	0.063	0.22	72.0 ± 11.1	0.850 ± 0.013	0.5722 ± 0.0230
		700 - 1300	0.221	0.13	51.3 ± 8.1	0.783 ± 0.015	0.5114 ± 0.0282
		1300 - 1900	0.154	0.08	42.2 ± 6.6	0.649 ± 0.016	0.4727 ± 0.0268
		1900 - 2500	0.090	0.05	32.3 ± 5.1	0.546 ± 0.013	0.4381 ± 0.0266
		2500 - 3500	0.090	0.04	26.1 ± 4.1	0.455 ± 0.012	0.3929 ± 0.0255
		3500 - 4000	0.090	0.03	22.2 ± 3.5	0.402 ± 0.013	0.3518 ± 0.0237
3	31-Aug	175 - 225	0.030	1.66	470.0 ± 47.0	0.921 ± 0.007	0.6659 ± 0.0079
		225 - 244	0.030	1.28	366.6 ± 36.7	0.914 ± 0.007	0.6504 ± 0.0069
		244 - 286	0.030	1.07	305.9 ± 30.7	0.908 ± 0.007	0.6368 ± 0.0063
		286 - 299	0.030	0.91	262.6 ± 26.4	0.904 ± 0.007	0.6244 ± 0.0058
		299 - 323	0.030	0.83	239.1 ± 24.0	0.901 ± 0.007	0.6158 ± 0.0056
		323 - 358	0.030	0.72	208.5 ± 21.0	0.897 ± 0.007	0.6017 ± 0.0052
		358 - 438	0.030	0.58	168.9 ± 17.4	0.889 ± 0.007	0.5761 ± 0.0060
		438 - 498	0.030	0.43	125.4 ± 13.3	0.880 ± 0.007	0.5466 ± 0.0071
		498 - 595	0.060	0.32	93.4 ± 9.7	0.854 ± 0.009	0.4887 ± 0.0093
		595 - 690	0.061	0.24	69.0 ± 7.4	0.826 ± 0.011	0.4466 ± 0.0107
		700 - 1300	0.286	0.11	31.7 ± 3.3	0.751 ± 0.013	0.3538 ± 0.0127
		1300 - 1900	0.248	0.06	17.3 ± 1.9	0.600 ± 0.018	0.2933 ± 0.0083
		1900 - 2500	0.126	0.05	13.1 ± 1.4	0.484 ± 0.015	0.2750 ± 0.0057
		2500 - 3500	0.126	0.04	9.8 ± 1.1	0.382 ± 0.012	0.2432 ± 0.0061
		3500 - 4000	0.126	0.03	7.9 ± 0.9	0.325 ± 0.013	0.2148 ± 0.0060

(cont.)



Table 5.1. (cont.)

ID	Date (2000)	$\lambda$ (nm)	band-averaged optical properties			
			$A_s$	$\tau$	$\sigma_{\text{ext}}$ ( $\text{Mm}^{-1}$ )	$g$
4	3-Sep	175 - 225	0.075	3.07	$838.9 \pm 98.2$	$0.863 \pm 0.006$
		225 - 244	0.075	2.45	$684.6 \pm 80.2$	$0.857 \pm 0.006$
		244 - 286	0.075	2.08	$589.9 \pm 69.1$	$0.852 \pm 0.006$
		286 - 299	0.075	1.81	$520.7 \pm 61.0$	$0.848 \pm 0.006$
		299 - 323	0.075	1.66	$482.0 \pm 56.5$	$0.845 \pm 0.006$
		323 - 358	0.075	1.46	$430.8 \pm 50.5$	$0.842 \pm 0.006$
		358 - 438	0.075	1.22	$361.2 \pm 42.9$	$0.835 \pm 0.007$
		438 - 498	0.075	0.92	$277.7 \pm 33.4$	$0.826 \pm 0.007$
		498 - 595	0.093	0.70	$207.0 \pm 24.1$	$0.823 \pm 0.007$
		595 - 690	0.124	0.51	$151.3 \pm 17.9$	$0.812 \pm 0.008$
		700 - 1300	0.270	0.22	$66.4 \pm 9.0$	$0.752 \pm 0.011$
		1300 - 1900	0.307	0.09	$32.6 \pm 5.3$	$0.600 \pm 0.017$
		1900 - 2500	0.307	0.06	$19.7 \pm 3.1$	$0.475 \pm 0.015$
		2500 - 3500	0.307	0.04	$12.7 \pm 2.0$	$0.370 \pm 0.009$
		3500 - 4000	0.307	0.03	$9.1 \pm 1.5$	$0.311 \pm 0.011$
5	6-Sep	175 - 225	0.052	3.05	$838.9 \pm 62.0$	$0.858 \pm 0.007$
		225 - 244	0.052	2.64	$716.4 \pm 52.9$	$0.856 \pm 0.007$
		244 - 286	0.052	2.38	$637.9 \pm 47.1$	$0.854 \pm 0.007$
		286 - 299	0.052	2.18	$578.9 \pm 42.8$	$0.852 \pm 0.007$
		299 - 323	0.052	2.06	$545.0 \pm 40.3$	$0.851 \pm 0.007$
		323 - 358	0.052	1.90	$499.4 \pm 36.9$	$0.849 \pm 0.007$
		358 - 438	0.052	1.65	$431.2 \pm 31.4$	$0.845 \pm 0.007$
		438 - 498	0.052	1.29	$338.0 \pm 25.2$	$0.836 \pm 0.007$
		498 - 595	0.083	0.99	$257.3 \pm 18.1$	$0.835 \pm 0.008$
		595 - 690	0.100	0.75	$196.8 \pm 14.5$	$0.834 \pm 0.008$
		700 - 1300	0.311	0.31	$80.8 \pm 5.6$	$0.778 \pm 0.011$
		1300 - 1900	0.322	0.12	$30.1 \pm 2.4$	$0.638 \pm 0.017$
		1900 - 2500	0.212	0.06	$16.5 \pm 1.2$	$0.519 \pm 0.015$
		2500 - 3500	0.212	0.04	$9.6 \pm 0.7$	$0.412 \pm 0.012$
		3500 - 4000	0.212	0.02	$6.3 \pm 0.5$	$0.353 \pm 0.015$
6	6-Sep	175 - 225	0.050	3.20	$777.6 \pm 40.7$	$0.868 \pm 0.006$
		225 - 244	0.050	2.75	$657.9 \pm 34.4$	$0.863 \pm 0.006$
		244 - 286	0.050	2.46	$581.8 \pm 30.4$	$0.859 \pm 0.006$
		286 - 299	0.050	2.24	$524.9 \pm 27.5$	$0.856 \pm 0.006$
		299 - 323	0.050	2.11	$492.5 \pm 25.8$	$0.854 \pm 0.006$
		323 - 358	0.050	1.94	$448.9 \pm 23.5$	$0.851 \pm 0.006$
		358 - 438	0.050	1.69	$386.0 \pm 20.8$	$0.845 \pm 0.007$
		438 - 498	0.050	1.28	$294.7 \pm 16.5$	$0.837 \pm 0.007$
		498 - 595	0.081	1.01	$231.3 \pm 13.0$	$0.836 \pm 0.007$
		595 - 690	0.097	0.75	$170.3 \pm 10.1$	$0.832 \pm 0.008$
		700 - 1300	0.306	0.32	$72.2 \pm 4.3$	$0.778 \pm 0.010$
		1300 - 1900	0.316	0.11	$25.9 \pm 1.5$	$0.632 \pm 0.015$
		1900 - 2500	0.204	0.06	$14.5 \pm 0.9$	$0.512 \pm 0.014$
		2500 - 3500	0.204	0.03	$8.4 \pm 0.5$	$0.411 \pm 0.011$
		3500 - 4000	0.204	0.02	$5.5 \pm 0.4$	$0.352 \pm 0.013$

*et al.*, 2003]. *Eck et al.* [2003] point out the diurnal range in aerosol optical depth can be as much as 25% in the tropical regions, but falls off to 5-10% in countries further to the south, and that in most cases fire activity peaks in the afternoon (local time is UTC+2, referring to the times of the vertical profiles listed in Table 5.1).

As described in Chapter 3, a regional perturbation like the River of Smoke is driven by meteorology and affects both extensive and intensive aerosol properties (Table 3.7). There are, however, no measurements of the diurnal variability in intensive aerosol optical properties, so we assume that the shorter timescale diurnal variations in smoke concentration primarily affects the extensive properties. Implicit in this assumption is that a *single* vertical profile of aerosol optical properties is an adequate model of the *diurnally averaged* vertical profile. Investigation of the radiative effects of the diurnal variation in southern African intensive and extensive aerosol optical properties is left for a future study.

### 5.2.2. Surface Albedo

The NASA Cloud-Absorption Radiometer (CAR) on the UW research aircraft measured the wavelength dependent surface albedo ( $A_{s,\lambda}$ ) and bidirectional reflectance distribution function of different land surfaces encountered during SAFARI-2000 [*Gatebe et al.*, 2003]. The CAR makes measurements of  $A_{s,\lambda}$  at  $\lambda = 472, 682, 870, 1036, 1219, \text{ and } 1273 \text{ nm}$ . In this study, we used  $A_{s,\lambda}$  from the CAR when it was available for a particular flight.

The CAR data processing for SAFARI-2000 was discussed in *Gatebe et al.* [2003].

For cases when CAR data is not available, we use the filled surface albedo product from the MODIS satellite [*Moody et al.*, 2005] which provides  $A_{s,\lambda}$  at  $\lambda = 300, 470, 555, 659, 699, 701, 858, 1240, 1640,$  and  $2130$  nm. Values of  $A_{s,\lambda}$  for each wavelength band of the Fu-Liou RTM are listed in Table 5.1, where we have interpolated the CAR or MODIS values of  $A_{s,\lambda}$  to the central wavelength of the Fu-Liou RTM wavelength bands where possible and assumed a constant value of  $A_{s,\lambda}$  beyond the wavelengths provided by the CAR or MODIS data ( $\lambda > 1273$  nm for CAR, for example).

### 5.3. Vertical Profiles of Aerosol Radiative Effects

The measurement-based vertical profiles of the diurnally-averaged radiative effects of biomass burning aerosol in southern Africa are shown in Fig. 5.1. Each column of the figure corresponds to a particular vertical profile (denoted by the date and time, which can be cross-referenced with information in Table 4.2), and each row corresponds to a different radiative calculation. The first row shows the aerosol radiative forcing (RF) as described in Section 1.3. The second row is the ratio of the diffuse downwelling radiation to direct downwelling radiation, or the diffuse-direct ratio, due to the presence of the aerosol layer. The third row shows the radiative heating rate in the atmosphere due to the presence of

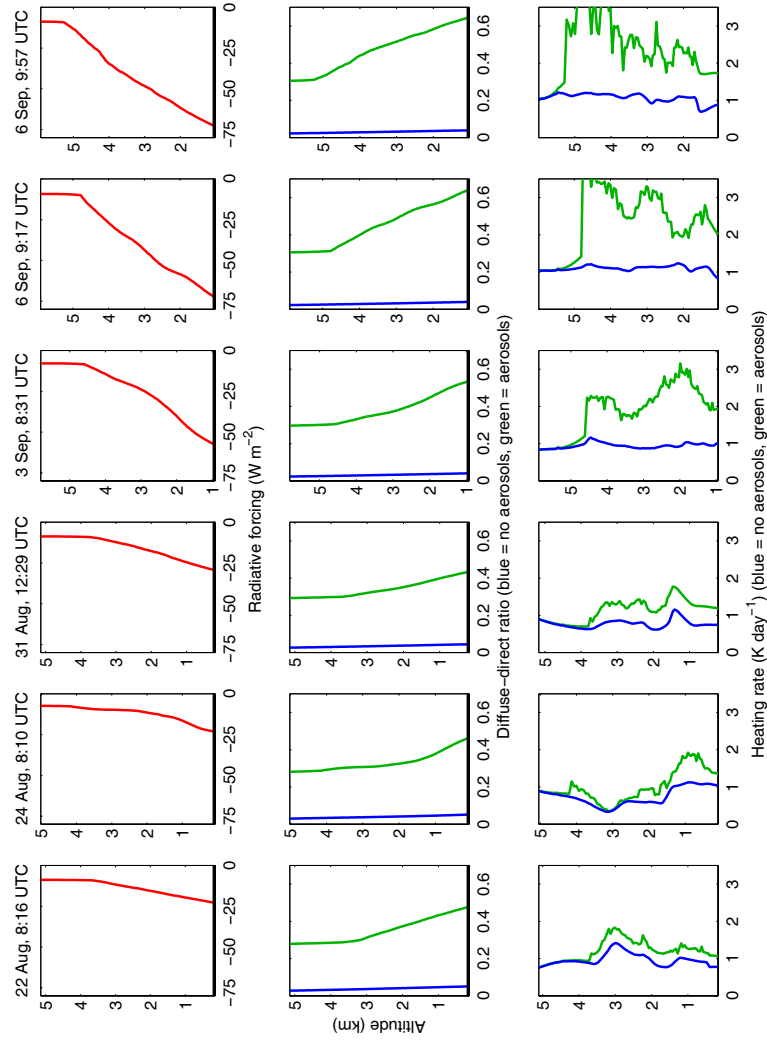


Fig. 5.1. Vertical profiles of the diurnally-averaged radiative effects of southern African biomass burning aerosol. The columns correspond to six different aircraft vertical profiles (see Table 4.2), where the August vertical profiles are during the period dominated by anticyclonic circulation and the September vertical profiles are during the River of Smoke. The rows correspond to the diurnally-averaged radiative forcing, diffuse-direct ratio, and heating rate. For the last two rows, the blue curves are calculations done with no biomass burning aerosol layer whereas the green curves are for an atmosphere with a biomass burning aerosol layer.

the aerosol layer. In all cases, the vertical profiles are limited to the lowest ~5 km of the atmosphere (where the surface is the lower limit on the y-axis of Fig. 5.1).

For the six cases examined, we see that the RF is nearly the same above the aerosol layer for each vertical profile, but markedly different at the surface. The surface, or bottom of the atmosphere radiative forcing ( $RF_{\text{boa}}$ ) is driven by the presence of the absorbing aerosol. During the three cases in September (during the River of Smoke, Section 3.1),  $RF_{\text{boa}}$  is enhanced by a factor of 2-3 due to a decrease in  $\omega_o$  and increase in  $\tau$ , as listed in Table 5.1. This enhancement is due to radiation being lost both by a more absorbing aerosol and larger concentrations of aerosol scattering more radiation away from the surface. Simply examining top of the atmosphere RF ( $RF_{\text{toa}}$ ) would give no indication that the aerosol optical properties changed. Less radiation is scattered back to space during the August vertical profiles, but less radiation is absorbed as well.

The diffuse-direct ratio is enhanced by about 50% during the River of Smoke vertical profiles to the point that more diffuse radiation reaches the surface during the day than direct radiation (in the 3 and 6 September vertical profiles). The radiative heating rates are enhanced by ~20-200% compared to an atmosphere with no aerosol layer (the blue curves). Again, the aerosol optical properties of smoke transported from tropical Africa during the River of Smoke suggest a very absorbing aerosol. The radiative heating rates are a factor of 2-3 greater than an atmosphere with no aerosol. This could have significant impacts on cloud formation [Ackerman *et al.*, 2000; Jiang and Feingold, 2006] in the

region if the optical properties are indeed representative of tropical biomass burning aerosol. At the very least, the large heating rates shown in Fig. 5.1 would de-stabilize the typically stratified atmosphere [Cosijn and Tyson, 1996] and create a more uniformly mixed polluted layer. Observations during the River of Smoke and shown in Figs. 3.8-3.13 confirm that the large heating rates during the River of Smoke were indeed coincident with a more well-mixed aerosol in the lowest 5 km of the atmosphere. This effect is most noticeable if Figs. 3.8-3.10 are visually compared with Figs. 3.11-3.13.

#### **5.4. Uncertainty Analysis**

A crucial step in understanding aerosol optical properties in the context of climate change is the assessment of the uncertainties in aerosol radiative forcing calculations, which ideally should be propagated directly from measurement errors. Kinne *et al.* [2003], Abel *et al.* [2005], and Kinne *et al.* [2005] show that there are discrepancies between the large-scale models and measurements that are difficult to account for. The aerosol chemical composition assumed in the models is certainly part of the problem [Kinne *et al.*, 2003], but there are very few measurements available to refute or confirm all the different aspects of a global distribution of aerosols. We suggest a method of estimating both the radiative forcing and the uncertainty in the radiative forcing that could provide a better foundation for understanding the weakest areas of knowledge about the study of aerosols.

The propagation of errors from measurements to the estimate of radiative forcing (RF) is not based on straight-forward analytical expressions. Using a model to simulate RF requires that errors be assessed with sensitivity tests of the simulation to the various input. We quantify the results of the sensitivity of RF to a number of different input parameters to the RTM. If the results are treated separately, then the total uncertainty in RF ( $\delta RF$ ) can be calculated by a simple quadratures method [Bevington and Robinson, 1992] as

$$\delta RF^2 = \delta RF_{ext}^2 + \delta RF_{ssa}^2 + \delta RF_{asy}^2 + \delta RF_{ua}^2 + \delta RF_{sa}^2 + \delta RF_{flrt}^2 \quad (5.2)$$

where RF is the diurnally-averaged radiative forcing for a particular vertical profile,  $\delta RF_{ext}$ ,  $\delta RF_{ssa}$ , and  $\delta RF_{asy}$  are the uncertainty in RF due to uncertainties in the optical properties  $\sigma_{ext}$ ,  $\omega_o$ , and  $g$ , respectively. Then  $\delta RF_{ua}$ ,  $\delta RF_{sa}$ , and  $\delta RF_{flrt}$  are the uncertainty in RF due to uncertainties in upper atmospheric aerosol properties [Vanhellemont *et al.*, 2005], surface albedo [Gatebe *et al.*, 2003; Moody *et al.*, 2005], and in the flux calculations in the Fu-Liou RTM discussed in Section 5.1 and in Liou *et al.* [1988].

#### 5.4.1. Uncertainty Related to Measured Aerosol Optical Properties

To assess how the uncertainty in the retrieved aerosol optical properties described in Chapters 3-4 (from  $\lambda = 354$ -1557 nm) affects RF, we systematically vary the input to the RTM by discrete percentages away from the base case. For every percent variation, we calculate RF having varied only one input parameter.

The change in RF ( $\Delta RF$ ) due to the percentage change of an optical property is the sensitivity of RF to that optical property for that particular vertical profile. For  $\sigma_{\text{ext}}$  (or  $\tau$ ), we vary the input values (summarized in Table 5.1) by  $\pm 20\%$ , while for  $\omega_o$  and  $g$  we vary the input values by  $\pm 10\%$  (making sure that  $\omega_o < 1$  and  $g < 1$ ).

We partition the sensitivity test into the visible wavelengths ( $\lambda = 400\text{-}700$  nm) and what we refer to as the *non-visible* wavelengths of the Sunphotometer ( $\lambda = 354\text{-}400$  nm and  $\lambda = 700\text{-}1557$  nm) to independently explore the dependence of  $\Delta RF$  to variability for optical properties in a wavelength range that has a good history of measurements (visible) and a range that does not (non-visible). The magnitude of  $\Delta RF$  should increase away from the base case. We perform this sensitivity study for the six vertical profiles to compile individual statistics on the relationship of  $\Delta RF$  to changes in the optical properties.

Figures 5.2 and 5.3 show the functional dependence of  $\Delta RF_{\text{toa}}$  and  $\Delta RF_{\text{boa}}$  on variations in the aerosol optical properties at visible and non-visible wavelengths. The values in the figures are expressed as percentages, and because the values are nearly symmetric about zero, we show the *absolute values* of the percent changes in the parameters. The values on the x-axes correspond to a percentage change away from the input value, such that 0% is the base case input. The values on the y-axes are the corresponding percentage change in  $RF_{\text{toa}}$  or  $RF_{\text{boa}}$  due to the percentage change in the particular optical property. For



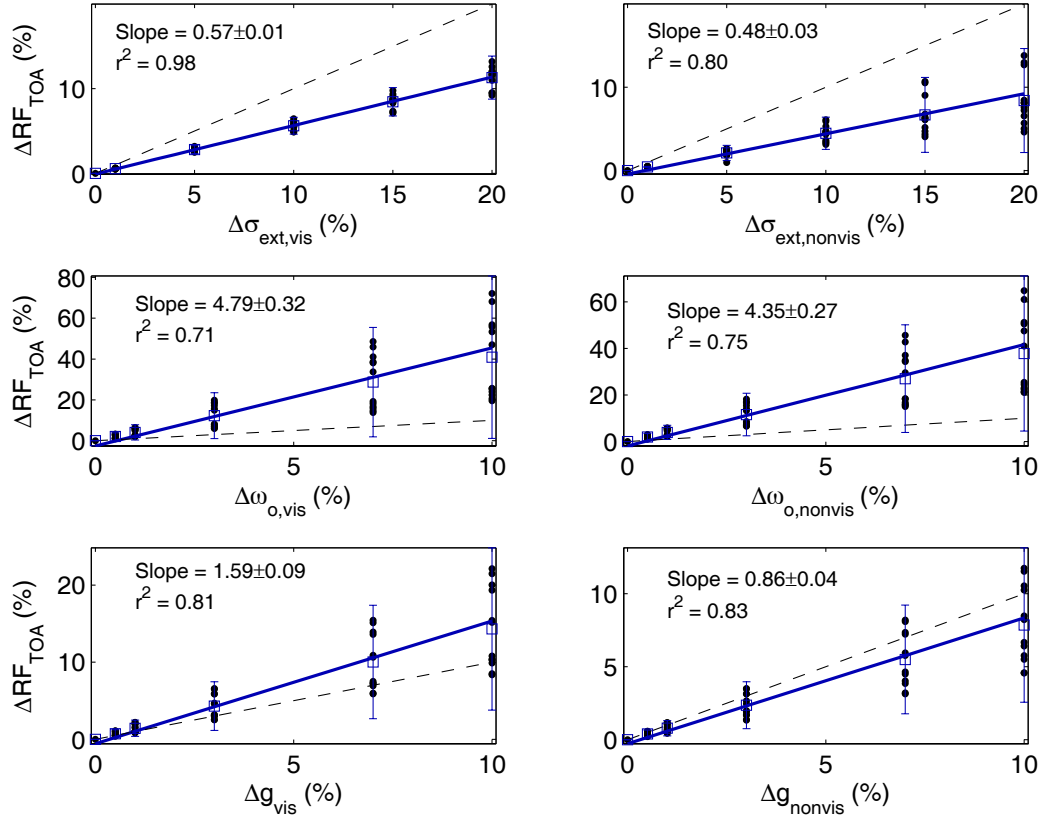


Fig. 5.2. The effects of changes in aerosol optical properties ( $\Delta \sigma_{ext}$ ,  $\Delta \omega_o$ ,  $\Delta g$ ) on the estimates of radiative forcing (RF) at the top of the atmosphere ( $RF_{toa}$ ). The x-axis shows the variation from the base case for the particular aerosol optical property, while the y-axis shows the percent change in  $RF_{toa}$  ( $\Delta RF_{toa}$ ) as a function of the percent change in the aerosol optical properties. The left column shows  $\Delta RF_{toa}$  as a function of changes in visible wavelength (subscript "vis") aerosol optical properties, while the right column shows  $\Delta RF_{toa}$  as a function of changes in non-visible (subscript "nonvis") wavelength aerosol optical properties. The thin dashed black line is the one-to-one line. The solid blue line is the regression to the mean values denoted by the blue squares (error bars are the 95% confidence intervals about the mean values). The black points are the values of  $\Delta RF_{toa}$  for the changes in the aerosol optical properties of the individual vertical profiles.

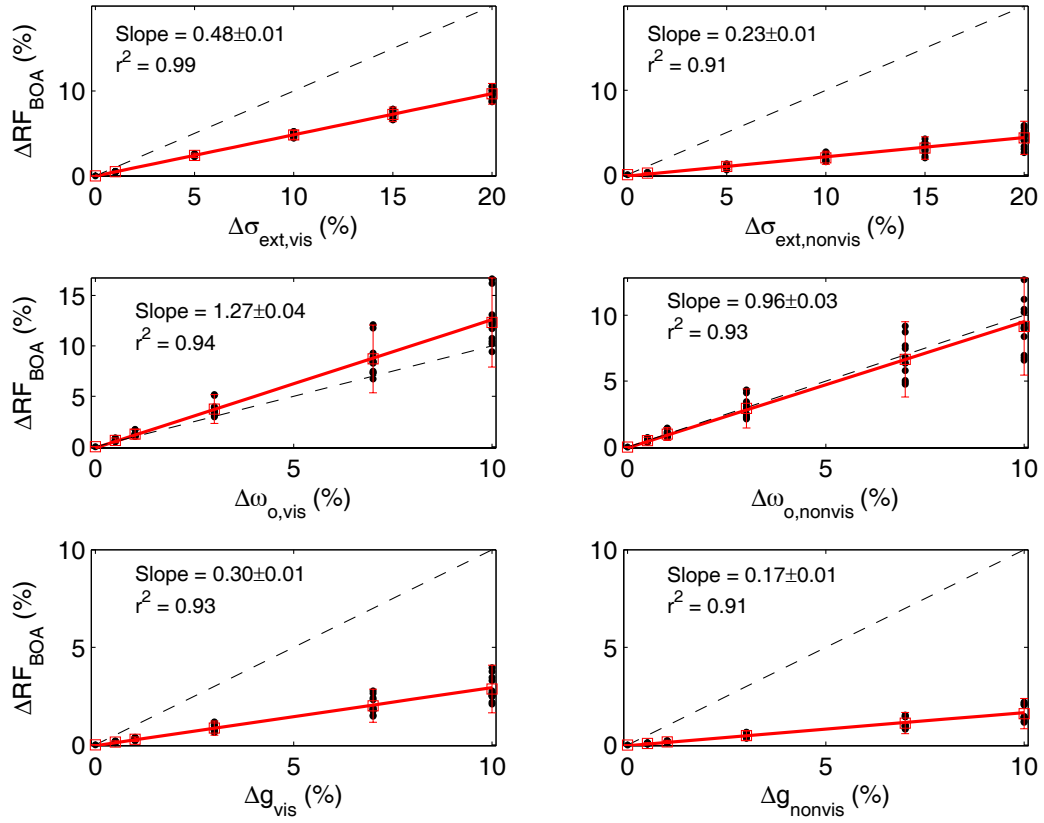


Fig. 5.3. As per Fig. 5.2, but now we plot the effects of changes in aerosol optical properties ( $\Delta \sigma_{ext}$ ,  $\Delta \omega_o$ ,  $\Delta g$ ) on the estimates of radiative forcing (RF) at the surface, or bottom of the atmosphere ( $RF_{boa}$ ). The solid red line is the regression to the mean values denoted by the red squares (error bars are the 95% confidence intervals about the mean values).

example, referring to Fig. 5.2, we can read the top left sub-plot as “A  $\pm 10\%$  change in visible wavelength extinction results in about a  $\pm 5\%$  change in radiative forcing at the top of the atmosphere.”

The specific linear regression coefficients of  $\Delta RF_{toa}$  or  $\Delta RF_{boa}$  versus the changes in the optical properties are listed in Table 5.2. The mean values of the linear regression coefficients listed in the last row are the coefficients used to produce the solid blue and red curves in Figs. 5.2-5.3. The smaller correlation coefficients for the mean case imply that the linear relationship breaks down if we vary from different base cases, but the flight specific correlation coefficients are usually very close to unity. The linear regression to the mean values is mainly for illustration purposes.

From Table 5.2 and Figs. 5.2-5.3, it is clear that RF is most sensitive to changes in both visible and non-visible values of  $\omega_o$  ( $\omega_{o,vis}$  and  $\omega_{o,nonvis}$ ). This has been pointed out in numerous studies [e.g. *Redemann et al.*, 2000b; *Russell et al.*, 2002; *Abel et al.*, 2005], but in addition to quantifying the effects, the slopes of the regressions listed in Figs. 5.2-5.3 show that there is a strong and *nearly equal* sensitivity of total shortwave RF to  $\omega_{o,vis}$  and  $\omega_{o,nonvis}$ . The sensitivity to  $\omega_{o,vis}$  applies to a more limited wavelength range, but also corresponds to the peak in incoming solar radiation. Roughly, the slopes imply that a 1% change in  $\omega_{o,vis}$  or  $\omega_{o,nonvis}$  results in  $\sim 4\text{-}5\%$  change in  $RF_{toa}$  and  $\sim 1\%$  change in  $RF_{boa}$ . For comparison, a 1% change in  $g_{vis}$  or  $g_{nonvis}$  results in  $\sim 0.9\text{-}1.6\%$  change in  $RF_{toa}$  and  $\sim 0.2\text{-}0.3\%$  change in  $RF_{boa}$ , a factor of 3-6 times less than the sensitivity of RF to

Table 5.2. The linear regression statistics (slope and correlation coefficient,  $r^2$ ) obtained from the relationship of a change in radiative forcing ( $\Delta RF$ ) at the top of the atmosphere ( $\Delta RF_{\text{toa}}$ ) and surface, or bottom of the atmosphere ( $\Delta RF_{\text{boa}}$ ), to a change in the extinction coefficient ( $\Delta \sigma_{\text{ext}}$ ), single scattering albedo ( $\Delta \omega_o$ ), or asymmetry parameter ( $\Delta g$ ) for either visible (vis) wavelengths ( $\lambda = 400\text{-}700$  nm) or non-visible (nonvis) wavelengths ( $\lambda = 354\text{-}400$  nm and  $\lambda = 700\text{-}1557$  nm). The regression to the mean values of  $\Delta RF_{\text{toa}}$  and  $\Delta RF_{\text{boa}}$  as functions of changes in the optical properties are listed in the last rows and correspond to the thick blue and red lines plotted in Figs. 5.2 and 5.3, respectively. The intercepts of the regressions are not listed since they are always close to zero. On average, the intercepts for the  $\Delta RF$  as a function of  $\Delta \sigma_{\text{ext}}$ ,  $\Delta \omega_o$ , and  $\Delta g$  are 0.5%, 0.09%, and 0.04% of the slopes, respectively.

ID	Date (2000)	$\lambda$ range	$\Delta\sigma_{\text{ext}}$			$\Delta\omega_0$		$\Delta g$	
			slope	$r^2$	slope	$r^2$	slope	$r^2$	
1	22-Aug	TOA	vis	$0.606 \pm 0.012$	0.997	$2.580 \pm 0.032$	0.999	$1.013 \pm 0.010$	0.999
			nonvis	$0.393 \pm 0.014$	0.989	$2.503 \pm 0.038$	0.998	$0.563 \pm 0.006$	0.999
		BOA	vis	$0.515 \pm 0.005$	0.999	$1.655 \pm 0.018$	0.999	$0.386 \pm 0.005$	0.999
			nonvis	$0.227 \pm 0.013$	0.973	$1.203 \pm 0.038$	0.991	$0.214 \pm 0.003$	0.999
2	24-Aug	TOA	vis	$0.531 \pm 0.025$	0.980	$5.175 \pm 0.191$	0.988	$1.531 \pm 0.008$	1.000
			nonvis	$0.541 \pm 0.089$	0.771	$4.622 \pm 0.210$	0.981	$0.835 \pm 0.008$	0.999
		BOA	vis	$0.471 \pm 0.009$	0.996	$1.012 \pm 0.028$	0.993	$0.214 \pm 0.002$	0.999
			nonvis	$0.221 \pm 0.022$	0.911	$0.758 \pm 0.040$	0.975	$0.119 \pm 0.001$	0.999
3	31-Aug	TOA	vis	$0.571 \pm 0.009$	0.998	$2.015 \pm 0.027$	0.998	$1.057 \pm 0.010$	0.999
			nonvis	$0.418 \pm 0.010$	0.995	$2.129 \pm 0.020$	0.999	$0.652 \pm 0.006$	0.999
		BOA	vis	$0.481 \pm 0.004$	0.999	$1.289 \pm 0.012$	0.999	$0.338 \pm 0.004$	0.999
			nonvis	$0.284 \pm 0.008$	0.992	$1.039 \pm 0.014$	0.998	$0.211 \pm 0.002$	0.999
4	3-Sep	TOA	vis	$0.632 \pm 0.014$	0.996	$2.323 \pm 0.036$	0.998	$0.845 \pm 0.003$	1.000
			nonvis	$0.354 \pm 0.019$	0.974	$2.280 \pm 0.025$	0.999	$0.457 \pm 0.002$	1.000
		BOA	vis	$0.514 \pm 0.005$	0.999	$1.192 \pm 0.009$	0.999	$0.252 \pm 0.001$	1.000
			nonvis	$0.226 \pm 0.013$	0.970	$0.924 \pm 0.014$	0.998	$0.140 \pm 0.001$	1.000
5	6-Sep	TOA	vis	$0.531 \pm 0.029$	0.973	$6.148 \pm 0.320$	0.976	$1.969 \pm 0.014$	1.000
			nonvis	$0.595 \pm 0.118$	0.673	$5.532 \pm 0.310$	0.972	$1.040 \pm 0.006$	1.000
		BOA	vis	$0.461 \pm 0.011$	0.995	$1.133 \pm 0.046$	0.985	$0.257 \pm 0.003$	0.999
			nonvis	$0.191 \pm 0.024$	0.863	$0.815 \pm 0.054$	0.961	$0.138 \pm 0.002$	0.999
6	6-Sep	TOA	vis	$0.545 \pm 0.029$	0.975	$6.516 \pm 0.330$	0.977	$2.182 \pm 0.014$	1.000
			nonvis	$0.568 \pm 0.116$	0.656	$5.908 \pm 0.312$	0.975	$1.163 \pm 0.004$	1.000
		BOA	vis	$0.458 \pm 0.010$	0.996	$1.148 \pm 0.042$	0.988	$0.270 \pm 0.003$	0.999
			nonvis	$0.200 \pm 0.021$	0.901	$0.816 \pm 0.047$	0.970	$0.145 \pm 0.001$	0.999
all	mean	TOA	VIS	$0.572 \pm 0.010$	0.977	$4.793 \pm 0.323$	0.711	$1.591 \pm 0.086$	0.807
			nonVIS	$0.482 \pm 0.027$	0.799	$4.350 \pm 0.272$	0.748	$0.861 \pm 0.043$	0.832
		BOA	VIS	$0.485 \pm 0.005$	0.992	$1.272 \pm 0.037$	0.943	$0.297 \pm 0.010$	0.926
			nonVIS	$0.228 \pm 0.008$	0.909	$0.956 \pm 0.032$	0.925	$0.169 \pm 0.006$	0.906

an equivalent percentage change in  $\omega_o$ . The small effect of  $g$  at non-visible wavelengths on RF has been suggested by other studies as well [*Pilewskie et al.*, 2003; *Zhou et al.*, 2005]. Percent changes in  $\sigma_{\text{ext}}$  result in the smallest percent changes in  $\text{RF}_{\text{toa}}$  and  $\text{RF}_{\text{boa}}$ , but then uncertainty in  $\sigma_{\text{ext}}$  is generally on the order of 8-10% compared to 3-4% for  $\omega_o$ .

To determine the case-by-case effects of the uncertainty in aerosol optical properties on RF, we calculate the ratio of the uncertainty in the aerosol optical properties to the value of the aerosol optical properties. The ratios are calculated by propagating the total absolute uncertainty in each aerosol optical property (described in Chapter 3 and used as constraints in Chapter 4) together with the structural errors of the retrieval we used to compile the optical properties (Section 4.4.2). As an example, the uncertainty in  $\sigma_{\text{ext}}$  due to measurement error or instrument noise ( $\delta\sigma_{\text{ext, meas}}$ ) is propagated together with the structural uncertainty in retrieved values of  $\sigma_{\text{ext}}$  ( $\delta\sigma_{\text{ext, lut}} = \pm 0.041 * \sigma_{\text{ext}}$ , per Section 4.4.2) as

$$\delta\sigma_{\text{ext}}^2 = \delta\sigma_{\text{ext, meas}}^2 + \delta\sigma_{\text{ext, lut}}^2 \quad (5.3)$$

and this is done in a similar manner for  $\omega_o$  and  $g$ . We find the average uncertainty for each profile, cross-reference this with the case specific linear regressions in Table 5.2, and arrive at an estimate of the effect of uncertainty in an optical property on RF. A rough estimate of this would be to determine the percent error in extinction measurements (~8%, say) and read the corresponding location on the y-axis on Fig. 5.2 or 5.3.

The fully processed values of the uncertainty in RF due to uncertainty in  $\sigma_{\text{ext}}$ ,  $\omega_o$ , or  $g$  ( $\delta\text{RF}_{\text{ext}}$ ,  $\delta\text{RF}_{\text{ssa}}$ ,  $\delta\text{RF}_{\text{asy}}$ , respectively) are listed in Table 5.3 for visible and non-visible wavelengths. However, since much of the determination of  $\delta\text{RF}_{\text{ssa}}$  at non-visible wavelengths is dependent on the choice of constraint used in the retrieval, we treat this uncertainty slightly differently in the next Section.

#### 5.4.2. Uncertainty Related to Non-measured Aerosol Optical Properties

Many aerosol optical properties are not based on a direct measurement and therefore, the measurement uncertainty in Eq. 5.3 ( $\delta\sigma_{\text{ext, meas}}$ , in the example) is set to zero. The errors in the values of  $\omega_{o, \text{nonvis}}$ ,  $g_{\text{vis}}$ , and  $g_{\text{nonvis}}$  ( $\delta\omega_{o, \text{nonvis}}$ ,  $\delta g_{\text{vis}}$ , and  $\delta g_{\text{nonvis}}$ , respectively) have no measurement uncertainty. The values of  $\delta\text{RF}_{\text{asy}}$  for visible and non-visible wavelengths presented in Table 5.3 are then strictly determined from uncertainty in  $g$  that arises from the retrieval discussed in Section 4.4.2 ( $\pm 3.8\%$  of the retrieved value of  $g$ ).

Recalling the discussion in Section 4.3.2, uncertainty in  $\omega_{o, \text{nonvis}}$  is assessed by re-running the aerosol optical property retrieval described in Chapter 4 with different constraints on  $\omega_{o, \text{nonvis}}$ , then using this new retrieval as input to the RTM to calculate the RF. Our base case in this sensitivity test is the  $\omega_{o, \text{nonvis}}$  constraint based on a combination of “urban” and “soot” aerosols described in *d’Almeida et al.* [1991] and also in *Hess et al.* [1998]. We compile other cases in this sensitivity test by using six other constraints on  $\omega_{o, \text{nonvis}}$ . Namely, we linearly

Table 5.3. The summary of the radiative forcing (RF) uncertainty ( $\delta\text{RF}$ ) at the top of the atmosphere (TOA) and the surface, or bottom of the atmosphere (BOA), due to uncertainty in extinction ( $\delta\text{RF}_{\text{ext}}$ ), single scattering albedo ( $\delta\text{RF}_{\text{ssa}}$ ), asymmetry parameter ( $\delta\text{RF}_{\text{asy}}$ ), upper atmospheric aerosol extinction ( $\delta\text{RF}_{\text{ua}}$ ), and surface albedo ( $\delta\text{RF}_{\text{sa}}$ ). The uncertainty is reported as a percent of the  $\text{RF}_{\text{toa}}$  or  $\text{RF}_{\text{boa}}$  for each of the six vertical profiles examined and  $\delta\text{RF}$  due to uncertainty in aerosol optical properties are partitioned into visible and non-visible wavelengths, like Table 5.2. The last column is an absolute uncertainty ( $\text{W m}^{-2}$ ) in the flux calculations by the Fu-Liou radiative transfer model and also contributes to the overall uncertainty in RF by a value of  $\delta\text{RF}_{\text{flrt}}$ .

ID	Date (2000)		visible wavelengths			non-visible wavelengths			$\delta\text{RF}_{\text{ua}}$ (%)	$\delta\text{RF}_{\text{sa}}$ (%)	$\delta\text{RF}_{\text{flrt}}$ ( $\text{W m}^{-2}$ )
			$\delta\text{RF}_{\text{ext}}$ (%)	$\delta\text{RF}_{\text{ssa}}$ (%)	$\delta\text{RF}_{\text{asy}}$ (%)	$\delta\text{RF}_{\text{ext}}$ (%)	$\delta\text{RF}_{\text{ssa}}$ (%)	$\delta\text{RF}_{\text{asy}}$ (%)			
1	22-Aug	TOA	4.7	9.1	3.8	6.4	13.8	2.1	6.3	10	2
		BOA	4.0	5.8	1.5	3.2	3.5	0.8	2.4	3	2
2	24-Aug	TOA	4.9	11.3	4.0	6.7	11.9	2.5	9.3	15	2
		BOA	4.1	7.2	1.3	4.3	4.5	0.8	2.8	3	2
3	31-Aug	TOA	5.5	14.8	3.2	5.7	11.7	1.7	6.5	12	2
		BOA	4.5	7.6	1.0	3.4	2.8	0.5	1.9	3	2
4	3-Sep	TOA	4.2	31.1	5.8	7.5	23.0	3.2	8.5	20	2
		BOA	3.7	6.1	0.8	3.4	2.5	0.4	1.1	2	2
5	6-Sep	TOA	4.5	34.9	7.5	8.2	30.6	4.0	6.8	22	2
		BOA	4.0	6.5	1.0	2.9	2.6	0.5	0.8	2	2
6	6-Sep	TOA	4.9	36.5	8.3	7.8	29.4	4.4	7.1	21	2
		BOA	4.1	6.5	1.0	3.0	2.8	0.5	0.7	3	2

combine the soot with “sulfate”, “continental”, and “soluble” aerosol using the method described in Section 4.3.2 and Eq. 4.15. We use the empirical equation described in *Ross et al.* [1998] as the fifth constraint on  $\omega_{o,nonvis}$  and the data published in *Bergstrom et al.* [2003] for the 6 September 2000 case as the sixth and final constraint on  $\omega_{o,nonvis}$ . As shown in the example in Fig. 4.3, different constraints will result in different behavior of  $\omega_o$  at non-visible wavelengths. We do not use the 24 August 2000 case from *Bergstrom et al.* [2003] since the values of  $\omega_{o,nonvis}$  provided are for a limited wavelength range  $\lambda \sim 350\text{-}900$  nm.

To assess the uncertainty in RF due to uncertainty in the constraint on  $\omega_{o,nonvis}$ , we then calculate RF for each of the different retrieved set of aerosol optical properties, having changed only the constraint on  $\omega_{o,nonvis}$ . Values of  $RF_{toa}$  are  $\pm 10\%$  to as much as  $\pm 30\%$  different than  $RF_{toa}$  calculated using the urban and soot aerosol, while values of  $RF_{boa}$  are about  $\pm 3\%$  different than  $RF_{boa}$  calculated using the urban and soot aerosol, keeping in mind the magnitude of  $RF_{toa}$  compared to  $RF_{boa}$ . The differences are often nearly symmetric since the urban and soot aerosol constraint on  $\omega_{o,nonvis}$  is bracketed by other constraints (Fig. 4.3).

We suggest that half the full range of calculated RF that result from the different constraints is the uncertainty associated with the constraint on  $\omega_{o,nonvis}$ . These values range from 10-30% for  $RF_{toa}$  and 2-5% for  $RF_{boa}$ . The largest percent effect on  $RF_{toa}$  are for vertical profiles with low  $\omega_o$  and high  $\tau$ , which are



generally during the River of Smoke. The percentage effect on  $RF_{\text{boa}}$ , however, has a much smaller range.

The value of  $\delta RF_{\text{ssa}}$  for non-visible wavelengths listed in Table 5.3 is then calculated as the effect of structural uncertainty in  $\omega_o$  on RF ( $\pm 1.2\%$  of the retrieved value of  $\omega_o$ , Section 4.4.2) propagated together with the uncertainty in the constraint on  $\omega_{o,\text{nonvis}}$  on RF. About 90% of the values of  $\delta RF_{\text{ssa}}$  for non-visible wavelengths are due to uncertainty in the constraint on  $\omega_{o,\text{nonvis}}$ . The surprising result is that values of  $\delta RF_{\text{ssa}}$  for visible and non-visible wavelengths are often similar in magnitude, revealing that choosing a constraint on unmeasured values of  $\omega_o$  in models is nearly as important as the values of  $\omega_o$  in the peak of the solar spectrum

#### 5.4.3. Uncertainty Related to Upper Atmospheric Aerosol Optical Properties

The upper atmospheric ( $\sim 500$  hPa to TOA) aerosol extinction ( $\sigma_{\text{ext,ua}}$ ) profiles provided by *Vanhellemont et al.* [2005] include confidence intervals. The base case used to estimate RF is the median (50<sup>th</sup> percentile) value of  $\sigma_{\text{ext,ua}}$ . We calculate RF for  $\sigma_{\text{ext,ua}}$  values from the 10-90<sup>th</sup> percentile range. The response of RF to changes in  $\sigma_{\text{ext,ua}}$  gives a range of RF values. We interpret half the full range of RF to be the uncertainty in RF due to uncertainty in  $\sigma_{\text{ext,ua}}$ , or  $\delta RF_{\text{ua}}$ . These are the values listed in Table 5.3. Since the values of  $\sigma_{\text{ext,ua}}$  are small, we

assume uncertainty in RF due to uncertainties in upper atmospheric values of  $\omega_0$  and  $g$  from *Fenn et al.* [1985] are negligible.

#### 5.4.4. Uncertainty Related to Surface Albedo

Although there is no specific uncertainty attributed to surface albedo ( $A_{s,\lambda}$ ) reported by either *Gatebe et al.* [2003] or *Moody et al.* [2005], it is clear that small scale spatial variations in  $A_{s,\lambda}$  are common. To explore the sensitivity of RF to changes in  $A_{s,\lambda}$ , we calculate RF using different values of  $A_{s,\lambda}$  reported in *Gatebe et al.* [2003] and *Moody et al.* [2005]. For example, *Gatebe et al.* [2003] published multiple values of  $A_{s,\lambda}$  data for a specific location. The values are partly dependent on the consideration of the atmosphere between the aircraft and surface. *Moody et al.* [2005] published MODIS satellite data that are finely resolved in a limited wavelength range, but also published MODIS data for broad wavelength bands. Half the full range of RF calculated from the different choices for  $A_{s,\lambda}$  are reported as the uncertainty in RF due to  $A_{s,\lambda}$  ( $\delta RF_{sa}$ ) and are listed in Table 5.3.

#### 5.5. Biomass Burning Aerosol Radiative Forcing

The best estimates of the measurement-based diurnally-averaged RF and the uncertainty are listed in Table 5.4. Values of  $RF_{toa}$  ranges from -7.1 to -8.9  $W m^{-2}$  and do not depend on whether the vertical profile was obtained during the River of Smoke or while the anticyclonic circulation dominated the area. The

Table 5.4. Measurement-based estimates of southern African biomass burning aerosol radiative forcing (RF) at the top of the atmosphere (TOA) and surface, or bottom of the atmosphere (BOA), and the uncertainty in RF estimates ( $\delta$ RF) for six vertical profiles. We also estimate the RF using available measurements from AERONET ( $RF_{\text{aeronet}}$ ) and estimate the uncertainty ( $\delta RF_{\text{aeronet}}$ ). AERONET comparisons are only available for three cases. The uncertainty is listed as an absolute value and as a percent of the RF. The numerical identifications (IDs) can be cross-referenced with information in Table 4.2. The August vertical profiles were collected during anticyclonic circulation more typical of the region, while the September profiles were collected during the period of enhanced smoke concentrations (the River of Smoke).

ID	Date (2000)		RF ( $W\ m^{-2}$ )	$\delta$ RF (%)	$RF_{\text{aeronet}}$ ( $W\ m^{-2}$ )	$\delta RF_{\text{aeronet}}$ (%)
1	22-Aug	TOA	$-8.6 \pm 2.8$	32	$-6.8 \pm 1.7$	26
		BOA	$-22.9 \pm 3.0$	13	$-23.1 \pm 2.6$	11
2	24-Aug	TOA	$-7.1 \pm 2.7$	38	-	-
		BOA	$-23.2 \pm 3.3$	14	-	-
3	31-Aug	TOA	$-8.4 \pm 2.9$	34	-	-
		BOA	$-29.5 \pm 3.7$	13	-	-
4	3-Sep	TOA	$-7.6 \pm 4.0$	53	$-15.0 \pm 6.3$	42
		BOA	$-57.8 \pm 5.4$	9	$-42.9 \pm 2.9$	7
5	6-Sep	TOA	$-8.9 \pm 5.2$	58	$-10.8 \pm 5.5$	51
		BOA	$-72.7 \pm 6.7$	9	$-72.0 \pm 4.7$	7
6	6-Sep	TOA	$-8.5 \pm 5.0$	58	-	-
		BOA	$-73.0 \pm 7.1$	10	-	-

uncertainty of  $RF_{\text{toa}}$  ( $\delta RF_{\text{toa}}$ ) ranges from 32-58%. The largest values of  $\delta RF_{\text{toa}}$  are due to the enhanced concentrations of absorbing particles (i.e. lower values of  $\omega_{o,\lambda}$ ) during the River of Smoke. The uncertainty increases as a result of greater uncertainty that originates from the PSAP measurements of the absorption coefficient, but as shown in Table 5.3, a large and nearly equivalent fraction of the uncertainty is due to uncertainty in the constraint on  $\omega_{o,\text{nonvis}}$ , as discussed in Section 5.4.2.

Values of  $RF_{\text{boa}}$  ranges from -22.9 to -73.0  $\text{W m}^{-2}$  and exhibit a strong dependency on the time period of sampling. Vertical profiles during the River of Smoke resulted in the largest values of  $RF_{\text{boa}}$  when  $\omega_{o,550}$  decreased by ~6% and  $\sigma_{\text{ext},550}$  increased by a factor of more than two (Table 3.8). The uncertainty of  $RF_{\text{boa}}$  ( $\delta RF_{\text{boa}}$ ) ranges from 9-14%.

For comparison, we estimate RF from retrieved and measured AERONET aerosol optical properties ( $RF_{\text{aeronet}}$ ) and list the values in Table 5.4. Three of the six vertical profiles in Table 5.4 were spatially and temporally co-located with AERONET stations in southern Africa [Eck *et al.*, 2003]. Leahy [2006] showed that AERONET retrievals matched closely with the UW research aircraft vertical profiles most of time, although both Magi and Hobbs [2004] and Leahy [2006] also show cases when the independent data sets did not agree.

We estimate  $RF_{\text{aeronet}}$  by assuming the column-integrated AERONET optical properties apply to the layer between the surface and 500 hPa, similar to the UW research aircraft vertical profiles. There is no additional retrieval

associated with AERONET measurements (i.e. we do not use the analysis in Chapter 4). Instead, we simply extrapolate the AERONET measurements to the solar spectrum using the same methods we used to extrapolate the in situ and Sunphotometer data (Section 5.2.1). Otherwise, we use exactly the same input to the RTM to calculate  $RF_{\text{aeronet}}$ .

The uncertainty in  $RF_{\text{aeronet}}$  ( $\delta RF_{\text{aeronet}}$ ) is estimated using the exact same methodology we used to estimate the uncertainty in  $RF$  from aircraft-based measurements. Uncertainties in  $\tau_\lambda$ ,  $\omega_{o,\lambda}$ , and  $g_\lambda$  from AERONET are estimated as  $\pm 0.02$ ,  $\pm 0.03$ , and  $\pm 0.04$ , respectively [Dubovik *et al.*, 2002; Zhou *et al.*, 2005]. We propagate these errors to arrive at the values of  $\delta RF_{\text{aeronet}}$  listed in Table 5.4.

Although the sample size is limited to three direct comparisons, the 22 August and 6 September cases compare well and are within the uncertainties associated with the  $RF$ . The 3 September case does not compare well. The difference is primarily associated with a difference in  $\omega_{o,\lambda}$  between AERONET and aircraft measurements [Magi and Hobbs, 2004; Leahy, 2006]. However, the fact that the column-integrated aerosol optical properties measured and retrieved by AERONET can so closely reproduce a much more detailed method is promising for more extensive applications of AERONET data in models [Chung *et al.*, 2005; Reddy *et al.*, 2005a] and in measurement-based calculations of aerosol radiative effects [Kaufman *et al.*, 2002; Zhou *et al.*, 2005; Yu *et al.*, 2006]. However, careful validation of AERONET retrieved products (especially  $\omega_{o,\lambda}$ ) is absolutely crucial to the calculations.

Other studies have published estimates of RF for the southern African region as well and a comparison of the results is presented here. *Ichoku et al.* [2003] estimated  $RF_{toa}$  from MODIS satellite measurements as  $-10 \text{ W m}^{-2}$  and  $RF_{boa}$  of  $-26 \text{ W m}^{-2}$  over the entire southern African region. *Keil and Haywood* [2003] used in situ data collected in Namibia [*Haywood et al.*, 2003a] during SAFARI-2000 and estimated  $RF_{toa}$  ranges from  $-12$  to  $-14 \text{ W m}^{-2}$  and  $RF_{boa}$  ranges from  $-22$  to  $-28 \text{ W m}^{-2}$ , keeping in mind that smoke aerosols in Namibia are most likely transported from other regions of southern Africa [*Haywood et al.*, 2003b]. Most recently, a regional modeling study by *Abel et al.* [2005], which built on studies by *Myhre et al.* [2003] and *Osborne et al.* [2004], *Keil and Haywood* [2003], and *Haywood et al.* [2003a-b], suggested  $RF_{toa}$  ranges from about  $-7$  to  $-9 \text{ W m}^{-2}$  and  $RF_{boa}$  ranges from  $-32$  to  $-35 \text{ W m}^{-2}$  for the southern African region. The values of  $RF_{toa}$  compare well with the values in Table 5.4 (both measurements and AERONET), but  $RF_{boa}$  is underestimated by a factor of two or more in southern tropical Africa by the *Abel et al.* [2005] study.

This work suggests that the differences in the aerosol optical properties measured the River of Smoke and during the anticyclonic circulation are not properly considered in models of southern African biomass burning. *Kinne et al.* [2003, 2005] discuss the median model treatment of aerosols from source regions around the world and showed that the models noticeably underestimate  $\tau$  for months most affected by biomass burning. The working hypothesis presented here is that southern African biomass burning aerosol should be treated as two distinct

aerosol with different optical properties. The result of the differences are similar values of  $RF_{\text{boa}}$ , but values of  $RF_{\text{boa}}$  that vary by a factor of two or more. Measurements in tropical Africa would be very useful.

## Chapter 6. Summary

In this thesis, we provided a detailed analysis of biomass burning aerosol optical properties in southern Africa. Combining measurements of optical properties with an original retrieval algorithm, we derived aerosol optical properties for the entire shortwave spectrum and used this information to model the radiative effects of the aerosol of southern Africa. Here we summarize the main conclusions of the study and offer a few recommendations for future work.

### 6.1. Southern African Aerosol Characteristics

We analyzed data collected during SAFARI-2000 [*Swap et al.*, 2003] and showed that southern African aerosols are dominated by absorbing aerosols from biomass burning [*Eck et al.*, 2003; *Kirchstetter et al.*, 2003] that occurs every year during the dry season [*Anyamba et al.*, 2003] to varying degrees [*Duncan et al.*, 2003].

Typically, southern African wintertime (dry season) meteorology is dominated by large scale subsidence due to a persistent anticyclonic circulation [*Cosijn and Tyson*, 1996]. During SAFARI-2000, a westerly disturbance created what qualitatively appeared to be a river and was dubbed the River of Smoke by *Annegarn et al.* [2002]. The River of Smoke transported smoke over the period of 1-3 days from regions of biomass burning in tropical southern Africa to the sample region of SAFARI-2000. Compared to the period dominated by



anticyclonic circulation, the mean extinction coefficient at a wavelength of 550 nm ( $\sigma_{\text{ext},550}$ ) measured during the River of Smoke increased from  $86 \pm 44 \text{ Mm}^{-1}$  to  $200 \pm 50 \text{ Mm}^{-1}$ . The single scattering albedo at 550 nm ( $\omega_{0,550}$ ) decreased from  $0.89 \pm 0.05$  to  $0.83 \pm 0.02$ . We attributed these changes in the mean optical properties to an increase in the aerosol number concentration driven primarily by the enhanced presence of absorbing particles originating from tropical biomass burning. The mean size of the aerosol did not change dramatically.

## 6.2. Southern African Radiative Forcing

We estimated the radiative forcing in southern Africa by using measurements to constrain an original retrieval algorithm that finds the optically-equivalent aerosol size distribution and wavelength-dependent refractive index that most accurately reproduce the available measurements. Using this set of optical properties, we estimated the radiative forcing (RF) at the top of the atmosphere ( $\text{RF}_{\text{toa}}$ ) and surface, or bottom of the atmosphere ( $\text{RF}_{\text{boa}}$ ) due to the southern African biomass burning aerosol (Table 5.4).

Estimates of  $\text{RF}_{\text{toa}}$  ranged from  $-7.1 \pm 2.7 \text{ W m}^{-2}$  to  $-8.9 \pm 5.2 \text{ W m}^{-2}$ , in good agreement with previously published regional modeling studies [e.g. *Abel et al.*, 2005]. In contrast,  $\text{RF}_{\text{boa}}$  varied from  $-22.9 \pm 3.0 \text{ W m}^{-2}$  to  $-73.0 \pm 7.1 \text{ W m}^{-2}$ . Uncertainty in  $\omega_{0,\lambda}$  accounted for 40-77% (mean of about 60%) of the total uncertainty in RF.

The  $RF_{\text{boa}}$  during the enhanced smoke concentrations of the River of Smoke period was a factor of 2-3 greater in magnitude than  $RF_{\text{boa}}$  during the more typical anticyclonic circulation. We attribute the differences to the increase in  $\sigma_{\text{ext},\lambda}$  and decrease in  $\omega_{\text{o},\lambda}$  during the River of Smoke. The aerosol during the River of Smoke was composed of effective scatterers and absorbers.

### 6.3. Implications for Modeling Southern African Aerosol

Past modeling studies have not attempted to model the aerosol in tropical Africa as more absorbing, but the River of Smoke, combined with the trajectory analysis implies that these aerosol optical properties may be representative of the tropical African region. In the most recent regional modeling study from southern Africa [Abel *et al.*, 2005], no regional dependence is applied to  $\omega_{\text{o},\lambda}$ . Although the effects of a decrease in  $\omega_{\text{o},\lambda}$  are smaller at the TOA, the surface RF reported here is markedly larger than the regionally averaged values presented in Abel *et al.* [2005]. This study, as well as Eck *et al.* [2003] and Leahy [2006] all suggest that there is a regional dependence for  $\omega_{\text{o},\lambda}$ . Given the sensitivity of RF to  $\omega_{\text{o},\lambda}$ , this is an important oversight.

### 6.4. Recommendations for Future Work

We have estimated RF and the uncertainty from six vertical profiles using a measurement-based approach. Application of the methods to other field campaigns with similar datasets [Christopher *et al.*, 2000; Clarke *et al.*, 2002;

*Doherty et al.*, 2005; *Quinn et al.*, 2005] would provide useful and comparable information. The methodology itself could be improved by increasing the resolution of the dimensions of the look-up table used in the retrieval to minimize structural uncertainties in the retrieved optical properties. Another improvement would be to include diurnal variability in the aerosol optical properties. The very basic suggestion presented here, however, is that the RF calculations are extremely sensitive to  $\omega_{o,\lambda}$  and without measurements beyond the visible wavelengths, uncertainty in RF due to aerosol [*Schwartz*, 2004] will remain large and unacceptable.

## REFERENCES

- Abel, S. J., E. J. Highwood, J. M. Haywood, and M. A. Stringer, The direct radiative effects of biomass burning aerosols over southern Africa, *Atmos. Chem. Phys.*, 5, 1999-2018, 2005.
- Ackerman, A. S., O. B. Toon, D. E. Stevens, A. J. Heymsfield, V. Ramanathan, and E. J. Welton, Reduction of tropical cloudiness by soot, *Science*, 288, 1042-1047, 2000.
- Ackerman, T. P., A. J. Braverman, D. J. Diner, T. L. Anderson, R. A. Kahn, J. V. Martonchik, J. E. Penner, P. J. Rasch, B. A. Wielicki, and B. Yu, Integrating and Interpreting Aerosol Observations and Models within the PARAGON Framework, *Bull. Amer. Meteor. Soc.*, 85, 1523-1533, 2004.
- Ackerman, T. P. and O. B. Toon, Absorption of visible radiation in atmosphere containing mixtures of absorbing and nonabsorbing particles, *Appl. Opt.*, 20, No. 20, 3661-3668, 1981.
- Ahlquist, N. C. and R. J. Charlson, Measurement of the Vertical and Horizontal Profile of Aerosol Concentration in Urban Air with the Integrating Nephelometer, *Envir. Sci. and Tech.*, 2, No. 5, 363-366, 1968.
- Anderson, T. L., D. S. Covert, S. F. Marshall, M. L. Laucks, R. J. Charlson, A. P. Waggoner, J. A. Ogren, R. Caldow, R. L. Holm, F. R. Quant, G. J. Sem, A. Wiedensohler, N. A. Ahlquist, and T. S. Bates, Performance Characteristics of a High-Sensitivity, Three-Wavelength Total Scatter/Backscatter Nephelometer, *J. Atmos. Ocean. Tech.*, 13, 967-986, 1996.
- Anderson, T. L., and J. A. Ogren, Determining aerosol radiative properties using the TSI 3563 integrating nephelometer, *Aerosol Sci. Tech.*, 29, 57-69, 1998.
- Anderson, T. L., D. S. Covert, J. D. Wheeler, J. M. Harris, K. D. Perry, B. E. Trost, D. J. Jaffe, and J. A. Ogren, Aerosol backscatter fraction and single scattering albedo: Measured values and uncertainties at a coastal station in the Pacific Northwest, *J. Geophys. Res.*, 104, No. D21, 26793-26807, 1999.
- Anderson, T. L., S. J. Masonis, D. S. Covert, R. J. Charlson, and M. J. Rood, In situ measurement of the aerosol extinction-to-backscatter ratio at a polluted continental site, *J. Geophys. Res.*, 105, No. D22, 26907-26915, 2000.
- Anderson, T. L., R. J. Charlson, S. E. Schwartz, R. Knutti, O. Boucher, H. Rodhe, J. Heintzenberg, Climate Forcing by Aerosols – a Hazy Picture, *Science*, 300, 1103-1104, 2003a.

- Anderson, T. L., R. J. Charlson, D. M. Winker, J. A. Ogren, and K. Holmen, Mesoscale Variations of Tropospheric Aerosols, *J. Atmos. Sci.*, *60*, 119-136, 2003b.
- Anderson, T. L., S. J. Masonis, D. S. Covert, N. C. Ahlquist, S. G. Howell, A. D. Clarke, and C. S. McNaughton, Variability of aerosol optical properties derived from in situ aircraft measurements during ACE-Asia, *J. Geophys. Res.*, *108*, No. D23, doi:10.1029/2002JD003247, 2003c.
- Anderson, T. L., et al., An “A-Train” Strategy for Quantifying Direct Climate Forcing by Anthropogenic Aerosols, *Bull. Amer. Meteor. Soc.*, *85*, 1795-1809, 2005.
- Andreae M. O., C. D. Jones, and P. M. Cox, Strong present-day aerosol cooling implies a hot future, *Nature*, *435*, 1187-1190, 2005.
- Annegarn, H. J., L. Otter, R. J. Swap, and R. J. Scholes, Southern Africa’s ecosystem in a test-tube, *S. Afr. J. Sci.*, *98*, 111-113, 2002.
- Anyamba, A., C. J. Tucker, and R. Mahoney, From El Nino to La Nina: Vegetation Response Patterns over East and Southern Africa during the 1997-2000 Period, *J. Clim.*, *15*, 3096-3103, 2002.
- Anyamba, A., C. O. Justice, C. J. Tucker, and R. Mahoney, Seasonal to interannual variability of vegetation and fires at SAFARI 2000 sites inferred from advanced very high resolution radiometer times series data, *J. Geophys. Res.*, *108*, D13, 8507, doi:10.1029/2002JD002464, 2003.
- Appenzeller, T., The Case of the Missing Carbon, *Nat. Geog.*, *205*, No. 2, 88-117, 2004.
- Appenzeller, T. and D. R. Dimick, The Heat Is On, *Nat. Geog.*, *206*, No. 3, 2-11, 2004.
- Appenzeller, T., The Coal Paradox, *Nat. Geog.*, *209*, No. 3, 96-103, 2006.
- Becker, J., China’s Growing Pains, *Nat. Geog.*, *205*, No. 3, 68-95, 2004.
- Bergstrom, R. W., P. Pilewskie, B. Schmid, and P. B. Russell, Estimates of the spectral aerosol single scattering albedo and aerosol radiative effects during SAFARI 2000, *J. Geophys. Res.*, *108*, doi:10.1029/2002JD002435, 2003.
- Bergstrom, R. W., P. Pilewskie, J. Pommier, M. Rabbette, P. B. Russell, B. Schmid, J. Redemann, A. Higurashi, T. Nakajima, and P. K. Quinn, Spectral absorption of solar radiation by aerosols during ACE-Asia, *J. Geophys. Res.*, *109*, doi:10.1029/2003JD004467, 2004.
- Bertschi, I. T., R. J. Yokelson, D. E. Ward, T. J. Christian, and W. M. Hao, Trace gas emissions from the production and use of domestic biofuels in Zambia

- measured by open-path Fourier transform infrared spectroscopy, *J. Geophys. Res.*, *108*, D13, 8469, doi:10.1029/2002JD002158, 2003.
- Bevington, P. R., and D. K. Robinson, *Data Reduction and Error Analysis for the Physical Sciences*, 2<sup>nd</sup> Ed., McGraw-Hill, New York, 1992.
- Bohren, C. F., and D. R. Huffman, *Absorption and Scattering of Light by Small Particles*, Wiley, New York, 530 pp, 1983.
- Bond, T. C., T. L. Anderson, and D. Campbell, Calibration and intercomparison of filter-based measurements of visible light absorption by aerosols, *Aerosol Sci. Technol.*, *30*, 582-600, 1999.
- Bond, T. C., Spectral dependence of visible light absorption by carbonaceous particles emitted from coal combustion, *Geophys. Res. Lett.*, *28*, No. 21, 4075-4078, 2001.
- Bond, T. C., D. G. Streets, K. F. Yarber, S. M. Nelson, J. Woo, and Z. Klimont, A technology-based global inventory of black and organic carbon emissions from combustion, *J. Geophys. Res.*, *109*, D14203, doi:10.1029/2003JD003697, 2004.
- Bond, W. J., F. I. Woodward, and G. F. Midgley, The global distribution of ecosystems in a world without fire, *New Phytologist*, *165*, 525-538, 2005.
- Boucher, O., On Aerosol Direct Shortwave Forcing and the Henyey-Greenstein Phase Function, *J. Atmos. Sci.*, *55*, 128-134, 1998.
- Buettel, R. G., and A. W. Brewer, Instruments for measurement of the visual range, *J. Sci. Instrum.*, *26*, 357-359, 1949.
- Bush, B. C., and F. P. J. Valero, Spectral aerosol radiative forcing at the surface during the Indian Ocean Experiment (INDOEX), *J. Geophys. Res.*, *107*, D19, doi:10.1029/2000JD000020, 2002.
- Carrico, C. M., P. Kus, M. J. Rood, P. K. Quinn, and T. S. Bates, Mixtures of pollution, dust, sea-salt, and volcanic aerosol during ACE-Asia: Radiative properties as a function of relative humidity, *J. Geophys. Res.*, *108*, No. D23, doi:10.1029/2003JD003405, 2003.
- Carroll, C., Hurricane Warning, *Nat. Geog.*, 72-85, *208*, No. 2, 2005.
- Chan, M. N., M. Y. Choi, N. L. Ng, and C. K. Chan, Hygroscopicity of Water-Soluble Organic Compounds in Atmospheric Aerosols: Amino Acids and Biomass Burning Derived Organic Species, *Environ. Sci. Technol.*, *39*, 1555-1562, 2005.
- Charlson, R. J., H. Horvath, and R. Pueschel, The direct measurement of atmospheric light scattering coefficient for studies of visibility and pollution, *Atmos. Environ.*, *1*, 469-478, 1967.

- Charlson, R. J., T. L. Anderson, and H. Rodhe, Direct Climate Forcing by Anthropogenic Aerosols: Quantifying the Link Between Atmospheric Sulfate and Radiation, *Contrib. Atmos. Phys.*, 72, No. 1, 79-94, 1999.
- Christopher, S. A., X. Li, R. M. Welch, J. S. Reid, P. V. Hobbs, T. F. Eck, and B. Holben, Estimation of Surface and Top-of-Atmosphere Shortwave Irradiance in Biomass-Burning Regions during SCAR-B, *J. Appl. Met.*, 39, 1742-1753, 2000.
- Chung, C. E., V. Ramanathan, D. Kim, and I. A. Podgorny, Global anthropogenic aerosol direct forcing derived from satellite and ground-based observations, *J. Geophys. Res.*, 110, D24207, doi:10.1029/2005JD006356, 2005.
- Chung, S. H., and J. H. Seinfeld, Climate response of direct radiative forcing of anthropogenic black carbon, *J. Geophys. Res.*, 110, No. D11102, doi:10.1029/2004JD005441, 2005.
- Chylek, P., V. Srivastava, R. G. Pinnick, and R. T. Wang, Scattering of electromagnetic waves by composite spherical particles: Experiment and effective medium approximations, *Appl. Opt.*, 27, 2396-2404, 1988.
- Chylek, P., G. Videen, D. Ngo, R. G. Pinnick, and J. D. Klett, Effect of black carbon on the optical properties and climate forcing of sulfate aerosols, *J. Geophys. Res.*, 100, No. D8, 16325-16332, 1995.
- Chylek, P., B. Henderson, and M. Mishchenko, Aerosol radiative forcing and the accuracy of satellite aerosol optical depth retrieval, *J. Geophys. Res.*, 108, No. D24, doi:10.1029/2003JD004044, 2003.
- Clarke, A. D., S. Howell, P. K. Quinn, T. S. Bates, J. A. Ogren, E. Andrews, A. Jefferson, A. Massling, O. Mayol-Bracero, H. Maring, D. Savoie, and G. Cass, INDOEX aerosol: A comparison and summary of chemical microphysical, and optical properties observed from land, ship, and aircraft, *J. Geophys. Res.*, 107, No. D19, doi:10.1029/2001JD000572, 2002.
- Cosijn, C. and P. D. Tyson, Stable discontinuities in the atmosphere over South Africa, *S. Afr. J. Sci.*, 92, 381-386, 1996.
- d'Almeida, G. A., P. Koepke, and E. P. Shettle, *Atmospheric Aerosols: Global Climatology and Radiative Characteristics*, A. Deepak Publishing, Hampton, VA, 561 pp., 1991.
- Dave, J. V., Coefficients of the Legendre and Fourier Series for the Scattering Functions of Spherical Particles, *Appl. Opt.*, 9, 1888-1896, 1970.
- Delmas, R. A., et al., Experiment for Regional Sources and Sinks of Oxidants (EXPRESSO) : An overview, *J. Geophys. Res.*, 104, No. D23, 30609-30624, 1999.

- Delworth, T. L., V. Ramaswamy, and G. L. Stenchikov, The impacts of aerosols on simulated ocean temperature and heat content in the 20<sup>th</sup> century, *Geophys. Res. Lett.*, *32*, L24709, doi:10.1029/2005GL024457, 2005.
- Doherty, S., P. K. Quinn, A. Jefferson, C. M. Carrico, T. L. Anderson, and D. Hegg, A comparison and summary of aerosol optical properties as observed in situ from aircraft, ship, and land during ACE-Asia, *J. Geophys. Res.*, *110*, D04201, doi:10.1029/2004JD004964, 2005.
- Dubovik, O., A. Smirnov, B. N. Holben, M. D. King, Y. J. Kaufman, T. F. Eck, and I. Slutsker, Accuracy assessments of aerosol optical properties retrieved from Aerosol Robotic Network (AERONET) Sun and sky radiance measurements, *J. Geophys. Res.*, *105*, No. D8, 9791-9806, 2000.
- Dubovik, O. and M. King, A flexible inversion algorithm for the retrieval of aerosol optical properties from Sun and sky radiance measurements, *J. Geophys. Res.*, *105*, 20673-20696, 2000.
- Dubovik, O., B. Holben, T. F. Eck, A. Smirnov, Y. J. Kaufman, M. D. King, D. Tanre, and I. Slutsker, Variability of Absorption and Optical Properties of Key Aerosol Types Observed in Worldwider Locations, *J. Atmos. Sci.*, *59*, 590-608, 2002.
- Duncan, B. N., R. V. Martin, A. C. Staudt, R. Yevich, and J. A. Logan, Interannual and seasonal variability of biomass burning emissions constrained by satellite observations, *J. Geophys. Res.*, *108*, D2, 4100, doi:10.1029/2002JD002378, 2003.
- Eatough, D. J., N. L. Eatough, Y. Pang, S. Sizemore, T. W. Kirchstetter, T. Novakov, and P. V. Hobbs, Semivolatile particulate organic material in southern Africa during SAFARI 2000, *J. Geophys. Res.*, *108*, No. D13, 8479, doi:10.1029/2002JD002296, 2003.
- Eck, T. F., B. N. Holben, D. E. Ward, M. M. Mukelabai, O. Dubovik, A. Smirnov, J. S. Schafer, N. C. Hsu, S. J. Piketh, A. Queface, J. LeRoux, R. J. Swap, and I. Slutsker, Variability of biomass burning aerosol optical characteristics in southern Africa during the SAFARI 2000 dry season campaign and a comparison of single scattering albedo estimates from radiometric measurements, *J. Geophys. Res.*, *108*, No. D13, doi:10.1029/2002JD002321, 2003.
- Ehrlick, G., Living on Thin Ice, *Nat. Geog.*, 78-101, 209, No. 1, 2006.
- Eliot, J. L., Seasons of the Snow Fox, *Nat. Geog.*, 206, No. 4, 70-87, 2004.
- Eliot, J. L., Polar Bears in Hot Water, *Nat. Geog.*, 208, No. 6, 46-57, 2005.
- Fenn, R. W., S. A. Clough, W. O. Gallery, R. E. Good, F. X. Kneizys, J. D. Mill, L. S. Rothman, E. P. Shettle, and F. E. Volz, Optical and Infrared Properties of the Atmosphere, In *Handbook of Geophysics and the Space*



- Environment*, edited by Adolph S. Jursa, Air Force Geophysics Laboratory, Hanscom Air Force Base, Bedford, MA, 1985.
- Formenti, P., W. Elbert, W. Maenhaut, J. Haywood, S. Osborne, and M. O. Andreae, Inorganic and carbonaceous aerosols during the Southern African Regional Science Initiative (SAFARI 2000) experiment: Chemical characteristics, physical properties, and emission data for smoke from African biomass burning, *J. Geophys. Res.*, *108*, No. D13, 8488, doi:10.1029/2002JD002408, 2003.
- Freiman, M. T., and S. J. Piketh, Air Transport into and out of the Industrial Highveld Region of South Africa, *J. Appl. Met.*, *42*, 994-1002, 2003.
- Fu, Q., and K. N. Liou, On the Correlated k-Distribution Method for Radiative Transfer in Nonhomogeneous Atmospheres, *J. Atmos. Sci.*, *49*, No. 22, 2139-2156, 1992.
- Fu, Q., S. K. Krueger, and K. N. Liou, Interactions of Radiation and Convection in Simulated Tropical Cloud Clusters, *J. Atmos. Sci.*, *52*, No. 9, 1310-1328, 1995.
- Fuller, K. A., W. C. Malm, and S. M. Kreidenweis, Effects of mixing on extinction by carbonaceous particles, *J. Geophys. Res.*, *104*, No. D13, 15941-15954, 1999.
- Ganguly, D., A. Jayaraman, H. Gadhavi, and T. A. Rajesh, Features in wavelength dependence of aerosol absorption observed over central India, *Geophys. Res. Lett.*, *32*, doi:10.1029/2005GL023023, 2005.
- Gao, S., D. A. Hegg, P. V. Hobbs, T. W. Kirchstetter, B. I. Magi, and M. Sadilek, Water-soluble organic components in aerosols associated with savanna fires in southern Africa: Identification, evolution, and distribution, *J. Geophys. Res.*, *108*, No. D13, doi:10.1029/2002JD002324, 2003.
- Garrett, T. J., Radiative Properties of Arctic Clouds, Ph. D Thesis, 2000.
- Garstang, M., P. D. Tyson, R. Swap, M. Edwards, P. Kallberg, and J. A. Lindesay, Horizontal and vertical transport of air over southern Africa, *J. Geophys. Res.*, *101*, No. D19, 23721-23736, 1996.
- Gerrold, David, "A conclusion is the place where you stopped thinking. An answer is the place where you stopped asking the question.", *A Season for Slaughter*, 1992.
- Gettelman, A., P. M. F. Forster, M. Fujiwara, Q. Fu, H. Voemel, L. K. Gohar, C. Johanson, and M. Ammerman, Radiation balance of the tropical tropopause layer, *J. Geophys. Res.*, *109*, doi:10.1029/2003JD004190, 2004.
- Glick, D., The Big Thaw, *Nat. Geog.*, *206*, No. 3, 12-33, 2004.

- Grant, K. E., C. C. Chuang, A. S. Grossman, and J. E. Penner, Modeling the spectral optical properties of ammonium sulfate and biomass burning aerosols: parameterizations of relative humidity effects and model results, *Atmos. Env.*, *33*, 2603-2620, 1999.
- Guyon, P., B. Graham, J. Beck, O. Boucher, E. Gerasopoulos, O. L. Mayol-Bracero, G. C. Roberts, P. Artaxo, and M. O. Andreae, Physical properties and concentration of aerosol particles over the Amazon tropical forest during background and biomass burning conditions, *Atmos. Chem. Phys. Discuss.*, *3*, 1367-1414, 2003.
- Haenel, G., The properties of atmospheric aerosols as functions of the relative humidity at thermodynamic equilibrium with surrounding air, *Adv. Geophys.*, *19*, 73-188, 1976.
- Hartley, W. S., Airborne Study of Aerosol Optical Properties and Direct Aerosol Radiative Forcing off the East Coast of the United States, Master's thesis, 2000.
- Hartley, W. S., P. V. Hobbs, J. L. Ross, P. B. Russell, and J. M. Livingston, Properties of aerosols aloft relevant to direct radiative forcing off the mid-Atlantic coast of the United States, *J. Geophys. Res.*, *105*, 9859-9885, 2000.
- Hartley, W. S., and P. V. Hobbs, An aerosol model and aerosol-induced changes in the clear-sky albedo off the east coast of the United States, *J. Geophys. Res.*, *106*, 9733-9748, 2001.
- Hartmann, D. L., L. A. Moy, and Q. Fu, Tropical Convection and the Energy Balance at the Top of the Atmosphere, *J. Clim.*, *14*, 4495-4511, 2001.
- Haywood, J. M., V. Ramaswamy, and L. J. Donner, A limited-area-model case study of the effects of sub-grid scale variations in relative humidity and cloud upon the direct radiative forcing of sulfate aerosol, *Geophys. Res. Lett.*, *24*, No. 2, 143-146, 1997.
- Haywood, J. M., S. R. Osborne, P. N. Francis, A. Keil, P. Formenti, M. O. Andreae, and P. H. Kaye, The mean physical and optical properties of regional haze dominated biomass burning aerosol measured from the C-130 aircraft during SAFARI 2000, *J. Geophys. Res.*, *108*, No. D13, doi:10.1029/2002JD002226, 2003a.
- Haywood, J., P. Francis, O. Dubovik, M. Glew, and B. Holben, Comparison of aerosol size distributions, radiative properties, and optical depths determined by aircraft observations and Sunphotometers during SAFARI 2000, *J. Geophys. Res.*, *108*, No. D13, doi:10.1029/2002JD002250, 2003b.

- Haywood, J. M., S. R. Osborne, and S. J. Abel, The effect of overlying absorbing aerosol layers on remote sensing retrievals of cloud effective radius and cloud optical depth, *Q. J. R. Meteor. Soc.*, *130*, 779-800, 2004.
- Hegg, D. A., T. Larson, and P. F. Yuen, A theoretical study of the effect of relative humidity on light scattering by tropospheric aerosols. *J. Geophys. Res.*, *98*, 18435-18439, 1993.
- Hegg, D. A., D. S. Covert, M. J. Rood, and P. V. Hobbs, Measurements of aerosol optical properties in marine air, *J. Geophys. Res.*, *101*, 12,893–12,903, 1996.
- Hegg, D. A., J. Livingston, P. V. Hobbs, T. Novakov, and P. Russell, Chemical apportionment of aerosol optical depth off the mid-Atlantic coast of the United States. *J. Geophys. Res.*, *102*, 25293-25303, 1997.
- Hegg, D. A., D. S. Covert, K. Crahan, and H. Jonssen, The dependence of aerosol light-scattering on RH over the Pacific Ocean, *Geophys. Res. Lett.*, *29*, No. 8, doi:10.1029/2001FL014495, 2002.
- Heintzenberg, J., and J. Ogren, On the Operation of the TSI-3020 Condensation Nuclei Counter at Altitudes up to 10 km, *Atmos. Environ.*, *19*, 1385-1387, 1985.
- Hess, M., P. Koepke, and I. Schult, Optical Properties of Aerosols and Clouds: The Software Package OPAC, *Bull. Am. Met. Soc.*, *79*, No. 5, 831-844, 1998.
- Hobbs, P. V., Twenty Years of Airborne Research at the University of Washington, *Bull. Amer. Meteor. Soc.*, *72*, No. 11, 1707-1716, 1991.
- Hobbs, P. V., J. S. Reid, R. A. Kotchenruther, R. J. Ferek, and R. Weiss, Direct radiative forcing by smoke from biomass burning, *Science*, *275*, 1776-1778, 1997.
- Hobbs, P. V., Clean air slots amid atmospheric pollution in southern Africa, *J. Geophys. Res.*, *108*, No. D13, 8490, doi:10.1029/2002JD002156, 2003.
- Hobbs, P. V., P. Sinha, R. J. Yokelson, I. T. Bertschi, D. R. Blake, S. Gao, T. W. Kirchstetter, T. Novakov, and P. Pilewskie, Evolution of gases and particles from a savanna fire in South Africa, *J. Geophys. Res.*, *108*, No. D13, 8485, doi:10.1029/2002JD002352, 2003.
- Holben, B. N., et al., AERONET – A federated instrument network and data archive for aerosol characterization, *Remote Sens. Environ.*, *66*, 1-16, 1998.
- Holben, B. N., et al., An emerging ground-based aerosol climatology: Aerosol optical depth from AERONET, *J. Geophys. Res.*, *106*, 12067-12097, 2001.

- Ichoku C., L. A. Remer, Y. J. Kaufman, R. Levy, D. A. Chu, D. Tanre, and B. N. Holben, MODIS observation of aerosols and estimation of aerosol radiative forcing over southern Africa during SAFARI 2000, *J. Geophys. Res.*, *108*, No. D13, doi:10.1029/2002JD002366, 2003.
- Intergovernmental Panel on Climate Change (IPCC), *Climate Change 2001: The Scientific Basis*, edited by J. T. Houghton et al., Cambridge Univ. Press, Cambridge, 896 pp, 2001.
- Jacobson, M. Z., A physically-based treatment of elemental carbon optics: Implications for global direct forcing of aerosols, *Geophys. Res. Lett.*, *27*, No. 2, 217-220, 2000.
- Jacobson, M. Z., Global direct radiative forcing due to multicomponent anthropogenic and natural aerosols, *J. Geophys. Res.*, *106*, No. D2, 1551-1568, 2001.
- Jacobson, M. Z., Control of fossil-fuel particulate black carbon and organic matter, possibly the most effective method of slowing global warming, *J. Geophys. Res.*, *107*, No. D19, doi:10.1029/2001JD001376, 2002.
- Jiang, H., and G. Feingold, Effect of aerosol on warm convective clouds: Aerosol-cloud-surface flux feedbacks in a new coupled large eddy model, *J. Geophys. Res.*, *111*, D01202, doi:10.1029/2005JD006138, 2006.
- Kahn, R. A., J. A. Ogren, T. P. Ackerman, J. Boesenberg, R. J. Charlson, D. J. Diner, B. N. Holben, R. T. Menzies, M. A. Miller, and J. H. Seinfeld, Aerosol Data Sources and Their Roles within PARAGON, *Bull. Amer. Meteor. Soc.*, *85*, 1511-1522, 2004.
- Kanakidou, M., et al., Organic aerosol and global climate modelling: a review, *Atmos. Chem. Phys.*, *5*, 1053-1123, 2005.
- Kasten, F., Visibility in the phase of pre-condensation, *Tellus*, *21*, 631-635, 1969.
- Kato, S., M. H. Bergin, N. Laulainen, R. Ferrare, D. Turner, J. Michalsky, T. P. Charlock, E. E. Clothiaux, G. G. Mace, and T. P. Ackerman, A comparison of the aerosol optical thickness derived from ground-based and airborne measurements. *J. Geophys. Res.*, *105*, 14,701-14,717, 2000.
- Kaufman, Y. J., D. Tanre, B. N. Holben, S. Mattoo, L. A. Remer, T. F. Eck, J. Vaughan, and B. Chatenet, Aerosol Radiative Impact on Spectral Solar Flux at the Surface, Derived from Principal-Plane Sky Measurements, *J. Atmos. Sci.*, *59*, 635-646, 2002.
- Keil, A., and J. M. Haywood, Solar radiative forcing by biomass burning aerosol particles during SAFARI 2000: A case study based on measured aerosol and cloud properties, *J. Geophys. Res.*, *108*, No. D13, doi:10.1029/2002JD002315, 2003.

- Kesten, J., A. Reineking, and J. Porstendoerfer, Calibration of a TSI Model 3025 Ultrafine Condensation Particle Counter, *Aer. Sci. and Tech.*, 15, 107-111, 1991.
- Kinne, S., et al., Monthly averages of aerosol properties: A global comparison among models, satellite data, and AERONET ground data, *J. Geophys. Res.*, 108, No. D20, doi:10.1029/2001JD001253, 2003.
- Kinne, S., et al., An AeroCom initial assessment – optical properties in aerosol component modules of global models, *Atmos. Chem. Phys. Discuss.*, 5, 8285-8330, 2005.
- Kirchstetter, T. W., T. Novakov, P. V. Hobbs, and B. Magi, Airborne measurements of carbonaceous aerosols in southern Africa during the dry, biomass burning season. *J. Geophys. Res.*, 108, No. D13, doi:10.1029/2002JD002171, 2003.
- Kirchstetter, T. W., T. Novakov, and P. V. Hobbs, Evidence that the spectral dependence of light absorption by aerosols is affected by organic carbon, *J. Geophys. Res.*, 109, No. D21, doi:10.1029/2004JD004999, 2004.
- Kluger, J., Global Warming: The Culprit?, *Time*, 166, No. 14, 42-46, 2005.
- Kolbert, E., The Climate of Man – I, *The New Yorker*, 81, No. 10, 56-59, 2005a.
- Kolbert, E., The Climate of Man – II, *The New Yorker*, 81, No. 11, 64-71, 2005b.
- Kolbert, E., The Climate of Man – III, *The New Yorker*, 81, No. 12, 52-62, 2005c.
- Korontzi, S., D. E. Ward, R. A. Susott, R. J. Yokelson, C. O. Justice, P. V. Hobbs, E. A. H. Smithwick, and W. M. Hao, Seasonal variation and ecosystem dependence of emission factors for selected trace gases and PM<sub>2.5</sub> for southern African savanna fires, *J. Geophys. Res.*, 108, No. D24, doi:10.1029/2003JD003730, 2003.
- Kotchenruther, R. A., and P. V. Hobbs, Humidification factors of aerosols from biomass burning in Brazil, *J. Geophys. Res.*, 103, 32,801-32,089, 1998.
- Kotchenruther, R. A., P. V. Hobbs, and D. A. Hegg, Humidification factors for atmospheric aerosols off the mid-Atlantic coast of the United States, *J. Geophys. Res.*, 104, 2239-2251, 1999.
- Leahy, L. V., A Synthesis of Single Scattering Albedo Values of Biomass Burning Aerosol, Observed over Southern Africa during the SAFARI 2000 Field Campaign, Master's Thesis, 2006.
- Li, J., M. Posfai, P. V. Hobbs, and P. R. Buseck, Individual aerosol particles from biomass burning in southern Africa: 2. Compositions and aging of inorganic particles, *J. Geophys. Res.*, 108, No. D13, doi:10.1029/2003JD002310, 2003.

- Liao, H., and J. H. Seinfeld, Radiative forcing by mineral dust aerosols: Sensitivity to key variables, *J. Geophys. Res.*, *103*, No. D24, 31637-31645, 1998.
- Liou, K. N., Q. Fu, and T. P. Ackerman, A Simple Formulation of the Delta-Four-Stream Approximation for Radiative Transfer Parameterization, *J. Atmos. Sci.*, *45*, No. 13, 1988.
- Liou, K. N., *An Introduction to Atmospheric Radiation*, 2<sup>nd</sup> ed., 583 pp., 2002.
- Liu, P. S. K., W. R. Leaitch, J. W. Strapp, and M. A. Wasey, Response of Particle Measuring Systems Airborne ASASP and PCASP to NaCl and Latex Particles, *Aer. Sci. and Tech.*, *16*, 83-95, 1992.
- Liu, Y. and P. H. Daum, The Effect of Refractive Index on Size Distributions and Light Scattering Coefficients Derived From Optical Particle Counters, *J. Aerosol Sci.*, *31*, No. 8, 945-957, 2000.
- Magi, B. I., and P. V. Hobbs, Effects of humidity on aerosols in southern Africa during the biomass burning season. *J. Geophys. Res.*, *108*, No. D13, doi:10.1029/2002JD002144, 2003.
- Magi, B. I., P. V. Hobbs, B. Schmid, and J. Redemann, Vertical profiles of light scattering, light absorption and single-scattering albedo during the dry, biomass burning season in southern Africa and comparisons of in-situ and remote sensing measurements of aerosol optical depth. *J. Geophys. Res.*, *108*, No. D13, doi:10.1029/2002JD002361, 2003.
- Magi, B. I., and P. V. Hobbs, Modeling the vertically stratified atmosphere of southern Africa during the biomass burning season, *EOS Trans. AGU*, *85*, No. 47, Fall Meet. Suppl., Abstract A31C-0069, 2004.
- Magi, B. I., P. V. Hobbs, T. W. Kirchstetter, T. Novakov, D. A. Hegg, S. Gao, J. Redemann, B. Schmid, Aerosol Properties and Chemical Apportionment of Aerosol Optical Depth at Locations off the United States East Coast in July and August 2001, *J. Atmos. Sci.*, *62*, No. 4, 919-933, doi:10.1175/JAS3263.1, 2005.
- Markowicz, K. M., P. J. Flatau, P. K. Quinn, C. M. Carrico, M. K. Flatau, A. M. Vogelmann, D. Bates, M. Liu, and M. J. Rood, Influence of relative humidity on aerosol radiative forcing: An ACE-Asia experiment perspective, *J. Geophys. Res.*, *108*, No. D23, doi:10.1029/2002JD003066, 2003.
- Mishchenko, M. I., J. W. Hovenier, and L. D. Travis, Eds., *Light Scattering by Nonspherical Particles: Theory, Measurements, and Applications*, Academic Press, San Francisco, 2000.

- Miller, G. H., M. L. Fogel, J. W. Magee, M. K. Gagan, S. J. Clarke, and B. J. Johnson, Ecosystem Collapse in Pleistocene Australia and a Human Role in Megafaunal Extinction, *Science*, *309*, 287-290, 2005.
- Ming, Y., V. Ramaswamy, P. A. Ginoux, and L. H. Horowitz, Direct radiative forcing of anthropogenic organic aerosol, *J. Geophys. Res.*, *110*, D20208, doi:10.1029/2004JD005573, 2005.
- Mitchell, J. G., When Mountains Move, *Nat. Geog.*, *209*, No. 3, 104-123, 2006.
- Montaigne, F., No Room to Run, *Nat. Geog.*, *206*, No. 3, 34-55, 2004.
- Moody, E. G., M. D. King, S. Platnick, C. B. Schaaf, and F. Gao, Spatially Complete Global Spectral Surface Albedos: Value-Added Datasets Derived From Terra MODIS Land Products, *IEEE Trans. on Geosci. and Rem. Sens.*, *43*, No. 1, 2005.
- Morell, V., Now What?, *Nat. Geog.*, *206*, No. 3, 56-75, 2004.
- Myhre, G., T. K. Berntsen, J. M. Haywood, J. K. Sundet, B. N. Holben, M. Johnsrud, and F. Stordal, Modeling the solar radiative impact of aerosols from biomass burning during the Southern African Regional Science Initiative (SAFARI-2000) experiment, *J. Geophys. Res.*, *108*, No. D13, doi:10.1029/2002JD002313, 2003.
- Osborne, S. R., J. M. Haywood, P. N. Francis, and O. Dubovik, Short-wave radiative effects of biomass burning aerosol during SAFARI2000, *Q. J. R. Meteorol. Soc.*, *130*, 1423-1447, 2004.
- Palle, E., P. Montanes-Rodriguez, P. R. Goode, S. E. Koonin, M. Wild, and S. Casadio, A multi-data comparison of shortwave climate forcing changes, *Geophys. Res. Lett.*, *32*, L21702, doi:10.1029/2005GL023847, 2005.
- Pandithurai, G., R. T. Pinker, T. Takamura, and P. C. S. Devara, Aerosol radiative forcing over a tropical urban site in India, *Geophys. Res. Lett.*, *31*, doi:10.1029/2004GL019702, 2004.
- Parfit, M., Powering the Future, *Nat. Geog.*, *208*, No. 2, 2-31, 2005.
- Penner, J. E., R. E. Dickinson, and C. A. O'Neill, Effects of Aerosols from Biomass Burning on the Global Radiation Budget, *Science*, *256*, 1432-1433, 1992.
- Piketh, S. J., H. J. Annegarn, and P. D. Tyson, Lower tropospheric aerosol loadings over South Africa: The relative contribution of aeolian dust, industrial emissions, and biomass burning, *J. Geophys. Res.*, *104*, No. D1, 1597-1607, 1999.
- Piketh, S. J., R. J. Swap, W. Maenhaut, H. J. Annegarn, and P. Formenti, Chemical evidence of long-range atmospheric transport over southern

- Africa, *J. Geophys. Res.*, *107*, No. D24, 4817, doi:10.1029/2002JD002056, 2002.
- Pilewskie, P., J. Pommier, R. Bergstrom, W. Gore, S. Howard, M. Rabbette, B. Schmid, P. V. Hobbs, and S. C. Tsay, Solar spectral radiative forcing during the Southern African Regional Science Initiative, *J. Geophys. Res.*, *108*, No. D13, doi:10.1029/2002JD002411, 2003.
- Posfai, M., R. Simonics, J. Li, P. V. Hobbs, and P. R. Buseck, Individual aerosol particles from biomass burning in southern Africa: 1. Compositions and size distributions of carbonaceous particles, *J. Geophys. Res.*, *108*, No. D13, doi:10.1029/200XJD002291, 2003.
- Posfai, M., A. Gelencser, R. Simonics, K. Arato, J. Li, P. V. Hobbs, and P. R. Buseck, Atmospheric tar balls: Particles from biomass and biofuel burning, *J. Geophys. Res.*, *109*, D06213, doi:10.1029/2003JD004169, 2004.
- Quinn, P. K., T. S. Bates, T. Baynard, A. D. Clarke, T. B. Onasch, W. Wang, M. J. Rood, E. Andrews, J. Allan, C. M. Carrico, D. Coffman, and D. Worsnop, Impact of particulate organic matter on the relative humidity dependence of light scattering: A simplified parameterization, *Geophys. Res. Lett.*, *32*, L22809, doi:10.1029/2005GL024322, 2005.
- Ramaswamy, V., O. Boucher, J. Haigh, D. Hauglustaine, J. M. Haywood, G. Myhre, T. Nakajima, G. Y. Shi, S. Solomon, Radiative Forcing of Climate Change, in *Climate Change 2001: The Scientific Basis, Contribution of Working Group I to the Third Assessment Report of the Intergovernmental Panel on Climate Change*, J. T. Houghton, Y. Ding, D. J. Griggs, M. Noguer, P. van der Linden, X. Dai, K. Maskell, Eds., pp. 349-416, Cambridge Univ. Press, New York, 2001.
- Reddy, M. S., O. Boucher, N. Bellouin, M. Schulz, Y. Balkanski, J. L. Dufresne, and M. Pham, Estimates of global multicomponent aerosol optical depth and direct radiative perturbation in the Laboratoire de Meteorologie-Dynamique general circulation model, *J. Geophys. Res.*, *110*, doi:10.1029/2004JD004757, 2005a.
- Reddy, M. S., O. Boucher, Y. Balkanski, and M. Schulz, Aerosol optical depths and direct radiative perturbations by species and source type, *Geophys. Res. Lett.*, *32*, L12803, doi:10.1029/2004GL021743, 2005b.
- Redemann, J., R. P. Turco, K. N. Liou, P. B. Russell, R. W. Bergstrom, B. Schmid, J. M. Livingston, P. V. Hobbs, W. S. Hartley, S. Ismail, R. A. Ferrare, and E. V. Browell, Retrieving the vertical structure of the effective aerosol complex index of refraction from a combination of aerosol in situ and remote sensing measurements during TARFOX, *J. Geophys. Res.*, *105*, No. D8, 9949-9970, 2000a.



- Redemann, J., R. P. Turco, K. N. Liou, P. V. Hobbs, W. S. Hartley, R. W. Bergstrom, E. V. Browell, and P. B. Russell, Case studies of the vertical structure of the direct shortwave aerosol radiative forcing during TARFOX, *J. Geophys. Res.*, *105*, No. D8, 9971-9979, 2000b.
- Redemann, J., P. B. Russell, and P. Hamill, Dependence of aerosol light absorption and single-scattering albedo on ambient relative humidity for sulfate aerosols with black carbon cores, *J. Geophys. Res.*, *106*, 27, 485-27,495, 2001.
- Redemann, J., S. J. Masonis, B. Schmid, T. L. Anderson, P. B. Russell, J. M. Livingston, O. Dubovik, and A. D. Clarke, Clear-column closure studies of aerosols and water vapor aboard the NCAR C-130 during ACE-Asia, 2001, *J. Geophys. Res.*, *108*, D23, 8655, doi:10.1029/2003JD003442, 2003.
- Redemann, J., B. Schmid, J. A. Eilers, R. Kahn, R. C. Levy, P. B. Russell, J. M. Livingston, P. V. Hobbs, W. L. Smith Jr., and B. N. Holben, Suborbital Measurements of Spectral Aerosol Optical Depth and Its Variability at Subsatellite Grid Scales in Support of CLAMS 2001, *J. Atmos. Sci.*, *62*, 993-1007, 2005a.
- Redemann, J., P. Pilewskie, P. B. Russell, J. M. Livingston, S. Howard, B. Schmid, J. Pommier, W. Gore, J. Eilers, and M. Wendisch, Airborne measurements of spectral direct aerosol radiative forcing in INTEx/ITCT 2004, submitted to *J. Geophys. Res.*, 2005b.
- Reid, J. S., P. V. Hobbs, R. J. Ferek, D. R. Blake, J. V. Martins, M. R. Dunlap, and C. Liousse, Physical, chemical and optical properties of regional hazes dominated by smoke in Brazil, *J. Geophys. Res.*, *103*, No. D24, 32059-32080, 1998.
- Reid, J. S., R. Koppmann, T. F. Eck, and D. P. Eleuterio, A review of biomass burning emissions part II: Intensive physical properties of biomass burning particles, *Atmos. Chem. Phys. Discuss.*, *4*, 5135-5200, 2004a.
- Reid, J. S., T. F. Eck, S. A. Christopher, R. Koppmann, O. Dubovik, D. P. Eleuterio, B. N. Holben, E. A. Reid, and J. Zhang, A review of biomass burning emissions part III: intensive optical properties of biomass burning particles, *Atmos. Chem. Phys. Discuss.*, *4*, 5201-5260, 2004b.
- Reist, P. C., *Aerosol Science and Technology*, McGraw-Hill, San Francisco, 2<sup>nd</sup> ed., 379 pp., 1993.
- Remer, L. A., S. Gasso, D. A. Hegg, Y. J. Kaufman, and B. N. Holben, Urban/industrial aerosol: Ground-based Sun/sky radiometer and airborne in situ measurements, *J. Geophys. Res.*, *102*, 16849-16859, 1997.

- Roden, C. A., T. C. Bond, S. Conway, A. B. O. Pinel, Emission Factors and Real-time Optical Properties of Particles Emitted from Traditional Wood Burning Cookstoves, submitted to *Env. Sci. Tech.*, 2005.
- Ross, J. L., P. V. Hobbs, and B. Holben, Radiative characteristics of regional hazes dominated by smoke from biomass burning in Brazil: Closure tests and direct radiative forcing, *J. Geophys. Res.*, *103*, No. D24, 31925-31941, 1998.
- Ross, K. E., S. J. Piketh, R. T. Bruintjes, R. P. Burger, R. J. Swap, and H. J. Annegarn, Spatial and seasonal variations in CCN distribution and the aerosol-CCN relationship over southern Africa, *J. Geophys. Res.*, *108*, No. D13, doi:10.1029/2002JD002384, 2003.
- Ruellan, S., H. Cachier, A. Gaudichet, P. Masclet, and J. Lacaux, Airborne aerosols over central Africa during the Experiment for Regional Sources and Sinks of Oxidants (EXPRESSO), *J. Geophys. Res.*, *104*, No. D23, 30673-30690, 1999.
- Russell, P. B., J. Redemann, B. Schmid, R. W. Bergstrom, J. M. Livingston, D. M. McIntosh, S. A. Ramirez, S. Hartley, P. V. Hobbs, P. K. Quinn, C. M. Carrico, M. J. Rood, E. Ostrom, K. J. Noone, W. von Hoyningen-Huene, and L. Remer, Comparison of Aerosol Single Scattering Albedos Derived by Diverse Techniques in Two North Atlantic Experiments, *J. Atmos. Sci.*, *59*, 609-619, 2002.
- Sateesh, S. K., and V. Ramanathan, Large differences in tropical aerosol forcing at the top of the atmosphere and Earth's surface, *Nature*, *405*, 60-63, 2000.
- Saxena, P., L. M. Hildemann, P. H. McMurry, and J. H. Seinfeld, Organics alter hygroscopic behavior of atmospheric particles, *J. Geophys. Res.*, *100*, No. D9, 18755-18770, 1995.
- Schmid, B., J. M. Livingston, P. B. Russell, P. A. Durkee, H. H. Jonsson, D. R. Collins, R. C. Flagan, J. H. Seinfeld, S. Gassó, D. A. Hegg, E. Öström, K. J. Noone, E. J. Welton, K. J. Voss, H. R. Gordon, P. Formenti, and M. O. Andreae, Clear sky closure studies of lower tropospheric aerosol and water vapor during ACE 2 using airborne sunphotometer, airborne in-situ, space-borne, and ground-based measurements, *Tellus*, *B52*, 568-593, 2000.
- Schmid, B., J. Redemann, P. B. Russell, P. V. Hobbs, D. L. Hlavka, M. McGill, B. N. Holben, E. J. Welton, J. Campbell, O. Torres, R. Kahn, D. Diner, and M. Helmlinger, D. A. Chu, C. Robles Gonzalez, and G. de Leeuw, Coordinated airborne, spaceborne, and ground-based measurements of massive, thick aerosol layers during the dry season in southern Africa. *J. Geophys. Res.*, *108*, No. D13, doi:10.1029/2002JD002297, 2003.

- Schmid, B., R. Ferrare, C. Flynn, R. Elleman, D. Covert, A. Strawa, E. Welton, D. Turner, H. Jonsson, J. Redemann, J. Eilers, K. Ricci, A. G. Hallar, M. Clayton, J. Michalsky, A. Smirnov, B. Holben, and J. Barnard, How well do state-of-the-art techniques measuring the vertical profile of tropospheric aerosol extinction compare?, *J. Geophys. Res.*, *111*, doi:10.1029/2005JD005837, 2006.
- Schwartz, S. E., Uncertainty Requirements in Radiative Forcing of Climate Change, *J. Air & Waste Manage. Assoc.*, *54*, 1351-1359, 2004.
- Seinfeld, J. H., and S. N. Pandis, *Atmospheric Chemistry and Physics: From Air Pollution to Climate Change*, Wiley, New York, 1326 pp., 1998.
- Sheridan, P. J., W. P. Arnott, J. A. Ogren, E. Andrews, D. B. Atkinson, D. S. Covert, H. Moosmuller, A. Petzold, B. Schmid, A. W. Strawa, R. Varma, and A. Virkkula, The Reno Aerosol Optics Study: An Evaluation of Aerosol Absorption Measurement Methods, *Aer. Sci. Technol.*, *29*, 1-16, 2005.
- Sinha, P., P. V. Hobbs, R. J. Yokelson, I. T. Bertschi, D. R. Blake, I. J. Simpson, S. Gao, T. W. Kirchstetter, and T. Novakov, Emissions of trace gases and particles from savanna fire in southern Africa, *J. Geophys. Res.*, *108*, No. D13, 8487, doi:10.1029/2002JD002325, 2003a.
- Sinha, P., P. V. Hobbs, R. J. Yokelson, D. R. Blake, S. Gao, and T. W. Kirchstetter, Distributions of trace gases and aerosols during the dry biomass burning season in southern Africa, *J. Geophys. Res.*, *108*, No. D17, 4536, doi:10.1029/2003JD003691, 2003b.
- Sinha, P., L. Jaegle, P. V. Hobbs, and Q. Liang, Transport of biomass burning emissions from southern Africa, *J. Geophys. Res.*, *109*, D20204, doi:10.1029/2004JD005044, 2004.
- Stein, D. C., R. J. Swap, S. Greco, S. J. Piketh, S. A. Macko, B. G. Doddridge, T. Elias, and R. T. Buintjes, Haze layer characterization and associated meteorological controls along the eastern coastal region of southern Africa, *J. Geophys. Res.*, *108*, No. D13, doi:10.1029/2002JD003237, 2003.
- Strapp, J. W., W. R. Leaitch, P. S. K. Liu, Hydrated and Dried Aerosol-Size-Distribution Measurements from the Particle Measuring Systems FSSP-300 Probe and the Deiced PCASP-100X Probe, *J. Atmo. Ocean. Tech.*, *9*, 548-555, 1992.
- Swap, R. J. and P. D. Tyson, Stable discontinuities as determinants of the vertical distribution of aerosols and trace gases in the atmosphere, *S. Afr. J. Sci.*, *95*, February, 1999.

- Swap, R. J., H. J. Annegarn, and L. Otter, Southern African Regional Science Initiative (SAFARI 2000): summary of science plan, *S. Afr. J. Sci.*, 98, 119-124, 2002a.
- Swap, R. J., et al., The Southern African Regional Science Initiative (SAFARI 2000): overview of the dry season field campaign, *S. Afr. J. Sci.*, 98, 125-130, 2002b.
- Swap, R. J., H. J. Annegarn, J. T. Suttles, M. D. King, S. Platnick, J. L. Privette, and R. J. Scholes, Africa burning: A thematic analysis of the Southern African Regional Science Initiative (SAFARI 2000), *J. Geophys. Res.*, 108, No. D13, 8465, doi:10.1029/2003JD003747, 2003.
- Tang, I. N., and H. R. Munkelwitz, Aerosol Phase Transformation and Growth in the Atmosphere, *J. Appl. Met.*, 33, 791-796, 1994.
- Tang, I. N., Thermodynamics and optical properties of mixed-salt aerosols of atmospheric importance, *J. Geophys. Res.*, 102, No. D2, 1883-1893, 1997.
- Tang, I. N., A. C. Tridico, and K. H. Fung, Thermodynamic and optical properties of sea salt aerosols, *J. Geophys. Res.*, 102, No. D19, 23269-23275, 1997.
- Takemura, T., T. Nozawa, S. Emori, T. Y. Nakajima, and T. Nakajima, Simulation of climate response to aerosol direct and indirect effects with aerosol transport-radiation model, *J. Geophys. Res.*, 110, D02202, doi:10.1029/2004JD005029, 2005.
- Textor, C., et al., Analysis and quantification of the diversities of aerosol life cycles within AeroCom, *Atmos. Chem. Phys. Discuss.*, 5, 8331-8420, 2005.
- Thompson, A. M., J. C. Witte, M. T. Freiman, A. Phahlane, and G. J. R. Coetzee, Lusaka, Zambia, during SAFARI-2000: Convergence of local and imported ozone pollution, *Geophys. Res. Lett.*, 29, 1976, doi:10.1029/2002GL015399, 2002.
- Thompson, A. M., J. C. Witte, R. D. McPeters, S. J. Oltmans, F. J. Schmidlin, J. A. Logan, M. Fujiwara, V. W. J. H. Kirchhoff, F. Posny, G. J. R. Coetzee, B. Hoegger, S. Kawakami, T. Ogawa, B. J. Johnson, H. Vömel and G. Labow, Southern Hemisphere Additional Ozonesondes (SHADOZ) 1998-2000 tropical ozone climatology 1. Comparison with Total Ozone Mapping Spectrometer (TOMS) and ground-based measurements, *J. Geophys. Res.*, 108, No. D2, doi:10.1029/2001JD000967, 2003.
- Thompson, T.M., J. H. Butler, B. C. Daube, G. S. Dutton, J. W. Elkins, B. D. Hall, D. F. Hurst, D. B. King, E. S. Kline, B. G. Lafleur, J. Lind, S. Lovitz, D. J. Mondeel, S. A. Montzka, F. L. Moore, J. D. Nance, J. L. Neu, P. A. Romashkin, A. Scheffer, and W. J. Snible, 5. Halocarbons and other Atmospheric Trace Species, in *Climate Monitoring and Diagnostics*

- Laboratory, Summary Report No. 27, 2002-2003, pp. 115-133, edited by R. C. Schnell, A.-M. Buggle, and R. M. Rosson, NOAA CMDL, Boulder, CO, 2004.
- Topping, D. O., G. B. McFiggans, and H. Coe, A curved multi-component aerosol hygroscopicity model framework: Part 1 – Inorganic compounds, *Atmos. Chem. Phys.*, 5, 1205-1222, 2005a.
- Topping, D. O., G. B. McFiggans, and H. Coe, A curved multi-component aerosol hygroscopicity model framework: Part 2 – Including organic compounds, *Atmos. Chem. Phys.*, 5, 1223-1242, 2005b.
- Trentmann, J., R. J. Yokelson, P. V. Hobbs, T. Winterrath, T. J. Christian, M. O. Andreae, and S. A. Mason, An analysis of the chemical processes in the smoke plume from a savanna fire, *J. Geophys. Res.*, 110, D12301, doi:10.1029/2004JD005628, 2005.
- Twomey, S., *Atmospheric Aerosols*, Elsevier Scientific Publishing Company, New York, 302 pp., 1977.
- Tyson, P. D., M. Garstang, and R. Swap, Large-Scale Recirculation of Air over Southern Africa, *J. Appl. Met.*, 35, 2218-2236, 1996.
- Van de Hulst, H. C., *Light Scattering by Small Particles*, Dover Publications, Inc., New York, 1981.
- Van Poppel, L. H., H. Friedrich, J. Spinsby, S. H. Chung, J. H. Seinfeld, and P. R. Buseck, Electron tomography of nanoparticle clusters: Implications for atmospheric lifetimes and radiative forcing of soot, *Geophys. Res. Lett.*, 32, L24811, doi:10.1029/2005GL024461, 2005.
- Vanhellemont, F., D. Fussen, C. Bingen, E. Kyrola, J. Tamminen, V. Sofieva, S. Hassinen, P. Verronen, A. Seppala, J. L. Bertaux, A. Hauchecorne, F. Dalaudier, O. Fanton d'Andon, G. Barrot, A. Mangin, B. Theodore, M. Guirlet, J. B. Renard, R. Fraisse, P. Snoeij, R. Koopman, and L. Saavedra, A 2003 stratospheric aerosol extinction and PSC climatology from GOMOS measurements on Envisat, *Atmos. Chem. Phys.*, 5, 2413-2417, 2005.
- Wallace, J. M., and P. V. Hobbs, *Atmospheric Science: An Introductory Survey*, Elsevier Inc., 2<sup>nd</sup> Ed., 483 pp., 2006.
- Wild, M., C. N. Long, and A. Ohmura, Evaluation of clear-sky solar fluxes in GCMs participating in AMIP and IPCC-AR4 from a surface perspective, *J. Geophys. Res.*, 111, D01104, doi:10.1029/2005JD006118, 2006.
- Wiscombe, W. J., and G. W. Grams, The backscattered fraction in two-stream approximations, *J. Atmos. Sci.*, 33, 2440-2451, 1976.

- Wiscombe, W. Improved Mie Scattering Algorithms, *Appl. Opt.*, 19, No. 9, 1505-1509, 1980.
- Yu, H., Y. J. Kaufman, M. Chin, G. Feingold, L. A. Remer, T. L. Anderson, Y. Balkanski, N. Bellouin, O. Boucher, S. Christopher, P. DeCola, R. Kahn, D. Koch, N. Loeb, M. S. Reddy, M. Schulz, T. Takemura, and M. Zhou, A review of measurement-based assessments of the aerosol direct radiative effect and forcing, *Atmos. Chem. Phys.*, 6, 613-666, 2006.
- Zhou, M., H. Yu, R. E. Dickinson, O. Dubovik, and B. N. Holben, A normalized description of the direct effect of key aerosol types on solar radiation as estimated from Aerosol Robotic Network aerosols and Moderate Resolution Imaging Spectroradiometer albedos, *J. Geophys. Res.*, 110, D19202, doi:10.1029/2005JD005909, 2005.

## VITA

Brian Indrek Magi was born in Washington D.C. on 11 September 1976 to Mai and Mart Magi. His grandparents immigrated to America before the end of World War II to escape the subsequent 51 year Russian occupation of their home country of Estonia. His first memories of the wonders of analytical thought came while learning chess from his fraternal grandfather. Brian earned a Bachelor of Science degree in Physics and Applied Mathematics from the University of Arizona in Tucson, Arizona, in 1998. While at the University of Arizona, he was given the opportunity to apply the science he learned in the classroom to real problems, first by modeling the passage of atoms through thin films with Professor K.C. (John) Hsieh and then by taking field measurements for satellite sensor calibration with Professor Kurt Thome. In September 1999, Brian drove from Tucson to Seattle to start graduate school at the University of Washington Department of Atmospheric Sciences. He participated in aircraft-based scientific field campaigns in southern Africa and off the east coast of the United States with Professor Peter V. Hobbs and the Cloud and Aerosol Research Group. These datasets provided the foundation for many years of research. In addition to graduate school, Brian has learned to speak Estonian, been an competitive foilist in a local sport fencing club, hiked hundreds of miles in the glorious mountains of Washington, coached his young cousin's baseball team, and learned how to polka with the Seattle Estonian Folkdance Group. In July 2003, he married the amazing Heidi Taylor, and currently lives with his wife, cat, and dog in a house near the trees.